DOCTORAL THESIS

Optimization of Structured Adsorbents for Gas Separation Processes

Fateme Rezaei

LULEÅ UNIVERSITY OF TECHNOLOGY

Optimization of Structured Adsorbents for Gas Separation Processes

Fateme Rezaei

Department of Chemical Engineering
Monash University
Melbourne, Australia

Chemical Technology
Luleå University of Technology
Luleå, Sweden

Printed by Universitetstryckeriet, Luleå 2011

ISSN: 1402-1544
ISBN 978-91-7439-233-3

Luleå 2011

www.ltu.se

ABSTRACT

Conventional gas separation processes using packed beds of beads or granules suffer from high pressure drop and mass transfer resistance when higher throughputs are required, leading to lower productivity and recovery and higher power consumption. This restricts the adsorption processes using traditional adsorbents in the form of beads or granules to low throughputs and makes such processes less attractive compared to other processes such as distillation for large volume production and high productivity. Such problems could be reduced if structured adsorbents are developed and replace the traditional beds of beads or granules.

Although much research has been devoted to the development of structured adsorbents over the last decade, there is still a need to increase the understanding of structured adsorbents. Therefore, this work aimed to increase the fundamental understanding of structured adsorbents using two different approaches; a general approach by which numerical models were developed to predict the performance of structured adsorbents with different geometries in pressure/vacuum swing adsorption (PSA/VSA) processes. The effects of parameters such as porosity, density and surface area, on the performance of structured adsorbents with different geometries were evaluated. Comparisons based on mass and heat transfer, adsorbent loading and pressure drop characteristics of PSA systems for CO_2/N_2 separation were carried out. The obtained results demonstrate the potential advantage of structured adsorbents in rapid cycle adsorption processes. The even flow distribution, very low mass and heat transfer resistances and low pressure drop in combination with considerable adsorption capacity in the best structured adsorbents indicate that these novel configurations are promising adsorbents for advanced PSA/VSA applications.

The second approach was to evaluate the performance of zeolite coated monoliths prepared and tested experimentally by numerical modelling. The effects of wall porosity, channel width distribution and zeolite film thickness on the dynamic behavior of the adsorbents were examined. The model indicated that the film thickness could be increased up to about 10 μm to increase adsorption capacity without increasing the dispersion in the system further. In addition, it was shown that employment of monoliths with lower wall porosity would lead to better performance of the structured adsorbents.

CONTENTS

ACKNOWLEDGMENTS

This study was carried out at the Department of Chemical Engineering, Monash University (Australia) and at Chemical Technology, Luleå University of Technology (Sweden) from March 2008 to March 2011. Financial supports from Monash Research Graduate School (MRGS) and Chemical Technology (LTU) are very much appreciated.

I would like to take this opportunity to express my utmost gratitude to my supervisor at Monash, Prof. Paul Webley, for his invaluable guidance throughout the course of this study. It is only with his patience and guidance that I have been able to complete this process, and I am grateful for all of the opportunities that he has provided me. I also would like to acknowledge Prof. Jonas Hedlund, my supervisor at LTU for his invaluable support and advice. His guidance and advice throughout the project have been very indispensable for completion of this thesis. My appreciation goes especially to Dr. Mattias Grahn, my co-supervisor at LTU for his help and support during my stay in Luleå.

Special thanks also go to my friends and colleagues at the Department of Chemical Engineering at both Monash and LTU Universities who helped me throughout this period. Many thanks go to Lilyanne Price from Monash University for her help in all administrative chores. Sincere thanks also to Dr. Alessandra Mosca; we have been working together since March 2009 and coming up with several publications.

Of course, none of this would be possible without the continual support of my husband Ali. There is no reasonable way I can describe how he has helped me over the last few years. He has been a great source of love, motivation, and encouragement and I will be forever grateful for his help.

Finally, my greatest appreciation will always go to my loving family for their sacrifices, love, patience and supports. More especially my mother for her unending support from distances far away from me, this dissertation would not have been possible without her love and encouragement during this tedious journey.

And at long last, I would like to dedicate this thesis to my late father who never lived long enough to see me through to the end of this study. You will always be the source of my inspiration and a part of me. May your soul rest in peace and I will always love you.

LIST OF PAPERS

This doctoral thesis is based on the work reported in the following papers:

PAPER A
Structured adsorbents in gas separation processes
F.Rezaei, P. Webley
Separation and Purification Technology 70 (2010) 243 - 256

PAPER B
Optimum structured adsorbents for gas separation processes
F.Rezaei, P. Webley
Chemical Engineering Science 64 (2009) 5182 - 5191

PAPER C
Structured zeolite NaX coatings on ceramic cordierite monolith supports for PSA applications
A. Mosca, J. Hedlund, P. A. Webley, M. Grahn, F. Rezaei
Microporous and Mesoporous Materials 130 (2010) 38 - 48

PAPER D
Comparison of traditional and structured adsorbents for CO_2 separation by vacuum-swing adsorption
F. Rezaei, A. Mosca, P. Webley, J. Hedlund, P. Xiao
Industrial & Engineering Chemistry Research 49 (2010) 4832 - 4841

PAPER E
The effect of wall porosity and zeolite film thickness on the dynamic behavior of adsorbents in the form of coated monoliths
F. Rezaei, A. Mosca, J. Hedlund, P. Webley, M. Grahn, J. Mouzon
Submitted to Separation and Purification Technology

PAPER F
Thermal management of structured adsorbents in CO_2 capture process
F. Rezaei, M. Grahn
Submitted to Environmental Science & Technology and under revision

Conferences presentations not included in the thesis:

Thermal management of structured adsorbents in gas separation processes
Fateme Rezaei, Paul Webley

Oral presentation at the AIChE09 Annual Meeting, Nashville, Tennessee, USA, November 8-13, 2009

Engineered gas adsorbents, optimum structure and performance
Fateme Rezaei, Jonas Hedlund, Paul Webley
Poster presentation at the AIChE10 Annual Meeting, Salt Lake City, Utah, USA, November 7-12, 2010

Other works not included in the thesis:

Innovative process for the synthesis of vanadyl pyrophosphate as a highly selective catalyst for n-butane oxidation
A.A. Rownaghi, Taufiq-Yap, F. Rezaei
Chemical Engineering Journal 165 (2010) 328 - 335

High surface area vanadium phosphate catalyst for n-butane oxidation
A.A. Rownaghi, Taufiq-Yap, F. Rezaei
Industrial Engineering Chemistry Research 48 (2009) 7517 - 7528

Influence of Rare-Earth and Bimetallic Promoters on Various VPO Catalysts for Partial Oxidation of n-Butane
A.A. Rownaghi, Taufiq-Yap, F. Rezaei
Catalysis Letters 130 (2009) 504 - 516

Solvothermal synthesis of vanadium phosphate catalysts for n-butane oxidation
A.A. Rownaghi, Taufiq-Yap, F. Rezaei
Chemical Engineering Journal 155 (2009) 514 - 522

My contribution to the papers included in the thesis:

PAPER A. *All the literature review and most of the evaluation and writing*
PAPER B. *All the simulation work and most of the evaluation and writing*
PAPER C. *Contribution to simulation part, its evaluation and writing*
PAPER D. *All the simulation work and approximately 2/3 of the evaluation and writing*
PAPER E. *Some of the sample characterization work, all the simulation work and most of the evaluation and writing*
PAPER F. *All the simulation work and most of the evaluation and writing*

Part I

CHAPTER 1

Introduction

1.1 Adsorption process and porous adsorbents

Adsorption is a process in which a component (adsorbate) is attached to a surface (adsorbent). Adsorption depends on the existence of a force field at the surface of a solid, which reduces the potential energy of an adsorbed molecule below that of the ambient fluid phase. Depending on the nature of the surface forces there are two broad classes of adsorption: physical adsorption and chemisorption. Physical adsorption is caused mainly by van der Waals forces and electrostatic forces between adsorbate molecules and the surface atoms of the adsorbent [1]. The forces involved in chemisorption are much stronger and involve a substantial degree of electron transfer or electron sharing, as in the formation of a chemical bond. Generally, adsorbents are characterized first by surface properties such as surface area and polarity. The most common commercial adsorbents in gas separation processes include activated carbon, zeolites and molecular sieves, silica gel and activated alumina. Separation processes utilizing adsorption may be cost and energy effective alternatives to other separation processes such as distillation and absorption, particularly at low to moderate throughput. Adsorption separation processes have become a common and efficient unit operation for the separation of multi-component gas mixtures in the chemical industry [2].

1.1.1 Zeolites: structure, properties and application

Zeolites are a group of crystalline porous materials with a diversity of structure, porosity and chemical composition. Generally the framework is comprised of silicon, aluminium and oxygen and cations and water and/or other molecules may be present in the pores [3]. A general formula for zeolites is:

$$M_{x/n}[(AlO_2)_x(SiO_2)_y].wH_2O \qquad (1.1)$$

where M is a cation of valence n, y/x is the silicon/aluminium ratio (Si/Al), and w is the number of water molecules. Zeolites occur naturally as minerals, and are mined in many parts of the world. Zeolites can also be prepared synthetically. All known zeolite frameworks have been assigned a three letter code and today there are over 190 known framework structures [4]. Zeolites find various applications in adsorption processes, heterogeneous catalysis, ion exchange and most recently heat pumps. Zeolites are one of the main components in detergents (zeolite A), where the ion-exchange properties are used to soften the water. In this work, zeolite X with FAU framework was studied. The

FAU framework has a three-dimensional pore system with pores running perpendicular to each other, as shown in Figure 1.1. Two zeolites have the same FAU framework, namely zeolite X and zeolite Y, and the difference between these two zeolites is only the Si/Al ratio, which varies between 1 and 1.5 for zeolite X, and between 1.5 and 5.6 for zeolite Y [3, 5].

Figure 1.1: The FAU framework.

Zeolite X is mainly used for O_2 enrichment from air and air dehumidification by adsorption, while the main application of zeolite Y is catalytic cracking in the FCC process. Zeolite NaX is the most common adsorbent for CO_2 capture [3]. In Figure 1.2, the CO_2 equilibrium isotherm on NaX at 298K is shown [6]. The isotherm shows that CO_2 is favourably adsorbed by NaX zeolite. The isotherm has a very steep slope at low pressures, and high loading is reached at high pressures, which illustrates the suitability of this kind of zeolite for CO_2 separations.

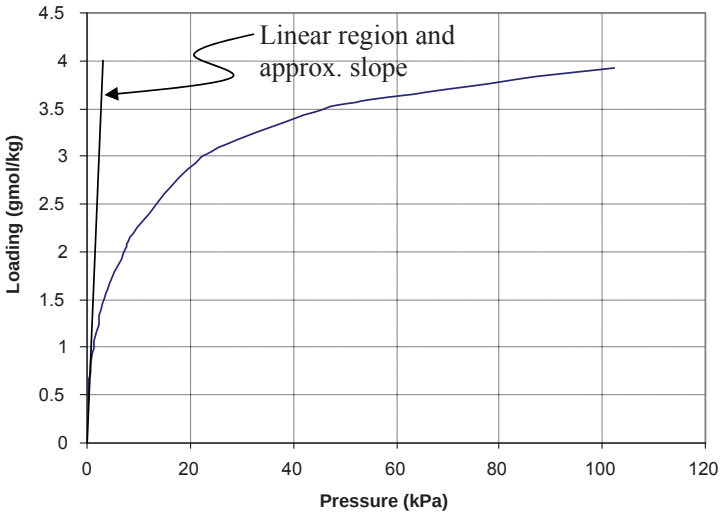

Figure 1.2: Adsorption isotherm for CO_2 on NaX zeolite at 298K [6].

1.2 Adsorptive gas separation

The most common applications for adsorption-based gas separation include air separation, H_2 purification, CO_2 removal, dehumidification of gas streams, hydrocarbon separation and natural gas upgrading. Basically, there are three different types of physical mechanisms through which the separation of a gas mixture can be accomplished by adsorption: equilibrium, kinetic, and steric mechanisms [2]. The equilibrium mechanism is based on differences in the strength of attraction of the adsorbate to the adsorbent; the kinetic mechanism is based on the differences in the rates of adsorption and/or transport of adsorbate on and through an adsorbent; the steric effect derives from the molecular sieving property and is based on the incompatibility between the size or shape of the pores in the adsorbent and those of the adsorbate gas molecules. Currently, the most common gas separations used at large scales in the industry are based on the equilibrium mechanism.

1.2.1 Cyclic adsorption processes

Adsorption/desorption is mainly performed by periodic variation of pressure or temperature of the adsorber column, as shown in Figure 1.3.

Pressure swing adsorption (PSA) is the most widely used technology for bulk gas separation. It was invented by *Skarstrom* in 1959 for separation of oxygen and nitrogen from air using a four step cycle [7]. The PSA process is mainly based on exploiting the difference in working capacity exhibited by an adsorbate-adsorbent system when step changes in the operating pressure are applied. In many PSA processes, the desired product is the less adsorbed component, and the more adsorbed component is discarded with no concern of purity. Over the last 30 years, there have been rapid growth in the development of PSA technology, leading to the advent of new configurations such as rapid PSA or piston-driven PSA systems, with cycle times much shorter (less than 20 sec.) than the conventional systems (120-1200 sec.) [8].

Temperature swing adsorption (TSA) has been a widely used technology for the removal and recovery of trace amount of pollutants such as volatile organic compounds (VOCs) from gaseous streams. The process is based on adsorption at low temperature and desorption at high temperature. TSA cycle times are usually quite long (several hours to several days), which results in high energy consumption and large adsorbent inventories. Therefore, TSA systems are not good candidates for bulk separation applications. TSA is however preferred to PSA in the case of strongly adsorbed species, for which a variation of pressure is not efficient to regenerate the adsorbent [7].

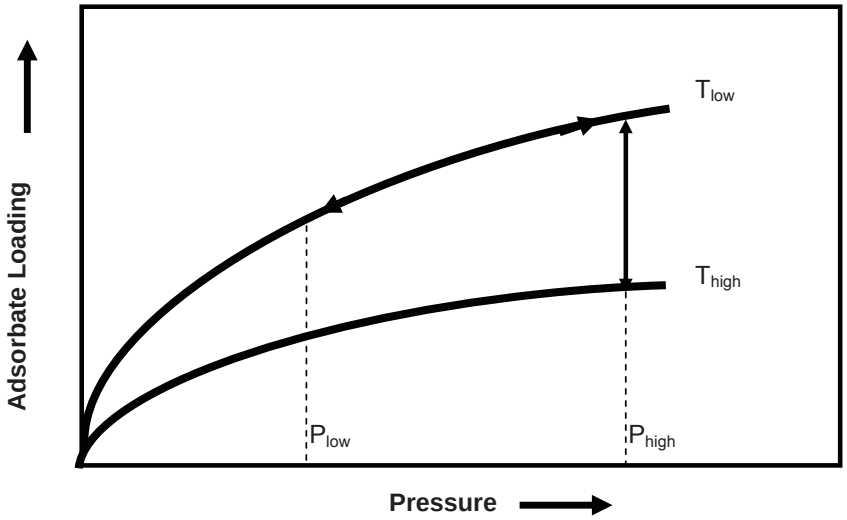

Figure 1.3: Schematic representation of cyclic adsorption-based separation.

In cyclic processes such as PSA and TSA, reducing cycle time is the primary means of achieving more production from a given quantity of material. However, as cycle time is reduced, cyclic processes usually face the problem of decreasing working capacity per cycle for the component of interest, decreasing product recovery and increasing pressure drop. The extent to which cycle time reduces working capacity and recovery and increases pressure drop is dependent on the structure of the adsorbent [9].

1.2.2 Conventional and novel adsorbents

Conventional gas separation systems are using adsorbents in the form of beads or granules. However, mass transfer and pressure drop drawbacks associated with conventional packed beds impose limitations in operating the process at optimum conditions in terms of energy consumption and overall system efficiency and do not allow operating the process at short cycle times (more than a few cycles per minute). Reducing particle size is the most obvious way to decrease mass transfer resistance (which is proportional to the square of particle size) and the trend over the last few decades has been a reduction of particle size from 2-3 mm to less than 0.7 mm. Combating the accompanying increase in pressure drop with reduction in particle size has led to bed geometries of a "pancake" nature *i.e.* height/diameter ratios considerably less than one. However, considerable gas maldistribution and channelling not to mention potential fluidization of packed beds becomes issues to tackle. An alternate approach to simply reducing particle size is to develop non-particulate, novel adsorbent structures.

The use of traditional adsorbent materials in the form of beads or granules in gas separation processes is compromised when an efficient process with high performance and low energy demand is required. Novel adsorbent geometries should satisfy a number

of requirements in order to be considered as suitable candidates for replacement of pellet/bead configurations. In particular, such structures should display good mass transfer kinetics with large external and solid mass transfer coefficients. Furthermore, the structured adsorbents must exhibit sufficient volume working capacity (loading per unit system volume) as well as sufficiently low voidage for minimizing the size of the adsorber. In addition, the structures should result in low pressure drop, even flow distribution and no fluidization.

Figure 1.4 illustrates some possible novel adsorbent structures as well as conventional beaded adsorbents. In this Figure, beads and granules are shown as examples of common adsorbent configurations currently used in industry; while activated carbon monoliths (black monoliths in the Figure), cordierite monoliths, activated carbon fabric and corrugated paper monoliths represent novel structures in adsorption-based separation processes.

Figure 1.4: Illustration of a variety of adsorbent structures including (left to right): ceramic and carbon adsorbent monoliths, corrugated paper monoliths (centre), fabric adsorbent and conventional beaded adsorbents.

1.3 Criteria for the evaluation of adsorbents

1.3.1 Volumetric working capacity and adsorbent loading

Volumetric working capacity is defined here as moles of gas processed per unit volume per cycle. This is the product of the working capacity (moles of gas adsorbed/desorbed per unit mass of adsorbent including binder, support, *etc.*) and the density of the composite adsorbent. The throughput attainable in a given volume of vessel in a cyclic adsorption system may be expressed as:

$$throughput\ (mole/s.m^3) = \frac{WC^*\rho_B}{\tau} \tag{1.2}$$

where WC is the working capacity (moles/$kg_{adsorbent}$/cycle), ρ_B is the bulk adsorbent density ($kg_{adsorbent}/m^3$) and τ is the cycle time (s/cycle). Although structured adsorbents are developed with the aim of operation at shorter cycle times (lower τ), any development which simultaneously reduces adsorbent density (ρ_B) is detrimental to throughput. Thus although structured adsorbents may have remarkable advantages over adsorbent pellets such as superior mass transfer kinetics (due to shorter diffusion path) and effective heat transfer in all directions, as well as more uniform temperature distribution, their throughput may be lower, if the adsorbent loading on a mass or volume basis is small compared to adsorbent materials in the form of pellets/beads.

It is worth mentioning that high adsorbent loading may not always be a desirable parameter in all adsorptive processes if other features are compromised. For instance, in some adsorptive systems, mass and heat transfer processes dominate system performance (*e.g.* removing moisture from air) and hence reducing the characteristic diffusion length is more important than adsorbent loading. In terms of equation 1.2, high ρ_B may compromise WC and hence an optimum throughput may exist.

1.3.2 Pressure drop

Pressure drop impacts system performance in several ways. The existence of a pressure profile in the axial direction in an adsorption process (both during adsorption and desorption) implies that not all of the adsorbent experiences the full pressure swing available to the system. This directly reduces the working capacity, WC. The problem is especially acute for vacuum swing adsorption processes, in which low pressures are needed for adsorbent regeneration *e.g.* CO_2VSA [10]. In addition, increased pressure drop increases energy consumption. One option to circumvent the high pressure drop problem of conventional packed beds without changing the type of adsorbent is to utilize radial bed adsorbers [11]. Radial beds produce lower pressure drop for the same mass flow rate due to the expanding radius in the direction of flow. Shorter cycle time and higher throughputs without fluidization are possible, although their design is complex and costly.

To describe the role of system parameters contributing to pressure drop in a packed bed, the well known *Ergun* equation [12] is considered here:

$$\frac{\Delta P}{L} = 150\frac{(1-\varepsilon)^2}{\varepsilon^3}\frac{\mu}{{d_p}^2}U + 1.75\frac{(1-\varepsilon)}{\varepsilon^3}\frac{\rho}{d_p}U^2 \tag{1.3}$$

where U is the superficial velocity, ρ and μ the density and viscosity of the gas respectively, d_p is the particle diameter and ε is the bed voidage. Clearly, decreased void volume and particle size both increase pressure drop.

1.3.3 Mass transfer characteristics

Theoretical and experimental studies [13-16] have shown the influence of adsorbent structure on mass transfer kinetics, which in turn influences the overall system efficiency.

The overall mass transfer coefficient, k, for systems with linear isotherms obeying the linear driving force model can be evaluated through the relationship [7]:

$$\frac{1}{kK} = \frac{R_p}{3k_f} + \frac{{R_p}^2}{15\varepsilon_p D_p} + \frac{{r_c}^2}{15KD_c} + \left(\frac{1-\varepsilon}{\varepsilon}\right)\frac{D_L}{U^2} \tag{1.4}$$

where K is the equilibrium constant, k_f is the external film coefficient, R_p and r_c are particle and crystal radii respectively, D_p and D_c are pore and intracrystalline diffusivity respectively and D_L is axial dispersion. The relative importance of internal and external resistances is expressed by the mass *Biot* number $k_f L/D$ where L is a characteristic dimension (particle diameter) and D the internal diffusion coefficient. Generally speaking, micropore diffusion resistance dominates over film and macropore resistances if [7]:

$$\frac{D_p / {R_p}^2}{D_c / {r_c}^2} >> 1 + \left(\frac{1-\varepsilon}{\varepsilon}\right)K \qquad \text{and} \qquad \frac{5D_p}{kR_p} << 1$$

The opposite situation holds for macropore diffusion.

For pellet adsorbents, the external film resistance is seldom limiting the overall mass transfer and can usually be neglected ($(Bi)_m >> 1$) [2]. However, external film diffusion may be important for structured adsorbents and should be considered when modelling and designing these systems.

The contribution of axial dispersion to k for pellets, is usually small (similar to external diffusion) and can justifiably be neglected. The plug flow assumption is therefore adequate.

It should be noted that the binder in adsorbent structures may influence the mass transfer. In certain applications such as dehumidification processes, wherein the diffusivity of the adsorbate molecule (water) through the binder layer is high, the binder material does not reduce the overall kinetics of the process. In contrast, in processes such as air separations, the binder serves as a kinetic barrier to adsorbate molecules.

1.3.4 Thermal management

Novel adsorbent structures should be optimized with respect to heat transfer. Since adsorption is exothermic and desorption endothermic, a thermal swing accompanies the pressure swing and is usually reducing the overall system performance (reducing capacity on adsorption and increasing it on desorption), sometimes by as much as 30% for traditional adsorbents [17]. Efficient transfer of heat to and from the adsorbent can significantly improve system performance and a structured adsorbent may offer opportunities to accomplish this. As a first estimate, the temperature swing at a point in the bed is given by [8]:

$$\Delta T = \frac{WC * \Delta H}{C_s} \tag{1.5}$$

where WC is the working capacity, ΔH is the heat of adsorption and C_s is the solid specific heat (kJ/kg). To reduce the effect of this temperature swing for packed beds, several approaches have been attempted including insertion of heat transfer devices into the packed bed [18], or use of metallic compounds or phase change materials to either increase C_s or absorb the heat of adsorption [19].

This is a fertile area for future research since not only can adsorbent structure manage heat more effectively in a passive mode, but they may in fact offer opportunities for "active" thermal management (in processes such as Electrical Swing Adsorption).

1.3.5 Trade-off between properties

The design of adsorbent structures involves, inevitably a trade-off between a number of parameters which govern the overall adsorbent performance. Adsorbents with high working capacity and fast kinetics would be ideal for cyclic separation processes, however these requirements can hardly be combined for traditional adsorbents [9].

In the case of beads there is always a trade-off between pressure drop and mass/heat transport characteristics, smaller pellets display better mass/heat kinetics, while the pressure drop is dramatically increased. External surface area per unit volume of adsorbent is one of the most important characteristics governing the performance of adsorbents but higher surface area is usually associated with lower adsorbent density. For laminate, cloth and monolith structures, in order to maintain a sufficient surface area and hence improved kinetic properties, the wall thickness and spacing should be kept small. Thinner wall thickness means shorter diffusion path but on the other hand, lower adsorbent loading associated with thinner walls will result in insufficient adsorbent density. The same argument is valid for adsorbent voidage. High voidage may be associated with faster kinetics, however, the bed density is low, which gives rise to lower working capacity. Small spacing between adjacent sheets or small channels increases the pressure drop as well. Such trade-off behaviours should always be taken into consideration when dealing with adsorbent structure [20].

1.4 Novel adsorbent configurations

A large variety of novel structured adsorbents have been studied by scientists and some has also been commercialized over the last 10 years. The structures are categorized here as monoliths, laminates, foams, fabric structures and other configurations. Alternatively, a film may be grown on the monoliths, laminates or foams to form an active adsorbent. Although decreased void volume also increases pressure drop for structured adsorbents however, it is easier in parallel channel adsorbents to control ε to obtain satisfactory performance. In addition, the tortuosity of the channels in a monolith or laminate structures is 1, compared with 2-3 for a packed bed of granules [21]. Therefore the pressure drop in a packed bed is larger than in a monolith structure for equal voidage. Furthermore, the system geometry in laminates and monoliths can be optimized to achieve lower head loss. This is achieved by decreasing cell density or wall thickness in monoliths and increasing sheet spacing and decreasing wall thickness in laminates. Generally, parallel channels exhibit better performance with respect to pressure drop; however they must be carefully designed to avoid too much loss of adsorbent loading and large diffusion paths (wall thickness) [13].

1.4.1 Monolithic adsorbents

In recent years, monolithic adsorbents have received considerable attention for use in adsorption systems [22-24]. Monoliths are structured materials composed of parallel channels with a variety of cross sectional shapes that usually display very low pressure drop. Such structures have been widely used as a catalyst support in various applications including catalytic combustion, biochemical and electrochemical reactors, automotive catalytic convertors, *etc*. [25].

Early attempts in the use of monolithic adsorbent structures for separation process were mostly related to elimination of VOCs from air [26, 27]. MAST Carbon, a developer of materials of activated carbon, produces a variety of activated carbon monoliths for a range of applications including (but not limited to) VOC removal.

The geometric parameters of monoliths which influence the processing requirements are defined in terms of cell density, cell spacing or wall thickness. The cell density of monoliths is defined as the number of cells per unit of cross-sectional area and expressed as cells per square inch (cpsi). For constant gas viscosity, monolith length, and open frontal area, the pressure drop of monolith adsorbents increases with increasing cell density. On the other hand, for constant cell density, the pressure drop decreases with decreasing wall thickness. Thus monoliths are one of the most efficient methods available to pack high external adsorbent surface area into a fixed volume while still maintaining low pressure drop. However, although the unique structure of monoliths significantly reduces many of the common problems of conventional adsorbents (*i.e.* fluidization, high pressure drop, *etc*.), these structures may display low loading of active adsorbent material. In addition, not all the adsorbent material present in the monolith wall may be accessible to the adsorbate molecules passing through the channels [28]. The active adsorbent material may be directly extruded in the form of a structured monolith (commonly done for carbon monoliths in which case the entire monolith is active adsorbent) or an active film may be deposited on the monolithic structures by various methods, namely, dip-coating, wash-coating, and slip-coating [29]. Alternatively, a film may be grown by hydrothermal treatment on the walls of porous ceramic cordierite monolith as explored by our research group [22, 23, 30-32]. The zeolite film grown by this method is dense and uniform and the mass transfer resistance is dependent of film thickness.

Monoliths have two major resistances to mass transfer; external film resistance, and pore diffusion within the monolith walls or alternatively, in the film grown on the monolith. The characteristic diffusion length can be shortened by employing a thinner adsorbent wall. Alternatively, a thin film of active material on a monolith support can also mitigate the problem related to diffusion length as explored by our research group. The low pressure drop of monoliths and laminates must be exploited by using long beds to give sufficient residence times. High cell density is advantageous since it results in high adsorbent loading and short diffusion lengths.

1.4.2 Laminate adsorbents

Laminate structures can be considered a simpler form of monoliths in which the channels are replaced by 1D slits. As with monoliths, laminates can potentially exhibit significantly better performance than a packed bed. The practical difficulties involved in reproducibly making such structures are not trivial however. The tolerances between

sheets should be tight (< 5%) to avoid flow maldistribution and the spacing should be small and uniform [13]. As a result of this difficult manufacturing process, the use of laminate adsorbents in separation processes is not common. There are a few patents which describe the use of adsorbent materials in the form of laminate sheets in adsorptive gas separation applications [20, 33-35].

In laminate structures, the pressure drop per unit length may be controlled by altering the space between adjacent sheets. Like monolithic structures, thin sheets with small spacing increases pressure drop but also increases adsorbent loading and decreases mass transfer resistance. Spacing can be achieved using different approaches such as corrugating the laminates or making ridges on the sheets. The spaces between adjacent layers could be also created using external spacing devices such as mesh or grid. Care must be taken to ensure that the spacer does not contribute to higher pressure drop nor obstruct the gas flow through the adsorbent.

Like monoliths, laminate adsorbents suffer from the problem of low adsorbent density due to several factors. A binder is usually present in the adsorbent matrix in addition to the presence of an external support. These non-adsorbent components directly reduce the volume loading of the adsorbent. This is in contrast to fabrics or self-supporting adsorbents that have higher adsorbent density. Laminate sheets can be packed into corrugated layers to increase adsorbent loading (and surface area) [36].

1.4.3 Foam structures

Ceramic foams have many attractive features as catalyst supports, however, reports on their utilization in adsorptive gas separation applications is scarce. These types of adsorbents may have substantial benefits over other adsorbent configurations. They offer high geometric surface area resulting in an increase in the rate of external mass transfer and due to their inherent large porosity, these structures are capable of maintaining a lower pressure drop than a packed bed of pellets/beads [37]. However, it is argued that such structures may not be suitable candidates in cyclic adsorption processes such as PSA or partial PSA processes because of the adsorbent's high tortuosity and porosity which decrease separation performance [38].

Due to the inherent high porosity of foam adsorbents, the amount of active material may not be adequate to exhibit the same volume activity as a packed bed of pellets, however, this problem could be reduced through adjusting the amount of adsorbent coating on the foam. As with monolith adsorbents, the flow friction and hence the pressure drop is decreased due to the larger flow channels and presence of large number of voids, which allows the radial mixing of flow. This is the advantage (high bed porosity) of foam adsorbents over monolithic structures in which laminar flow does not allow radial mixing. Typically, higher voidage in the bed is favoured for operation at high velocities (*i.e.* high cycle frequency in cyclic operations) where pressure drop become crucial [38].

There has been extensive research on preparation of zeolite foams using polymeric templates [38, 39], but despite the promising advantages offered by foam structures, the employment of zeolitic foams in gas separation processes have not been studied yet. Yoon et al. [39] prepared zeolite foams using a polymeric template capable of releasing an amine to crystallize zeolite or zeotype materials. The template and the final adsorbent had a sponge structure. According to the authors, since there is no blocking problem due

to a binding agent and since the zeolite is formed in the form of a thin layer in the foam, gas can freely move inside the zeolite foam and the accessibility of the zeolite should be high. Moreover, due to the presence of macropores which are spatially connected to each other and are large enough for molecules to freely enter and leave, the pressure drop should be low.

In another work reported by Buciuman and Kraushaar-Czarnetzki [40], ceramic foams were partially coated with nano particles of MFI zeolites (100-650 nm) by a dipping technique without the addition of binder materials. However, the practical application of such zeolite coated ceramic foam was not investigated.

1.4.4 Fabric structures

Adsorbent fabrics present advantageous features for gas separation application. The use of adsorbent fabrics in adsorption processes was first reported in the early 1980s when Bailey et al. [41] described the application of charcoal cloth in adsorptive filters for air purification process. Golden, et al. [9] reports the use of adsorbent fabrics with average pore diameter from 12-15 Å in rapid PSA systems for CO_2 capturing and H_2 recovery. Sawad, et al. [38] demonstrated coating activated carbon powder onto a fabric, cloth or felt made from activated carbon fibres. Since these adsorbents are comprised entirely of active material of thin fibres, high adsorbent loadings and rapid mass transfer may be provided. Adsorbent fabric can be prepared in various configurations in such a way that it still maintains the benefits of the fabric. The preferred configurations are parallel sheets and spiral wound structures. Additional advantages potentially offered by flexible adsorbent fabrics are lower attrition rates and higher mechanical strength [9]. There is often no requirement for external support or spacers [20]. The heat transport characteristics of fabric adsorbents could be enhanced by employing materials with high thermal conductivity (by coating or impregnation techniques or weaving). Self-supporting cloths offer low resistance to gas flow and of course eliminate fluidization issues [41].

1.4.5 Other structures

In the case of traditional pellets used in adsorptive gas separation, recent advances have been achieved for preparation of binderless pellets by converting the binder material to an active adsorbent in order to maximize the density of the active adsorbent material. Attempts have been made to improve the fabrication process of beads/pellets; synthesizing of particles with controllable physical properties and well-ordered structures with uniform pore size distribution are among them. However, the most important drawback with high pressure drop remains a large challenge which motivates the use of other structures [38].

Monolithic carbon discs combined with aluminium fins, are among other configurations that have recently gained interest in adsorption applications such as heat pumps, adsorption refrigerators, *etc*. [42-44].

Another class of structured materials is zeolite coated alumina beads, steel, quartz or glass; these kinds of structures have been evaluated as catalysts. For example, Öhrman et al. [45] reported the application of MFI coated alumina beads for *para*-xylene isomerization and triisopropylbenzene cracking.

1.5 Scope of the present work

In this work, the performance of structured adsorbents was numerically evaluated to increase the fundamental understanding of these materials in gas separation processes. Two different approaches were used:

- The general approach: to evaluate the general characteristics of structured adsorbents in gas separation systems by numerical modelling.

- The specific approach: to prepare and evaluate the performance of zeolite coated monoliths in CO_2 adsorption processes by combining breakthrough experiments and numerical modelling.

CHAPTER 2

Numerical simulation

2.1 General characteristics of structured adsorbents, Papers B & F

A variety of analytical and numerical models were used to examine the performance of different adsorbent configurations. In particular, monolithic, laminate, and foam structures were evaluated and compared to a packed bed of pellets. The physical characteristics of structures considered for comparison are presented in Table 2.1 while in Figure 2.1, some geometrical parameters of monoliths and laminates are shown. Simulations were performed using COMSOL 3.5a employing the Lagrange Quadratic Finite Element method. The considered gas was 10% CO_2 in N_2 and the adsorbent was taken to be NaX. Under isothermal condition, a linear isotherm was assumed for calculating equilibrium parameters (see Figure 1.2) which was adapted from Hyun and Danner [6] while under non-isothermal conditions, a Dual-Site Langmuir isotherm was used. The physical properties of the adsorbent were considered to be the same for all geometries. Brief descriptions of the models are given below and details are reported in papers B and F and in references therein.

2.1.1 Mass transfer models

A differential mass balance for the adsorbate in the gas phase flowing through a structure (independent of geometry) gives:

$$\varepsilon_b \frac{\partial C}{\partial t} - D_L \frac{\partial^2 C}{\partial z^2} + \frac{\partial UC}{\partial z} = -\bar{k} a \left(C - \overline{C}^{\,p} \right) \tag{2.1}$$

where C and $\overline{C}^{\,p}$ are the concentration of the adsorbate in the gas phase and the average concentration in the pores of the adsorbent, respectively. Also, in the above equation a is the specific surface area per unit bed volume, U is the superficial fluid velocity, $\bar{k}$ is the total mass transfer coefficient, D_L is the axial dispersion coefficient and ε_b is the bed void fraction. As written, equation 2.1 includes axial dispersion explicitly. A differential mass balance for the adsorbate inside the solid phase is given by:

$$\varepsilon_p \frac{\partial \overline{C}^{\,p}}{\partial t} + \rho_s \frac{\partial \bar{q}}{\partial t} = +\bar{k} \alpha \left(C - \overline{C}^{\,p} \right) \tag{2.2}$$

Table 2.1: Physical properties of structures used in the computations.

Structure	Bed voidage	Adsorbent mass, g	Bed density (g/cm^3)	Specific surface area (cm^2/cm^3)	Adsorbent width (mm)	Cell size (mm)	Total voidage
Pellet 0.7 mm	0.37	64.7	0.69	54.0	0.35	-------	0.75
Monolith 200 cpsi	0.65	35.9	0.38	18.0	0.35	1.45	0.86
Monolith 400 cpsi	0.65	35.9	0.38	25.4	0.25	1.02	0.86
Monolith 600 cpsi	0.65	35.9	0.38	31.1	0.20	0.84	0.86
Laminate 0.5×0.5 mm	0.50	51.3	0.54	20.0	0.50	0.50	0.80
Laminate 0.3×0.3 mm	0.50	51.3	0.54	33.3	0.30	0.30	0.80
Laminate 0.2×0.2 mm	0.50	51.3	0.54	50.0	0.20	0.20	0.80
Laminate, 0.1×0.1 mm	0.50	51.3	0.54	100.0	0.10	0.10	0.80
Foam 20 ppi	0.80	20.5	0.22	19.7	0.81	-------	0.80
Foam 30 ppi	0.80	20.5	0.22	26.7	0.60	-------	0.82
Foam 45 ppi	0.80	20.5	0.22	37.2	0.43	-------	0.81

where ε_p is the solid void fraction, α is a geometric factor which is different for each adsorbent structure, see Table 2.2, ρ_s is the adsorbent density (includes binder, support, *etc.*) and $\bar{q}$ is the average adsorbent loading.

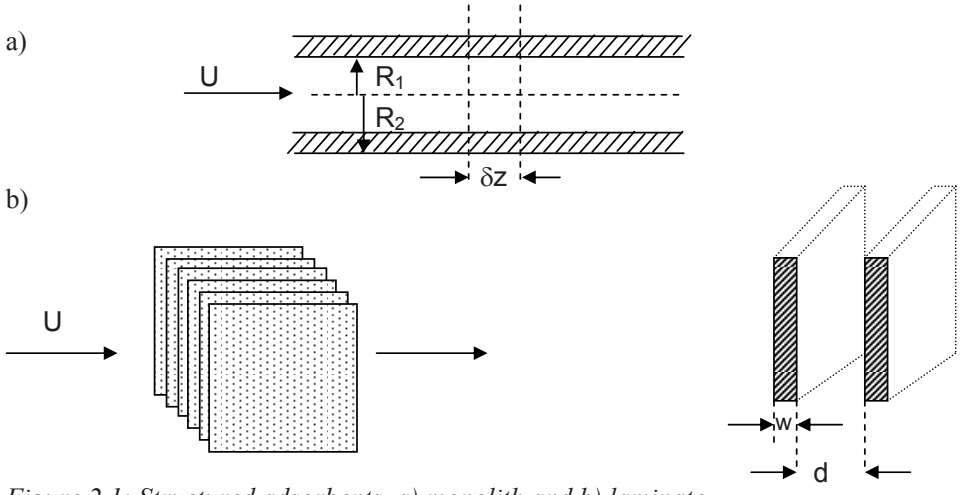

Figure 2.1: Structured adsorbents, a) monolith and b) laminate.

The initial and boundary conditions appropriate to a breakthrough simulation for the above equations are:

$$C\ (t = 0) = 0,\ \bar{q}(t=0) = 0\ ,\ \overline{C}^{p}(t=0) = 0 \tag{2.3}$$

$$C_0 + \left.\frac{\partial C}{\partial z}\right|_{z=0} = 0 \tag{2.4}$$

$$\left.\frac{\partial C}{\partial z}\right|_{z=L} = 0 \tag{2.5}$$

Equations 2.1 and 2.2 are based on the assumption that the concentration profile in the solid phase is parabolic and the constants in these equations related to each structure have been summarized in Table 2.2. In this model, local equilibrium is assumed to exist between the adsorbed and the gas species within the pores (*i.e.* there is only pore resistance in the system).

The total mass transfer coefficient can be represented as follow:

$$\frac{1}{\bar{k}} = \frac{1}{k_f} + \frac{1}{k_p} \tag{2.6}$$

where k_f and k_p are film and pore mass transfer coefficients respectively.

Table 2.2: Adsorption parameters related to each structured adsorbent, Paper B.

Adsorbent	$\bar{k}$	a	α	ε_b
Pellet/Bead	$\frac{1}{\frac{1}{k_f} + \frac{R_p}{5D_e}}$	$\frac{3(1-\varepsilon_b)}{R_p}$	$\frac{3}{R_p}$	0.35-0.4
Monolith	$\frac{1}{\frac{1}{k_f} + \frac{R_2^2 - R_1^2}{4R_1 D_e}}$	$\frac{2\varepsilon_b}{R_1}$	$\frac{2R_1}{R_2^2 - R_1^2}$	$\left(\frac{2R_1}{R_1 + R_2}\right)^2$
Laminate	$\frac{1}{\frac{1}{k_f} + \frac{W}{6D_e}}$	$\frac{2\varepsilon_b}{d}$	$\frac{2}{\mathrm{W}}$	$\left(\frac{d}{d + 2W}\right)$
Foam	$\frac{1}{\frac{1}{k_f} + \frac{R_P}{4D_e}}$	$\frac{2\varepsilon_b}{R_p}$	$\frac{2}{R_p}$	0.75-0.85

For linear adsorption isotherm models, the contribution of dispersion can alternatively be estimated by adding the term D_L/U^2 to the mass transfer coefficient of the adsorbent [7], thus the overall rate constant is:

$$\left(\frac{1}{k}\right)_{overall} = \left(\frac{1}{k}\right)_{mass\_trans\ fer} + \frac{D_L}{U^2} \tag{2.7}$$

Estimation of the mass transfer rate constant, $k_{mass\_transfer}$ is performed by assuming a parabolic concentration profile in the adsorbent material and a linear driving force based on a gas concentration driving force (LDF) model.

2.1.2 Mass Transfer Zone (MTZ)

The mass transfer zone (MTZ) is created by dispersion resulting from all of the dispersive forces in the system as encapsulated by the overall (total) rate constant *k*. Figure 2.2 illustrates the MTZ in an adsorption bed.

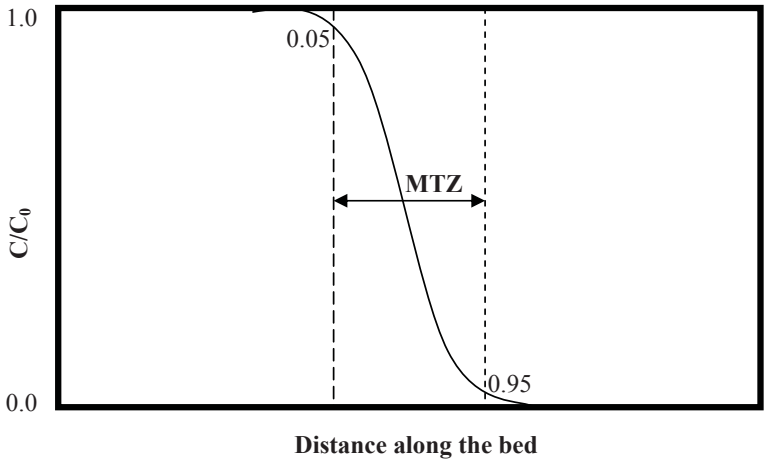

Figure 2.2: Illustration of mass transfer zone (MTZ).

The width of the mass transfer zone is the product of the zone velocity and the extent of spreading:

$$MTZ = \beta(t_2 - t_1) \tag{2.8}$$

where t_2 and t_1 are the two times of breakthrough (5% and 95% of the outlet concentration). The zone velocity, β, can be obtained from a simple rearrangement of the governing equations. Assuming constant velocity, the velocity of the mass transfer zone, β may be approximated by:

$$\beta = \frac{U}{\varepsilon_b + \left(\frac{a}{\alpha}\right)\rho_s\left(\frac{\partial \bar{q}}{\partial C}\right)} \tag{2.9}$$

The difference in breakthrough time t_1 and t_2 can be derived from constant pattern analyses as shown by Sircar and Kumar [46] and it follows that (t_2 - t_1) is inversely

proportional to the total rate constant, $\bar{k}$, for constant pattern conditions *i.e.* $(t_2-t_1) \propto 1/(\alpha\bar{k})$. Combining these equations gives proportionality for the mass transfer zone:

$$MTZ \propto \frac{U}{\alpha\varepsilon_b\bar{k} + a\bar{k}\rho_s\left(\partial\bar{q}/\partial C\right)} \tag{2.10}$$

This equation shows the major dependency of the MTZ on superficial velocity, U, and rate constant as well as geometric factors a and α.

2.1.3 Pressure drop

The pressure drop for pellets was estimated using the *Ergun* equation [12]:

$$\frac{\Delta P}{L} = 150\frac{(1-\varepsilon)^2}{\varepsilon^3}\frac{\mu}{{d_p}^2}U + 1.75\frac{(1-\varepsilon)}{\varepsilon^3}\frac{\rho}{d_p}U^2 \tag{2.11}$$

where, ρ and μ are density and viscosity of the flowing gas. For monolithic and laminate structures, the *Hagen-Poiseuille* equation [47] was applied:

$$\frac{\Delta P}{L} = \frac{32\mu}{{d_p}^2\varepsilon_b}U \tag{2.12}$$

The pressure drop in the foam adsorbents was calculated from equations recently proposed by Richardson et al. [48] in which the authors, based on the work of Gibson and Ashby [49] considered that the cellular medium is formed by uniform tri-dimensional cells.

$$\frac{\Delta P}{L} = \frac{\alpha_1 s^2(1-\varepsilon)^2}{\varepsilon^3}\mu U + \frac{\alpha_2 s(1-\varepsilon)}{\varepsilon^3}\rho U^2 \tag{2.13}$$

where α_1 and α_2 and s can be calculated using following expressions:

$$\alpha_1 = 973{d_p}^{0.743}(1-\varepsilon)^{-0.0982} \tag{2.14}$$

$$\alpha_2 = 368{d_p}^{-0.7523}(1-\varepsilon)^{0.07158} \tag{2.15}$$

$$s = \frac{12.979[1-0.971(1-\varepsilon)^{0.5}]}{d_p(1-\varepsilon)^{0.5}} \tag{2.16}$$

2.1.4 Specific productivity

In a gas separation process, the goal is usually to maximize specific productivity *i.e.* to be able to maximize throughput in a given amount of adsorbent [50]. It is therefore necessary to consider an appropriate combination of process parameters to demonstrate

how the pressure drop, cycle time and adsorption front affect system performance. The specific productivity is given by:

$$specific\ \ productivity(\text{mol/Kg.s}) = k'\frac{WC}{\tau} \tag{2.17}$$

where k' is a proportionality constant. The effect of pressure drop on the productivity is a reduction of the overall working capacity. Instead of operating between the highest possible pressure P_H and lowest possible pressure P_L generated in the system, the average bed pressure on adsorption is only P_H-$\Delta P/2$ and the average bed pressure on desorption is P_L+$\Delta P/2$. Generally (for any isotherm), the working capacity will be reduced by some function of ΔP written as $f_1(\Delta P)$.

The effect of MTZ on the specific productivity is a reduction on the effective length of bed which also translates to a reduction in working capacity. Again, this can be represented generally as some function f_2 of the MTZ. The specific productivity can therefore be written as:

$$specific\ \ productivity = \frac{k'[WC - f_1(\Delta P) - f_2(MTZ)]}{\tau} \tag{2.18}$$

where f_1 and f_2 are functions of ΔP and MTZ, respectively. Since the cycle time is inversely proportional to bed velocity:

$$\tau \propto \frac{1}{U}$$

the specific productivity equation can be further rearranged to:

$$\begin{aligned} specific\ \ productivity &= k''[WC - f_1(\Delta P) - f_2(MTZ)]U \\ &= k''[WC - f_1(\Delta P(U)) - f_2(MTZ(U))]U \end{aligned} \tag{2.19}$$

where k'' is another proportionality constant and the dependence of pressure drop and mass transfer zone on velocity is made explicit. For no pressure drop in the system and a linear isotherm, the ideal amount of adsorbate loading per mass of adsorbent is given by:

$$WC = \Delta n_{ideal} = K(P_H - P_L) \tag{2.20}$$

The working capacity for the system with pressure drop and a mass transfer zone is therefore (to a first approximation):

$$\begin{aligned} \Delta n_{non-ideal} &= \left(K((P_H - \frac{\Delta P}{2}) - (P_L + \frac{\Delta P}{2})) \right)\left(1 - \frac{MTZ}{L}\right) \\ &= \left(K(P_H - P_L) - K\Delta P\right)\left(1 - \frac{MTZ}{L}\right) \end{aligned} \tag{2.21}$$

$$\Delta n_{non-ideal} = \left(\Delta n_{ideal} - K\Delta P\right)\left(1 - \frac{MTZ}{L}\right) \tag{2.22}$$

The specific productivity of the adsorbent system can hence be represented by the following correlation:

$$specific\ \ productivity = k''(\Delta n_{ideal} - K\Delta P)\left(1 - \frac{MTZ}{L}\right)U \tag{2.23}$$

Equation 2.23 indicates that specific productivity is proportional to the superficial velocity and inversely proportional to MTZ and ΔP. Therefore any factor affecting the MTZ and ΔP may influence the specific productivity. Specifically, the trade-off in specific productivity as a function of velocity is clear.

2.1.5 Heat transfer models

A one dimensional mathematical model was developed to simulate the column behavior in terms of temperature profiles under two different non-isothermal conditions: adiabatic and non-adiabatic [51]. For a non-isothermal system, a differential energy balance for the adsorbate in the gas phase flowing through the bed gives:

$$\rho_g C_{pg}\frac{\partial T_b}{\partial t} - \lambda_L\frac{\partial^2 T_b}{\partial z^2} + \rho_g C_{pg}\frac{\partial (UT_b)}{\partial z} = -(\frac{1-\varepsilon_b}{\varepsilon_b})\bar{h}a(T_b - \bar{T}) - \frac{2h_w}{\varepsilon_b R_w}(T_b - T_w) \tag{2.24}$$

where C_{pg} is bulk heat capacity, $\bar{h}$ is heat transfer coefficient between the gas and solid phases, h_w is heat transfer coefficient between the gas and adsorber wall, λ_L is thermal axial dispersion coefficient, R_w is adsorber wall radius and T_b and $\bar{T}$ are respectively, bulk and adsorbent temperatures. A differential heat balance for the adsorbate inside the solid phase is given by:

$$\rho_s C_{ps}\frac{\partial \bar{T}}{\partial t} - (1-\varepsilon_p)\rho_s(-\Delta H)\frac{\partial \bar{q}}{\partial t} = \bar{h}\alpha\left(T_b - \bar{T}\right) \tag{2.25}$$

where $-\Delta H$ is the isosteric heat of adsorption. Linear driving force model (LDF) was used for estimating the rate of adsorption. The temperature-dependent Dual-Site Langmuir isotherm equation was considered to represent adsorption equilibrium:

$$q_i = \frac{m_1 b_i P_i}{1 + b_i P_i + b_j P_j} + \frac{m_2 d_i P_i}{1 + d_i P_i + d_j P_j} \tag{2.26}$$

where temperature dependent parameters b_i and d_i are given by:

$$b_i = b_{0i}\exp\left(\frac{\Delta H_{1i}}{R\bar{T}}\right); d_i = d_{0i}\exp\left(\frac{\Delta H_{2i}}{R\bar{T}}\right) \tag{2.27}$$

Concerning the heat transfer through the column wall, the following equation was used to describe the energy balance in the column wall:

$$\rho_w C_{pw} \frac{\partial T_w}{\partial t} - a_{w1} h_w (T_b - T_w) + a_{w2} U_w (T_w - T_{out}) = 0 \tag{2.28}$$

where a_{w1} and a_{w2} are wall internal and logarithmic specific surface areas respectively, U_w is global heat transfer coefficient and T_{out} is ambient temperature. The a_{w1} and a_{w2} are calculated using the following expressions:

$$a_{w1} = \frac{d_w}{t_w (d_w + t_w)} \qquad a_{w2} = \frac{1}{(d_w + t_w) \ln\left(\frac{d_w + t_w}{d_w}\right)} \tag{2.29}$$

in which t_w and d_w are respectively column wall thickness and internal column wall diameter. The initial and boundary conditions applied to above equations are:

$$T_b\ (t = 0) = 0,\ \bar{q}(t = 0) = 0,\ \bar{T}(t = 0) = 0 \tag{2.30}$$

$$T_b\ (z = 0) = T_0 \tag{2.31}$$

$$\left.\frac{\partial T_b}{\partial z}\right|_{z=L} = 0 \tag{2.32}$$

Applying the analogy with mass transfer, the heat transfer coefficients corresponding to each structure were calculated using the appropriate correlations; the details are given in papers B and F.

2.2 Zeolite coated monolith performance, Papers C & E

The goal of the work described in paper C was to prepare zeolite coated monoliths and evaluate their adsorption performance by breakthrough experiments. The mass transfer coefficient k and the effective diffusivity D_e in the zeolite adsorbents were estimated from breakthrough data. The analytical solution for the breakthrough front by *Klinkenberg* was used [7, 52]:

$$\frac{c}{c_0} = \frac{1}{2}\, erfc\,(\sqrt{\xi} - \sqrt{\tau} - \frac{1}{8}\sqrt{\xi} - \frac{1}{8}\sqrt{\tau}\,) \tag{2.33}$$

$$\xi = \frac{kKz}{v}\left(\frac{1 - \varepsilon_b}{\varepsilon_b}\right) \tag{2.34}$$

$$\tau = k(t - z/v) \tag{2.35}$$

where c/c_0 is the dimensionless concentration and ξ and τ are dimensionless bed length and time, respectively. The *Klinkenberg* solution is valid for isothermal plug flow

systems in which a single trace component with linear adsorption isotherm is adsorbed. The mass transfer coefficient k in the model was fitted to experimental data by minimizing the sum S of squared residuals:

$$S = \sum_{i=1}^{n} \left[\left(\frac{c}{c_0} \right)_{model} - \left(\frac{c}{c_0} \right)_{exp} \right]^2 \tag{2.36}$$

where n is the number of data points.

In paper E, gas transport in the monolith adsorbent was modelled considering a single cylindrical channel with two layers accounting for monolith channel and channel wall in the case of two-layer model (Figure 2.3 (a)) and three layers accounting for monolith channel, zeolite film and channel wall in the case of three-layer model, as depicted in Figure 2.3 (b). The effects of structural parameters of the monolithic adsorbents such as wall porosity, channel width distribution and zeolite film thickness on dynamic behaviour of monoliths with different cell densities were then evaluated using these two models.

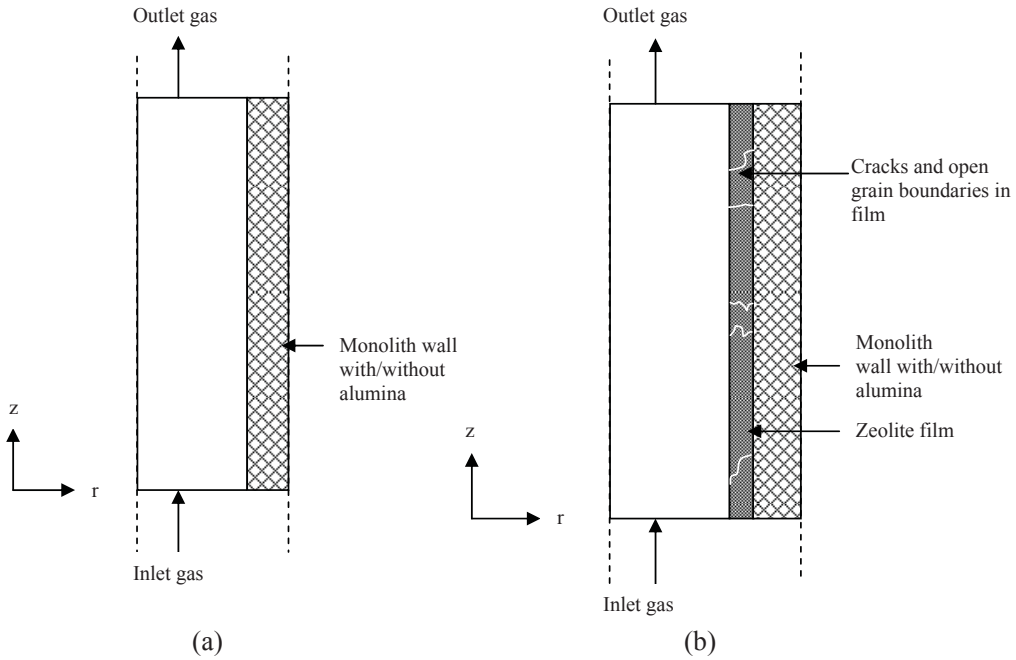

Figure 2.3: Monolith channel geometry composed of channel wall, zeolite film and monolith channel layers, (a) two-layer model (b) three-layer model.

A simplified mathematical model considering axially dispersed plug flow was fitted to experimental data. This model differs from *Klinkenberg* approximation used in paper C.

The set of conservation equations describing adsorptive behaviour of coated monoliths are as follows. The component mass balance in the gas phase is given by:

$$\frac{\partial C}{\partial t} - D_L \frac{\partial^2 C}{\partial z^2} + U \frac{\partial C}{\partial z} = -\left(\frac{1-\varepsilon_b}{\varepsilon_b}\right)\rho_s \frac{\partial \bar{q}}{\partial t} \tag{2.37}$$

The component mass balance in the solid phase, *i.e.* the zeolite and/or alumina particles, is expressed by:

$$\frac{\partial \bar{q}}{\partial t} = k_i\left(q^* - \bar{q}\right) \tag{2.38}$$

in this particular model, k_i is expressed by $k_i = {3D_i}/{l_i^2}$ where l_i is diffusion length. In the two-layer model (Figure 2.3(a)), a modified version of equation (2.38) was used for adsorbate mass balance in monolith wall to account for gas uptake due to pore filling in the voids of the monolith wall and was taken as:

$$\frac{\partial \bar{q}}{\partial t} = k_p a\left(C - \bar{C}\right) \tag{2.39}$$

where $\bar{C}$ is adsorbate concentration in the pores of monolith wall and a is the pore volume of the monolith wall ($cm^3/g_{monolith}$). The initial and boundary conditions appropriate to a breakthrough simulation for the above equations are given by equations 2.3-2.5.

2.3 VSA separation performance, Paper D

The goal of the work described in paper D was to prepare zeolite coated monoliths and evaluate their adsorption performance experimentally by breakthrough experiments. The mass transfer coefficients for the monoliths determined from breakthrough data were used to evaluate the VSA separation performance of the monoliths by modelling. A three-step VSA cycle of adsorption/desorption/re-pressurization was considered for evaluating system performance for structured adsorbents and conventional adsorbents in the form of beads (see Figure 2.4). Simulations of a three-step VSA cycle with a packed bed of conventional adsorbents and the structured adsorbents were performed using the adsorption simulator MINSA, (Monash Integrator for Numerical Simulation of Adsorption) which numerically solves the coupled partial differential equations of mass and energy balances using the finite volume method with flux limiters as described previously [53, 54]. The linear driving force (LDF) model was employed to model mass transfer. The experimentally recorded adsorption isotherms for CO_2 and N_2 over a range of temperatures were fitted to a Dual-Site Langmuir isotherm. The fitted parameters were calculated according to the equations 2.26 and 2.27.

In the first step, feed gas containing 10% CO_2/N_2 at different flow rates (0.2, 0.5 and 1 litre/minute) at 300 K and 1.2 bar pressure enters the bottom of the bed. The CO_2 front propagates through the bed and the N_2 exits to the atmosphere through the top of the bed. The position of the CO_2 mass transfer front at the end of this step is controlled by monitoring the concentration of CO_2 in the exit gas and adjusting the exit flow rate. In the second step, the bed is evacuated counter-currently and the bed pressure at the end of this step is controlled by adjusting the valve leading to the vacuum pump. In the third step, N_2 is used to re-pressurize the bed to feed pressure in a counter-current direction. The CO_2 recovery and purity is calculated to characterize the VSA performance using different adsorbent structures.

These simulations were performed to explore the behaviour of different adsorbent structures in particular to judge the merits of structured adsorbents at short cycle times, which correspond to high flow rates.

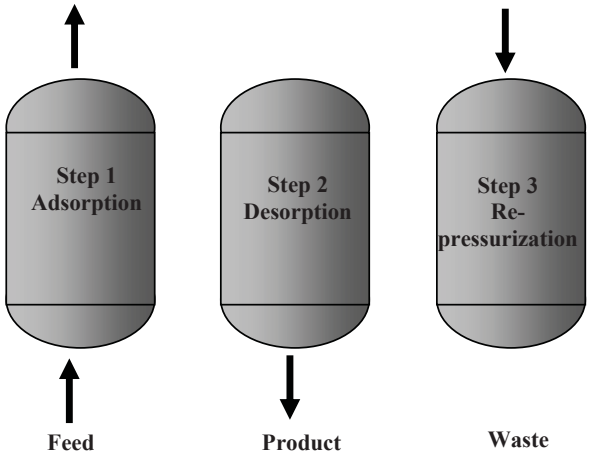

Figure 2.4: Three-step VSA cycle used to assess the performance of adsorbent structures.

It is worth noting that the three-step cycle tested here is not indicative of the typical cycle which would be used in an industrial CO_2 capture plant [55]. However, the major steps of adsorption and desorption (regeneration) are captured, which is sufficient in order to demonstrate the impact of adsorbent structure on VSA performance.

2.4 Cyclic adsorption simulation, Paper F

To demonstrate the potential advantage of structured adsorbents (*i.e.* laminate, monolith and foam) under conditions of known variation in external concentration (or pressure), the simulation of an adsorbent structure under PSA condition was considered. The PSA cycle involves two steps: adsorption and desorption. The simulations are accomplished by switching the boundary conditions cyclically to account for pressure change at the

surface of adsorbent during pressurization (adsorption) and depressurization (desorption). A cyclic adsorption process as described below was used. The adsorption step finishes when the CO_2 partial pressure at the product end of the column reaches 95% of the feed partial pressure. During the desorption step, the product end is closed and the feed end is opened to desorb CO_2. This step continues until 5% of feed partial pressure is reached.

For all simulations considered in this part, external mass transfer resistance at the external surface was included in the model. Each structure was simulated under both adiabatic and non-isothermal conditions, and the CO_2 concentration was cycled between an upper value of C_0 down to 0 for two dimensionless half cycle times: (dimensionless time for adsorption and desorption steps) $\theta_c = 0.04$ and 0.1. To ensure a valid comparison is made between each structure, the same amount of adsorbent mass per unit volume was assumed for all configurations.

CHAPTER 3

Results and discussion

3.1 Evaluation of general characteristics of structured adsorbents by modelling, Papers B & F

3.1.1 Mass transfer

CO_2 breakthrough curves for different adsorbent structures are shown in Figure 3.1. The Figure shows that adsorbents in the form of 0.2×0.2 mm laminate can offer superior performance to a packed bed of pellets. This is explained by the much higher overall mass transfer coefficient $k_{overall}$ for laminates than for pellets, see Table 3.1. The Figure also illustrates that foam 30 ppi and monolith 600 cpsi display similar breakthrough fronts as the pellet at the conditions considered here. This can be attributed to the comparable values of the pore diffusion coefficient, k_p, of these materials. However, the performance of monoliths and foams can be improved by optimizing the geometry *i.e.,* increasing cell density for monoliths, *etc*. To summarize, structured adsorbents in the form of 600 cpsi monoliths or 30 ppi foams will give similar and 0.2×0.2 mm laminate will give better performance compared with a packed bed of 0.7 mm beads for adsorptive gas separation processes at the specific conditions considered here.

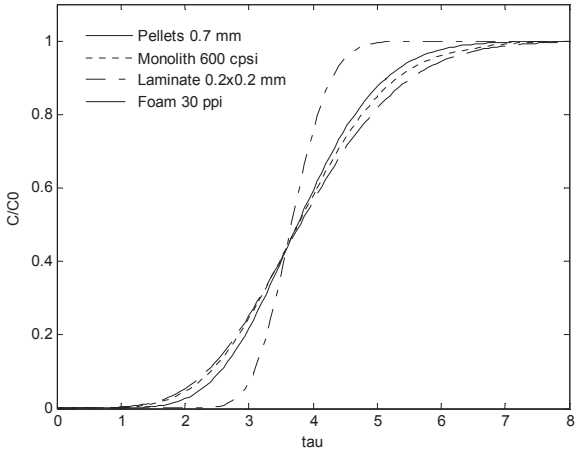

Figure 3.1: Breakthrough curves of CO_2 for adsorbents with different geometries.

Table 3.1: Mass transfer properties of different adsorbent structures.

Structure	*Sc*	*Re*	*Sh*	k_f, cm/s	k_p, cm/s	U^2/D_L, s^{-1}	$k_{mass\_transfer}$, s^{-1}	$k_{overall}$, s^{-1}
Pellet 0.7 mm	0.51	83	14.50	34.30	4.74	543	608.0	287.0
Monolith 200 cpsi	0.51	172	2.82	3.23	1.53	1480	40.7	39.6
Monolith 400 cpsi	0.51	121	2.76	4.49	2.13	2920	80.6	78.5
Monolith 600 cpsi	0.51	100	2.74	5.41	2.68	4200	120.5	117.1
Laminate 0.5×0.5 mm	0.51	59	2.70	9.00	3.98	10500	65.3	65.2
Laminate 0.3×0.3 mm	0.51	36	2.70	14.95	6.64	22300	181.1	181.1
Laminate 0.2×0.2 mm	0.51	24	2.70	22.40	9.96	34300	407.4	407.4
Laminate, 0.1×0.1 mm	0.51	12	2.70	44.76	19.92	50700	1629. 5	1629. 5
Foam 20 ppi	0.51	50	4.72	6.59	2.23	1380	56.1	53.9
Foam 30 ppi	0.51	36	4.09	9.76	3.82	1560	156.7	143.5
Foam 45 ppi	0.51	24	3.43	8.38	3.91	1740	158.1	143.7

As Table 3.1 shows, for certain structures *e.g.* monoliths $k_{mass\_transfer}$ is different for different characteristic sizes (*i.e.* cell density for monoliths) as a result of different values of k_f, k_p and ε_b, which implies that the size should be optimized for each application.

The dynamic behaviour of the mass transfer zone (MTZ) was evaluated for different operating conditions such as gas flow rates, *etc*. Figure 3.2 shows the length of the MTZ as a function of superficial gas velocity for different adsorbent configurations. As expected, for all cases, the length of the MTZ was increased by increasing gas velocity. The mass transfer zone length for the foam and monolith was considerably longer than that of the laminate and pellet structures at the conditions considered here, due to a slower overall mass transfer rate of CO_2 as characterized by lower values of $k_{overall}$, see Table 3.1. On the contrary, laminates with wall thickness of 0.2 mm show much shorter length of the mass transfer zone compared to a packed bed of 0.7 mm beads at the conditions considered here due to the much higher value of overall rate coefficient ($k_{overall}$ shown in Table 3.1).

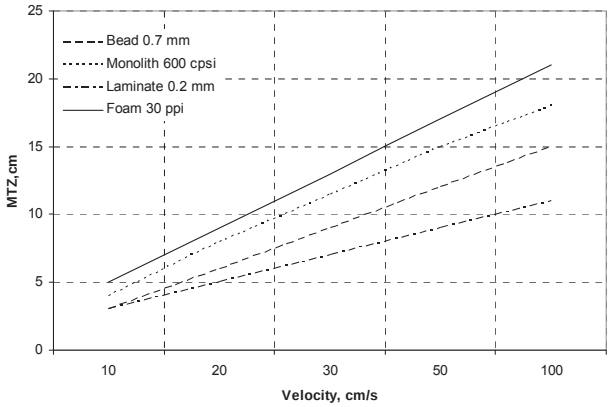

Figure 3.2: Length of MTZ for pellet, laminate, foam and monolith as a function of gas velocity.

3.1.2 Pressure drop

Figure 3.3 shows the pressure drops associated with different adsorbent configurations for superficial velocities ranging from 0.1 to 1 m/s. The Figure illustrates that the low density monolith (200 cpsi) exhibited the lowest pressure drop, while as expected, the highest pressure drop was displayed by the beads (0.7 mm). The cell density of monoliths can be increased to increase adsorbent loading. The Figure also illustrates that increasing cell density of monoliths does not increase the pressure drop much and the monolithic adsorbents still display the lowest pressure drop compared to laminate, foam and beads. According to Giani et al. [56] and Patcas et al. [16], the pressure drop of foam structures is somewhat between those of monoliths and packed beds, as we observed.

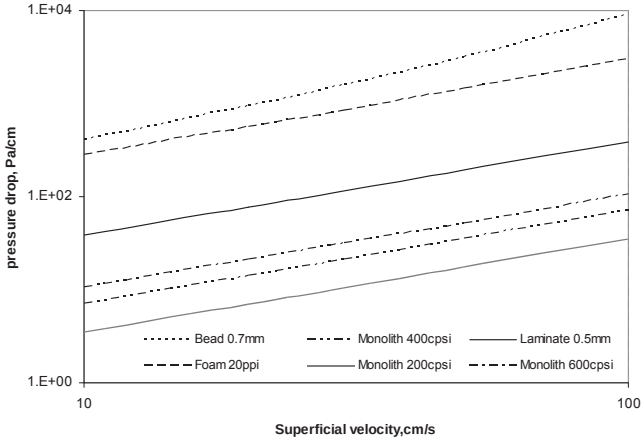

Figure 3.3: Comparison of pressure drop for pellet, laminate foam and several monoliths as a function of superficial gas velocity.

3.1.3 Heat effects

Figure 3.4 shows breakthrough curves of the considered structured adsorbents in a non-isothermal, non-adiabatic system. Laminate 0.2×0.2 mm displays the sharpest breakthrough profile due to better mass transfer characteristics (*i.e.* larger $k_{mass\_transfer}$, see Table 3.1) than the other structures under the conditions studied. However, structured adsorbents in the form of laminate 0.2×0.2 mm result in earlier CO_2 breakthrough compared to pellets because of lower adsorption capacity at higher bed temperature (338 K) when considering heat effects, see Figure 3.5. Although monolith 600 cpsi and foam 30 ppi adsorbents can dissipate the thermal effects more effectively than the pellets (with a temperature rise of 29 K and 13 K, respectively compared to 36 K for the pellets, see Figure 3.5) the monolith and foam adsorbents displayed more disperse breakthrough fronts compared to a bed of 0.7 mm pellets. This is mainly due to the larger mass transfer resistance indicated by lower values of $k_{mass\_transfer}$.

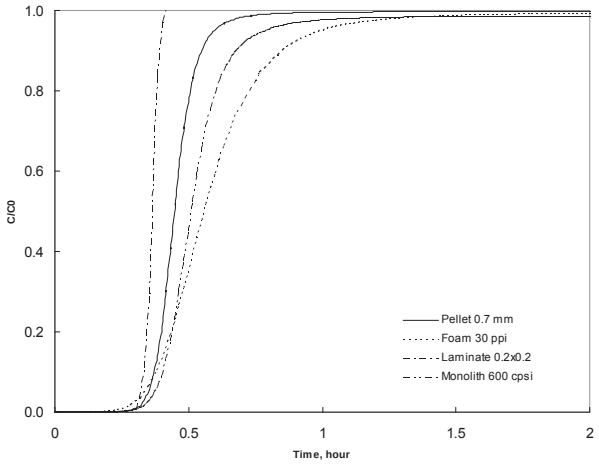

Figure 3.4: CO_2 breakthrough curves for different structured adsorbents under non-isothermal, non-adiabatic conditions.

The bulk gas temperatures (T_b) as a function of time in beds of different adsorbents are shown in Figure 3.5. For all cases, the temperature starts to rise simultaneously with the CO_2 breakthrough, *i.e.* there are both temperature and concentration fronts in the system as expected. The temperature rises up sharply as the result of adsorption and evolution of the heat of adsorption in the bed during the first few minutes to a maximum and starts to decrease as a result of heat loss from the column wall and by cooling from the gas flow. These results clearly reveal that thermal effects of adsorption can be managed by structured adsorbents characterized by more homogenous bed temperature. By using other support materials, with higher heat capacity, it should be possible to obtain even smaller heat effects and thus better performance.

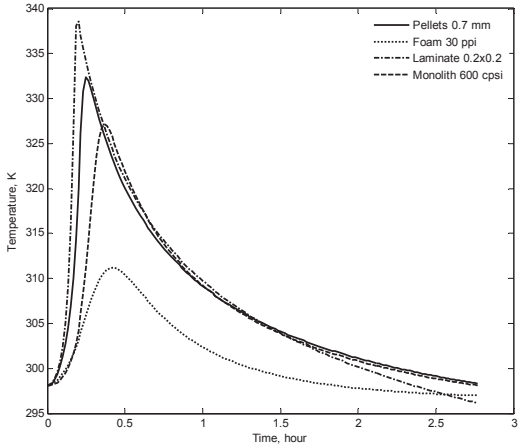

Figure 3.5: Comparison of bulk gas temperature profiles (T_b) in different bed configurations under non-adiabatic condition.

3.1.4 Specific productivity

Figure 3.6 shows qualitatively the specific productivity as a function of superficial velocity for different structures as given by equation 2.23. The parameters Δn_{ideal}, K and ΔP were calculated according to the procedure described in section 2.1. It can be seen that at lower velocities, the productivity is almost the same for different structures because all dispersive effects are negligible. In contrast, at higher velocities the structured adsorbents perform better than the conventional pellets and display larger specific productivity. It is in this region of higher velocity that structured adsorbents are advantageous. Comparison of the optimal velocity shows that at these conditions, the laminate can reach almost twice the specific productivity of a packed bed of pellets. Quantitative estimations would require detailed simulations for the specific system of interest. The intention here however was to illustrate the qualitative trends expected in performance as a function of throughput.

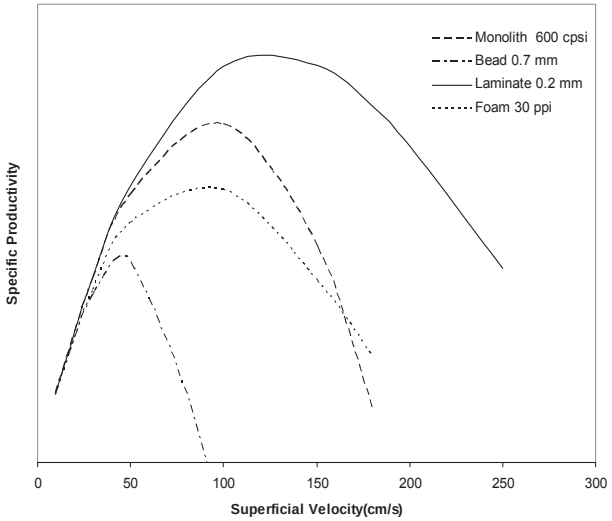

Figure 3.6: Comparison of specific productivity for pellet, laminate, foam and monolith as a function of superficial gas velocity.

3.2 Evaluation of zeolite coated monoliths prepared and tested experimentally by modelling, Papers C - E

3.2.1 Breakthrough profiles

Experimental and numerical results of CO_2 breakthrough curves for uncoated 400 cpsi, 1200 cpsi and 1200 cpsi+Al (monolith coated with alumina particles to fill the pores in the monolith walls) monoliths at a volumetric flow rate of 1 litre/minute are displayed in Figure 3.7. Curves illustrate the fitted models and it is evident that the model (equations 2.37-2.39) can adequately describe the experimental observations. As described in section 2.2, both pore filling and adsorption mechanisms were assumed to contribute to the mass balance. For the 400 cpsi monolith, CO_2 breaks through slightly before the 1200 cpsi monolith whereas for the 1200 cpsi+Al sample, breakthrough occurs somewhat later. The difference in breakthrough curves between the 400 and 1200 cpsi samples is captured in the model through different diffusion coefficients for pore filling D_p and pore filling capacity $\rho_s a C^*$, see Table 3.2. Moreover, the ratios between the contributions from adsorption and pore filling ($k_w q^* / k_p a C^*$) are 6×10^{-5} and 1×10^{-3} for the 400 and 1200 cpsi samples, respectively, see Table 3.2. This shows that the contribution from adsorption on the monoliths was negligible for both samples and D_w (monolith wall diffusivity) can not be accurately fitted for these two samples. On the contrary, adsorption was found to contribute to the breakthrough curve of 1200 cpsi+Al sample. In this case, the ratio of adsorption and pore filling capacity is 0.25. The additional adsorption capacity and the lower diffusion coefficient for pore filling D_p for the sample 1200 cpsi+Al are thus capturing the difference in breakthrough curves for samples 1200 cpsi and 1200 cpsi+Al. D_p for the latter sample was taken as the Knudsen diffusivity since the pore size is about

0.1 μm and the mean free path of CO_2 at 300 K and 1 atm is approximately the same, indicating that the diffusion is mostly of *Knudsen* type.

The results show that for the supports not coated with alumina, the breakthrough behaviour may be explained by pore filling in the voids of the monolith walls whereas both pore filling and adsorption affect the breakthrough behaviour of the support treated with alumina. It is worth pointing out here that due to high adsorption capacity of traditional adsorbents, pore filling is unimportant as opposed to the monolith supports with very low adsorption capacity. Our obtained values of macropore diffusivities are close to previously reported data for CO_2 adsorption on NaX adsorbent using uptake curve measurements [29]. The parameters determined for the three monolith supports using the two-layer model were then used in the three-layer model for the zeolite coated monoliths.

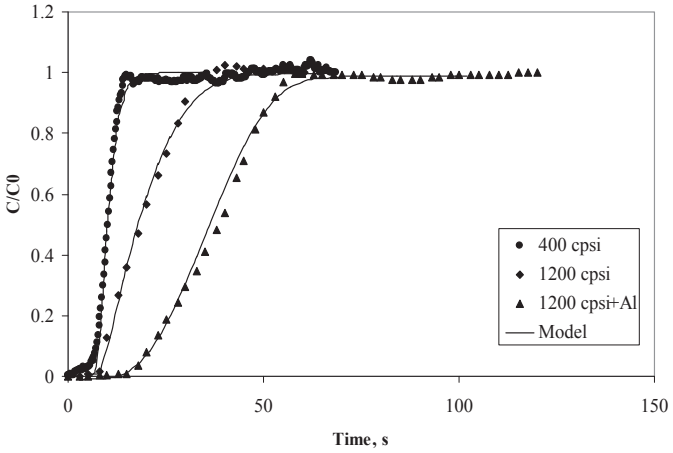

Figure 3.7: Experimental (points) and simulated (lines) breakthrough curves of carbon dioxide of uncoated monoliths at 1 litre/minute of 10% CO_2 in N_2.

There was a good fit between the three-layer model and experimental data for all zeolite coated samples, see Figure 3.8. The breakthrough time is shortest for the 400 cpsi+1.5μm film followed by the 1200 cpsi+Al+1.5μm film and finally the 1200 cpsi+Al+2.5μm film; this trend is in agreement with the zeolite loading data of the samples. The differences between the breakthrough curves are captured in the model by differences in the support parameters as described above and in addition, differences in zeolite film thickness. The mass transfer coefficients k_i decreased with increasing zeolite film as could be expected, see Table 3.2.

Table 3.2: Adsorption parameters of monoliths.

Sample code	D_p, (m^2/s)	D_w, (m^2/s)	D_z, (m^2/s)	k_i, (s^{-1})	$\rho_s aC^*$, ($mmol/cm^3$)	$k_i q^*/k_p aC^*$
400 cpsi	1.4×10^{-5}	4.0×10^{-12}	-	-	1.1×10^{-3}	5.7×10^{-5}
1200 cpsi	5.8×10^{-6}	7.6×10^{-12}	-	-	2.2×10^{-3}	9.6×10^{-4}
1200 cpsi +Al	2.5×10^{-7}	3.7×10^{-11}	-	-	2.0×10^{-3}	0.25
400 cpsi+1.5µm film	1.4×10^{-5}	4.0×10^{-12}	4.1×10^{-12}	5.50	-	-
1200 cpsi+Al+1.5µm film	5.8×10^{-6}	7.6×10^{-12}	3.9×10^{-12}	2.70	-	-
1200 cpsi+Al+2.5µm film	2.5×10^{-7}	3.7×10^{-11}	2.7×10^{-12}	1.30	-	-

The fitted diffusivities for the zeolite films, D_z are nearly constant, as expected, and in the range 2.7- 4.1×10^{-12} m^2/s. Literature data on the diffusivity of CO_2 in NaX is scarce and scatters significantly. Plant et al. [57] reported a diffusivity of 6×10^{-10} m^2/s, whereas data presented by Bülow [58] indicated that the diffusion of CO_2 in NaX was significantly lower than 3×10^{-11} m^2/s as we observed.

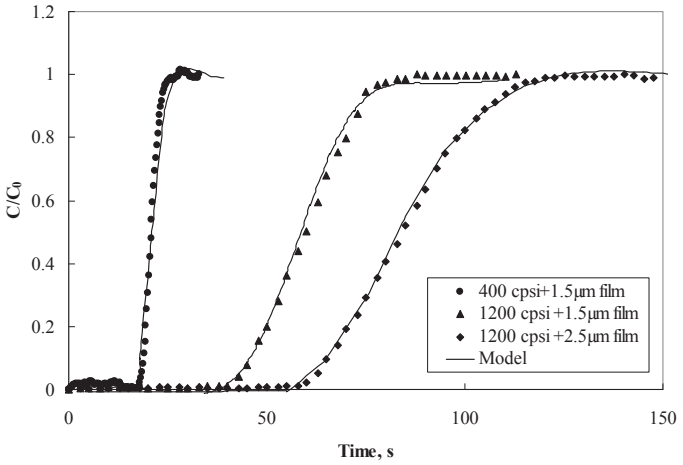

Figure 3.8: Comparison of experimental breakthrough curves of samples 400 cpsi+1.5µm film, 1200 cpsi+Al+1.5µm film and 1200 cpsi+Al+2.5µm film.

To investigate the impact of wall porosity, simulations using the three-layer model were performed by keeping all parameters constant as fitted for sample 1200 cpsi+Al+1.5µm film while varying wall porosity from 0.0 to 0.7; the predicted concentration fronts are shown in Figure 3.9. As can be noticed, the dense support (ε_w= 0.0) displayed the sharpest breakthrough front with longer breakthrough time, while the least dense monolith (ε_w= 0.7) gave rise to the broadest front and a short breakthrough time. The wall porosity of the experimentally prepared monoliths was 0.25. Figure 3.9 illustrates that reduced wall porosity may improve the process performance of structured adsorbents in the form of coated monoliths significantly.

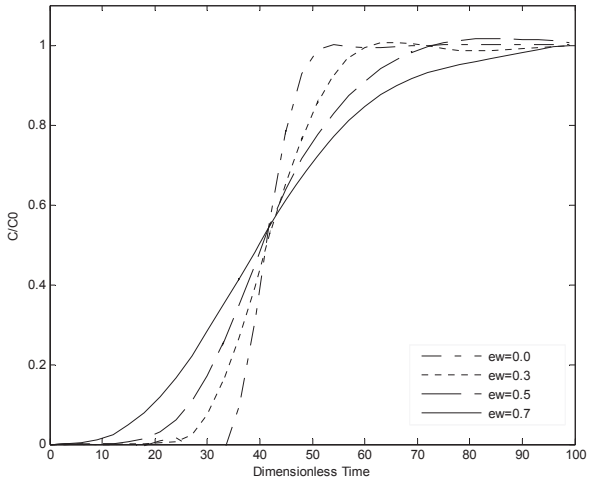

Figure 3.9: Effect of monolith wall porosity on CO_2 concentration profile.

In order to evaluate the effect of thickness of active material on the adsorption properties of the adsorbent, the zeolite film thickness was varied from 1.5 microns to 30 microns while the other parameters were kept as for a 1200 cpsi monolith with zero wall porosity. Figure 3.10 shows that for increased film thickness, the CO_2 breakthrough time increases as expected due to the higher zeolite loading, but film thicknesses larger than 10 μm results in broadening of the CO_2 front due to an increased diffusion path. The gain in capacity with larger film thicknesses than 10 μm may offset the loss due to reduced mass transfer. To examine this trade-off, it is necessary to perform cyclic adsorption runs as a function of cycle time to find the optimal thickness. However, based on single breakthrough runs, our results indicate that 10 μm is a safe margin thickness for a zeolite film grown on a nonporous 1200 cpsi monoliths support. The CO_2 adsorption capacity of a 1200 cpsi monolith coated with a 2.5 μm film was 0.13 mmol/cm^3 adsorbent. If the film thickness is increased to 10 μm, the adsorption capacity would increase to about 0.5 mmol/cm^3 adsorbent, which is about 25% of the adsorption capacity of zeolite X beads. A structured adsorbent, with zero wall porosity and such a high adsorption capacity, low pressure drop and sharp breakthrough front seems as a very competitive adsorbent.

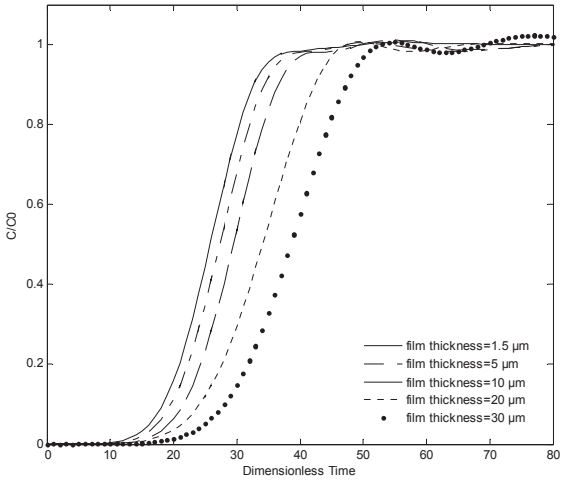

Figure 3.10: Effect of zeolite film thickness on CO_2 concentration profile for zeolite coated monoliths.

3.2.2 Simulated VSA performance for zeolite coated monoliths and comparison with beads

Process cycle time in PSA and VSA processes is an important parameter determining the adsorbent volume and total size of the adsorber. Shorter cycles on one hand give rise to higher throughput for the same amount of adsorbent; on the other hand, too short cycles may lead to insufficient time for adsorption due to mass transfer limitations. To investigate the impact of adsorbent geometry for zeolite coated monoliths and traditional adsorbent beads on VSA performance at different cycle times, a series of simulations were conducted using the MINSA software for a three-step cycle (Figure 2.4).

The product purity is calculated as the ratio of CO_2 to total flow obtained in the desorption gas during step 2 of the cycle. Figure 3.11 shows that the product purity obtained with an adsorbent in the form of beads was higher than for the 900 and 400 cpsi zeolite coated monoliths. This can be attributed to the higher voidage and lower zeolite loadings for the monolith structures. The channel voids in the structured adsorbents lead to significant contamination of the product with N_2. Figure 3.11 also shows that for all cases, a plateau value of product purity was reached by increased cycle times. This was due to the reduction in gas velocity resulting in a sharper mass transfer front and hence improved CO_2 purity. The product purity for all adsorbents approached feed purity (10%) as the cycle time was decreased. When cycle time was decreased below 120 s, the CO_2 purity underwent a gradual decline in the case of monoliths whereas a much larger decrease was experienced for the packed bed. This reduction was due to pressure drop in the packed bed which leads to broadening of the mass transfer front and hence contamination of the top of the bed.

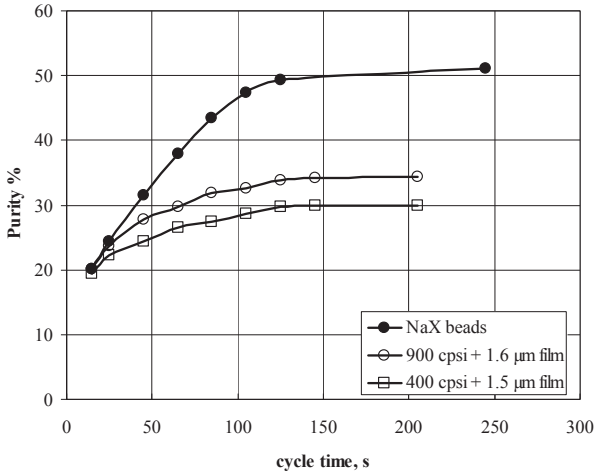

Figure 3.11: Product purity as a function of cycle time for different adsorbents.

Product recovery is defined as the total amount of CO_2 recovered during step 2 (evacuation step) to the total CO_2 amount fed to the system. Figure 3.12 shows that the recovery obtained with the structured adsorbents was higher than that obtained with the packed bed. This was directly related to the sharpness of the mass transfer front during the feed step. The sharper front for the structured adsorbents resulted in less breakthrough of CO_2 during step 1 and therefore a higher recovery in the product stream. The CO_2 recovery is a function of CO_2 working capacity (*WC*) which decreases as cycle time decreases. As evident from Figure 3.12, in the case of 400 and 900 cpsi zeolite coated monoliths, a decrease from 86% to 75% and 90% to 80% occurred respectively when cycle time was decreased from 205 to 15 s, while in the case of NaX pellets, the recovery only reaches 80% for long cycle times. Longer cycle time gives higher purity and recovery because the lower resulting velocities lead to sharper mass transfer zones. The recovery could be improved by replacing the three-step cycle with a more complex cycle incorporating product rinse and pressure equalisation. However, the scope of the VSA simulation was not to optimize system performance but rather to explore and illustrate the advantages and disadvantages of structured adsorbents versus conventional adsorbent beads.

As expected, all three adsorbents displayed a hyperbolic pattern for productivity as a function of cycle time as suggested by equation 2.23. The throughput was highest for a packed bed because of the higher zeolite loading per unit volume. However, at very short cycle times beads followed the expected inverse trend of productivity and structured adsorbents displayed larger throughput than the packed bed. It was clear that the dispersive effects of pressure drop and mass transfer were becoming more important at shorter cycle times for the packed bed. Cycle times below 15 s eventually lead to a drop in throughput for the packed bed as observed in Figure 3.13. Thus the structured adsorbents show promising performance at short cycle times provided that higher zeolite loadings can be obtained.

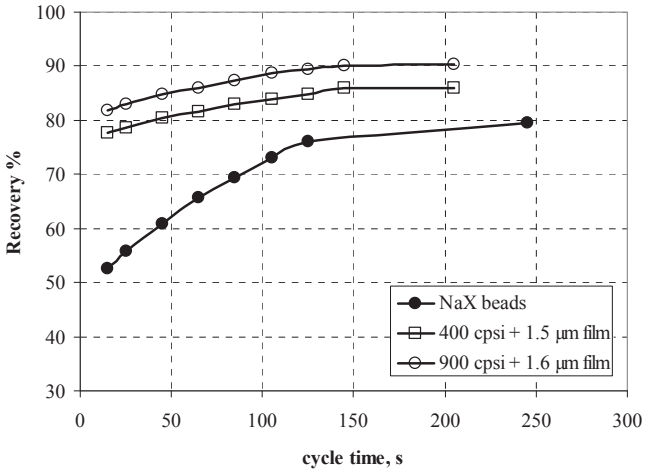

Figure 3.12: Product recovery as a function of cycle time for different adsorbents.

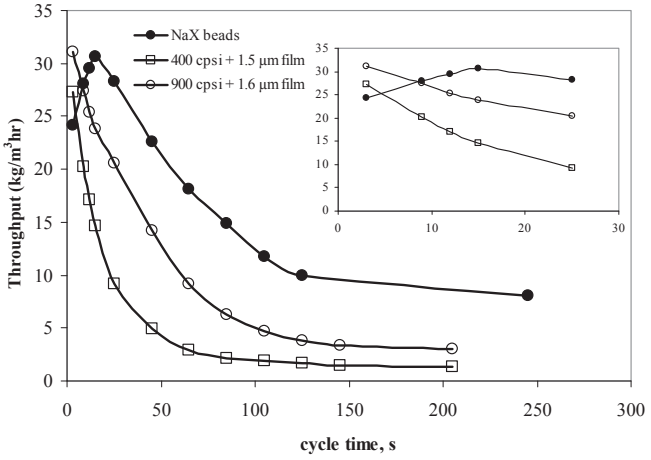

Figure 3.13: Productivity as a function of cycle time for different adsorbents.

3.3 Cyclic adsorption simulation considering thermal effects, Paper F

Thermal effects were investigated for four different configurations of adsorbents *i.e.* 0.7 mm pellet, 0.2×0.2 mm laminate, 600 cpsi monolith and 30 ppi foam; some of the properties of these adsorbents are given in Table 3.1. Figure 3.14 shows the CO_2 loading

profiles for dimensionless half cycle times (dimensionless time for adsorption and desorption steps) of 0.1 (a) and 0.04 (b), respectively. The cycle simulation was performed according to the procedure described in section 2.4 under non-isothermal, non-adiabatic conditions. The plots display the adsorbate loading for the duration of the cyclic steady state. The difference in CO_2 loadings for pellets compared to the other structures is quite substantial, especially at shorter cycle time. Again, these results illustrate that structured adsorbents are most suited for short cycle times, where their superiority is displayed. At the conditions studied here, the laminate structures exhibit best performance at both dimensionless cycle times as evident from the highest CO_2 loading, however the other structured adsorbents are not that inferior and their performance could be improved by optimizing the geometry. These results show that structured adsorbents are good candidates for advanced PSA units where the aim is to run as short cycles as possible in order to reduce the adsorbent inventory. A similar trend was observed for adsorbents under adiabatic conditions.

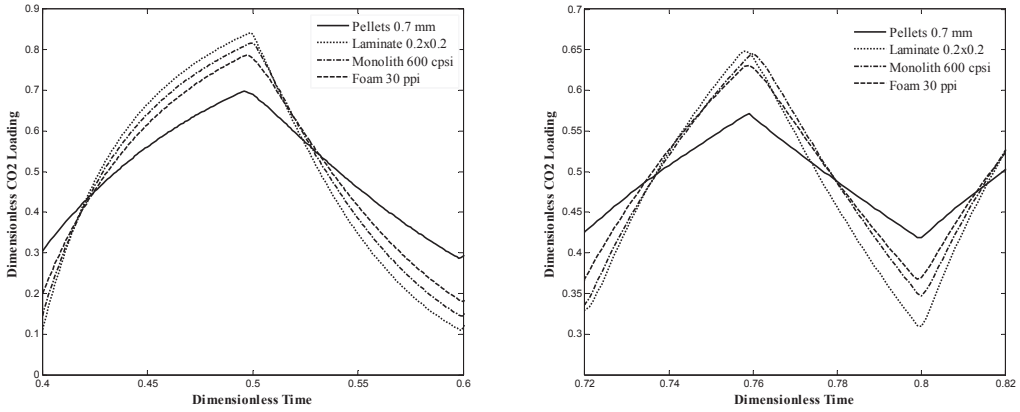

Figure 3.14: Dimensionless CO_2 loading in a two-step PSA cycle with half cycle times of θ_c= 0.1 (a) and of θ_c= 0.04 (b) for different adsorbent structures.

To further examine the performance of laminate structures, simulations of the dimensionless CO_2 loading for different thickness and spacing of the laminates are shown in Figure 3.15. This Figure illustrates that the laminates with thickness and spacing of 0.5 mm and less perform better, while laminates with thickness and spacing of 0.7 mm performs worse than 0.7 mm pellets. These results show that the replacement of conventional adsorbents with structured adsorbents is only beneficial when structured adsorbents with appropriate dimensions are used. The same conclusion holds for monoliths and foams.

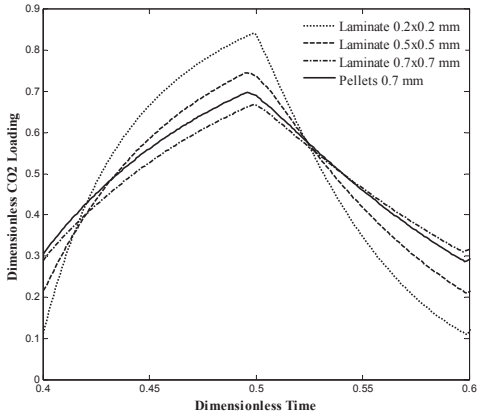

Figure 3.15: Dimensionless CO_2 loading in a two-step PSA cycle with half cycle time of θ_c= 0.1 for laminate adsorbents with different dimensions.

CHAPTER 4

Conclusions

4.1 Conclusions

The impact of geometry of structured adsorbents on overall performance of adsorption-based gas separation systems has been studied using experiments and modelling. The main finding was that structured adsorbents with optimized geometry are potentially better adsorbents compared to traditional adsorbents at short cycle times. Two different approaches were used for the studies. The general approach was to evaluate general characteristics of structured adsorbents in gas separation systems by numerical modelling and this work showed that structured adsorbents with optimized geometry may provide following advantages compared to traditional adsorbents:

- Lower pressure drop
- Better mass transfer properties characterized by sharper breakthrough fronts
- Better thermal management characterized by more uniform bed temperature
- Higher loading specially at short cycle time
- Higher throughput at optimum cycle time

The specific approach was to evaluate the performance of zeolite X coated monoliths in CO_2/N_2 separation processes, both experimentally and by numerical modelling and the main outcomes of this work were:

- Product purity in a VSA process using zeolite coated monoliths is reduced by higher voidage and lower zeolite loadings for the zeolite coated monoliths compared to beads. The channel voids in the structured adsorbents lead to significant contamination of the product with N_2 and must be minimized in order to compete with traditional adsorbents.
- The product recovery in a VSA process using zeolite coated monoliths was higher compared to a process using beads thanks to the greater sharpness of the mass transfer front during the feed step for the structured adsorbents.
- Beads showed higher productivity at long cycle times, but at very short cycle times, the structured adsorbents showed higher productivity.
- The pores in the support introduced dispersion to the system by pore filling with gas, not adsorption, and the model indicated that the use of monoliths with lower

wall porosity would lead to less dispersion and thereby better performance of structured adsorbents.

- The model indicated that a zeolite X film with a thickness of 10 microns is optimal on a nonporous 1200 cpsi monolith for adsorption of CO_2 from N_2. The adsorption capacity of such a structured adsorbent would be about 25% of the adsorption capacity of zeolite X beads. A structured adsorbent, with such a high adsorption capacity, low pressure drop and sharp breakthrough front seems as a very competitive adsorbent.

CHAPTER 5

Future work

5.1 Future work

Improved adsorbent materials are needed for the future improved gas separation processes. This study gives an insight in how these materials should be designed. However, there is still a need for research to address the following issues:

- The models developed in the present work should be validated against real structures and then used to guide preparation of the materials. It would for instance be interesting to prepare a 10 μm zeolite film on a nonporous 1200 cpsi monolith and evaluate it experimentally.

- The improved materials should be tested in a real rapid PSA or TSA processes.

- The role of adsorbent morphology (pore size distribution, and interconnectivity of pores) on transport, separation and adsorption performance of structured adsorbents should be identified using the pore network modelling concept.

REFERENCES

[1] M. Suzuki, *Adsorption Engineering (Chemical Engineering Monographs, Volume 25)*. New York: Elsevier, 1990.

[2] RT. Yang, *Gas Separation by Adsorption Processes (Series on Chemical Engineering)*. London: Imperial College Press, 1997.

[3] S. Auerbach, K. Carraco, P. Dutta, *Handbook of Zeolite Science and Technology*. Upper Saddle River, New Jersey: Marcel Dekker, Inc., 2003.

[4] C. Baerlocher, L. McCusker, D. Olson, *Atlas of zeolite framework types.* Netherlands: Elsevier, 2007.

[5] D. Breck, *Zeolite molecular sieves: structure, chemistry and use.* New York: Krieger Publ. Company, 1984.

[6] S.H. Hyun, R.P. Danner,"Equilibrium adsorption of ethane, ethylene, isobutane, CO_2, and their binary mixtures on NaX molecular sieves", *J. Chem. Eng. Data.,* vol. 27, pp. 196-200, 1982.

[7] D. Ruthven, *Principles of Adsorption and Adsorption Processes*. John Wiley and Sons Inc., 1984.

[8] D. Ruthven, S. Farooq, K. Knaebel, *Pressure Swing Adsorption.* John Wiley and Sons Inc., 1993.

[9] T.C. Golden, C.M.A. Golden, D.P. Zwilling, "Self-supported structured adsorbent fabric for gas separation", *U.S. Patent*, US6565627, 2003.

[10] P. Xiao, J. Zhang, P. Webley, G. Li, R. Singh, R. Todd, "Capture of CO_2 from flue gas streams with zeolite 13X by vacuum-pressure swing adsorption", *Adsorption,* vol. 14, pp. 575-582, 2008.

[11] J. Smolarek, F.W. Leavitt, J.J. Nowobilski, V.E. Bergsten, J.H. Fassbaugh, "Radial bed vacuum/pressure swing adsorber vessel", *European Patent*, EP0820798, 1998.

[12] S. Ergun, "Fluid flow through packed columns", *Chem. Eng. Prog.,* vol. 48, pp. 89-94, 1952.

[13] D.M. Ruthven, C. Thaeron, "Performance of a parallel passage adsorbent contactor", *Gas. Sep. Purif.*, vol. 10, pp. 63-73, 1996.

[14] Y.Y. Li, S.P. Perera, B.D. Crittenden, "Zeolite monoliths for air separation, part 2: Oxygen enrichment, pressure drop and pressurization", *Chem. Eng. Res. Des.,* vol. 76, pp. 921-930, 1998.

[15] A. Patton, B.D. Crittenden, S.P. Perera, "Use of the linear driving force approximation to guide the design of monolithic adsorbents", *Chem. Eng. Res. Des.,* vol. 82, pp. 999-1009, 2004.

[16] F.C. Patcas, G.I. Garrido, B. Kraushaar-Czarnetzki, "CO oxidation over structured carriers: A comparison of ceramic foams, honeycombs and beads", *Chem. Eng. Sci.,* vol. 62, pp. 3984-3990, 2007.

[17] S. Sircar, "Rapid thermal swing adsorption", *U.S. Patent*, US0037672, 2003.

[18] J. Collins, "Air separation by adsorption", *U.S. Patent*, US4026680, 1977.

[19] V. Gueret, C. Monereau, P. Pullumbi, "PSA method using a composite adsorption bed comprising an adsorbent and PCM agglomerates", *W.I.P.O. Patent,* WO2008037904, 2008.

[20] T.C. Golden, C.M.A. Golden, P.J. Battavio, "Multilayered adsorbent system for gas separations by pressure swing adsorption", *U.S. Patent*, US6893483, 2005.

[21] E.J Rode, A.J.J. Boulet, A.M. Pelman, M.L. Babicki, B.G. Keefer, J.A. Sawad, S. Alizadeh-khiavi, S. Roy, A.C. Gibbs, S.M. Kuznicki, "Engineered adsorbent structures for kinetic separation", *U.S. Patent*, US7645324, 2010.

[22] A. Mosca, J. Hedlund, F.N. Ridha, P. Webley, "Optimization of synthesis procedures for structured PSA adsorbents", *Adsorption,* vol. 14, pp. 687-693, 2008.

[23] O. Öhrman, J. Hedlund, J. Sterte, "Synthesis and evaluation of ZSM-5 films on cordierite monoliths", *Appl. Catal. A:Gen.,* vol. 270, pp. 193-199, 2004.

[24] J. Sterte, J. Hedlund, D. Creaser, O. Öhrman, Z. Wang, M. Lassinantti, Q. Li, F. Jareman, "Application of the seed-film method for the preparation of structured molecular sieve catalysts", *Catal. Today,* vol. 69, pp. 323-329, 2001.

[25] D.M. Ruthven, "Rectangular isotherm model for adsorption kinetics", *Ind. Eng. Chem. Res.,* vol. 39, pp. 2127-2131, 2000.

[26] A. Kodama, M. Goto, T. Hirose, T.J Kuma, "Experimental study of optimal operation for a honeycomb adsorber operated with thermal swing", *Chem. Eng. Japan,* vol. 26, pp. 530-535, 1993.

[27] K.P. Gadkaree, "Carbon honeycomb structures for adsorption applications", *Carbon,* vol. 36, pp. 981-989, 1998.

[28] J.L. Williams, "Monolith structures, materials, properties and uses", *Catal. Today,* vol. 69, pp. 3-9, 2002.

[29] L. Li, B. Xue, J. Chen, N. Guan, F. Zhang, D. Liu, H. Feng, "Direct synthesis of zeolite coatings on cordierite supports by in situ hydrothermal method", *Appl. Catal. A:Gen.,* vol. 292 pp. 312-321, 2005.

[30] A. Mosca, O. Öhrman, J. Hedlund, I. Perdana, D. Creaser, "NO_2 and N_2 sorption in MFI films with varying Si/Al and Na/Al ratios", *Micropor. Mesopor. Mater.,* vol. 120, pp. 195-205, 2009.

[31] I. Perdana, D. Creaser, O. Öhrman, J. Hedlund, "A comparison of NOx adsorption on Na, H and BaZSM-5 films", *Appl. Catal. B*:*Environ.,* vol. 72, pp. 82-91, 2007.

[32] I. Perdana, D. Creaser, O. Öhrman, J. Hedlund, "NOx adsorption over a wide temperature range on Na-ZSM-5 films", *J. Catal.*, vol. 234, pp. 219-229, 2005.

[33] B.G. Keefer, C.R. Mclean, "High frequency rotary pressure swing adsorption apparatus", *U.S. Patent*, US6056804, 2000.

[34] D.J. Connor, D.G. Doman, L. Jeziorowski, B.G. Keefer, B. Larisch, C. McLean, I. Shaw, "Rotary pressure swing adsorption apparatus", *U.S. Patent*, US6406523, 2002.

[35] B.G. Keefer, A. Carel, B. Sellars, I. Shaw, B. Larisch, "Adsorbent laminate structures", *U.S. Patent*, US6692626, 2004.

[36] H.S. Kim, J.W. Kim, J.E. Yie, H. Moon, "Temperature-programmed adsorption and characteristics of honeycomb hydrocarbon adsorbers", *Ind. Eng. Chem. Res.,* vol. 41, pp. 6589-6592, 2002.

[37] J.T. Richardson, D. Remue, J.K. Hung, "Properties of ceramic foam catalyst supports: Mass and heat transfer" *Appl. Catal. A:Gen.,* vol. 250, pp. 319-329, 2003.

[38] J.A. Sawad, S. Alizadeh-Khiavi, S. Roy, S.M. Kuznicki, "High density adsorbent structures", *W.I.P.O. Patent,* WO2005032694, 2005.

[39] K.B. Yoon, Y.J. Lee, Y.S. Park, J.S. Lee, "Macroporous foams comprising microporous zeolite or zeotype material and preparation thereof by using polymeric templates having sponge structure", *W.I.P.O. Patent,* WO2002028775, 2002.

[40] F.C. Buciuman, B. Kraushaar-Czarnetzki, "Preparation and characterization of ceramic foam supported nanocrystalline zeolite catalysts", *Catal. Today,* vol. 69, pp. 337-342, 2001.

[41] A. Bailey, F.A.P. Maggs, "Filter assemblies with layers of activated carbon fibrous cloth", *U.S. Patent,* US4234326, 1980.

[42] W.B. Leedy, J.F. Eichelsbacher, T.H. Shelton, "Impregnated Monoliths", *U.S. Patent,* US200810236389, 2008.

[43] L. Bonaccorsi, A. Freni, E. Proverbio, G. Restuccia, F. Russo, "Zeolite coated copper foams for heat pumping applications", *Micropor. Mesopor. Mater.,* vol. 91, pp. 7-14, 2006.

[44] R.E. Critoph, T.Z. Telto, G.N.L. Davies, "A prototype of a fast cycle adsorption refrigerator utilizing a novel carbon–aluminium laminate", Proceedings of the institution of mechanical engineers, vol. 214, 2000.

[45] O. Öhrman, J. Hedlund, V. Msimang, K. Möller, "Thin ZSM-5 film catalysts on quartz and alumina supports", *Micropor. Mesopor. Mater.,* vol. 78, pp. 199-208, 2005.

[46] S. Sircar, R. Kumar, K.J. Anselmo, "Effects of column nonisothermality or nonadiabaticity on the adsorption breakthrough curves", *Ind. Eng. Chem. Proc. Des. Dev.,* vol. 22, pp. 10-15, 1983.

[47] A. Cybulski, J.A. Moulijn, *Structured Catalysts and Reactors*, New York: Marcel Dekker, 1998.

[48] J.T. Richardson, Y. Peng, D. Remue, "Properties of ceramic foam catalyst supports: Pressure drop", *Appl. Catal. A: Gen.,* vol. 204, pp. 19-32, 2000.

[49] L.J. Gibson, M.F. Ashby, *Cellular Solids: Structure and Properties,* London: Cambridge University Press, 1997.

[50] R.S. Todd, P.A. Webley, "Mass-Transfer Models for Rapid Pressure Swing Adsorption Simulation", *AIChE J.*, vol. 52, pp. 3126-3145.

[51] I. Pentchev, K. Paev, I. Seikova, "Dynamics of non-isothermal adsorption in packed bed of biporous zeolites", *Chem. Eng. J.,* vol. 85, pp. 245-257, 2002.

[52] A. Klinkenberg, "Heat Transfer in Cross-Flow heat Exchangers and Packed Beds", *Ind. Eng. Chem.,* vol. 46, pp. 2285-2289, 1954.

[53] P.A. Webley, J. He "Fast solution-adaptive finite volume method for PSA/VSA cycle simulation; 1 single step simulation", *Comput. Chem. Eng.,* vol. 23, pp. 1701-1712, 2001.

[54] R.S. Todd, G.B. Ferraris, D. Manca, P.A. Webley, "Improved ODE integrator and mass transfer approach for simulating a cyclic adsorption process", *Comput. Chem. Eng.,* vol. 27, pp. 883-899, 2003.

[55] J. Zhang, P. Xiao, P.A. Webley "Cycle development and design for CO_2 capture from flue gas by vacuum swing adsorption", *Environ. Sci. Technol.,* vol. 42, pp. 563-569, 2008.

[56] L. Giani, G. Groppi, E. Tronconi, "Mass-transfer characterization of metallic foams as supports for structured catalysts", *Ind. Eng. Chem. Res.* vol. 44, pp. 4993-5002, 2005.

[57] D. Plant, H. Jobic, P. Llewellyn, G. Maurin, "Diffusion of CO_2 in NaY and NaX faujasite systems: quasi-elastic neutron scattering experiments and molecular dynamics simulations", *Eur. Phys. J. Special Top.,* vol. 141, pp. 127-132, 2007.

[58] M. Bülow, "Complex Sorption Kinetics of Carbon Dioxide in NaX-Zeolite Crystals", *Adsorption,* vol. 8, pp. 9-14, 2002.

Part II

PAPER A

Structured adsorbents in gas separation processes

Authors:
F.Rezaei, P. Webley

Separation and Purification Technology 70 (2010) 243 - 256

Separation and Purification Technology 70 (2010) 243–256

Contents lists available at ScienceDirect

Separation and Purification Technology

journal homepage: www.elsevier.com/locate/seppur

Review

Structured adsorbents in gas separation processes

F. Rezaei, P. Webley*

Department of Chemical Engineering, Monash University, Wellington Road, Clayton, VIC 3800, Australia

ARTICLE INFO

Article history:
Received 31 March 2009
Received in revised form 4 October 2009
Accepted 6 October 2009

Keywords:
Structured adsorbent
Adsorptive gas separation
Pressure drop
Novel adsorbents
Mass transfer

ABSTRACT

In this review, novel structured adsorbents for gas separation processes are discussed. General requirements are elucidated and illustrated with respect to specific structures such as monoliths, foams, laminates, and fabric structures. Geometrical parameters of adsorbents which affect the system performance are identified and discussed. It is clear that opportunities for improvement and optimization of adsorptive gas separation processes should include the development of improved structured adsorbents. These novel structures can fulfil many of the requirements of advanced gas separation processes such as enhanced mass transfer, reduced pressure drop, and improved thermal management.

Contents

1. Introduction

Developments in adsorption processes usually focus attention on improved adsorbents especially with regard to the adsorption isotherm and selectivity for the separation of interest. However, improvements in performance and reduction in cost of cyclic adsorption processes including pressure swing adsorption (PSA) and temperature swing adsorption (TSA) are also dependent on parameters which are dictated by adsorbent loading per unit volume, mass transfer properties, pressure drop, and thermal management. These factors play an important role in the size of the process equipment, the attainable product recovery, and the resulting power consumption. All of these affect system cost. These factors are strongly influenced by the structure of the adsorbent used in the gas separation device.

Over the last decade, there has been considerable interest in the intensification of separation processes. In cyclic devices such as PSA and TSA, reducing cycle time is the primary means of achiev-

* Corresponding author. Tel.: +61 3 9905 3445; fax: +61 3 9905 5686.
E-mail address: paul.webley@eng.monash.edu.au (P. Webley).

1383-5866/$ – see front matter © 2009 Elsevier B.V. All rights reserved.
doi:10.1016/j.seppur.2009.10.004

ing more production from a given quantity of material. However, as cycle time is reduced, cyclic devices usually face the problem of decreasing working capacity per cycle for the component of interest, decreasing product recovery and increasing pressure drop. The extent to which cycle time reduces working capacity and recovery and increases pressure drop is dependent on the structure of the adsorbent. Conventional gas separation systems are usually performed using adsorbents in the form of beads or granules. However, mass transfer and pressure drop drawbacks associated with conventional packed beds impose limitations in operating the process at optimum conditions in terms of energy consumption and overall system efficiency. Reducing particle size is the most obvious way to decrease mass transfer resistance (which varies as the square of particle size) and trends over the last few decades have seen particle sizes reducing from 2 to 3 mm down to less than 0.7 mm. Combating the accompanying increase in pressure drop with reduction in particle size has led to bed geometries of a "pancake" nature, i.e. L/D ratios considerably less than one. However, considerable gas maldistribution and channelling not to mention potential fluidization of packed beds are issues which emerge when shallow, large diameter packed beds are used.

An alternate approach to simply reduce particle size is to investigate entirely non-particulate, novel adsorbent structures. Alternate adsorbent geometries should satisfy a number of requirements in order to be considered as suitable candidates for the replacement of pellet/bead configurations. In particular, such structures should yield high mass transfer kinetics with large film and solid mass transfer coefficients. Furthermore, they must exhibit high volume working capacity (loading per unit system volume) as well as low voidage for minimizing the size of the adsorber. In addition, the gas flow path in these novel adsorbent structures should produce low pressure drop to minimize energy consumption. Finally, the use of novel adsorbent structures permits simultaneous engineering of heat transfer into the adsorbent, an often overlooked consideration in design of adsorption processes. By this is meant the process of heat transfer to/from the gas and the adsorption sites. Since adsorption is exothermic and desorption endothermic, a thermal swing accompanies the pressure swing and is usually detrimental to the overall system performance, sometimes by as much as 30%. Efficient transfer of heat to and from the adsorbent can significantly improve system performance and a structured adsorbent affords opportunities to accomplish this.

The present review examines the approaches taken in the published literature on fundamental and applied research of adsorbent geometries using novel adsorbent structures in gas separation systems. The review highlights in particular, monoliths, laminates, foams and fabrics structures along with their applications in adsorption based gas separation processes. The role of the geometric parameters of these structured adsorbents is also evaluated. The aim in this review is to illustrate and analyse recent advances in the application of novel adsorbents in gas separation and purification processes. Finally, based on the review, a number of suggestions for future research are made. Fig. 1 illustrates some typical adsorbent structures which have been used either commercially or in research studies.

Table 1 summarizes a large number of studies in which non-particulate adsorbent structures have been used with the key results reported. These will be discussed in more detail below.

2. Role of geometric parameters in overall performance

A number of physical adsorbent parameters govern the performance of adsorptive gas separation processes for a given adsorption isotherm. As mentioned above, these parameters include volumetric working capacity, pressure drop, mass transfer characteristics, as well as thermal management. It is possible to develop a structured adsorbent with superior performance to a packed bed (on a volume or mass basis) provided the parameters listed above are at their "optimal" values. However, care must be taken when using a structured adsorbent for a particular process since there is always a trade-off between these aforementioned parameters during operation.

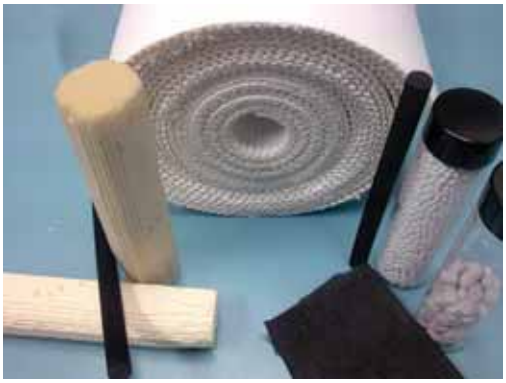

Fig. 1. Illustration of a variety of adsorbent structures including (left to right): ceramic and carbon adsorbent monoliths, corrugated paper monoliths (center), fabric adsorbent and conventional beaded adsorbents.

2.1. Volumetric working capacity and adsorbent loading

Volumetric working capacity is defined here as the moles of gas processed per unit volume per cycle. This is a product of the working capacity (moles of gas adsorbed/desorbed per unit mass of adsorbent including binder, support, etc.) and the density of the composite adsorbent. The throughput attainable in a given volume of vessel in a cyclic adsorption system may be expressed as:

$$\text{Throughput } (\text{mole/s m}^3) = \frac{WC * \rho_B}{\tau} \quad (1)$$

where WC is the working capacity (moles/kg adsorbent/cycle), ρ_B is the bulk adsorbent density (kg adsorbent/m^3) and τ is the cycle time (s/cycle). Although structured adsorbents are developed with the aim of operation at faster cycle times (lower τ), any development which simultaneously reduces adsorbent density (ρ_B) is detrimental to throughput. Thus although structured adsorbents may have remarkable advantages over adsorbent pellets such as fast mass transfer kinetics (due to shorter diffusion path) and easier heat transfer in all directions, as well as more uniform temperature distribution, their throughput is often lower, since the adsorbent loading on a mass or volume basis is often small compared to adsorbent materials in the form of pellets/beads.

It is worth mentioning that high adsorbent loading may not always be a desirable parameter in all adsorptive processes if other features are compromised. For instance, in some adsorptive systems, mass and heat transfer processes dominate system performance (e.g. removing moisture from air) and hence reducing the characteristic diffusion length may necessitate the use of thin layers of adsorbent which may actually lead to reduced adsorbent loading. In terms of Eq. (1), high ρ_B may compromise WC and hence an optimum loading may exist.

A feature related to adsorbent loading which becomes increasingly important as cycle time is reduced is "switching" losses. Switching losses are losses in throughput and separation due to pressurizing and depressurizing "dead" space. These losses become

Table 1
A summary of structured adsorbent applications in adsorptive processes.

Reference	Structure	Packing details	System	Experimental conditions	Results
Kodama et al. [21]	Monolith	Honeycomb rotor with a thin sheet of silica gel	Air dehumidification	Air velocity of 1.2 m/s through a 0.2-m long honeycomb	10–20% humidity reduction
Gadkaree [23]	Monolith, 400 cpsi	Activated carbon honeycomb structures	VOC removal	Honeycombs with about 18 wt% carbon	Breakthrough curves similar to packed beds
Li et al. [24]	Monolith	5A zeolite monolith	Oxygen-enriched air	3.8 bar feed pressure	3–5 times lower pressure drop
Brandani et al. [32]	Monolith	Carbon monolith	CO_2–He and CO_2–N_2	Pressure: 23 Torr, temperature: 23 °C	Dispersion is controlled by mass transfer resistance rather than axial dispersion
Yates et al. [34]	Monolith, 50 cpsi	Honeycomb monolith	Effluent gas purification	Pressure: 1 atm, temperature: room temperature	Allowing adsorbent regeneration up to 300 °C
Yu et al. [35]	Monolith, 400 cpsi	Activated carbon monolith	VOC removal	Pressure: 1 atm, temperature: 20, 60, 100, and 140 °C	Good correlation of VOCs adsorption data on activated carbon monolith using Langmuir–Freundlich and Toth equations
Valdes-Solis et al. [37]	Monolith, 200–900 cpsi	Carbon-coated ceramic monoliths	VOC removal	Pressure: 1 atm, temperature: room temperature	Better breakthrough performance than a packed bed
Grande et al. [41]	Monolith, 424,900 cpsi	4A honeycomb monolith	Propane and propylene adsorption	Pressure: 1.5, 5.6 and 10.0 kPa, temperature: room temperature	Smaller diffusivity coefficients than extrudates
Cutler et al. [44]	Monolith, 50–3000 cpsi	Honeycomb monolith	Desulphurization process	Pressure: 1 atm, temperature: 25–400 °C	Lower pressure drop per volume
Ribeiro et al. [45]	Monolith, 300 cpsi	Activated carbon honeycomb monolith	CO_2, CH_4, and N_2 Adsorption	Pressure: 1 atm, temperature: 303–423 K	Adsorption capacity honeycomb monolith: $CO_2 > CH_4 > N_2$
Jain et al. [46]	Monolith	Monolithic wheel	Air separation	–	Cycle time of 35 s for rapid PSA
Kaboord et al. [48]	Monolith, 120 cpsi	Honeycomb monolith	Vehicle exhaust systems	–	Suitable for diesel engines
Jale et al. [49]	Monolith	Honeycomb monolith	Air separation	–	Improved N_2/O_2 selectivity and N_2 capacity
Gorbach et al. [55]	Monolith, 100, 200, 400 cpsi	Zeolite 4A-polyamide monolith	Rapid PSA (RPSA)	Extrusion of polymer matrices filled with zeolite powder using thermoplastic materials as plasticizing aid and binder	Enhancement of productivity, lower pressure drop
Yu et al. [105,106]	Monolith, 400 cpsi	Activated carbon monolith	Electrothermal swing adsorption(ESA)	Pressure: 1 atm, temperature: room temperature	High toluene vapour removal
Grande and Rodrigues [107]	Monolith, 190 cpsi	Activated carbon honeycomb monolith	CO_2 removal ESA	Pressure: 101 kPa temperature: 297 K	CO_2 recovery: more than 89%, CO_2 purity: 16%
Keefer et al. [66,67] and Connor et al. [65]	Laminate	Adsorbent sheet	Rotary PSA, rapid PSA	–	Lower pressure drop
Keefer [70]	Laminate	Laminated parallel passage contactor	PSA system	–	Operation at high frequency
Maurer [68]	Laminate	Spirally wound adsorbent	VOC removal	–	Longer adsorbent life alternative for a thermal swing adsorption process
Ruthven and Thaeron [4]	Laminate	Parallel passage contactor coated with ACF sheets	CO_2 removal	Pressure: 1 atm, temperature: room temperature	High selectivity ratio diffusion time constant of 10 ms
Keefer [70]	Laminate	Layered adsorbent beds	Ultra rapid PSA	–	100 cycle/min
Keefer [67]	Laminate	Adsorbent laminate coated with X-zeolite	Oxygen enrichment PSA	Channel width: 50–75 μm, wall thickness: 50–75 μm	200 cycle/min
Rode et al. [72]	Laminate	Parallel passage sheets	Air separation	–	Increased productivity and/or recovery
Patcas et al. [8]	Foam	Ceramic foams	Oxidation of CO	Foam 20, 45 PPI	Better performance compared to packed bed

Table 1 (*Continued*).

Reference	Structure	Packing details	System	Experimental conditions	Results
Bonaccorsi et al. [97]	Foam	Copper foams coated with 4A zeolite	Heat pumps	Pressures: 10–65 mbar, temperature: 328–493 K	High rate of water uptake
Golden et al. [75]	Fabric structure	Multilayered adsorbent	H_2 recovery by rapid PSA	Adsorbent surface area > 500 m^2/g	H_2 purity: 99.9%H_2 recovery: 70%
Golden, et al. [6]	Fabric structure	Self-supporting adsorbent fabric	H_2 production by rapid PSA (RPSA)	Feed temperature: 0–100 °C feed pressure: 1.5–40 atm	H_2 purity: 99.9%H_2 recovery: 70%
Bailey et al. [76]	Fabric structure	Charcoal cloth	Air purification		Lower resistance to gas flow, high adsorptive capacity
Sullivan et al. [78]	Fabric structure	Activated carbon cloth	Air purification	Electrothermal regeneration	Capture efficiency: 99.9%
Kim et al. [36] and Yamauchi et al. [61]	Paper honeycomb	Corrugated paper rolled to form honeycomb shaped cylinder	VOC abatement	VOC concentration: 150–420 ppm, flow rate: 150 600 L/min	More than 95% VOC removal
Matsukuma et al. [62,63]	Paper honeycomb	Rotary bed	CO_2 recovery	Adsorber: 460 mm diameter, 480 mm height	More than 80% CO_2 recovery
Kodama et al. [60]	Honeycomb rotary adsorber	Sandwich arrangement	Desicant cooling	Adsorber: 0.3 m diameter, 0.2 m height	Dehumidifying performance was much lower than that we expected
Leedy et al. [96]	Honeycomb monolith	Impregnated with alkaline or caustic salts	H_2S removal	Impregnated with 10% Na_2CO_3	Improved adsorption capacity, shorter MTZ
Ohrman et al. [92]	Monolith	Cordierite monolith coated with ZSM-5 film	P-xylene isomerisation	Seed-film method	Films became less deactivated than the films prepared on alumina beads
Matsuoka et al. [94]	Zeolite paper	Paper monolith	NOx removal VSA	Pilot plant pressure: 120 kPa adsorption, 5 kPa desorption, temperature: 298 K	More than 95% NOx recovery
Mosca et al. [26]	Monolith, 400 cpsi	Cordierite monolith coated with NaX zeolite	CO_2 capturing	Pressure: 1 atm, temperature: room temperature	100 times lower pressure drop
Belding et al. [50–53]	Adsorbent paper	Corrugated paper or honeycomb structure	Heat exchange wheel	–	Adsorbing moisture from a humid air stream

proportionally larger as the ratio of adsorbent volume to non-adsorbent void volume decreases. Typically, large low pressure PSA process vessels adsorb up to two magnitudes more gas on the adsorbent than exists in the void space. As the amount of adsorbent decreases (due to faster cycling), the proportion of void space to adsorbent volume increases and therefore increasingly work is done to simply compress and depress void space gas with no separation. Reductions in switching losses can only be achieved by higher adsorbent densities and careful engineering to minimize void space as well as investigation of alternate non-switching technologies, e.g. rotary valve systems.

2.2. Role of pressure drop

Pressure drop impacts system performance in several ways. The existence of a pressure profile in the axial direction in an adsorption process (both during adsorption and desorption) implies that not all of the adsorbent experiences the full pressure swing available to the system. This directly reduces working capacity, *WC*. The problem is especially acute for vacuum swing adsorption in which low vacuum pressures are needed for adsorbent regeneration, e.g. CO_2VSA [1]. In this application, a vacuum pressure of 3 kPa may be needed to produce sufficient CO_2 recovery and throughput. Hence a pressure drop of just 1 kPa in the bed during the vacuum step can reduce CO_2 recovery by as much as 5%. In addition to this effect, increased pressure drop increases energy consumption. One option to circumvent the high pressure drop problem of conventional packed beds without changing the type of adsorbent is to utilize radial bed adsorbers [2]. Radial beds produce lower pressure drop for the same mass flow rate due to the expanding radius in the direction of flow. Lower cycle time and higher throughputs without fluidization are possible, although their design is complex and costly.

To describe the role of system parameters contributing to pressure drop in a packed bed, the well known *Ergun* equation [3] is considered here:

$$\frac{\Delta P}{L} = 150\frac{(1-\varepsilon)^2}{\varepsilon^3}\frac{\mu}{{d_p}^2}U + 1.75\frac{(1-\varepsilon)}{\varepsilon^3}\frac{\rho}{d_p}U^2 \tag{2}$$

where U is the superficial velocity, ρ and μ are the density and viscosity of the gas, respectively, d_p is the particle diameter and ε is the bed voidage. Clearly decreasing void volume and particle size both increase pressure drop. Although decreasing void volume also increases pressure drop for structured adsorbents (not necessarily according to (2) however), it is easier in parallel channel adsorbents to control ε to obtain satisfactory performance. In addition, the tortuosity of the channels in monolith or laminate structures is 1, compared with 2–3 for a packed bed of granules. Therefore the pressure drop in a packed bed is larger than in a monolith structure for equal voidage. Furthermore, the system geometry in laminates and monoliths can be easily manipulated to achieve lower head loss. This is achieved by decreasing cell density or wall thickness in monoliths and increasing sheet spacing and decreasing wall thickness in laminates. Generally, parallel channels exhibit better performance with respect to pressure drop; however they must be carefully designed to avoid too much loss of adsorbent loading and large diffusion paths (wall thickness).

2.3. Mass transfers characteristics

Theoretical and experimental studies [4–8] have shown the influence of adsorbent structure on mass transfer kinetics which in turn influences the overall system efficiency. The separation performance may be degraded by dissipative effects of mass transfer resistance (internal and external) and axial dispersion. At higher gas velocities associated with higher cycle frequencies, the deleterious effects of mass transfer resistances typically increase, since in these conditions, the adsorption time scale becomes more comparable to cycle time. The diffusion time constant for the limiting resistance in adsorption systems is of order $\mathcal{L}^2/\mathcal{D}$ where $\mathcal{L}$ is the limiting length parameter and $\mathcal{D}$ the corresponding diffusivity. For pellets, $\mathcal{L}$ is the pellet radius and $\mathcal{D}$, the "effective" diffusivity. In conventional packed bed processes, with cycle times of the order of hours or even minutes, the timescale for adsorption into/out of the pellets is approximately 5–100 times shorter than the residence time and hence mass transfer resistance is not dominant. This picture changes dramatically when rapid cycles are used. If interstitial velocities are 10–100 times higher, then the time scale for adsorption becomes comparable to, or even greater than the residence time leading to immediate breakthrough of the gas and unacceptable operation. To reduce the timescale for adsorption, smaller particles can be used, however, the resultant pressure drop and low mechanical stability rapidly becomes unmanageable. Moreover, with increasing space velocity, conventional packed bed adsorbents can be fluidized. The advantages of a rigid adsorbent structure are therefore readily apparent.

Some adsorption process models developed are based on local equilibrium, i.e. ignore the mass transfer resistances in the system. In reality, those resistances are not always negligible and must be taken into account for more reliable prediction of system performance. The overall mass transfer coefficient, k, for systems with linear isotherms obeying the linear driving force model can be evaluated through the relationship [9]

$$\frac{1}{kK} = \frac{R_p}{3k_f} + \frac{R_p^2}{15\varepsilon_p D_p} + \frac{r_c^2}{15KD_c} + \left(\frac{1-\varepsilon}{\varepsilon}\right)\frac{D_L}{v^2} \tag{3}$$

where K is the equilibrium constant, k_f is the external film coefficient, R_p and r_c are particle and crystal radii, respectively, D_p and D_c are pore and intracrystalline diffusivity, respectively, D_L is axial dispersion and v is velocity. The relative importance of internal and external resistances is expressed by the *Biot* number k_fL/D where L is a characteristic dimension (particle diameter) and D the internal diffusion coefficient. The mass transfer *Biot* number for packed beds for most applications is in the range of 5–500 and hence the major resistance for mass transfer is within the particle [10]. Generally speaking, micropore diffusion resistance dominates over film and macropore resistances if

$$\frac{D_p/R_p^2}{D_c/r_c^2} \gg 1 + \left(\frac{1-\varepsilon}{\varepsilon}\right)K \text{ and } \frac{5D_p}{kR_p} \ll 1$$

The opposite situation holds for macropore diffusion. In pelleted systems and foam structures, the external film resistance seldom plays a role in overall mass transfer and is usually neglected. According to Patcas et al. [8], the external mass transfer coefficient of foam structures is somewhat between those of monoliths and packed beds. Typically, the mass transfer coefficient of foams would increase by increasing the pore count at constant hydrodynamic conditions due to enhanced surface area available for adsorption. In the case of laminates and monoliths, however, we expect film resistance to be very important, even governing, depending on channel and wall thickness dimensions. Larger film coefficients can be obtained by smaller channel diameters and sheet spacing. Unfortunately, the dependence of the film coefficient on Reynolds number is quite weak as shown below. Higher velocities are therefore not a practical way of achieving better mass transfer. We expect laminar flow to prevail in the channels for all typical cycle times. The film resistance is comparable to the pore diffusion resistance in this situation especially when the laminate or monolith walls are very thin and internal mass transfer is very rapid.

The appropriate dimensionless group characterising film diffusion is the *Sherwood* Number, *Sh*. For pelleted systems the Wakao–Funazkri equation [11] is typically used to estimate k_f

$$Sh = 2 + 1.1Re^{0.6}Sc^{0.33} \quad (4)$$

For monolithic and laminate structures, *Hawthorn*'s equation [12] for laminar flow is employed

$$Sh = \frac{dk_f}{D_m} = A\left(1 + 0.139ReSc\frac{d_h}{L}\right)^{0.81} \quad (5)$$

where the parameter A is 3.6 for circular channels, 2.35 for triangular channels and 2.95 for square channels. D_m, d_h and L are molecular diffusion coefficients, channel hydraulic mean diameter and column length, respectively. Typically, d/L is very small since channels are of diameter 1 mm and length 100 mm while Re is usually small (<500). A generalised correlation proposed by Groppi et al. [13] is appropriate to describe the external film mass transfer coefficient in foam structures

$$Sh = 0.91Re^{0.43}Sc^{0.33} \quad (6)$$

subject to the constraint

$$15 < Re < 200$$

It is clear therefore that external film diffusion which is typically neglected for particulates may be important for adsorbent structures and should be considered when modelling and designing these systems. A more detailed assessment of the impact of external film resistance has recently been conducted by Rezaei and Webley [14].

The contribution of axial dispersion to k for pellets, is usually small (similar to external diffusion) and can justifiably be neglected. The plug flow assumption is therefore adequate. Note however that very small particles (<1.0 mm) have significantly increased axial dispersion and D_L/v^2 may become comparable to pore diffusion resistance and indicates that for small diameter pellets, gains in kinetic effects from reducing particle size can be rapidly offset by increased axial dispersion. In monoliths, axial dispersion is much more dependent on channel diameter and flow rate. For laminates, resistances in the porous material and external film are far greater than axial dispersion in the gas phase. Axial dispersion in a packed bed is correlated in terms of the *Peclet* number ($Pe = Ud/D_L$), and can be obtained from

$$\frac{\varepsilon_b D_L}{D_m} = 20 + 0.5Re\,Sc \quad (7)$$

where D_m is the molecular diffusion coefficient and d is particle diameter. The same expression is used for foam structures. In laminar flow, axial dispersion in monolithic structures can be calculated from *Taylor*'s [15] analysis

$$Pe = \frac{Ud}{D_L} \approx 192\frac{D_m}{Ud} \quad (8)$$

For laminates, a similar approach holds as with monoliths. In turbulent flow, *Taylor* analysis gives:

$$Pe = \frac{0.28}{\sqrt{f}}, \quad f = 0.046Re^{-0.2} \quad (9)$$

For this case, the extent of axial dispersion is greater but still significantly less than the other factors causing broadening of the mass transfer zone. In fact, more detailed analysis reveals that axial dispersion is usually negligible even in monolithic and laminate structures [14]. Of course maldistribution and channelling are more likely in monolith systems and laminates and require attention to detail in the fabrication process.

It should be noted that the binder in adsorbent structures may influence the role of mass transfer. In certain adsorptive applications such as dehumidification processes wherein the diffusivity of the adsorbate molecule (water) through the binder layer is high enough to reach the adsorbent particles, the binder material does not degrade the overall kinetics of the process. In contrast, in several adsorptive processes such as air separation application, the binder serves as a kinetic barrier to adsorbate molecules from reaching the adsorbent particle. The detailed pore engineering required for efficient mass transfer at the micro- and meso-scopic scale applies to all adsorbent structures.

2.4. Thermal management

As mentioned earlier, pressure swing systems are affected by the thermal swing accompanying the adsorption/desorption process. As a first estimate, the temperature swing at a point in the bed is given by

$$\Delta T = \frac{WC * Q_{ads}}{C_s} \quad (10)$$

where WC is the working capacity, Q_{ads} is the heat of adsorption and C_s is the solid specific heat (kJ/kg). In turn, the temperature swing affects the adsorption and desorption detrimentally, reducing capacity on adsorption and increasing it on desorption. To reduce the effect of this temperature swing several approaches have been attempted including insertion of heat transfer devices into the packed bed [16], or use of metallic compounds or phase change materials to either increase C_s or absorb the heat of adsorption [17]. These approaches have met with limited success since in the case of pellets having a size more than several micrometers, there is a temperature gradient between the surface and the inner part of the particle during adsorption and desorption due to poor thermal conductivity of the adsorbent material. Therefore it is difficult to obtain a uniform temperature across the particle regardless of external heat transfer devices.

Adsorbents in the form of laminates, monoliths, cloths and foams can positively influence the thermal behaviour of an adsorber bed by selecting a suitable support material with a favourable thermal conductivity. Consequently, the thermal properties of the system can be carefully engineered. In the case of monoliths, foams and laminates, a macropore wall structure can facilitate the dissipation of heat and consequently more nearly achieve a uniform temperature distribution across the adsorbent. With regard to laminate structures, metallic supports exhibit favourable thermal properties with high thermal conductivity and heat capacity. Care must be taken however to avoid relative stresses induced in the system during cyclic heating and cooling which may result in detachment of the adsorbent material from the support.

Foamed adsorbents offer a unique structure of high porosity (75–90%) and tortuosity, and hence we expect a more uniform temperature distribution in the adsorbent. This is due to improved turbulence and an inherent structure which means that heat can be transported not only by conduction, but other mechanisms such as convection and even radiation. This a fertile area for future research since not only can adsorbent structure manage heat more effectively in a passive mode, but they may in fact offer opportunities for "active" thermal management (see Section 3.6).

2.5. Trade-off of properties

The design of adsorbent structures involves, inevitably a trade-off between a number of parameters which govern the overall adsorbent performance. Adsorbents with high working capacity and fast kinetics are favoured for cyclic separation processes, however these requirements can only be met at ideal conditions.

External surface area per unit volume of adsorbent is one of the most important characteristics governing the performance of adsorbents but higher surface area is usually associated with lower adsorbent density. For laminate, cloth and monolith structures, in order to maintain a sufficient surface area and hence improved kinetic properties, the wall thickness and spacing should be kept small. Thinner wall thickness means shorter diffusion path but on the other hand, lower adsorbent loading associated with thinner walls will result in insufficient adsorbent density [14]. The same argument is valid for adsorbent voidage. High voidage may be associated with faster kinetics, however, the bed density is low which gives rise to lower working capacity. Small spacing between adjacent sheets or small channels increases the pressure drop as well. In the case of beads there is always a trade-off between pressure drop and mass/heat transport characteristics, smaller pellets display clearly high surface area and mass/heat kinetics, while the system pressure drop is dramatically increased.

Such trade-off behaviours should always take into consideration when dealing with adsorbent structure. In this regard, a formal optimization approach could be employed by conducting appropriate simulations or experiments to identify the optimum conditions for a particular application. A general procedure to illustrate this interplay of features is provided below in Section 3.7.

3. Alternate adsorbent configurations

A large variety of structured adsorbents have been studied and commercialized over the last 20 years. Table 1 provides a summary of these reported structures together with details of the experiments and key experimental results. The structures can be categorized as monoliths (including honeycomb topologies), laminates, foams, fabric structures and "other" structures.

3.1. Monolithic adsorbents

In recent years, monolithic adsorbents have received considerable attention for use in adsorption systems [18]. Monoliths are structured supports composed of parallel channels with a variety of cross-sectional shapes. They have been widely used as a catalyst support in various applications including catalytic combustion, biochemical and electrochemical reactors, automotive catalytic convertors, etc. [18,19]. The use of monoliths in adsorption process is rather new compared to its applications in the catalytic field [20–22]. The characteristic difference between adsorptive and catalytic monoliths stems from the need for sorption capacity in the former. Hence monoliths for adsorption are often entirely comprised of adsorbent (or at least highly filled) while catalytic monoliths usually rely on a wash coat of active catalyst on a monolithic support.

Early attempts in the use of monolithic adsorbent structures for separation process were mostly related to elimination of VOCs from air [21,23]. MAST carbon, a specialist developer of activated carbon produces a variety of activated carbon monoliths for a range of applications including (but not limited to) VOC removal. Li et al. [24] examined the technical feasibility of 5A zeolite monolith (containing 25% Na-bentonite) for the production of oxygen-enriched air. They compared their results to a packed bed of commercial pellets and showed while the separation performance of the monoliths was inferior to the pellets, the pressure drop in the monolith system was almost 3–5 times lower than the one in the packed bed, resulting in a 3–5 times faster pressurization time.

Although the unique structure of monoliths (continuous body with identical channels) significantly reduces the common problems of conventional adsorbents (i.e. fluidization, high pressure drop, etc.), these structures may very low loading of active adsorbent material. In addition, not all the adsorbent material present in the skeleton of the monolith wall is accessible to the adsorbate molecules passing through the channels. The active adsorbent material may be directly extruded in the form of a structured monolith (commonly done for carbon monoliths in which case the entire monolith is active adsorbent) or an active film may be grown on the monolithic structures by various methods, namely, dip-coating, wash-coating, and slip-coating [25]. Mosca et al. [26] have shown how films of NaX zeolite may be deposited on cordierite monolith supports. In order for monolithic adsorbents to meet the mass transfer requirements for efficient performance, both channel and wall thickness should be as small as possible [27]. It is known that monoliths with higher cell densities would give proportionally better performance because of their higher geometrical surface area and solid loading; however, the improvement gained by higher density must be weighed against the added cost of their manufacturing, since the manufacturing of such structures is complex and difficult. Furthermore, monoliths at such high density (several hundred to over one thousand cpsi) with a large loading capacity of active adsorbent are not available yet in commercial quantities. An interesting and dramatic demonstration of the effectiveness of ultra-high cell density monoliths was provided by the work of Li et al. [28] in which a cuttlebone was used as a biomorphic template to produce a monolith of NaX with 16,000 cells per square inch. These materials showed excellent mass transfer properties and still exhibited lower pressure drop than a packed bed.

The geometric parameters of monoliths which influence the processing requirements are defined in terms of cell density, cell spacing or wall thickness. The cell density of monoliths is defined as the number of cells per unit of cross-sectional area and expressed as cells per square inch (cpsi). As discussed earlier, monoliths provide lower pressure drop per unit length of the bed than a packed bed. Given constant gas viscosity, monolith length, and open frontal area (OFA), the pressure drop of monolith adsorbents increases with increasing cell density. On the other hand, given a constant cell density, the pressure drop decreases with decreasing wall thickness. Thus monoliths are one of the most efficient methods available to pack high adsorbent surface area into a fixed volume while still maintaining low pressure drop.

Monoliths have two major resistances to mass transfer; external film resistance, and pore diffusion within the walls. The characteristic diffusion length can be shortened by employing a thinner adsorbent wall. Unfortunately, the residence time in the monolith is likely to be much shorter than in a packed bed so that the timescales of diffusion and transport through the channels may be comparable. The low pressure drop of monoliths and laminates must be exploited by using long beds to give large gas residence times. High cell densities are favoured since these produce high adsorbent loading and short diffusion lengths.

Meyers and Liapis [29,30] have employed pore network theory to determine in an *a priori* manner, the mass transfer and pressure drop characteristics of monoliths and in columns packed with porous particles. The outcome of their microscopic model was then employed in a dynamic macroscopic model to describe the dynamic behaviour of chromatographic columns. In another study conducted by Liapis et al. [31], the dynamic behaviour of monolith adsorbents in a chromatographic column was evaluated through mathematical modelling. Their result indicated remarkable benefits of monolithic adsorbents over spherical particles if a suitable monolith (large through pores and small-sized skeleton) with controllable dimension is employed.

In another study, the adsorption kinetics and diffusion of CO_2 in carbon based monoliths was studied using the zero length column (ZLC) method by Brandani et al. [32]. These authors showed that the dispersion in the monoliths is mainly controlled by mass transfer resistance rather than axial mixing. Recently, Mosca et

al. [26] have used structured adsorbents in the form of thin zeolite films supported on cordierite monoliths for CO_2 capture in PSA systems. The pressure drop was 45 times lower than a comparable packed bed although the adsorption capacity of the new configuration adsorbents was 67 times lower than conventional beads. Their results suggest the potential of monolith structured adsorbents as a competitive alternative to traditionally used packed beds in PSA processes providing a high cell density can be used.

Activated carbon monoliths such as those produced by MAST carbon, are another class of adsorbents which offer great potential for use in various applications such as electric swing adsorption (ESA) and military filtration applications. The monoliths are typically synthesized from a phenolic resin precursor followed by carbonization step which offers high surface area available for adsorption [33]. Due to inherent electrical conductivity of activated carbon, rapid thermal swing operation can be achieved by regeneration of the monolith through electrical heating. In contract to hot purge gas, this method will achieve far faster cycles. In addition, activated carbon monoliths are self-supporting and hence are virtually 100% active material. This advantage offered by carbon monoliths makes them suitable candidates for electrical swing adsorption (ESA) processes. A more detailed discussion of ESA devices is presented in Section 3.6.

A number of studies have reported monolithic adsorbents for the removal of volatile organic compounds (VOCs) from air [23,34–38]. Shah et al. [39] studied the removal of volatile organic compounds (VOCs) from air using monoliths and performed simulations for comparing the performance of their novel adsorbents with a packed bed of pellets. In another study Lee et al. [40] showed that the adsorptive performance of hydrophobic zeolite monoliths in the removal of VOCs from air improves by increasing the cell density and reducing wall thickness.

Patton et al. [7] observed that by optimizing the design of monolithic structures such as appropriate wall thickness, channel width and shape, it would be possible to improve the separation performance of monoliths. They further suggest the use of regular hexagonal channels, for efficient internal mass transfer performance. The authors then evaluated the performance of hexagonal monoliths with a wall thickness of 0.4 mm and a channel dimension of 0.6 mm for the removal of VOCs from air and showed that the internal mass transfer performance of these adsorbents are comparable with a typical packed bed containing 1 mm pellets.

Grande et al. [41] demonstrated the behaviour of zeolite 4A honeycomb monolith for the adsorption of propane and propylene at different pressures and temperatures. Adsorption equilibrium data of both gases were reported to be identical to commercial extrudates, while the kinetic parameters were three orders of magnitude smaller than extrudates. In other studies performed by Zabka et al. [42,43] the main focus was devoted to the utilization of silica-based monoliths in HPLC columns and the equilibrium and kinetics of adsorption was examined by taking into account Darcy's law and HETP concepts.

Cutler et al. [44] discloses the use of honeycomb monolithic adsorbents for fuel desulphurization process. The authors further recommend the utilization of such adsorbers in fuel reforming apparatus for generating hydrogen fuel for hydrogen-powered fuel cells, or in fuel delivery systems for supplying low-sulphur fuel to combustion engines, or in other systems supporting combustion processes requiring the use of low-sulphur fuel. Adsorption of CO_2, CH_4 and N_2 in activated carbon honeycomb monoliths was performed by Ribeiro et al. [45]. This investigation aimed at the generation of bio-methane from renewable fuels. The authors conducted mathematical modelling for further evaluation of adsorption performance of honeycomb monoliths. A recently published patent by Jain et al. [46] reports the operation of rapid PSA systems for air separation processes for a cycle time of 35 s using monolith adsorbents.

Desulphurization process can be performed using adsorbents or catalysts in different forms including pellets/beads, foams or monoliths. He et al. [47] studied the development of high surface area structured monolith adsorbents for sulphur removal. These honeycomb sulphur traps were fabricated by extruding commercially available sulphur removal catalysts such as zinc based materials into monolithic honeycombs, however, no information regarding the application of this honeycomb sulphur adsorbent was provided.

Monolithic adsorbents are found to be suitable for use in NOx adsorbers. In these cases, the active adsorbent materials such as zeolites, silicas or alkali/alkaline earth metal oxides are wash-coated on the monolithic structure. Kaboord et al. [48] disclosed pollution control devices, especially adsorbent and catalyst beds for diesel engines using monolith structures.

Jale et al. [49] disclosed the use of alkali or alkaline metal salts in preparing zeolite containing adsorbent sheets, their preparation into adsorbent monoliths and their subsequent use in air separation process. Based on the author's claims, the prepared monolith adsorbent exhibits improved nitrogen capacity (around 0.6 mmol/g by addition of LiOH to the sheet) and nitrogen/oxygen selectivity (9.1 at 300 mbar) in air separation process via either PSA or VSA.

The rapid heating and cooling features of monolithic and thin walled zeolite systems make them ideally suited to TSA applications. One such application is dehumidification of air [50–54]. In these applications, monoliths are fabricated into large rotary wheels, permitting alternate adsorption and desorption to occur at different parts of the wheel as it is rotated. For instance, Belding et al. [50], describe the employment of Y-zeolite in the fabrication of a desiccant wheel to provide a body which readily adsorbs moisture contained in ambient air. They further showed through experiments that the zeolite wheel is very efficient in water removal with a capacity of 5.41 tons and a coefficient of performance of 0.92 [53].

The potential application of adsorbent polymer monoliths in particular, zeolite 4A-polyamide adsorbent, in rapid PSA for the adsorption of water vapour was evaluated by Gorbach et al. [55]. According to their results, although the adsorption capacity of the polymeric adsorbents was found to be the same as pellets, the mass transfer kinetics was enhanced substantially. The advantage of polymeric monoliths over conventional ceramic monoliths could be in the manufacturing step, which is simple and avoids energy-intensive high temperature treatment steps, although the after-treatment step (creating a secondary pore structure) is an energy demanding step.

Although many studies have been undertaken to evaluate the mass transfer and pressure drop characteristics of monoliths in adsorption applications, the effect of thermal management and adsorbent loading in adsorptive efficiency has been scarcely discussed. Future work should carefully consider the potential enhancement in performance by examining the options of thermal management for monolithic structures.

The introduction of thermal swing honeycomb rotor adsorbers into the market in 1980s for VOC removal opened a new path toward development of air treatment process and stimulated researchers to study this area. This developed technology utilizes the adsorbent material in the form of a honeycomb or monolith configuration rather than particles. The employment of the adsorbent in these configurations (honeycomb or monoliths) gives rise to a rapid response to temperature swing in the regeneration step. Initially, activated carbon was chosen to act as adsorbent material, however, soon, it was replaced by zeolite type adsorbents (high silica adsorbents) in order to avoid the possibility of adsorbent ignition during thermal regeneration by hot air.

Zeolite paper honeycomb structures have found several applications in adsorption processes mainly VOC removal and air treatment by TSA apparatus. These adsorbents are usually made by impregnation of ceramic papers and corrugating the sheets in order to create the honeycomb structure [21,56–60]. In the study conducted by Kim et al. [36] zeolite paper in the form of honeycomb rotors was employed in the removal of trace amount of VOCs. Their honeycomb adsorbent showed a remarkable efficiency for removing toluene, MEK and cyclohexanone. In another recent study by Yamauchi et al. [61], a zeolite honeycomb rotor adsorbent was applied to the VOC abatement systems operating with TSA. These authors showed that the VOC removal efficiency depends mainly on variables such as rotation speed, gas flow rate, regeneration temperature. By operating at optimum condition based on these variables, it is possible to achieve a high performance with more than 95% VOC elimination from the feed gas. Although the honeycomb adsorbers were first employed for elimination of VOCs and other pollutants, recently, some researchers have reported the application of this type of adsorbents for CO_2 recovery [62]. Matsukuma et al. [63] showed through pilot plant experiments that the CO_2 recovery in rotary adsorption towers having an inner diameter of 460 mm and adsorbent height of 480 mm could attain more than 80%.

Another application of multi-pass honeycomb rotary adsorbers is in desiccant cooling systems with a sandwich arrangement of honeycomb shaped adsorbed blocks and aluminium passages [60]. In terms of thermal management, this structure offers advantages in terms of operating at semi-isothermal condition. The authors suggest the direct regeneration of this system by hot water heating instead of air.

3.2. Laminate adsorbents

Laminate structures can be considered a simpler form of monoliths in which the channels are replaced by 1D slits. As with monoliths, they can potentially exhibit significantly better performance than a packed bed. The practical difficulties involved in reproducibly making such structures are not trivial however. The tolerances between sheets must be tight (<5%) to avoid maldistribution. This requires that the spacing must be maintained to within less than 0.01 mm generally speaking. As a result of this difficult manufacturing process, the use of laminate adsorbents in separation processes is not common. There are few published patents which describe the use of adsorbent materials in the form of laminate sheets in adsorptive gas separation applications [6,64–66].

Like monoliths, laminate adsorbents suffer from the problem of low adsorbent density due to several factors. A binder is usually present in the adsorbent matrix in addition to the presence of an external support. These non-adsorbent components directly reduce the volume loading of the adsorbent. This is in contrast to fabrics or self-supporting adsorbents where the structure itself would be able to compensate the problem of low adsorbent density. Laminate sheets can be packed into corrugated layers to increase adsorbent loading (and surface area) [36].

In laminate structures, the pressure drop per unit length is controlled mainly by altering the space between adjacent sheets. Like monolithic structures, thin sheets with small spacing not only increase pressure drop but also increase adsorbent loading and decrease mass transfer resistance. To achieve a practical configuration, some spacing technology is needed to ensure uniform channel width. These spacing devices can be manufactured by different methods, such as corrugating the laminates or making ridges on the sheets. The spaces between adjacent layers could be also created using external spacing devices such as mesh or grid. Care must be taken to ensure the spacer technology does not significantly contribute to higher pressure drop nor obstruct the gas flow through the adsorbent.

In 1992, Keefer [67] studied the operation of gas separation by PSA at high cycle frequencies using laminated parallel passage adsorbers. The adsorbent sheets were layered as a stack of flat sheets with channel width between adjacent sheets ranging from 15 to 75 μm. They showed that the attainable cycle frequency of these laminate sheet configurations is superior by almost an order of magnitude to that attainable in a packed bed, while the bed length could be reduced by a similar factor. They further employed their structured adsorbents for extraction of trace levels of H_2 isotopes from helium in which the H_2 recovery was shown to be 100% with 34% purity. Maurer [68] described the application of a spirally wound adsorbent in TSA systems for gas purification. The adsorbent layers contain adsorbent particles and the layers are separated by screens located between them. Ruthven and Thaeron [4] performed some theoretical and experimental studies on the application of a parallel passage adsorbent (coated with activated carbon fiber) for separation of CO_2 and N_2. Their results revealed that such adsorbent configurations are well suited to a dual piston rapid PSA system, and offer a combination of low pressure drop and a large number of theoretical stages for applications like CO_2 removal from stack gases. Another interesting outcome of this investigation was that macropore diffusion is a dominant mass transfer resistance in ACF sheets. Furthermore, numerical simulation of such parallel passage contactors used in piston-driven PSA was performed in another study [69]. The model developed could efficiently predict the pressure dynamics of parallel-passage piston-driven PSA.

In more recent published patents [64,70] Keefer and co-workers illustrate the utilization of adsorbent laminate structures at ultra rapid PSA systems operating at cyclic frequency of 100 cycle per minute (corresponding to a cycle time of 0.6 s) while the cycle time of conventional PSA devices for gas separation processes is on the order of several minutes. Such laminate adsorbents could be created in different configurations such as rectangular, spiral-wound or annular stack. Moreover, a support or a reinforcement material is required in their fabrication.

Keefer et al. [66] discloses methods of fabricating zeolite adsorbent laminate structures with various sheet supports such as metal foils, woven wire mesh, woven glass fiber cloth and nonwoven fiber glass scrims for the use in PSA systems. The adsorbent laminates coated with X-zeolites were then used in oxygen enrichment PSA with cycle frequencies up to 200 cycles per minutes. The adsorbent laminates had a channel width of 50–75 μm with adsorbent thickness of 50–75 μm on both sides of the sheets. Although methods for forming adsorbent laminate structures particularly for use in PSA devices have been addressed in detail, no report on the utilization of such structures in real processes has been reported.

Laminate adsorbent structures have been described by Sawad et al. [71]. The authors teach the fabrication of high density adsorbent sheets by different technologies. Based on the patent claims, it would be possible to couple the benefits of metallic monoliths (i.e. heat transfer characteristics) and those self-supporting adsorbent sheets through impregnating sheets by materials with high heat transport rate.

Rode et al. [72] illustrated the application of improved adsorbent sheet-based parallel passage structures for PSA, TSA and partial PSA devices. According to this patent, the adsorbent can be constructed by adhering a suitable adsorbent to a support sheet, mesh or grid on one or both sides of the sheet. These sheet layers may include a binder to immobilize the adsorbent particles or fibrous materials for reinforcement of structure. These authors examined the performance of laminate sheets by employing them for air, CH_4–N_2 and CH_4–CO_2 separation systems. This patent reports the utilization of such configurations not only in kinetic-controlling processes but also in different adsorptive separation systems by incorporat-

ing suitable adsorbent materials. In the case of air separation over a modified 4A zeolite in the form of adsorbent laminates, their results showed that cycle frequency can be intensified by a factor of 4, when the zeolite crystal diameter is reduced by a factor of 4. Alternatively, the adsorbent structure may use zeolite crystals of 1 μm diameter to achieve a 16-fold intensification (increasing cycle frequency toward 160 cycles/min), while retaining approximately equal kinetic selectivity and thus separation performance. Moreover, based on the author's claims, for separation of carbon dioxide from methane, the ideal kinetic-controlled adsorptive selectivity could be as high as around 100 which may be very favourable for effective separation.

3.3. Foam structures

Ceramic foams have many attractive features as catalyst supports, however, their utilization in adsorptive gas separation applications is scarce. These types of adsorbents may have substantial benefits over other adsorbent configurations. They offer high geometric surface area resulting in an increase in the rate of external mass transfer and due to their inherent large porosity these structures are capable of maintaining a lower pressure drop than a packed bed of pellets/beads [73]. However, it is argued that such structures may not be suitable candidates in several cyclic processes such as PSA or partial PSA devices because of the adsorbent's high tortuosity and porosity which decrease separation performance.

Due to the inherent high porosity of foam adsorbents, the amount of active material may not be adequate to exhibit the same volume activity as a packed bed of pellets, however, this problem could be solved through adjusting the amount of adsorbent coating on the structure of the foam. As with monolith adsorbents, the flow friction and hence the pressure drop is decreased due to the larger flow channels and presence of large number of voids which allows the radial mixing of flow. This is the advantage (high bed porosity) of foam adsorbents over monolithic structures in which laminar flow does not allow radial mixing. Typically, higher voidage in the bed is favoured for operation at high velocities (i.e. high cycle frequency in cyclic operations) where pressure drop becomes crucial.

More recently, Patcas et al. [8] have performed an experimental comparison of catalysts with different carriers, namely, honeycomb monoliths, ceramic foams and spherical particles based on their pressure drop and mass and heat transfer characteristics in the oxidation of carbon monoxide. Their result showed that the performance of foam catalysts in terms of combined high mass transfer and low pressure drop was superior to particles and inferior to that honeycomb structures.

There has been extensive research on the preparation of zeolite foams using polymeric templates [71,74], but in spite of the promising advantages offered by foam structures, their employment in gas separation processes has not been studied yet. According to Yoon et al. [74], since there is no blocking problem owing to a binding agent and since zeolite is formed in the form of a thin layer in the foam even without any separate support, gas can freely move inside the zeolite foam having various outer shapes and thus the zeolite usage efficiency is substantially increased to nearly 100%. Moreover, due to the presence of macropores which are spatially communicated with each other and are large enough for molecules to freely enter and leave, the pressure drop could be substantially reduced in adsorption processes.

3.4. Fabric structures

Adsorbent fabrics present advantageous features for gas separation application. Due to the self-supporting nature of these configurations, they can potentially provide high adsorbent loadings while simultaneously providing very rapid mass transfer through the thin fibers of which the fabric is composed. Adsorbent fabric can be fabricated into various configurations in such a way that it still maintains the benefits of the fabric. The preferred configurations are parallel sheets and spiral-wound structures. Additional advantages offered by flexible adsorbent fabrics are lower attrition rates and higher mechanical strength. There is often no requirement for external support or spacers [75]. The heat transport characteristics of fabric adsorbents could be enhanced by modifying the materials present in the structure through employing materials with high thermal conductivity (by coating or impregnation techniques or weaving). Self-supporting cloths offer a lower resistance to gas flow and give rise to a lower pressure drop in the bed and of course eliminate fluidization issues.

The use of adsorbent fabrics in adsorption processes was first reported in the early 1980s when Bailey et al. [76] described the application of charcoal cloth configuration in adsorptive filters for air purification process. This patent claims that such cloth form adsorbents offer an appreciable adsorptive capacity and a much lower resistance to gas flow when compared to conventional pellets/beads. These charcoal cloths could be preferentially positioned parallel to the direction of gas flow for better performance.

Golden et al. [6] reports the use of adsorbent fabrics with average pore diameter from 12 to 15 Å in rapid PSA systems for CO_2 capturing and H_2 recovery. They found that these configurations are particularly suitable at shorter cycle times where mass transfer characteristics play a key role in separation. Employment of fabric adsorbents at longer cycle times where separation is performed based on equilibrium, does not give rise to any advantage over packed beds of pellets. Later, Golden et al. [75] reported data for the capture of CO_2 and H_2 recovery by rapid PSA and compared the results with monolithic and granules geometries. They claim a hydrogen recovery of at least 70% and a productivity of 99.9%. In the case of CO_2 adsorption using self-supported fabrics, a CO_2 mass transfer coefficient of at least 0.5 s^{-1} can be obtained which corresponds to a larger mass transfer rate than that attainable in a packed bed.

Sawad et al. [71] demonstrated coating activated carbon powder onto a fabric, cloth or felt made from activated carbon fibers. According to the authors' claims, such adsorbent structures have the advantage that the substrate itself is an active adsorbent material which leads to a higher density adsorbent compared to the same system using an inert or non-adsorbent support.

By using an organic binder system, an activated carbon-coated activated carbon fabric, cloth, or felt may be treated under the appropriate conditions (including high temperature pyrolysis and a steam- or CO_2-activation stage) to convert the binder to active adsorbent. Using either or both of the above inventive modifications, the resulting adsorbent sheet possesses a high adsorbent density because a greater portion of the sheet structure may actively adsorb gases compared to systems where the binder and/or substrate are inert toward the desired adsorption process [71].

In the case of electrothermal desorption of adsorbents, Petkovska et al. [77] employed a bed with layers of activated carbon cloths in TSA process. A few years later, Sullivan et al. [78] used the same adsorbent configuration for removing hazardous air pollutants such as MEK, with a capture efficiency of more than 99.9% by mass. The adsorbent cloths were used in annular-cartridge configuration with the advantage of rapid electrothermal regeneration as well as low pressure drop. In another study Baudu et al. [79] applied the principle of thermal regeneration by Joule effect to a bed of activated charcoal cloth/or grains, for air treatment application.

As with fabric adsorbents, very little research has been performed with respect to thermal management or adsorbent loading considerations. Based on the unique feature of such adsorbents and

noticeable benefits gained by utilizing them in advanced adsorptive separation processes, there is a large opportunity to exploit their features for thermal management.

3.5. Other structures

In the case of traditional pellets used in adsorptive gas separation, recent advances have been achieved for fabrication of binderless pellets by converting the binder material to an active adsorbent. This dense packing technology tends to maximize the density of active adsorbent material. Attempts have been made to improve the fabrication process of beads/pellets; synthesizing of particles with controllable physical properties and well-ordered structures with uniform pore size distribution are among them. However, the most important drawback of particles configurations (high pressure drop) remains a large challenge which motivates the application of other structures.

The film growing method is another widely used technology for improving the adsorbent performance by increasing the active material loading [80–90]. Nikolajsen et al. [91] developed a structured sintered metal fiber plate covering a thin film of MFI-type zeolite for adsorption applications. This configuration was shown to be an efficient adsorbent in VOC removal. Ohrman et al. [92] grew well-defined ZSM-5 films on 400 cpsi cordierite monoliths using the seed-film method. They further tested their structured catalysts for P-xylene isomerisation. In another approach, Perdana et al. [93] reported the modelling of cordierite monoliths coated with a thin film of NaZSM-5, for NOx adsorption application. Matsuoka et al. [94] describes the bench and pilot scale NOx removal by adsorption process using VSA apparatus. The recovery of NOx from the denitrator was reported to be more than 95%.

Barrett et al. [95] fabricated adsorbent beads with higher mass transfer rates than ordinary pellets. The method employed for making these pellets involves the steps of low pressure extrusion and spherization. Although a detailed description of manufacturing steps was provided, the potential application of these improved pellets was not discussed.

Recently Leedy et al. [96], employed adsorbent honeycomb monoliths impregnated with alkaline or caustic salts to remove acidic gases, specifically H_2S. According to the disclosed claims of this patent, impregnated activated carbon monoliths exhibit improved adsorption capacity with a shorter mass transfer zone (MTZ) at a substantially lower pressure drop, compared to activated carbon pellets impregnated with the same alkaline salt with a similar loading. The impregnated monolith structures showed a mass transfer zone of 2–4 in. while the mass transfer zone related to impregnated pellets was 8–12 in. The pressure drops related to these structures were 0.1 and 2 in. H_2O/ft, respectively. The adsorption capacity of impregnated monoliths was reported to be 70 kg H_2S/m^3 bed, while the impregnated particles showed 17 kg H_2S/m^3 adsorption capacity.

An important application of structured adsorbents is in adsorption heat pump systems. Due to strict environmental regulations, adsorption heat pumps have gained more attention than conventional mechanical heat pump systems. In spite of rigorous advantages offered by such systems, their coefficient of performance (COP) is still lower than mechanical ones, therefore a wide variety of studies have been conducted to improve the performance of adsorption heat pumps. Among them, the adsorbent bed structure has received attention. Currently, the adsorption heat pump uses the adsorbent materials in the form of pellets, granules or fibers.

In the study conducted by Bonaccorsi et al. [97] open cell copper foams coated with active adsorbent material (zeolite 4A) was applied. In another study, a fast cycle adsorption refrigerator was evaluated using monolithic carbon discs combined with aluminium fins aimed at enhancing the heat and mass transfer rates by Critoph et al. [98]. Due to low thermal conductivity of the adsorbent materials used in adsorption heat pumps, designers attempted to overcome this deficiency by employing fins or metallic supports such as aluminium, steel or copper for coating adsorbent materials.

3.6. Use of adsorbent structures in electrical swing adsorption (ESA)

The concepts of "in situ" heating of adsorbents by electric current in the regeneration step was first proposed 40 years ago [99] and since then many studies have been devoted to apply this principle and develop TSA processes [77–79,100–104]. In electrothermal desorption devises, there are two electric resistances when pellets are being used, namely, the intrinsic resistance of each grain, as well as the resistance due to contact between particles. This implies that the resistance in the bed is anisotropic and the temperature is inhomogeneous along the bed. The use of ohmic heating necessitates a continuous adsorbent for electrical continuity and therefore structured adsorbents are desirable. In the case of fabric or cloth configurations being used in ESA devices, the problem of inhomogeneous temperature and the existence of hot points does not seem to be a severe issue, due to the movement of current in the direction of fibers although there might be a resistance at a microscopic scale between fibers. Monolithic structures are well adapted to application in ESA since the problem of electric contacts between particles in packed beds or even cloths is completely removed.

ESA confers remarkable benefits compared to conventional thermal regenerations, since the heat is delivered directly to the adsorbent media not to the vessel. Furthermore, heating by electricity allows the control of purge gas flow rate and the bed temperature independently from the power applied to obtain the maximum amount of effluent concentration. On the other hand, it must not be forgotten that the electric current is derived from a power station in which heat is used to generate power. Thus using electric current to generate heat is not thermodynamically desirable and should only be examined in cases where direct thermal regeneration is impractical.

Yu et al. [35] used activated carbon monoliths for VOCs removal using electrothermal desorption method. Yu et al. [105,106] investigated the electrothermal swing adsorption (ESA) process with an activated carbon monolith (400 cpsi) as adsorbent for adsorption of toluene vapours. They showed that activated carbon monoliths behave as a semi-conductor and the resistivity decreases as temperature decreases and amount adsorbed increases. The authors showed that the toluene vapours could be effectively enriched to high concentration. Also, they emphasized that the process performance is strongly dependent on the operating conditions and the desorption rate could be controlled by adjusting the electric current and purge gas flow rate. In a more recent study by Grande and Rodrigues [107], electric swing adsorption was employed for the removal of low molar fractions of CO_2 from flue gas. These authors utilized carbon honeycomb monolith as an adsorbent in ESA system which showed low electrical resistivity. Based on their findings, direct Joule effect enhanced CO_2 desorption rate. However, in order to obtain a higher recovery (more than 89%), the CO_2 purity was sacrificed to 16%. Place et al. [108] in their patent describe the application of porous monolithic carbon adsorbents for removing of VOCs from gas stream in an ESA system. The regeneration of monoliths that are electrically connected is performed using direct heating by electric current. According to author's claims, due to the low regenerant gas flows required in this system, the additional load on the adsorber is minimized. This is only possible with the electrically heated monoliths where large regenerant gas flows to carry the heat to the reactor are not required. Moreover, due to the low thermal capacity of the monolithic structures they can be

cooled back sufficiently quickly to the normal adsorption temperatures using feed gases without any adverse effect on the overall adsorption cycle.

3.7. Criteria for the assessment of adsorbent structure

From the preceding discussion it is clear that a large number of adsorbent structures are available and some have received close study. It is of interest however to attempt to derive criteria for the assessment of these competing structures for an application. Optimization of adsorbent structures for gas separations was recently studied by Rezaei and Webley [14]. The key results from that study are discussed here.

In a gas separation process, the goal is usually to maximize specific productivity, i.e. to be able to maximize throughput in a given amount of adsorbent. It is therefore necessary to consider an appropriate combination of process parameters to demonstrate how the pressure drop, cycle time and adsorption front affect system performance. As pointed out in Section 2.1, the system specific productivity is the product of the working capacity (moles of gas adsorbed/desorbed per unit mass of adsorbent including binder, support, etc.) and the density of the composite adsorbent. The throughput attainable in a given volume of vessel in a cyclic adsorption system may be expressed as

$$\text{Throughput (TPD)} \propto \frac{\text{gas\_production}}{\text{cycle} \times m_{ads}} \times \frac{\text{cycle}}{\text{day}} \tag{11}$$

$$\text{Specific productivity} = k\frac{WC}{\tau} \tag{12}$$

where m_{ads} is the mass of adsorbent and k is a proportionality constant. The effect of pressure drop on the productivity is to reduce the overall working capacity. Instead of operating between a high pressure P_H and a low pressure P_L, the average bed pressure on adsorption is only $P_H - \Delta P/2$ and the bed pressure on desorption is $P_L + \Delta P/2$. In practice, the bed pressure drop on adsorption and desorption is not equal since the gas velocity is different in these steps. For simplicity in this analysis, we assume they are equal. Thus the pressure difference between adsorption and desorption is approximately diminished from $P_H - P_L$ to $P_H - P_L - \Delta P$. Generally (for any isotherm), the working capacity will be reduced by some function of ΔP written as $f_1(\Delta P)$. The situation for linear isotherms is shown in more detail below. A more exact analysis of the effect of pressure can only be obtained through detailed numerical simulations.

The effect of mass transfer zone (MTZ) on specific productivity is to reduce the effective length of bed which also translates to a reduction in working capacity. Again, this can be represented generally as some function f_2 of the MTZ. The specific productivity can therefore be written as:

$$\text{Specific productivity} = \frac{k[WC - f_1(\Delta P) - f_2(\text{MTZ})]}{\tau} \tag{13}$$

where f_1 and f_2 are functions of ΔP and MTZ, respectively. Since the cycle time is inversely proportional to bed velocity

$$\tau \propto \frac{1}{U}$$

The specific productivity equation can be further rearranged to

$$\begin{aligned}\text{specific productivity} &= k'[WC - f_1(\Delta P) - f_2(\text{MTZ})]U \\ &= k'[WC - f_1(\Delta P(U)) - f_2(\text{MTZ}(U))]U\end{aligned} \tag{14}$$

where k' is another proportionality constant and the dependence of pressure drop and mass transfer zone on velocity is made explicit. In order to find f_1 and f_2, consider a linear isotherm. For no pressure drop in the system, the ideal amount of adsorbate loading per mass of adsorbent is given by

$$WC = \Delta n_{\text{ideal}} = K(P_H - P_L) \tag{15}$$

As mentioned earlier, pressure drop affects the process by reducing the average pressure swing between feed and blowdown in PSA system. The working capacity for the system with pressure drop and a mass transfer zone is therefore (to a first approximation)

$$\begin{aligned}\Delta n_{\text{non-ideal}} &= \left(K\left(\left(P_H - \frac{\Delta P}{2}\right) - \left(P_L + \frac{\Delta P}{2}\right)\right)\right)\left(1 - \frac{MTZ}{L}\right) \\ &= (K(P_H - P_L) - K\Delta P)\left(1 - \frac{MTZ}{L}\right)\end{aligned} \tag{16}$$

$$\Delta n_{\text{non-ideal}} = (\Delta n_{\text{ideal}} - K\Delta P)\left(1 - \frac{MTZ}{L}\right) \tag{17}$$

Therefore, the specific productivity of the adsorbent system can be represented by the following correlation

$$\text{specific productivity} = k'(\Delta n_{\text{ideal}} - K\Delta P)\left(1 - \frac{MTZ}{L}\right)U \tag{18}$$

Eq. (18) indicates that specific productivity is proportional to the superficial velocity and inversely proportional to MTZ and pressure drop. Therefore any factor affecting the MTZ and pressure drop may influence the specific productivity. Specifically, the trade-off in specific productivity as a function of velocity is clear. At high velocities, cycle time is reduced however, the pressure drop and MTZ length increases which decrease overall system performance. At low velocities, pressure drop and MTZ effects are small but the long cycle times lead to low specific productivity. The maximum specific productivity as a function of velocity therefore depends strongly on how much MTZ and pressure drop are negatively affected by high velocities. Our earlier study showed that different adsorbent structures achieve their optimum performance at different velocities with structured adsorbents most suited to regions of high velocity where they display their superiority [14].

3.8. Key areas for future research

A major driver toward the development of future adsorptive gas separation processes lies in the development of improved sorbent materials. However, these improved materials with better adsorption–desorption capacity must ultimately find their way into a real process for commercial applications that should operate within a rapid PSA or TSA regime or other intensive separation processes to maximize product output per unit mass of adsorbent. As shown above, a wide variety of possible structures have been advanced over the last two decades to overcome existing limitations of pressure drop, mass transfer, etc. In many cases however, some feature of the process is compromised so that inferior performance to a packed bed results. There is a need for research to address the following questions and issues:

(a) What is the optimum generalised gas–solid contacting topology to effect a particular separation and to what extent do the existing structures approach this optimal topology? Research should be directed to developing useful mathematical models which encompass the compensating effects of adsorbent loading, mass transfer, pressure drop, and heat transfer as a function of gas/solid contacting geometry and a function of adsorbent type. These general models should be validated against existing structures and then used to guide further experimental efforts.
(b) The role of thermal management in TSA/PSA processes has not received sufficient attention. Modern manufacturing techniques can create adsorbent structures with heat transfer

characteristics superior to conventional beads or pellets and future research should be directed to understanding the relationship between adsorbent structure, heat transfer properties and overall system performance. Such techniques may involve the process of producing binderless material to improve heat and mass transport characteristics, production of composite adsorbents with high electrical and thermal conductivity in order to dissipate adsorption heat easier and efficient, employment of suitable support to tailor the thermal properties of the support with mass transfer properties of active material and production of activated carbon monoliths.

(c) The relationship between separation performance, macroscopic adsorbent structure (the subject of this review) and the macro/meso/micropore hierarchy of the adsorbent has not been explored to date. Thus pore engineering must be integrated with systems engineering to produce an overall optimal structure. This is a fertile area for future research into adsorbent structures particularly with the explosion in development of nanoporous materials.

4. Conclusion

Conventional gas separation processes using packed beds of beads or granules suffer predominantly from high pressure drop and mass transfer resistance when higher throughputs are required, leading to lower productivity and recovery and higher power consumption. This restricts their application to low throughputs and makes them less attractive compared to the cryogenic processes for large volume production and high productivity. These problems could be overcome by employing alternate adsorbent structures. The major trends toward the design of more compact processes with lower capital and operating cost suggest the use of adsorbent configurations which offer a low pressure drop, fast mass transfer kinetics and high working capacity. The new generation of cyclic adsorption systems with cycle time much shorter than conventional ones necessitates not only an improved process cycle but the employment of novel adsorbent configurations which satisfy almost all requirements of gas process systems in terms of performance and process efficiency.

In this short review, the use of different adsorbent structures with improved performance as a competitive alternate to conventional packed beds of pellets/beads was discussed. Although the advances achieved in the utilization of structured adsorbents during the last decade have been significant, there is still a need to develop generalised rules or criteria for optimizing the selection and design of a particular adsorbent structure for a particular application. These criteria must take into account all of the important characteristics of adsorbents which affect the system behaviour. In our recent study [14] we have qualitatively studied the impact of adsorbent structure on overall performance of adsorption based gas separation systems and formulated a new methodology for evaluating different adsorbent configurations. This methodology could help provide a general overview of adsorbent evaluation and selection. Future work should focus on examining optimal gas–solid contact topologies in a more general sense to provide a theoretical limit to which practical devices could be compared. Such a study could employ concepts such as pore network models coupled to macroscopic flow models to study the dynamic behaviour of the interaction of the adsorption process with the macroscopic flow process. This modelling effort is currently underway in our laboratory. In addition, advanced thermal management opportunities which are possible with adsorbent structures should be studied.

Acknowledgment

The authors would like to acknowledge the Monash Research Graduate School (MRGS) for providing scholarship support for Fateme Rezaei.

References

[1] P. Xiao, J. Zhang, P. Webley, G. Li, R. Singh, R. Todd, Adsorption 14 (2008) 575–582.
[2] J. Smolarek, F.W. Leavitt, J.J. Nowobilski, V.E. Bergsten, J.H. Fassbaugh, European Patent, EP0820798 (1998).
[3] S. Ergun, Chem. Eng. Prog. 48 (1952) 89–94.
[4] D.M. Ruthven, C. Thaeron, Gas Sep. Purif. 10 (1996) 63–73.
[5] Y.Y. Li, S.P. Perera, B.D. Crittenden, Chem. Eng. Res. Des. 76 (1998) 921–930.
[6] T.C. Golden, C.M.A. Golden, D.P. Zwilling, US Patent US6,565,627 (2003).
[7] A. Patton, B.D. Crittenden, S.P. Perera, Chem. Eng. Res. Des. 82 (2004) 999–1009.
[8] F.C. Patcas, G.I. Garrido, B. Kraushaar-Czarnetzki, Chem. Eng. Sci. 62 (2007) 3984–3990.
[9] D.M. Ruthven, Principles of Adsorption and Adsorption Processes, John Wiley & Sons, Inc., 1984, p. 243.
[10] R.T. Yang, Gas Separation by Adsorption Processes, John Wiley and Sons, Inc., 1987.
[11] N. Wakao, T. Funazkri, Chem. Eng. Sci. 33 (1978) 1375–1384.
[12] R.D. Hawthorn, AIChE Symp. 70 (1974) 428–438.
[13] G. Groppi, L. Giani, E. Tronconi, Ind. Eng. Chem. Res. 46 (2007) 3955–3958.
[14] F. Rezaei, P. Webley, Chem. Eng. Sci. (2009), doi:10.1016/j.ces.2009.08.029.
[15] G.I. Taylor, Proc. Phys. Soc. Sect. B 67 (1954) 857–869.
[16] J. Collins, US Patent, US4,026,680 (1977).
[17] V. Gueret, C. Monereau, P. Pullumbi, PCT Int. Appl., W.I.P.O. Patent WO2008037904 (2008).
[18] D.M. Ruthven, Ind. Eng. Chem. Res. 39 (2000) 2127–2131.
[19] S. Irandoust, B. Andersson, Catal. Rev. Sci. Eng. 30 (1988) 341–392.
[20] I.L. Maclaine-Cross, P.J. Banks, Int. J. Heat Mass Transf. 15 (1972) 1225–1242.
[21] A. Kodama, M. Goto, T. Hirose, T.J. Kuma, Chem. Eng. Jpn. 26 (1993) 530–535.
[22] R.E. Kenson, Environ. Prog. 4 (1985) 161–164.
[23] K.P. Gadkaree, Carbon 36 (1998) 981–989.
[24] Y.Y. Li, S.P. Perera, B.D. Crittenden, Chem. Eng. Res. Des. 76 (1998) 931–941.
[25] L. Li, B. Xue, J. Chen, N. Guan, F. Zhang, D. Liu, H. Feng, Appl. Catal. A: Gen. 292 (2005) 312–321.
[26] A. Mosca, J. Hedlund, F.N. Ridha, P. Webley, Adsorption 14 (2008) 687–693.
[27] M. Park, et al., US Patent US 6,171,373 (2001).
[28] G. Li, R. Singh, D. Li, C. Zhao, L. Liu, P. Webley, J. Mater. Chem. (2009), doi:10.1039/b912329f.
[29] J.J. Meyers, A.I. Liapis, J. Chromatogr. A 827 (1998) 197–213.
[30] J.J. Meyers, A.I. Liapis, J. Chromatogr. A 852 (1999) 3–23.
[31] A.I. Liapis, J.J. Meyers, O.K. Crosser, J. Chromatogr. A 865 (1999) 13–25.
[32] F. Brandani, A. Rouse, S. Brandani, D.M. Ruthven, Adsorption 10 (2004) 99–109.
[33] B. Crittenden, A. Patton, C. Jouin, S. Perera, S. Tennison, J.A.B. Echevarria, Adsorption 11 (2005) 537–541.
[34] M. Yates, J. Blanco, P. Avila, M.P. Martin, Micropor. Mesopor. Mater. 37 (2000) 201–208.
[35] F.D. Yu, L.A. Luo, G. Grevillot, J. Chem. Eng. Data 47 (2002) 467–473.
[36] H.S. Kim, J.W. Kim, J.E. Yie, H. Moon, Proceedings of the Third Pacific Basin Conference on Adsorption Science and Technology, vol. 1, 2003, pp. 286–290.
[37] T. Valdes-Solis, M.J.G. Linders, F. Kapteijn, G. Marban, A.B. Fuertes, Chem. Eng. Sci. 59 (2004) 2791–2800.
[38] A. Lapkin, L. Joyce, B.D. Crittenden, Environ. Sci. Technol. 38 (2004) 5815–5823.
[39] D.B. Shah, S.P. Perera, B.D. Crittenden, in: Fundamentals of Adsorption, Boston, 1996, pp. 813–820.
[40] L.Y. Lee, S.P. Perera, B.D. Crittenden, S.T. Kolaczkowski, Adsorpt. Sci. Technol. 18 (2000) 147–170.
[41] C.A. Grande, S. Cavenati, P. Barcia, J. Hammer, H.G. Fritz, A.E. Rodrigues, Chem. Eng. Sci. 61 (2006) 3053–3063.
[42] M. Zabka, M. Minceva, A.E. Rodrigues, Chem. Eng. Process: Process Intens. 45 (2006) 150–160.
[43] M. Zabka, P.S. Gomes, A.E. Rodrigues, Sep. Purif. Technol. 63 (2008) 324–333.
[44] W.A. Cutler, L. He, C.M. Sorensen, L.K. Owens, W.I.P.O. Patent WO2004058372 (2005).
[45] R.P. Ribeiro, T.P. Sauer, F.V. Lopes, R.F. Moreira, C.A. Grande, A.E. Rodrigues, J. Chem. Eng. Data 53 (2008) 2311–2317.
[46] R. Jain, A.I. LaCava, A. Maheshwary, J.R. Ambriano, D.R. Acharya, F.R. Fitch, US Patent US6,521,019 (2003).
[47] L. He, L.K. Owens, W.A. Cutler, C.M. Sorensen, Ceram. Eng. Sci. Proc. 25 (2004) 529–534.
[48] W.S. Kaboord, J.A. Kovacich, D.M. Becher, F.J. Begale, US Patent US2005249645 (2005).
[49] S.R. Jale, F.R. Fitch, S. Dongmin, US Patent US6,436,173 (2002).
[50] W.A. Belding, M.F.P. Delmas, W.D. Holeman, D.A. McDonald, US Patent, US5,685,897 (1997).

[51] W.A. Belding, M.F.P. Delmas, W.D. Holeman, D.A. McDonald, US Patent US 5,650,221 (1997).
[52] W.A. Belding, W.D. Holeman, Z. Lavan, R.L. Jones, US Patent US5,580,369 (1996).
[53] W.A. Belding, C.H. Lam, W.D. Holeman, S.L. Janke, US Patent US5,890,372 (1999).
[54] R.A. Macriss, W.F. Rush, S.A. Weil, US Patent US4,012,206 (1977).
[55] A.B. Gorbach, M. Stegmaier, G. Eigenberger, J. Hammer, H.G. Fritz, Adsorption 11 (2005) 515–520.
[56] A. Kodama, Memoirs of the Faculty of Engineering, vol. 40, Kumamoto University, 1996, pp. 313–351.
[57] A. Kodama, K. Andou, M. Ohkura, M. Goto, T. Hirose, J. Chem. Eng. Jpn. 36 (2003) 819–826.
[58] A. Kodama, M. Goto, T. Hirose, T. Kuma, J. Chem. Eng. Jpn. 28 (1995) 19–24.
[59] A. Kodama, M. Goto, T. Hirose, T. Kuma, J. Chem. Eng. Jpn. 27 (1994) 644–649.
[60] A. Kodama, N. Watanabe, T. Hirose, M. Goto, H. Okano, Adsorption 11 (2005) 603–608.
[61] H. Yamauchi, A. Kodama, T. Hirose, H. Okano, K.I. Yamada, Ind. Eng. Chem. Res. 46 (2007) 4316–4322.
[62] Y. Matsukuma, Y. Matsushita, H. Kakigami, G. Inoue, M. Minemoto, A. Yasutake, N. Oka, Kagaku Kogaku Ronbunshu 32 (2006) 138–145.
[63] Y. Matsukuma, K. Sadagata, H. Kakigami, G. Inoue, M. Minemoto, A. Yasutake, N. Oka, Kagaku Kogaku Ronbunshu 32 (2006) 146–152.
[64] B.G. Keefer, C.R. Mclean, US Patent US6,056,804 (2000).
[65] D.J. Connor, D.G. Doman, L. Jeziorowski, B.G. Keefer, B. Larisch, C. McLean, I. Shaw, US Patent US 6,406,523 (2002).
[66] B.G. Keefer, A. Carel, B. Sellars, I. Shaw, B. Larisch, US Patent, US6,692,626 (2004).
[67] B.G. Keefer, US Patent US5,082,473 (1992).
[68] R.T. Maurer, US Patent US5,338,450 (1994).
[69] S. Farooq, C. Thaeron, D.M. Ruthven, Sep. Purif. Technol. 13 (1998) 181–193.
[70] B.G. Keefer, US Patent US6,176,897 (2001).
[71] J.A. Sawad, S. Alizadeh-Khiavi, S. Roy, S.M. Kuznicki, W.I.P.O. Patent WO2005032694 (2005).
[72] E.J. Rode, A.J.J. Boulet, A.M. Pelman, M.L. Babicki, B. Keefer, J.A. Sawada, S. Alizadeh-Khiavi, S. Roy, A.C. Gibbs, S.M. Kuznicki, W.I.P.O. Patent WO200660743432 (2007).
[73] J.T. Richardson, D. Remue, J.K. Hung, Appl. Catal. A: Gen. 250 (2003) 319–329.
[74] K.B. Yoon, Y.J. Lee, Y.S. Park, J.S. Lee, US Patent US2,002,183,407 (2002).
[75] T.C. Golden, C.M.A., Golden, P.J. Battavio, US Patent US6,893,483 (2005).
[76] A. Bailey, F.A.P. Maggs, US Patent US4,234,326 (1980).
[77] M. Petkovska, D. Tondeur, G. Grevillot, J. Granger, M. Mitrovic, Sep. Sci. Technol. 26 (1991) 425–444.
[78] P.D. Sullivan, M.J. Rood, K.J. Hay, S. Qi, J. Environ. Eng. 127 (2001) 217–223.
[79] M. Baudu, P. Le Cloirec, G. Martin, De Charbons Actifs Utilises Pour Le Traitement D'air 13 (1992) 423–435.
[80] J.E. Antia, R. Govind, Appl. Catal. A 131 (1995) 107–120.
[81] J. Hedlund, B.J. Schoeman, J. Sterte, Stud. Surf. Sci. Catal. 105 (1997) 2203–2210.
[82] R. Aiello, F. Crea, F. Testa, A.S. Gattuso, in: I. Kiricsi, J.B. Nagy, H.G. Karge (Eds.), Porous Materials in Environmental Friendly Processes, Elsevier, Amsterdam, 1999, p. 29.
[83] Z. Shan, W.E.J. Van Kooten, O.L. Oudshoorn, J.C. Jansen, H. Van Bekkum, C.M. Van Den Bleek, H.P.A. Calis, Micropor. Mesopor. Mater. 34 (2000) 81–91.
[84] C.D. Madhusoodana, R.N. Das, Y. Kameshima, A. Yasumori, K. Okada, Micropor. Mesopor. Mater. 46 (2001) 249–255.
[85] J. Sterte, J. Hedlund, B.J. Schoeman, Catal. Today 69 (2001) 323–329.
[86] E.I. Basaldella, A. Kikot, J.F. Bengoa, J.C. Tara, Mater. Lett. 52 (2002) 350–354.
[87] M.A. Ulla, R. Mallada, J. Coronas, L. Gutierrez, E. Miro, J. Santamaria, Appl. Catal. A: Gen. 253 (2003) 257–269.
[88] A.E.W. Beers, T.A. Nijhuis, N. Aalders, F. Kapteijn, J.A. Moulijn, Appl. Catal. A: Gen. 243 (2003) 237–250.
[89] J. Coronas, J. Santamaria, Chem. Eng. Sci. 59 (2004) 4879–4885.
[90] J. Hedlund, O. Ohrman, V. Msimang, E. van Steen, W. Bohringer, S. Sibya, K. Moller, Chem. Eng. Sci. 59 (2004) 2647–2657.
[91] K. Nikolajsen, L. Kiwi-Minsker, A. Renken, Chem. Eng. Res. Des. 84 (2006) 562–568.
[92] O. Ohrman, J. Hedlund, J. Sterte, Appl. Catal. A: Gen. 270 (2004) 193–199.
[93] I. Perdana, D. Creaser, I. Made Bendiyasa, Rochmadi, B. Wikan Tyoso Chem. Eng. Sci. 62 (2007)3882-3893.
[94] S. Matsuoka, T. Kodama, J. Izumi, H. Tsutaya, K. Kurosu, H. Someya, J. Nucl. Sci. Technol. 41 (2004) 466–472.
[95] P.A. Barrett, N.A. Stephenson, S.J. Pontonio, W.I.P.O. Patent WO2008051904 (2008).
[96] W.B. Leedy, J.F. Eichelsbacher, T.H. Shelton, US Patent US200810236389 (2008).
[97] L. Bonaccorsi, A. Freni, E. Proverbio, G. Restuccia, F. Russo, Micropor. Mesopor. Mater. 91 (2006) 7–14.
[98] R.E. Critoph, T.Z. Telto, L.N.G. Davies, Proc. Inst. Mech. Eng. 214 (2000).
[99] B.M. Fabuss, W.H. Dubois, 63rd Annual Meeting of the Air Pollution Control Association 18 (1970).
[100] W. Hauck, G. Grevillot, A.S. Lamine, Chemie-Ingenieur-Technik 69 (1997) 1138–1142.
[101] M. Petkovska, M. Mitrovic, Chem. Eng. J. Biochem. Eng. J. 53 (1994) 157–165.
[102] M. Petkovska, M. Mitrovic, Chem. Eng. Res. Des. 72 (1994) 713–722.
[103] M. Rood, P. Sulliva, K.J. Hay, US Patent, US6,364,936 (2002).
[104] E. Crezee, B.D. Tennison, B.D. Crittenden, Proceedings of 7th World Congress on Chemical Engineering, Glasgow, 2005.
[105] F.D. Yu, L.A. Luo, G. Grevillot, J. Environ. Eng. 130 (2004) 242–248.
[106] F.D. Yu, L. Luo, G. Grevillot, Chem. Eng. Process: Process Intens. 46 (2007) 70–81.
[107] C.A. Grande, A.E. Rodrigues, Int. J. Greenhouse Gas Control 2 (2008) 194–202.
[108] R.N. Place, A.J. Blackburn, S.R. Tennison, A.P. Rawlinson, B.D. Crittenden, US Patent US6,964,695 (2005).

PAPER B

Optimum structured adsorbents for gas separation processes

Authors:
F.Rezaei, P. Webley

Chemical Engineering Science 64 (2009) 5182 - 5191

Chemical Engineering Science 64 (2009) 5182 – 5191

Contents lists available at ScienceDirect

Chemical Engineering Science

journal homepage: www.elsevier.com/locate/ces

Optimum structured adsorbents for gas separation processes

Fateme Rezaei, Paul Webley*

Department of Chemical Engineering, Monash University, VIC 3800, Australia

ARTICLE INFO

Article history:
Received 2 June 2009
Received in revised form 19 August 2009
Accepted 22 August 2009
Available online 1 September 2009

Keywords:
Structured adsorbent
Mass transfer zone
Pressure drop
Adsorbent loading

ABSTRACT

Recent developments in separation technology by adsorption have included the development of new structured adsorbents which offer some attractive characteristics compared to a typical packed bed. These improved features include lower energy consumption, higher throughput and superior recovery and purity of product. However, the exact combination of structural, geometric parameters which yields optimum performance is unknown. This study formulates a methodology for comparison based on a variety of analytical and numerical models and uses it to examine the performance of different adsorbent configurations. In particular, monolithic, laminate and foam structures are evaluated and compared to a packed bed of pellets. The effects of physical adsorbent parameters which govern the performance of a PSA process are considered during model development. Comparisons are carried out based on mass transfer kinetics, adsorbent loading and pressure drop of a PSA system for CO_2/N_2 separation. The results indicated that structured adsorbents can provide superior throughput to packed beds provided their geometrical parameters exceed certain values. For example, laminate structures can offer superior performance to a packed bed of pellets only if the critical sheet thickness and spacing are less than about 0.2 mm. Each adsorbent structure should be designed to operate at its "optimal" velocity. When operating at velocities higher than the "optimal" value, the increase in pressure drop and length of the mass transfer zone more than offsets gains accrued through reduction in cycle time.

1. Introduction

Efficient gas separation processes operating at high throughput are compromised when adsorbent materials in the form of beads or granules are used. High pressure drop associated with gas flow through a packed bed of beads/pellets and mass transfer limitations related to gas diffusion into or out of the beads rapidly reduce system performance. To address these drawbacks, different adsorbent structures may be considered.

Recently, various structured adsorbents with enhanced adsorption characteristics such as monolithic, laminate and foam structures have gained considerable attention as substitutes for traditional adsorbent particles (Kodama et al., 1993; Maurer, 1994; Gadkaree, 1997; Li et al., 1998; Golden et al., 2003; Brandani et al., 2004; Keefer et al., 2004; Sawad et al., 2005; Golden et al., 2005; Zabka et al., 2006; Grande et al., 2006; Rode et al., 2007).

Parallel channel monolithic structures with controllable shape, cell density and wall thickness have been reported for their use in adsorptive gas separation systems (Kodama et al., 1993; Gadkaree, 1997; Li et al., 1998; Lee et al., 2000; Yu et al., 2002; Yates et al., 2003). The main advantage of such configurations resides in their low pressure drop and higher mass transfer rates. Although it has been reported that the mass transfer characteristics of monolithic adsorbents is somewhat inferior to a comparable packed bed, this is more a consequence of early monolithic structures with thick walls rather than any intrinsic limitation. It would be possible to improve the mass transfer behaviour of monoliths by utilizing structures with reduced channel width and wall thickness or more appropriate shape. Patton et al. (2004) suggests the employment of hexagonal channels rather than ordinary square or circular channels. These authors applied the linear driving force model (LDF) to optimize practical monolith channels taking mass transfer and pressure drop characteristics into account. In recent study performed by Zabka et al. (2008), the performances of the separation of chiral species by the simulated moving bed (SMB) unit packed with conventional adsorbent beads and monolithic adsorbents were compared. The authors concluded that the selection of particle diameter or different bed morphologies is a trade-off between the productivity and eluent consumption.

The use of parallel laminate structures for adsorption processes is rather new with a few patents describing the use of adsorbent materials in the form of laminate sheets in adsorptive gas separation applications. Rode et al., 2007 demonstrated the application of improved adsorbent sheet based parallel passage structures for PSA, TSA and partial PSA devices. In order for laminates to be effective

* Corresponding author. Tel.: +61 3 9905 3445; fax: +61 3 9905 5686.
E-mail address: paul.webley@eng.monash.edu.au (P. Webley).

0009-2509/$ - see front matter © 2009 Elsevier Ltd. All rights reserved.
doi:10.1016/j.ces.2009.08.029

adsorbents, the thickness of the sheets and the space between adjacent sheets must be as small as possible but not so small so as to result in excessive pressure drop. Ruthven and Thaeron (1996) carried out an experimental and theoretical study on the performance of a parallel passage contactor based on HETP (height equivalent to a theoretical plate) and pressure drop. Their results emphasize the advantage of such an adsorber over the conventional beads for applications in which pressure drop is a key factor.

Ceramic foams have many attractive features as catalyst supports; however, their utilization in adsorptive gas separation applications is scarce. Open cell foams comprising a network of solid struts and pores offer substantial benefits over configurations comprising external supports; namely, a low pressure drop operation with tortuous flow path and high geometric surface area which enhance the rate of external mass transfer (Richardson et al., 2003; Patcas et al., 2007).

Recently, Patcas et al. (2007), performed an experimental comparison of catalysts with different carriers, namely, honeycomb monoliths, ceramic foams and spherical particles based on their pressure drop and mass and heat transfer characteristics in the oxidation of carbon monoxide. Their results showed that the performance of foam catalysts with respect to combined high mass transfer and low pressure drop were superior over particles and inferior to that of honeycomb structures.

In our recent review of the use of structured adsorbents (Rezaei and Webley, 2009), we identified the important structural parameters that impact the overall performance of gas separation processes. These are: (1) amount of adsorbent contained in a given volume (adsorbent loading), (2) pressure drop through the structure per unit length, (3) external surface area per unit volume, (4) total void volume and (5) channelling and dispersion parameter characteristics. Some of these parameters are constants of the zeolite structure (1), (3), (4) while others also depend on gas velocity (2), (5).

As is well established, for cyclic processes such as PSA or TSA, reducing cycle time is the most important factor to improving the process in terms of reducing adsorbent inventory and cost since shorter cycles result in smaller beds. However, product recovery often decreases as cycle time is decreased unless adsorption rate is correspondingly increased (Ackley et al., 2003). In order to capture this feature, the well known mass transfer zone (MTZ) concept (also referred to as length of unused bed or LUB) was used here to assess the performance of a range of adsorbent structures.

It is clear that the parameters of a particular adsorbent structure will influence the separation performance and cost. It is also evident that a trade-off will exist between mass transfer, pressure drop and adsorbent loading as the geometry of the adsorbent structures are altered. It follows that for each structure there is an optimum set of geometric parameters which will provide the "best" performance as defined by a particular objective function. It is the goal of this study to develop the analytical framework required to determine this optimum set of geometric parameters and to use this model to examine laminate, monolith and foam structures.

2. Model description

2.1. Mass transfer models

A number of simplified mathematical models were developed for different geometries to describe the adsorption of a single component in an inert carrier. A differential mass balance for the adsorbate in the gas phase flowing through a structure (independent of geometry) gives

$$\varepsilon_b \frac{\partial C}{\partial t} - D_L \frac{\partial^2 C}{\partial z^2} + \frac{\partial UC}{\partial z} = -\bar{k}a(C - \overline{C}^p) \tag{1}$$

Table 1
Adsorption parameters related to each structured adsorbent.

Adsorbent	$\bar{k}$	a	α	ε_b
Pellet/bead	$\frac{1}{\frac{1}{k_f}+\frac{R_p}{5D_e}}$	$\frac{3(1-\varepsilon_b)}{R_p}$	$\frac{3}{R_p}$	0.35–0.4
Monolith	$\frac{1}{\frac{1}{k_f}+\frac{R_2^2-R_1^2}{4R_1D_e}}$	$\frac{2\varepsilon_b}{R_1}$	$\frac{2R}{R_2^2-R_1^2}$	$\left(\frac{2R_1}{R_1+R_2}\right)^2$
Laminate	$\frac{1}{\frac{1}{k_f}+\frac{W}{6D_e}}$	$\frac{2\varepsilon_b}{d}$	$\frac{2}{W}$	$\left(\frac{d}{d+2W}\right)$
Foam	$\frac{1}{\frac{1}{k_f}+\frac{R_p}{4D_e}}$	$\frac{2\varepsilon_b}{R_p}$	$\frac{2}{R_p}$	0.75–0.85

where C and $\overline{C}^p$ are the concentration of the adsorbate in the gas phase and the average concentration in the pores of the adsorbent, respectively, a is specific surface area per unit bed volume; U is the superficial fluid velocity; $\bar{k}$ is the overall (or total) mass transfer coefficient; D_L is the axial dispersion coefficient and ε_b is the bed void fraction. As written, Eq. (1) includes axial dispersion explicitly. A differential mass balance for the adsorbate inside the solid phase is given by

$$\varepsilon_p \frac{\partial \overline{C}^p}{\partial t} + \rho_s \frac{\partial \overline{q}}{\partial t} = +\bar{k}\alpha(C - \overline{C}^p) \tag{2}$$

where ε_p is the solid void fraction; α is the geometric factor which is different for each adsorbent structure; ρ_s is the adsorbent density (includes binder, support, etc.) and $\overline{q}$ is the average adsorbent loading. The initial and boundary conditions appropriate to a breakthrough simulation for the above equations are

$$C(t=0) = 0, \quad \overline{q}(t=0) = 0, \quad \overline{C}^p(t=0) = 0 \tag{3}$$

$$C_0 + \left.\frac{\partial C}{\partial z}\right|_{z=0} = 0 \tag{4}$$

$$\left.\frac{\partial C}{\partial z}\right|_{z=L} = 0 \tag{5}$$

The boundary condition at the inlet of the column is given by Danckwert's boundary condition (Eq. (4)). This entry condition matches the combined advective and dispersive concentration flux. However, after running models, it was found that the term $\left.\frac{\partial C}{\partial z}\right|_{z=0}$ is negligible and the inlet boundary condition can be simplified to

$$C(z=0) = C_0$$

A detailed description of the model development for monoliths is included in Appendix A. Eqs. (1) and (2) are based on the assumption that the concentration profile in the solid phase is parabolic. The constants in Eqs. (1) and (2) related to each structure have been summarized in Table 1. In this model, local equilibrium is assumed to exist between the adsorbed and the gas species within the pores (i.e. there is only pore resistance in the system). It is worth mentioning here that the monolith is represented by a series of parallel cylinders, however, for the sake of simplicity we assume the same behaviour for all the cylinders (no maldistribution), and that the monolith can be described by a single channel (Young and Finlayson, 1974). Foams are characterized in terms of a pore diameter, d_p, or pore radius, R_p, which corresponds to the average size of interconnecting windows and correlates well with the pore density (pores per inch or PPI). In Fig. 1 the geometrical parameters of monoliths and laminates are shown. R_1 and R_2 are the inner and outer wall radii of the monolith channel, respectively, and d and w are the laminate gap and wall thickness, respectively.

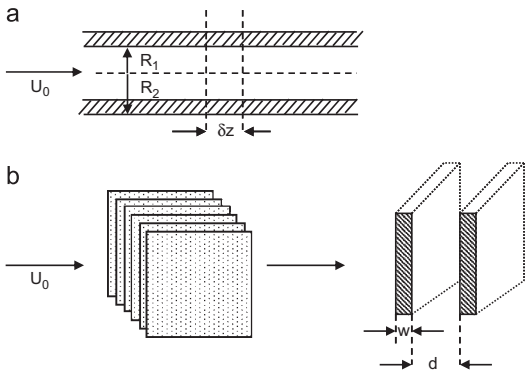

Fig. 1. Structured adsorbents: (a) monolith and (b) laminate.

The total mass transfer coefficient can be represented as follows:

$$\frac{1}{k}=\frac{1}{k_f}+\frac{1}{k_p} \tag{6}$$

where k_f and k_p are film and pore mass transfer coefficients, respectively. The pore mass transfer coefficient, k_p, for pellets, monoliths, foam and laminate structures are

$$(k_p)_{pellets}=\frac{5D_e}{R} \tag{7}$$

$$(k_p)_{monoliths}=\frac{4D_eR_1}{R_2^2-R_1^2} \tag{8}$$

$$(k_p)_{foams}=\frac{4D_e}{R} \tag{9}$$

$$(k_p)_{laminates}=\frac{6D_e}{w} \tag{10}$$

where D_e is the effective diffusivity which is taken to be identical for different structures, since we assume here that the intrinsic pore structure of the adsorbent is the same. This latter constraint is not required but was adopted here for simplicity in the comparison of structures. Indeed, some advantages of novel adsorbent structures may well be that superior D_e can be achieved by engineering the pore structure into the adsorbent structure. The solid adsorbent is assumed to have the same properties in all adsorbent structures.

The appropriate dimensionless group characterising film diffusion is the Sherwood number, *Sh*. For pelleted systems the Wakao and Funazkri (1978) equation was used to estimate k_f

$$Sh=2+1.1\,Re^{0.6}Sc^{0.33} \tag{11}$$

For monolithic and laminate structures, Hawthorn (1974) equation for laminar flow was employed

$$Sh=\frac{dk_f}{D_m}=A\left(1+0.139\,Re\,Sc\frac{d}{L}\right)^{0.81} \tag{12}$$

where the parameter A is 3.6 for circular channels, 2.35 for triangular channels and 2.95 for square channels. D_m and L are molecular diffusion coefficients and column length, respectively.

A generalized correlation proposed by Groppi et al. (2007) was employed to describe the external film mass transfer coefficient in foam structures

$$Sh=0.91\,Re^{0.43}Sc^{0.33} \tag{13}$$

Table 2
Film and pore mass transfer expressions for structured adsorbents.

Adsorbent	k_f expression	k_p expression
Pellet/bead	$Sh=2+1.1\,Re^{0.6}\ Sc^{0.33}$	$k_p=\frac{5D_e}{R}$
Monolith	$Sh=2.696\left[1+0.139\left(\frac{2R_1}{L}\right)Re\,Sc\right]^{0.81}$	$k_p=\frac{4D_eR_1}{R_2^2-R_1^2}$
Laminate	$Sh=2.696\left[1+0.139\left(\frac{d}{L}\right)Re\,Sc\right]^{0.81}$	$k_p=\frac{6D_e}{w}$
Foam	$Sh=0.91\,Re^{0.43}\ Sc^{0.33}$	$k_p=\frac{4D_e}{R}$

subject to the constraint

$$15<Re<200$$

A summary of k_f and k_p expressions related to each configuration is presented in Table 2.

Since axial dispersion acts to disperse the breakthrough front in an adsorbent system, it is important to include its effect. Axial dispersion in a packed bed is correlated in terms of the Peclet number ($Pe=Ud/D_L$), and can be obtained from

$$\frac{\varepsilon_bD_L}{D_m}=20+0.5\,Re\,Sc \tag{14}$$

where D_m is the molecular diffusion coefficient. The same expression was used for foam structures. In laminar flow, axial dispersion in monolithic structures can be calculated from Taylor (1954) analysis

$$D_L=D_m+\frac{1}{192}\frac{U^2(2R_1)^2}{D_m} \tag{15}$$

For laminates, a similar approach holds as with monoliths.

The inclusion of axial dispersion can be done either through the term $D_L\partial^2C/\partial z^2$ or, since its effect is to disperse the mass transfer front, it can be represented through the mass transfer coefficient, *k*. In our numerical study presented later, it was included explicitly through the term $D_L\partial^2C/\partial z^2$. However, for linear adsorption isotherm models, the contribution of dispersion can alternatively be estimated by adding the term D_L/U^2 to the mass transfer coefficient of the adsorbent (Ruthven, 1984), thus the overall rate constant is

$$\left(\frac{1}{k}\right)_{overall}=\left(\frac{1}{k}\right)_{mass\_transfer}+\frac{D_L}{U^2} \tag{16}$$

Estimation of mass transfer rate constant, $k_{mass\_transfer}$ is performed by assuming a parabolic concentration profile in the adsorbent material (as discussed earlier and derived in the appendix) and a linear driving force based on a gas concentration driving force model. The mass transfer coefficient $k_{mass\_transfer}$ for different structures is

$$\text{Pellets}: \quad \left(\frac{1}{k}\right)_{mass\_transfer}=\frac{\varepsilon_b}{1-\varepsilon_b}\left(\frac{R_p}{3k_f}+\frac{R_p^2}{15D_e}\right) \tag{17}$$

$$\text{Monolith}: \quad \left(\frac{1}{k}\right)_{mass\_transfer}=\frac{R_1}{2k_f}+\frac{R_2^2-R_1^2}{8D_e} \tag{18}$$

$$\text{Laminate}: \quad \left(\frac{1}{k}\right)_{mass\_transfer}=\frac{d}{2k_f}+\frac{Wd}{6D_e} \tag{19}$$

$$\text{Foam}: \quad \left(\frac{1}{k}\right)_{mass\_transfer}=\frac{R_p}{2k_f}+\frac{R_p^2}{8D_e} \tag{20}$$

2.2. Pressure drop

The pressure drop of the adsorbent structures was calculated using well known equations for each case. For pellets, the Ergun (1952) equation was used

$$\frac{\Delta P}{L} = 150\frac{(1-\varepsilon)^2}{\varepsilon^3}\frac{\mu}{d_p^2}U + 1.75\frac{(1-\varepsilon)}{\varepsilon^3}\frac{\rho}{d_p}U^2 \tag{21}$$

where, ρ and μ are density and viscosity of the flowing gas. For monolithic and laminate structures, the Hagen–Poiseuille equation (Cybulski and Moulijn, 1998) was applied

$$\frac{\Delta P}{L} = \frac{32\mu}{d_p^2\varepsilon_b}U \tag{22}$$

Although the Ergun equation has often been used to describe the pressure drop of open-cell foams, in this work the pressure drop in the foam adsorbents was calculated from equations recently proposed by Richardson et al. (2000) in which the authors, based on the work of Gibson and Ashby (1997) considered that the cellular medium is formed by uniform tri-dimensional cells.

$$\frac{\Delta P}{L} = \frac{\alpha_1 s^2(1-\varepsilon)^2}{\varepsilon^3}\mu U + \frac{\alpha_2 s(1-\varepsilon)}{\varepsilon^3}\rho U^2 \tag{23}$$

where α_1 and α_2 and s can be calculated using following expressions:

$$\alpha_1 = 973 d_p^{0.743}(1-\varepsilon)^{-0.0982} \tag{24}$$

$$\alpha_2 = 368 d_p^{-0.7523}(1-\varepsilon)^{0.07158} \tag{25}$$

$$s = \frac{12.979[1-0.971(1-\varepsilon)^{0.5}]}{d_p(1-\varepsilon)^{0.5}} \tag{26}$$

2.3. Characterisation and calculation of the mass transfer zone (MTZ)

Adsorbent systems with non-linear and favourable isotherms exhibit constant pattern behaviour during adsorption (Sircar et al., 1983). By employing such constant pattern conditions, it is possible to evaluate the mass transfer zone characteristics of the system. In this work, the MTZ is created by dispersion resulting from all of the dispersive forces in the system as encapsulated by the overall (total) rate constant k. The width of the mass transfer zone is the product of the zone velocity and the extent of spreading

$$MTZ = \beta(t_2 - t_1) \tag{27}$$

where t_2 and t_1 are the two times of breakthrough (5% and 95% of the outlet concentration). The zone velocity, β, can be obtained from a simple rearrangement of the governing equations. If we add the balance equations for the solid and gas phases, we obtain the single equation

$$\varepsilon_b\frac{\partial C}{\partial t} + \frac{\partial UC_i}{\partial z} + \left(\frac{a}{\alpha}\right)\rho_s\frac{\partial \bar{q}}{\partial t} = 0 \tag{28}$$

This balance equation is obtained based on these assumptions that the accumulation in the particle pores is neglected and axial dispersion term is also neglected. Assuming constant velocity, the velocity of the mass transfer zone, β is therefore approximately by

$$\beta = \frac{U}{\varepsilon_b + \left(\frac{a}{\alpha}\right)\rho_s\frac{q_{feed}}{c_{feed}}} \tag{29}$$

The isotherm slope therefore appears in the expression for the MTZ, as expected. The difference in breakthrough time t_1 and t_2 can be derived from constant pattern analyses as shown by Sircar et al. (1983) and it follows that t_2-t_1 is inversely proportional to the overall rate constant, $\bar{k}$, for constant pattern conditions. Thus $(t_2 - t_1) \propto 1/(\alpha\bar{k})$. Combining these equations gives proportionality for the mass transfer zone

$$MTZ \propto \frac{U}{\alpha\varepsilon_b\bar{k} + a\bar{k}\rho_s(q_{feed}/c_{feed})} \tag{30}$$

This equation is simple enough to be implemented in a spreadsheet and shows the major dependency of the *MTZ* on superficial velocity, U, and rate constant as well as geometric factors a and α. It should be noted that linear systems do not show constant pattern behaviour in the presence of dispersive phenomena such as mass transfer resistance and axial dispersion although qualitatively Eq. (30) will indicate the expected trends. Although (30) is useful to provide a relative assessment of the impact of variables on *MTZ* (and is used later to derive a heuristic model), it is possible and desirable to read off the length of the mass transfer directly from the numerical simulations in the z-domain. This was done as described below.

2.4. Numerical solution of the conservation equations and basis for simulation

Simulations of the numerical models for different adsorbent geometries were performed using COMSOL 3.5a. The conservation equations were solved using the Lagrange quadratic finite element method, with a total number of 2424 elements. To confirm that numerical dispersion was not affecting the results, the simulations were routinely tested with more elements (double) with no change in results. The simulations of breakthrough curves in each case do not take more than 20 s. The physical characteristics of structures considered for comparison are presented in Table 3. A cylindrical bed size of 2 cm diameter and 30 cm length was chosen arbitrarily. The adsorbent voidage in each case was taken to be the same (0.6) and the amount of binder was taken to be the same (10% by weight). The density of the foam, monolith wall and laminate sheet was taken to be the same as a pellet density. This may not be true of an actual laminate or monolith especially if a support structure is needed. For the sake of comparison, there should be the same amount of adsorbent mass per unit volume of bed for all configurations, while as can be seen from Table 3, the adsorbent mass is different for all geometries. Therefore, in order to compensate the lower amount of active adsorbent in laminates, foams and monolithic configurations, and ensure the same stoichiometric breakthrough time (to allow comparison of breakthrough fronts), the superficial velocity was adjusted for each adsorbent structure.

The gas system used for calculations was 10% CO_2 in N_2 and the adsorbent was taken to be NaX. The equilibrium data for CO_2 on NaX at 298.15 K were taken from Hyun and Danner (1982). Although the actual isotherm is non-linear, the simulation we performed was based on a linear isotherm with the equilibrium constant, K, taken from the CO_2 adsorption isotherm at lower pressures (up to 10 kPa). A linear constant of 41 g mol/kg kPa was used. It was also assumed that the functionality of the effective diffusion coefficient, D_e, can be evaluated from the equivalent molecular diffusion coefficient scaled by a voidage–tortuosity term in the molecular diffusion regime in which macropore diffusion is rate-limiting step.

3. Results and discussion

3.1. External surface area comparison

One of the most important parameters which govern the performance of an adsorbent is its external surface area per unit volume, since the mass transfer rate is directly proportional to this parameter. In Fig. 2, the comparison between the external surface areas

Table 3
Physical properties of structures used in the computations.

Structure	Bed voidage	Adsorbent mass (g)	Bed density (g/cm^3)	Specific surface area (cm^2/cm^3)	Adsorbent width (mm)	Cell size (mm)	Total voidage	Superficial velocity (m/s)
0.7 mm pellet	0.37	64.69	0.686	54.0	0.35	–	0.75	1
Monolith, 200 cpsi	0.65	35.93	0.381	18.0	0.35	1.45	0.86	0.444
Monolith, 400 cpsi	0.65	35.93	0.381	25.4	0.25	1.02	0.86	0.444
Monolith, 600 cpsi	0.65	35.93	0.381	31.1	0.20	0.84	0.86	0.444
Laminate, 0.5 mm×0.5 mm	0.50	51.30	0.544	20.0	0.50	0.50	0.80	0.6344
Laminate, 0.3 mm×0.3 mm	0.50	51.30	0.544	33.3	0.30	0.30	0.80	0.6344
Laminate, 0.2 mm×0.2 mm	0.50	51.30	0.544	50.0	0.20	0.20	0.80	0.6344
Laminate, 0.1 mm×0.1 mm	0.50	51.30	0.544	100.0	0.10	0.10	0.80	0.6344
Foam, 20 PPI	0.80	20.54	0.218	19.75	0.81	–	0.804	0.318
Foam, 30 PPI	0.80	20.54	0.218	26.66	0.60	–	0.816	0.318
Foam, 45 PPI	0.80	20.54	0.218	37.20	0.43	–	0.813	0.318

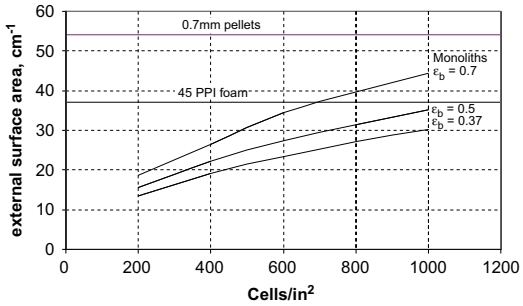

Fig. 2. Comparison of external surface areas for pellet, foam and several monoliths.

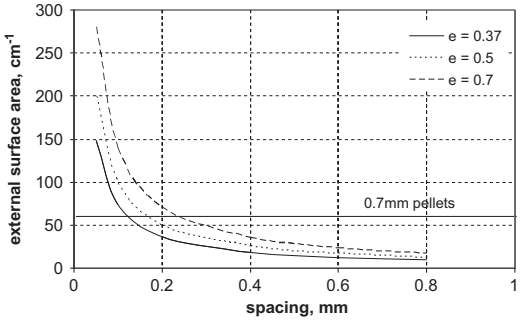

Fig. 3. Comparison of external surface areas for packed bed and several laminates with varying voidages.

per unit volume of 1 mm bead diameter, 45 PPI foam and different voidage monolithic structures is shown. It is clear that small beaded packed beds and foam adsorbents have very high external surface area which is difficult to match with monolithic structures.

For comparison, a 45 PPI foam and 0.7 mm pellet diameter packed bed have an external area of 37 and 54 cm^2/cm^3, respectively. Monoliths can only match the external surface area by using very high cell densities and high voidages. Unfortunately, high voidage compromises system performance and reduces overall density which more than offsets the gain in external surface area. Practical cell densities of 400 cpsi and voidages of 0.5 will give about 22 cm^2/cm^3, a little over half of the surface area of a 1 mm packed bed. To compensate the smaller surface area of monolithic adsorbents, a thin layer of active film with desirable voidage may be grown on the wall surface. The presence of such a film does not obstruct the gas flow through the channel (due to the small thickness in the range of several microns) while it could enhance the cell density of the active adsorbent.

Fig. 3 shows that the surface area per unit volume of laminate systems compares favourably with packed beds for small laminate spacings and wall thickness. However, practical difficulties associated with maintaining small spacing may complicate deployment of these systems. Furthermore, lower adsorbent loading associated with thinner walls will result in insufficient overall adsorbent density.

3.2. Comparison of mass transfer characteristics

The typical mass transfer characteristics of adsorbent structures were calculated using equations presented in Section 2.1 and the values at a constant superficial velocity of 1 m/s are given in Table 4. It is clear from this table that although kinetic properties of beads are somewhat superior to other structures, increasing cell density in monolithic adsorbents, decreasing the spacing between adjacent sheets in laminate configurations or choosing foams with higher number of pore per inch (PPI), can give proportionally improved performance.

Laminate structures can exhibit significantly better performance than a packed bed ($>50\%$) but only if the critical sheet thickness and spacing is less than about 0.2 mm. As stated earlier, the practical difficulties involved in reproducibly making such structures are not trivial. The tolerances must be quite tight ($<5\%$) in the channels to avoid maldistribution. This requires that the spacing must be maintained to within <0.01 mm. Typically, the mass transfer coefficient of foams would increase by increasing the pore count at constant hydrodynamic conditions due to enhanced surface area available for adsorption. The axial dispersion coefficient of foams is much smaller than dispersion resulting from pore diffusion coefficients and could be justifiably neglected. For example, for 30 PPI foam with characteristic diameter of 0.695 mm, D_L/U^2 is about 6.4×10^{-4}.

The influence of monolith external voidage on performance is subtle. At high voidages (>0.7), cell walls are thin, high external surface area per unit volume is obtained leading to good mass transfer, however, bed densities are low. These effects counteract each other. The opposite situation occurs at low voidage. The optimal voidage

Table 4
Mass transfer properties of different adsorbent structures.

Structure	*Sc*	*Re*	*Sh*	k_f (cm/s)	k_p (cm/s)	U^2/D_L (s^{-1})	$k_{mass\_transfer}$ (s^{-1})	$k_{overall}$ (s^{-1})
0.7 mm pellet	0.51	83	14.50	34.3	4.74	543	608.00	287.00
Monolith, 200 cpsi	0.51	172	2.82	3.23	1.53	1480	40.7	39.61
Monolith, 400 cpsi	0.51	121	2.76	4.49	2.13	2920	80.63	78.51
Monolith, 600 cpsi	0.51	100	2.74	5.41	2.68	4200	120.49	117.13
Laminate, 0.5 mm×0.5 mm	0.51	59	2.70	9.00	3.98	10 500	65.24	65.24
Laminate, 0.3 mm×0.3 mm	0.51	36	2.70	14.95	6.64	22 300	181.11	181.11
Laminate, 0.2 mm×0.2 mm	0.51	24	2.70	22.4	9.96	34 300	407.41	407.41
Laminate, 0.1 mm×0.1 mm	0.51	12	2.70	44.76	19.92	50 700	1629.45	1629.45
Foam, 20 PPI	0.51	50	4.72	6.59	2.23	1380	56.04	53.86
Foam, 30 PPI	0.51	36	4.09	9.76	3.82	1560	156.71	143.49
Foam, 45 PPI	0.51	24	3.43	8.38	3.91	1740	158.06	143.74

can only be determined once a good idea of the effective diffusion coefficient in the monolith walls is known. Axial dispersion in packed beds ranges from 0 to 2 cm^2/s at Reynolds numbers greater than 100 which covers most of our region of interest. The axial dispersion contribution to overall mass transfer coefficient for pellets is usually very small (similar to external diffusion) and can justifiably be neglected. Note, however, that very small particles (< 1.0 mm) have significantly more axial dispersion. For example, the limiting Peclet number for 0.7 mm diameter pellets is about 0.4 giving $D_L = 18.4\ cm^2/s$ and $D_L/U^2 = 0.0018$ s. This is comparable to pore diffusion resistance and indicates that for small diameter pellets, gains in kinetic effects from reducing particle size can be rapidly offset by increased axial dispersion. In monoliths, the axial dispersion is much more dependent on channel diameter and flow rate. In laminar flow, the axial dispersion can be calculated from Taylor's analysis

$$Pe = \frac{Ud}{D_L} \approx 192\frac{D_m}{Ud}$$

This gives $D_L/U^2 = d^2/(192D_m)$. For 1 mm diameter channel and a molecular diffusivity of 0.1 cm^2/s, $D_L/U^2 = 5\times10^{-4}$ s. This is a negligible contribution to overall dispersion of the mass transfer front. For laminates, a similar conclusion holds as with monoliths. Resistances in the porous material and external film are far greater than axial dispersion in the gas phase.

3.3. Pressure drop

The pressure drop at different superficial velocities ranging from 0.1 to 1 m/s was calculated using correlations presented at Section 2.2. Fig. 4 shows the pressure drop associated with different adsorbent configurations. As can be seen from this figure, the low density monolith (200 cpsi) exhibited the lowest pressure gradient, while as expected, the highest pressure drop was found to be represented by beads (0.7 mm). Increasing the monolith cell density to increase adsorbent loading and geometric surface area does not change bed pressure drop as significantly as other adsorbent configurations and the monolithic adsorbents still display the lowest head loss compared to laminate, foam and bead systems. Laminate adsorbents with 0.5 mm thickness showed a lower pressure drop than foam and beads. According to Giani et al. (2005) and Patcas et al. (2007), the pressure drop characteristics of foam structures are somewhat between those of monoliths and packed beds, our results are in agreement with their findings.

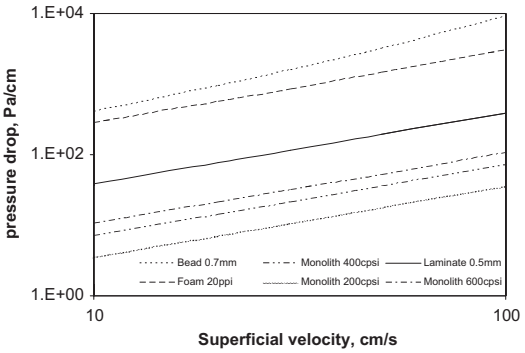

Fig. 4. Comparison of pressure drop for pellet, laminate, foam and several monoliths as a function of superficial gas velocity.

3.4. Mass transfer zone (MTZ)

The dynamic behaviour of mass transfer zone was evaluated using different adsorption column operating conditions such as gas flow rates, etc. Fig. 5 shows the mass transfer zone (MTZ) as a function of superficial gas velocity for different adsorbent configurations taken directly from the COMSOL simulations. As expected, for all cases, the mass transfer length was increased by increasing gas velocity. The mass transfer zone length in the case of foam and monolith was considerably longer that of laminate and pellet structures. Laminates with wall thickness of 0.2 mm show superior mass transfer behaviour to a packed bed of 0.7 mm beads.

The comparison of CO_2 breakthrough curves in different bed configurations is shown in Fig. 6. As can be seen, laminate adsorbents with wall and spacing of 0.2 mm exhibits a very steep breakthrough front compared to pellets, foams and monoliths. This sharp front is attributed to the much higher value of pore diffusion coefficient, k_p, in laminate adsorbents as presented in Table 4. The other structures namely, foam 30 PPI, pellet 0.7 mm and monolith 600 cpsi, represent a similar breakthrough front trend, although the times to reach 5% and 95% of the outlet concentration are longer in the case of foam adsorbents. As with the same MTZ, the 600 cpsi monolith, 30 PPI foam and 0.2×0.2 laminate display the same performance. In other words, for adsorptive gas separation processes, using structured adsorbents

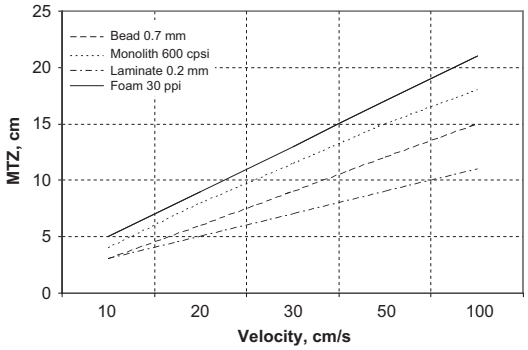

Fig. 5. Comparison of MTZ for pellet, laminate, foam and several monoliths as a function of gas velocity.

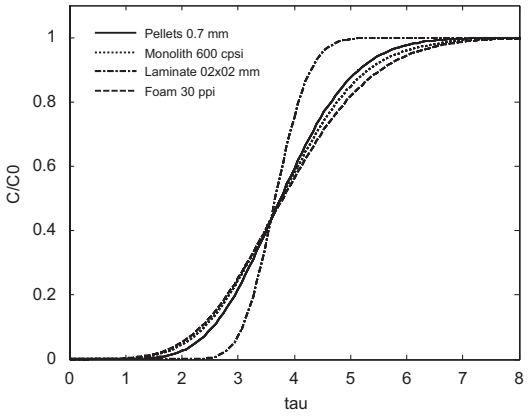

Fig. 6. Comparison of breakthrough curves of CO_2 in different bed configurations.

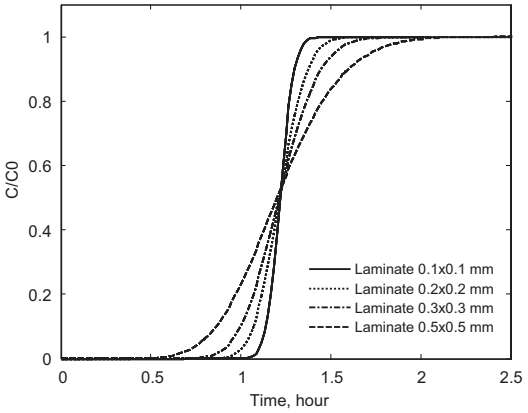

Fig. 7. Comparison of breakthrough curves of CO_2 in laminate bed structures with different wall thickness and spacing.

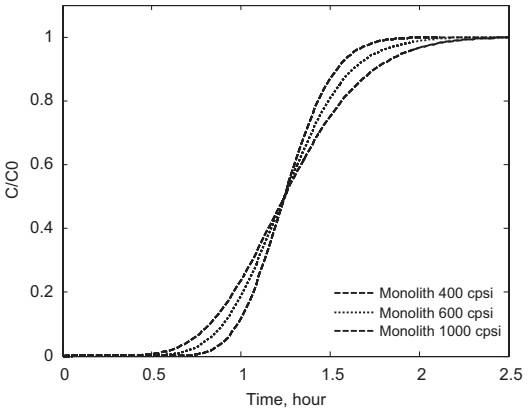

Fig. 8. Comparison of breakthrough curves of CO_2 in monolith beds with different cell densities.

in the form of 600 cpsi monolith, 30 PPI foam and 0.2×0.2 laminate will give somewhat similar performance to a packed bed of 0.7 mm diameter beads.

Fig. 7 shows the effect of laminate geometry on breakthrough performance. It is clear that wall thickness and spacing play critical roles in adsorptive performance of laminate structures. Increasing the wall thickness and spacing leads to broadening of breakthrough profiles over a longer time and hence deteriorate the overall system efficiency, while thinner sheets with smaller spacing give sharp breakthrough fronts indicating negligible mass transfer resistance through the bed. A longer MTZ will reduce both working capacities and selectivity of adsorbent.

A similar trend was observed for monolithic structures. Fig. 8 shows that using monoliths with low cell density would give rise to early breakthrough and a longer time until 95% of outlet concentration is reached. This is due to thicker walls and lower adsorbent mass transfer coefficient (k_p) in the case of lower cell density. Table 4 indicates that axial dispersion in the monolith does not influence the breakthrough front significantly even though axial dispersion increases with increase in cell density.

Breakthrough data for foam adsorbents are shown in Fig. 9. Decreasing pore numbers per inch (PPI) leads to earlier breakthrough and broadening of the front. The effect of axial dispersion on the breakthrough curves of foam adsorbents is clear. By increasing the number of pores (higher PPI) the axial dispersion coefficient is decreased (higher U^2/D_L), however, as evident from Table 4, the contribution of axial dispersion coefficient on overall rate constant is trivial and hence does not influence the shape of breakthrough front.

3.5. Effect of adsorbent structure on specific productivity

The analysis above is useful in identifying features of the adsorbent which impact on pressure drop, mass transfer and adsorbent loading. However, in a process, the goal is usually to maximize specific productivity, i.e. to be able to maximize throughput in a given amount of adsorbent. It is therefore necessary to consider an appropriate combination of process parameters to demonstrate how the pressure drop, cycle time and adsorption front affect system performance. The system specific productivity is the product of the working capacity (moles of gas adsorbed/desorbed per unit mass of adsorbent including binder, support, etc.) and the density of the composite adsorbent. The throughput attainable in a given volume

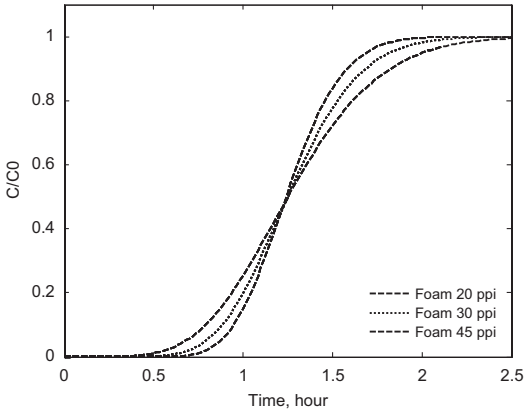

Fig. 9. Comparison of breakthrough curves of CO_2 in foam beds with different PPI.

of vessel in a cyclic adsorption system may be expressed as

$$throughput\ (TPD) \propto \frac{gas\_production}{cycle \times m_{ads}} \times \frac{cycle}{day} \tag{31}$$

$$specific\ productivity = k\frac{WC}{\tau} \tag{32}$$

where WC is adsorbent working capacity (mol/kg adsorbent/cycle), m_{ads} is the mass of adsorbent, τ is the cycle time (s/cycle) and k is a proportionality constant. The effect of pressure drop on the productivity is to reduce the overall working capacity. Instead of operating between a high pressure P_H and a low pressure P_L, the average bed pressure on adsorption is only $P_H-\Delta P/2$ and the bed pressure on desorption is $P_L+\Delta P/2$. Thus the pressure difference between adsorption and desorption is approximately diminished from P_H-P_L to $P_H-P_L-\Delta P$. Generally (for any isotherm), the working capacity will be reduced by some function of ΔP written as $f_1(\Delta P)$. The situation for linear isotherms is shown in more detail below. A more exact analysis of the effect of pressure can only be obtained through detailed numerical simulations.

The effect of MTZ on specific productivity is to reduce the effective length of bed which also translates to a reduction in working capacity. Again, this can be represented generally as some function f_2 of the MTZ. The specific productivity can therefore be written as

$$\text{specific productivity} = \frac{k[WC - f_1(\Delta P) - f_2(MTZ)]}{\tau} \tag{33}$$

where f_1 and f_2 are functions of ΔP and MTZ, respectively. Since the cycle time is inversely proportional to bed velocity

$$\tau \propto \frac{1}{U}$$

The specific productivity equation can be further rearranged to

$$\begin{aligned}&\text{specific productivity}\\ &= k'[WC - f_1(\Delta P) - f_2(MTZ)]U\\ &= k'[WC - f_1(\Delta P(U)) - f_2(MTZ(U))]U\end{aligned} \tag{34}$$

where k' is another proportionality constant and the dependence of pressure drop and mass transfer zone on velocity is made explicit. In order to find f_1 and f_2, we can consider a linear isotherm. For no pressure drop in the system, the ideal amount of adsorbate loading per mass of adsorbent is given by

$$WC = \Delta n_{ideal} = K(P_H - P_L) \tag{35}$$

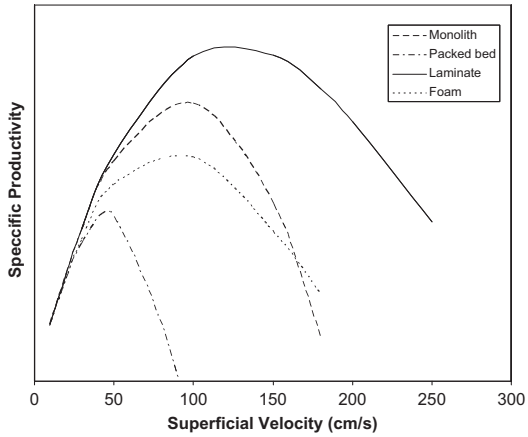

Fig. 10. Comparison of specific productivity for pellet, laminate, foam and monolith as a function of superficial gas velocity.

As mentioned earlier, pressure drop affects the process by reducing the average pressure swing between feed and blowdown in PSA system. The working capacity for the system with pressure drop and a mass transfer zone is therefore (to a first approximation)

$$\begin{aligned}\Delta n_{non-ideal} &= \left(K\left(\left(P_H - \frac{\Delta P}{2}\right) - \left(P_L + \frac{\Delta P}{2}\right)\right)\right)\left(1 - \frac{MTZ}{L}\right)\\ &= (K(P_H - P_L) - K\Delta P)\left(1 - \frac{MTZ}{L}\right)\end{aligned} \tag{36}$$

$$\Delta n_{non-ideal} = (\Delta n_{ideal} - K\Delta P)\left(1 - \frac{MTZ}{L}\right) \tag{37}$$

Therefore, the specific productivity of the adsorbent system can be represented by following correlation:

$$\text{specific productivity} = k'(\Delta n_{ideal} - K\Delta P)\left(1 - \frac{MTZ}{L}\right)U \tag{38}$$

Eq. (38) indicates that specific productivity is proportional to the superficial velocity and decreases with increase in MTZ and pressure drop. Therefore any factor affecting the MTZ and pressure drop may influence the specific productivity. Specifically, the trade-off in specific productivity as a function of velocity is clear. At high velocities, cycle time is reduced, however, the pressure drop and MTZ length increase which decrease overall system performance. At low velocities, pressure drop and MTZ effects are small but the long cycle time lead to low specific productivity.

Fig. 10 shows qualitatively the specific productivity as a function of superficial velocity for different structures as given by Eq. (38). Δn_{ideal}, K and ΔP values were calculated based on isotherm data. It can be seen that although at lower velocities, the productivity is almost the same for different structures since all dispersive effects are negligible, however, at higher velocities, the structured adsorbents display better performance than the conventional packed bed of pellets. It is precisely this higher velocity region that structured adsorbents are most suited to and display their superiority. Comparison of the optimal velocity shows that a laminate is capable of almost twice the specific productivity of a packed bed of pellets. To convert the y-axis in Fig. 10 to a quantitative scale will require detailed simulations for the specific system of interest. The intention

here, however, is to illustrate the qualitative trends expected in performance as a function of throughput.

4. Conclusion

In this study, some important features of different adsorbent structures were derived and their performance compared. Mathematical models were developed based on structural and geometric parameters that impact overall system performance such as voidage, external surface area per unit volume and bulk density. Limiting LDF type expressions were derived for laminates, monoliths and foam structures. Pressure drop and mass transfer characteristics were investigated. Based on the simulation results, laminate systems were shown to be potentially very promising structures provided they can be made with small spacings (< 0.2 mm) and sheet widths (0.2 mm). Monoliths can be considered as successful candidates if appropriate cell densities (> 1000 cpsi) and voidages are used. The actual values to use depend on the effective diffusivities that can be obtained for diffusion in the monolith walls. Low density monoliths are penalized not only by having less mass per unit volume, but also by having far less external surface area per unit volume than a packed bed. The overall rate constant is, therefore, diminished considerably compared to a packed bed. As shown theoretically, the contribution of axial dispersion to overall rate constant was trivial for almost all adsorbent configurations, while the internal rate and external film contributions were, respectively, about 75% and 25%. To compensate for reduced mass, a faster cycle is needed; however, the interstitial velocity rapidly rises and stretches the mass transfer zone, so that it may be impossible to match a packed bed performance with a low density monolith. As we progress in monolith development, it will be important to attempt to lower the voidage and increase the cell density. Foam structures on the other hand show comparable properties to packed beds.

Finally, we show that the throughput for alternate adsorbent structures may be substantially higher than a packed bed provided the structure is operated at its optimal velocity. Increasing beyond this value leads to an increase in pressure drop and mass transfer zone which more than offsets the gains in cycle time reduction.

Notation

a	specific surface area per unit bed volume, cm^2/cm^3
C	bulk concentration, g mol/cm^3
$\overline{C}p$	average solid concentration, g mol/cm^3
C^p	gas concentration in voids in adsorbent, g mol/cm^3
C_s	gas concentration at adsorbent surface, g mol/cm^3
D_e	effective diffusivity, cm^2/s
D_L	axial dispersion coefficient, cm^2/s
D_m	molecular diffusion coefficient, cm^2/s
k	equation constant parameter
$\overline{k}$	total mass transfer coefficient, cm/s
k'	equation constant parameter
k_f	film mass transfer coefficients, cm/s
k_p	pore mass transfer coefficients, cm/s
L	column length, cm
N	molar (radial) flux of component, g mol/cm^2 s
N_s	molar flux at adsorbent surface, g mol/cm^2 s
$\overline{q}$	average adsorbent loading, g mol/kg adsorbent
q^p	adsorbent loading, g mol/kg zeolite
R_1	inner wall radii of monolith channel, cm
R_1	outer wall radii of monolith channel, cm
U	superficial fluid velocity, cm/s
w	wall thickness, cm

Greek letters

α	geometry's factor, cm^{-1}
ε_b	bed void fraction
ε_p	solid void fraction
ρ_s	adsorbent density (includes binder, support, etc.), g/cm^3

Acknowledgement

The authors would like to acknowledge the Monash Research Graduate School (MRGS) for providing scholarship support for Fateme Rezaei.

Appendix A. Model for monoliths

A.1. Gas phase equations

Single-component adsorption is considered. The monolith is represented by a series of parallel cylinders. We solve for the breakthrough in one cylinder only since all the cylinders are the same (assume no maldistribution). A differential mass balance for the adsorbate in the gas phase flowing through the bed gives

$$\left(\frac{\partial C}{\partial t}\right)_z - \frac{D_L}{\varepsilon_b}\frac{\partial^2 C}{\partial z^2} + \frac{1}{\varepsilon_b}\frac{\partial (UC)}{\partial z} + \frac{ak_f}{\varepsilon_b}(C - C_s) = 0$$

The specific surface area for the monolith per unit volume can be represented as

$$a = \frac{2}{R_1}$$

A.2. Solid phase equations

A differential mass balance for the adsorbate inside the monolith wall is given by

$$\varepsilon_p\left(\frac{\partial C^p}{\partial t}\right)_r + \rho_s w\left(\frac{\partial q^p}{\partial t}\right)_r + \frac{1}{r}\left(\frac{\partial (rN)}{\partial r}\right)_t = 0$$

The volume-mean concentration is given by

$$\bar{C}^p = \frac{1}{\pi(R_2^2 - R_1^2)}\int_{R_1}^{R_2} 2\pi C^p\, dr = \frac{2}{R_2^2 - R_1^2}\int_{R_1}^{R_2} rC^p\, dr$$

$$\overline{q}^p = \frac{2}{R_2^2 - R_1^2}\int_{R_1}^{R_2} rq^p\, dr$$

Considering the boundary condition of $\left.\frac{\partial C}{\partial r}\right|_{r=R_2} = 0$ and substituting the above equations into the differential equation gives

$$\varepsilon_p\left(\frac{\partial \bar{C}^p}{\partial t}\right) + \rho_s w\left(\frac{\partial \overline{q}^p}{\partial t}\right) + \frac{2R_1}{R_2^2 - R_1^2}N_s = 0$$

In this equation, N_s is the flux at $R = R_1$ which is given by

$$N = k_f(C - C_s)$$

In terms of an overall driving force this can also be written as

$$N_s = k_p(C_s - \overline{C}^p)$$

In order to specify N_s, continuity at the pellet surface is considered:

$$k_f(C - C_s) = -D_e\left(\frac{\partial C^p}{\partial r}\right)_{R_1}$$

In this equation, D_e is the "effective diffusion coefficient" for the adsorbate in the adsorbent wall. To apply this equation, the concentration profile within the adsorbent is approximated by a parabola:

$$C^p = A(t) + B(t)r^2$$

Considering $C^p = C_s$ at $r = R_1$, it follows that

$$\left(\frac{\partial C^p}{\partial r}\right)_{R_1} = \frac{4R_1}{R_2^2 - R_1^2}(C_s - \overline{C}^p)$$

Finally, the surface flux and concentration can be solved in terms of C and $\overline{C}_1^p$ as

$$N = \frac{k_f k_p}{k_f + k_p}(C - \overline{C}^p)$$

$$N = \bar{k}(C - \overline{C}^p)$$

$$\frac{1}{\bar{k}} = \frac{1}{k_f} + \frac{1}{k_p}$$

Considering $k_p = 4D_eR_1/R_2^2 - R_1^2$, the overall mass transfer coefficient is given by

$$\bar{k} = \frac{1}{\dfrac{1}{k_f} + \dfrac{R_2^2 - R_1^2}{4R_1D_e}}$$

Assuming constant velocity and linear isotherm ($q = KC$), the gas and solid phase conservation equations can be summarized as

$$\left(\frac{\partial C}{\partial t}\right)_z - \frac{D_L}{\varepsilon_b}\frac{\partial^2 C}{\partial z^2} + \frac{U}{\varepsilon_b}\frac{\partial C}{\partial z} + \frac{a\bar{k}}{\varepsilon_b}(C - \overline{C}^p) = 0$$

$$\left(\frac{\partial \overline{C}^p}{\partial t}\right)_z = \frac{2\varepsilon_p R_1 \bar{k}(C - \overline{C}^p)}{(R_2^2 - R_1^2)(\varepsilon_p + \rho_s wK)}$$

References

Ackley, M.W., Smolarek, J., Leavitt, F.W., 2003. Pressure swing adsorption gas separation method, using adsorbents with high intrinsic diffusivity and low pressure ratios, United States Patent and Trademark Office Granted US6506234.

Brandani, F., Rouse, A., Brandani, S., Ruthven, D.M., 2004. Adsorption kinetics and dynamic behavior of a carbon monolith. Adsorption 10 (2), 99–109.

Cybulski, A., Moulijn, J.A., 1998. Structured Catalysts and Reactors, p. 1.

Ergun, S., 1952. Fluid flow through packed columns. Chemical Engineering Progress 48 (2), 89–94.

Gadkaree, K.P., 1997. System and method for adsorbing contaminants and regenerating the adsorber, United States Patent and Trademark Office Granted US5658372.

Giani, L., Groppi, G., Tronconi, E., 2005. Mass-transfer characterization of metallic foams as supports for structured catalysts. Industrial and Engineering Chemistry Research 44 (14), 4993–5002.

Gibson, L.J., Ashby, M.F., 1997. Cellular Solids: Structure and Properties. Cambridge University Press, Cambridge.

Golden, T.C., Golden, C.M.A., Zwilling, D.P., 2003. Self-supporting absorbent fabric for gas separation, United States Patent and Trademark Office Granted US6565627.

Grande, C.A., Cavenati, S., Barcia, P., Hammer, J., Fritz, H.G., Rodrigues, A.E., 2006. Adsorption of propane and propylene in zeolite 4A honeycomb monolith. Chemical Engineering Science 61 (10), 3053–3063.

Groppi, G., Giani, L., Tronconi, E., 2007. Generalized correlation for gas/solid mass-transfer coefficients in metallic and ceramic foams. Industrial and Engineering Chemistry Research 46 (12), 3955–3958.

Hawthorn, R.D., 1974. Afterburner catalysts-effects of heat and mass transfer between gas and catalyst surface. A.I.Ch.E. Symposium 70 (137), 428–438.

Hyun, S.H., Danner, R.P., 1982. Equilibrium adsorption of ethane, ethylene, isobutane, CO_2, and their binary mixtures on 13X molecular sieves. Journal of Chemical Engineering Data 27, 196–200.

Keefer, B.G., Carel, A., Sellars, B., Shaw, I., Larisch B., 2004. Adsorbent laminate structures, United States Patent and Trademark Office Granted US6692626.

Kodama, A., Goto, M., Hirose, T., Kuma, T., 1993. Experimental study of optimal operation for a honeycomb adsorber operated with thermal swing. Journal of Chemical Engineering of Japan 26 (5), 530–535.

Lee, L.Y., Perera, S.P., Crittenden, B.D., Kolaczkowski, S.T., 2000. Manufacture and characterisation of silicalite monoliths. Adsorption Science and Technology 18 (2), 147–170.

Li, Y.Y., Perera, S.P., Crittenden, B.D., 1998. Zeolite monoliths for air separation, part 2: Oxygen enrichment, pressure drop and pressurization. Trans, p. 76.

Maurer, R.T., 1994. Spiral-wound adsorber module, United States Patent and Trademark Office Granted US5338450.

Patcas, F.C., Garrido, G.I., Kraushaar-Czarnetzki, B., 2007. CO oxidation over structured carriers: a comparison of ceramic foams, honeycombs and beads. Chemical Engineering Science 62 (15), 3984–3990.

Patton, A., Crittenden, B.D., Perera, S.P., 2004. Use of the linear driving force approximation to guide the design of monolithic adsorbents. Chemical Engineering Research and Design 82 (8), 999–1009.

Rezaei, F., Webley, P.A., 2009. Application of structured adsorbents in gas separation Processes—a review. Separation Science and Technology, in review.

Richardson, J.T., Peng, Y., Remue, D., 2000. Properties of ceramic foam catalyst supports: pressure drop. Applied Catalysis A: General 204 (1), 19–32.

Richardson, J.T., Remue, D., Hung, J.K., 2003. Properties of ceramic foam catalyst supports: mass and heat transfer. Applied Catalysis A: General 250 (2), 319–329.

Rode, E.J., Boulet, A.J.J., Pelman, A.M., Babicki, M.L., Keefer, B., Sawada, J.A., Alizadeh-Khiavi, S., Roy, S., Gibbs, A.C., Kuznicki, S.M., 2007. Engineered adsorbent structures for kinetic separation, World Intellectual Property Organization Patent WO200660743432.

Ruthven, D.M., 1984. Principles of Adsorption and Adsorption Processes. Wiley, New York.

Ruthven, D.M., Thaeron, C., 1996. Performance of a parallel passage adsorbent contactor. Gas Separation and Purification 10 (1), 63–73.

Sawad, J.A., Alizadeh-Khiavi, S., Roy, S., Kuznicki, S.M., 2005. High density adsorbent structures, United States Patent and Trademark Office Granted WO2005032694.

Sircar, S., Kumar, R., Anselmo, K.J., 1983. Effects of column nonisothermality or nonadiabaticity on the adsorption breakthrough curves. Industrial and Engineering Chemistry Process Design and Development 22 (1), 10–15.

Taylor, G.I., 1954. Diffusion and mass transport in tubes. Proceedings of the Physical Society Section B 67 (12), 857–869.

Wakao, N., Funazkri, T., 1978. Effect of fluid dispersion coefficients on particle-to-fluid mass transfer coefficients in packed beds: correlation of sherwood numbers. Chemical Engineering Science 33 (10), 1375–1384.

Yates, M., Blanco, J., Martin-Luengo, M.A., Martin, M.P., 2003. Vapour adsorption capacity of controlled porosity honeycomb monoliths. Microporous and Mesoporous Materials 65 (2–3), 219–231.

Young, L.C., Finlayson, B.A., 1974. Mathematical modeling of the monolith converter. Advances in Chemistry Series (13), 629–643.

Yu, F.D., Luo, L.A., Grevillot, G., 2002. Adsorption isotherms of VOCs onto an activated carbon monolith: experimental measurement and correlation with different models. Journal of Chemical and Engineering Data 47 (3), 467–473.

Zabka, M., Minceva, M., Rodrigues, A.E., 2006. Experimental and modeling study of adsorption in preparative monolithic silica column. Chemical Engineering and Processing: Process Intensification 45 (2), 150–160.

Zabka, M., Gomes, P.S., Rodrigues, A.E., 2008. Performance of SMB with conventional and monolith columns. Separation Purification Technology 63 (2), 324–333.

PAPER C

Structured zeolite NaX coatings on ceramic cordierite monolith supports for PSA applications

Authors:
A. Mosca, J. Hedlund, P. A. Webley, M. Grahn, F. Rezaei

Microporous and Mesoporous Materials 130 (2010) 38 - 48

Microporous and Mesoporous Materials 130 (2010) 38–48

Contents lists available at ScienceDirect

Microporous and Mesoporous Materials

journal homepage: www.elsevier.com/locate/micromeso

Structured zeolite NaX coatings on ceramic cordierite monolith supports for PSA applications

Alessandra Mosca [a,*], Jonas Hedlund [a], Paul A. Webley [b], Mattias Grahn [a], Fateme Rezaei [b]

[a] Div. of Chemical Technology, Luleå University of Technology, SE-97187 Luleå, Sweden
[b] Dept. of Chemical Engineering, Monash University, Clayton, VIC 3800, Australia

ARTICLE INFO

Article history:
Received 3 June 2009
Received in revised form 12 October 2009
Accepted 13 October 2009
Available online 17 October 2009

Keywords:
Structured adsorbents
NaX film
Monolith
CO_2 adsorption

ABSTRACT

Novel structured adsorbents in the form of thin zeolite films grown on substrates designed for low pressure drop have a great potential to improve pressure swing adsorption (PSA) processes. In the present work, template free films of NaX zeolite were grown on the walls of ceramic cordierite supports using a seeding technique. The supports had 400 parallel channels per square inch. Films were grown both from a gel and a clear synthesis solution. The materials were analyzed by scanning electron microscopy, X-ray diffraction, N_2 adsorption/desorption measurements, Hg-porosimetry as well as CO_2 breakthrough experiments. When a gel was used for film growth, a film consisting of well intergrown crystals with a thickness of about 1 μm was obtained. However, a large amount of sediments were deposited on top of the film, which resulted in a dispersed CO_2 adsorption breakthrough front. Zeolite films grown in one longer hydrothermal treatment in a clear solution were less intergrown and consisted of both NaX and hydroxysodalite crystals and, in addition, some sediments were deposited on top of the film, which again resulted in a dispersed breakthrough front. By using a multiple-step synthesis procedure and a clear synthesis solution, well intergrown NaX films, free from sediments and with only a very small fraction of hydroxysodalite crystals could be prepared. The CO_2 breakthrough front for the latter adsorbent was sharper than the front for an empty adsorption column and only shifted in time. This indicates that the flow distribution in the adsorbent is even and that the mass transfer resistance in the film is very low due to the small film thickness and high effective diffusivity for CO_2 in the NaX film and still, the adsorption capacity is considerable. The even flow distribution, very low mass transfer resistance and low pressure drop in combination with considerable adsorption capacity in this adsorbent indicates that it is a promising adsorbent for PSA applications. The findings from the present work will be important for the development of structured adsorbents to use as a competitive alternative to traditionally used adsorbents in PSA.

1. Introduction

Pressure swing adsorption (PSA) is a commonly used technology for gas separation which is relying on selective adsorption of one of the components in a gas mixture at elevated pressure on certain materials, such as zeolites [1–4]. A typical PSA system involves a number of connected columns containing adsorbent material that undergo successive pressurization and depressurization steps in order to produce a continuous stream of purified product gas.

Zeolites are porous crystalline aluminosilicates of SiO_4^{4-} and AlO_4^{5-} tetrahedra connected by oxygen bridges [5]. Zeolites are widely used in PSA gas separation processes and are particularly suitable for oxygen enrichment from air by PSA (low silica zeolite X) [6,10,54] or H_2 recovery from refinery fuel gas or coke oven gases [38,56], whereas zeolite 5A is used in carbon-zeolite layered beds to obtain a high purity (>99.99%) hydrogen stream.

Zeolite NaX is particularly suitable for carbon dioxide capture from flue gas or oxygen enrichment from air by PSA [6–10]. CO_2 and N_2 are adsorbed in the zeolite pores due to the strong quadrupolar interaction between the molecules and the electric field generated by the charge balancing cations in the micropores of the zeolite [5]. The possibility to exchange the cations represents a valuable measure for tuning the volume available for adsorption, as well as the selectivity. Consequently, the adsorption capacity of CO_2 in zeolite X increases with decreasing ion size and increasing charge density, in the order Cs^+, Rb^+, K^+, Na^+, Li^+ [11]. Low silica zeolite X in the Li^+ form (Li-LSX) exhibits a higher selectivity with respect to N_2 than zeolite NaX, due to the higher polarizing power of the small Li^+ cation, and is therefore the most widely used zeolite adsorbent in air separation processes [10,52,53]. The adsorption capacity may also be controlled by tuning the Si/Al ratio of the zeolite.

* Corresponding author. Tel.: +46 920 491293; fax: +46 920 491199.
E-mail address: Alessandra.Mosca@ltu.se (A. Mosca).

1387-1811/$ - see front matter © 2009 Elsevier Inc. All rights reserved.
doi:10.1016/j.micromeso.2009.10.010

Nomenclature

t	time, s
c	concentration at time t, vol%
c_0	concentration at time 0, vol%
K	dimensionless Henry constant
k	coefficient of mass transfer, s^{-1}
k^*	geometric factor, m^{-2} [12]
z	column length, m
v	superficial velocity, m/s
$\frac{dq}{dt}$	uptake rate
q^*	equilibrium adsorbate loading, kg/kg
$\bar{q}$	adsorbate loading, kg/kg
D_{eff}	effective diffusivity, m^2/s
R	radius of sediments, m
l	film thickness, m

Greek letters

ξ	dimensionless concentration
τ	dimensionless time
ε	void fraction

In PSA processes there is a trade-off between pressure drop and mass- and heat-transfer limitations [12]. The adsorbents in industrial PSA processes are usually in the form of beads, pellets or extrudates. Larger adsorbent particles results in lower pressure drop, but increased mass- and heat-transfer limitation due to the long mass- and heat-transfer path along the radius of the particles resulting in a reduced performance of the process [38,51]. Thus, it is of great importance to develop novel structured adsorbents, which may exhibit higher mass transfer coefficients, higher throughputs, and lower pressure drop, and represent a competitive alternative to adsorbents in form of beads/pellets [13–15,48–51].

High mass transfer coefficients may be achieved by using thin films of an adsorbent material grown on structured supports, with the advantage of having a short diffusion path. Although the adsorbent loading is often small compared to traditional adsorbents, high throughputs may be achieved by increasing the cycle frequency and still maintain a low pressure drop [51]. In this context, monolithic adsorbents are of great interest, and a few reports on the use of monolith structures in adsorption processes have been published [13–15,51]. Monoliths are structured materials with parallel channels, available with various cell densities and cell shapes. Low pressure drop, uniform flow distribution, thermal stability and unproblematic scale-up are some of the advantages with these materials [13,15]. The mineral cordierite, $2MgO \times 2Al_2O_3 \times 5SiO_2$, is often used as the main material in monoliths. Cordierite monoliths with tailored macrostructure, high porosity and low thermal expansion are used as supports in automotive catalytic converters and as diesel particulate filters (DPF) [16,17]. Monolith substrates may be wash-coated, dip-coated, slip-coated, slurry-coated or extruded directly into catalytic bodies using appropriate materials [18,19]. Due to the difficulty in washcoating the zeolite, a binder material is needed, which causes a reduction in the accessible surface area of the zeolite coating and increases the diffusion resistance of the adsorbing species. Due to surface tension effects of the washcoat during manufacturing, more material is deposited at the corners of the monolith channels, consequently increasing the diffusion path of the adsorbing species [18]. However, the performance of a zeolite coating is dependent on its morphology. A perfect, smooth film without intercrystalline pores will have other transport properties than a coating comprised of a multilayer of crystals with intercrystalline porosity. For well defined zeolite films, the mass transfer resistance can be controlled by varying the film thickness. This was demonstrated recently by our group [20], where thin ZSM-5 zeolite films without binder material were grown on 400 cells per square inch (cpsi) cordierite monoliths by first depositing a monolayer of colloidal zeolite seed crystals on the monoliths and then growing the crystals to thin films. The catalytic activity of the films was subsequently evaluated by *p*-xylene isomerisation, and the effect of film thickness on mass transfer was clearly demonstrated. As opposed to washcoated monoliths, these films had an even thickness, i.e., no effects of surface tension in the corners. Growth of zeolite films without binder material on ceramic cordierite supports was previously also reported by Zamaro et al. [46] (mordenite) and our group [30] (faujasite).

In another work, the adsorption and diffusion of CO_2 in a carbon monolith adsorbent were studied with the Zero Length Column (ZLC) method by Brandani et al. [21]. The ZLC data showed that the dispersion in the monolith was controlled by mass transfer resistance rather than axial mixing. Zeolite monoliths consisting of 5A zeolite and Na-bentonite with square lattice channels and a wall thickness of 0.98 mm were prepared by Li et al. [14,19,22]. The adsorption performance of the zeolite monolith was compared with that of 5A zeolite pellets (1.5 mm in diameter and 3.6 mm long) used for the production of oxygen enriched air. The main outcomes of the work were that the adsorption performance of the zeolite monolith was of the same magnitude as the pellets whilst the pressure drop through the zeolite monolith was 3–5 times lower than that for the packed bed. The lower pressure drop resulted in a 3–5 times faster pressurization time when the PSA unit was loaded with the zeolite monolith. Shorter pressurization time is an advantage [14,19,22,51] and allows faster PSA cycles which results in a higher productivity and should compensate for the lower adsorbent loading when using monoliths instead of traditional adsorbents [51].

Possible ways of improving the separation performance of the zeolite monoliths would thus be to reduce further the mass- and heat-transfer resistance by reducing the wall thickness and increasing the cell density of the zeolite monolith [12,51].

In the present work, another approach, i.e., zeolite coated monoliths, was pursued to arrive at adsorbent monoliths with low mass- and heat-transfer resistance. Instead of preparing zeolite monoliths, very thin zeolite NaX films with thicknesses ranging from 0.4 to 1.5 μm were grown on 400 cpsi cordierite monoliths to arrive at zeolite coated monoliths. The zeolite coated monoliths were characterized by scanning electron microscopy (SEM), X-ray diffraction (XRD), mercury intrusion porosimetry (MIP), N_2 adsorption and desorption at liquid nitrogen temperature, and CO_2 adsorption breakthrough profiles.

2. Experimental section

2.1. Synthesis

A seeding method was used for zeolite film growth on monoliths. The method is very flexible and allows for control of the thickness and preferred [23–25,47] orientation of the crystals in the film. In addition, the adsorption [26,27] as well as diffusion [28,29] properties of the film has been studied and reported. In the present work, cordierite monoliths with a cell density of 400 cpsi (Corning) were used as supports. Twelve monolith

samples were cut with a sharp tool to a cylindrical shape (11 cm long and 2 cm in diameter) from the original monolith and NaX films were grown on the monolith samples in a similar way as described in previous works [20,30].

In order to remove contaminants that could affect zeolite crystallization, the monoliths were cleaned by rinsing in toluene, acetone and several times in a 0.1 M NH_3 solution. The monoliths were subsequently first dried at room temperature, then in a ventilated oven at 110 °C, and thereafter cooled in a desiccator.

The seeding method used for film preparation consisted of three main steps. (i) *Preparation of 80 nm template free colloidal faujasite seeds.* A 1 wt% template free colloidal faujasite seed sol was prepared as described earlier [31,55]. (ii) *Deposition of seeds onto the surface of substrates by electrostatic adsorption.* An aqueous solution of 0.4 wt% cationic polymer was prepared by diluting a commercial polymer mixture (Redifloc 4150, EKA Chemicals) in distilled water. The pH was adjusted to 8.0 by addition of a dilute ammonia solution. The surface charge of the substrates was reversed by treatment in the cationic polymer solution for 10 min. After charge reversal, the substrates were rinsed with a 0.1 M NH_3 solution six times to remove excess polymer and were subsequently immersed in the seed sol for 10 min to adsorb a monolayer of the 80 nm faujasite seeds. Excess seeds were removed by rinsing six times in a 0.1 M NH_3 solution. The sample was left in a 0.1 M NH_3 solution prior to film growth. (iii) *Growth of the colloidal seed crystals into a continuous polycrystalline film.* A gel with molar composition of $14Na_2O{:}Al_2O_3{:}10SiO_2{:}800H_2O$ or a clear synthesis solution with molar composition of $80Na_2O{:}Al_2O_3{:}9.0SiO_2{:}5000H_2O$ was used for film growth. To prepare the solutions, sodium metasilicate ($Na_2SiO_3{\cdot}9H_2O$, 98%, Sigma–Aldrich) was mixed with pelletized sodium hydroxide (99.9% NaOH, Merck) and distilled water. An aqueous solution of aluminum sulfate ($Al_2(SO_4)_3{\cdot}18H_2O$, Riedel-de-Häen) was added. Thereafter, the mixture was vigorously stirred for 2 min or 2 h for the clear solution and the gel, respectively.

Hydrothermal treatment was performed in an oil bath under reflux at 100 °C at atmospheric pressure. During synthesis, the channels of the support were oriented vertically to reduce zeolite sedimentation from the bulk synthesis mixture onto the walls of the substrate. When using the clear solution, zeolite films were grown in two ways. In the first method, a single hydrothermal treatment was performed for 4 h. In the second method, a multistep procedure was used, and the hydrothermal treatment was carried out in five steps of 1 h and 20 min. When performing the multiple-step synthesis procedure, 91 g of fresh synthesis solution was used for each step. Films grown from the gel were grown in one step for 9 h, using 91 g of synthesis mixture. The sample codes start with the letter C or G for clear solution or gel, respectively, followed by a number indicating the duration of the hydrothermal treatment in hours, see Table 1. After hydrothermal treatment, the samples were carefully rinsed several times in a 0.1 M NH_3 solution and then dried at room temperature and thereafter for 5–6 h at 100 °C in a ventilated oven. The samples were subsequently cooled in a desiccator prior to characterization. The top ends of all samples were polished to a final length of 10 cm, in order to remove any potentially sedimented zeolite.

The zeolite film samples were not calcined as they are grown from template free seeds (as discussed above) in a template free synthesis mixtures, and thus template free.

Relatively large discrete crystals (sample label DC) of NaX zeolite were also grown and the powder was used as a reference material. A synthesis mixture with a molar composition of $4.76Na_2O{:}Al_2O_3{:}3.50SiO_2{:}450H_2O{:}2.00TEA$ was used, similarly as described by Hamilton et al. [32]. Aluminum wire (Aldrich, 99.999%) was dissolved under gentle heating and reflux in a 0.8 M NaOH solution prepared from NaOH pastilles (Merck, NaOH >99.999%) and distilled water. The resulting aluminate solution was then filtered through 0.2 μm syringe filters (Acrodisc® Syringe Filters). Thereafter, TEA (98%+, Aldrich) was added to the filtered aluminate solution. A silicate solution was prepared by dissolving sodium metasilicate pentahydrate ($Na_2SiO_3{\cdot}5H_2O$, 98%, Sigma–Aldrich) in distilled water. The silicate solution was also filtered through 0.2 μm syringe filters after dissolution of the sodium metasilicate pentahydrate. Thereafter, the aluminate and silicate solutions were mixed, and the resulting solution was stirred for 1 min and a gel formed. The gel was then placed in a Teflon lined autoclave and synthesis was performed under autogenous pressure at 115 °C for 3 days. The crystals obtained were purified by repeated centrifugations (14,000*g*) and redispersion in distilled water, four times in total. The crystals were subsequently used for SEM observations and as a reference for N_2 adsorption and desorption at liquid nitrogen temperature.

2.2. Physical characterization

The weight gain ($g_{zeolite}/g_{sample}$) was calculated by measuring the weight increase of the support before and after hydrothermal treatment.

A Philips XL 30 scanning electron microscope (SEM) equipped with a LaB_6 emission source was used for studies of surface morphology of crystals and films and also to measure film thickness. The monoliths were cut in the channel direction prior to SEM investigation. Images were recorded on samples covered with a thin layer of gold (about 10 nm) deposited by sputtering. For each structured adsorbent sample, more than 10 SEM pictures were recorded at various locations (i.e., close to the walls, at the end and in the center) in order to fully appreciate the morphology of each sample. The selected SEM pictures shown in this paper are representative for each sample.

The average particle size of 100 crystals in sample DC was estimated by measurements in SEM images to 7 μm, with a standard deviation of ±200 nm. Due to the size of these crystals, there are only macropores between these crystals (that cannot be detected by nitrogen adsorption) and these crystals should thus be an ideal reference material for nitrogen adsorption measurements with minimum mesoporosity between the crystals.

X-ray diffraction data (XRD) in the two-theta range 5–35° were recorded with a Siemens D 5000 powder diffractometer equipped with a Cu-target and running in Bragg-Brentano geometry.

Nitrogen adsorption/desorption isotherms at liquid N_2 temperature were measured for all samples with a Micromeritrics ASAP

Table 1
Sample characteristics.

Sample code	Synthesis conditions	Film thickness (μm)	Weight gain ($g_{zeolite}/g_{sample}$)	BET surface area (m^2/g_{sample})	Zeolite loading[a] ($g_{zeolite}/g_{sample}$)	Mesop. vol.[b] ($cm^3/g_{zeolite}$)
G9	Gel, 100 °C, 9 h	1.1	0.060	33.16	0.046	0.024
C4	Clear solution, 100 °C, 4 h	0.4	0.015	8.65	0.012	0.111
C5∗1h20 min	Clear solution, 100 °C, 5 steps of 1 h 20 min	1.5	0.036	18.02	0.025	0.082

[a] From BET.
[b] From BJH method.

2010 instrument after outgassing for 12 h at 300 °C. The BET equation was used to calculate the zeolite loading ($g_{zeolite}/g_{sample}$) of the samples from N_2 adsorption data. It was assumed that the surface area of the zeolite in the film was 721 m^2/g in accordance with the measured surface area for the reference material, sample DC. The pore size distribution was determined by the Barrett–Joyner–Halenda (BJH) method applied to the desorption branch.

Mercury Intrusion Porosimetry (MIP) was performed using a Micromeritics Autopore 9220 V1.04 mercury porosimeter, operated between 0.1 and 3500 bar.

2.3. Breakthrough experiments

The films were also characterized by measuring the CO_2 breakthrough profile with step change experiments. The experimental set-up consisted of a gas feed section, an adsorption column and a gas analysis section. Three identical coated monolith samples, each 10 cm long and 2 cm in diameter were used in the step change experiment.

The samples where placed in series in the adsorption column (30 cm long and 2 cm diameter). The adsorbents were activated under a nitrogen flow of 0.2 l/min at 300 °C for 3 h with a heating and cooling rate of 2 °C/min. The samples were thereafter cooled to room temperature (26 °C and 101 kPa, respectively). At time zero, the feed was switched from N_2 (99.995%, Linde Gas) to a 0.2, 0.5 or 1 l/min flow of 10% CO_2 in N_2 (9.99% CO_2 in N_2, Linde Gas) using a pneumatic switching valve (switching time of less than 0.1 s). The concentration of CO_2 in the gas exiting the column was measured as a function of time using a CO_2 analyzer (IR 1507 fast response CO_2 infrared transducer). The response of the analyzer is less than 1 s to reach 95% of its final value and the dispersion by axial diffusion in the line is small (Peclet number: 36) and hence it was assumed that dispersion in the line is mainly caused by the mass transfer kinetics [57,58], which justified the use of the analytical solution by Klinkenberg [37,38] to model the data.

The goal of the experiments was to estimate the mass transfer coefficient k and from that derive the effective diffusivity D_e in the zeolite adsorbents. It was assumed that all the channels in the monolith samples were identical and that the velocity in all channels were the same [33–36]. To model the data, the experimental breakthrough curves were shifted by the delay-time stemming from the volume of tubing and valves, and simulation was performed on the resulting curves. The analytical solution for the breakthrough front by Klinkenberg was used [37,38]:

$$\frac{c}{c_0} = \frac{1}{2}\mathrm{erfc}\left(\sqrt{\xi} - \sqrt{\tau} - \frac{1}{8}\sqrt{\xi} - \frac{1}{8}\sqrt{\tau}\right) \quad (1)$$

$$\xi = \frac{kKz}{v}\left(\frac{1-\varepsilon}{\varepsilon}\right) \quad (2)$$

$$\tau = k(t - z/v) \quad (3)$$

where c/c_0 is the dimensionless concentration, k (s^{-1}) the mass transfer coefficient, K the dimensionless Henry constant, z (m) the column length (m), t (s) the time, v (m/s) the superficial velocity, ε the void volume, defined as the ratio between the square of the channel width and the square of the sum of channel width, zeolite layer thickness, and wall thickness, ξ and τ the dimensionless bed length and time, respectively. The Klinkenberg solution is valid for an isothermal plug flow systems in which a single trace component with linear adsorption isotherm is adsorbed. The dimensionless Henry constant K (estimated from CO_2 adsorption isotherm recorded at 20 °C, not shown here) is equal to 32.1 or 55.7, and the void volume ε is 0.84 for samples C5*1 h20 min or G9. The mass transfer coefficient k in the model was fitted to experimental data by minimizing the sum S of squared residuals:

$$S = \sum_{i=1}^{n}\left[\left(\frac{c}{c_0}\right)_{\mathrm{model}} - \left(\frac{c}{c_0}\right)_{\mathrm{exp}}\right]^2 \quad (4)$$

where n is the number of data points. The standard deviation σ for the fitted model to experimental results was also estimated by:

$$\sigma = \sqrt{\frac{S}{n-1}} \quad (5)$$

The effective diffusivity D_e was estimated from the mass transfer coefficient and a geometrical model of the adsorbent. For samples where the zeolite film dominated the mass transfer resistance, the geometry of the adsorbent was approximated with a slab, and the effective diffusivity for the film was estimated from:

$$D_e^{\mathrm{film}} = \frac{k \cdot l^2}{3} \quad (6)$$

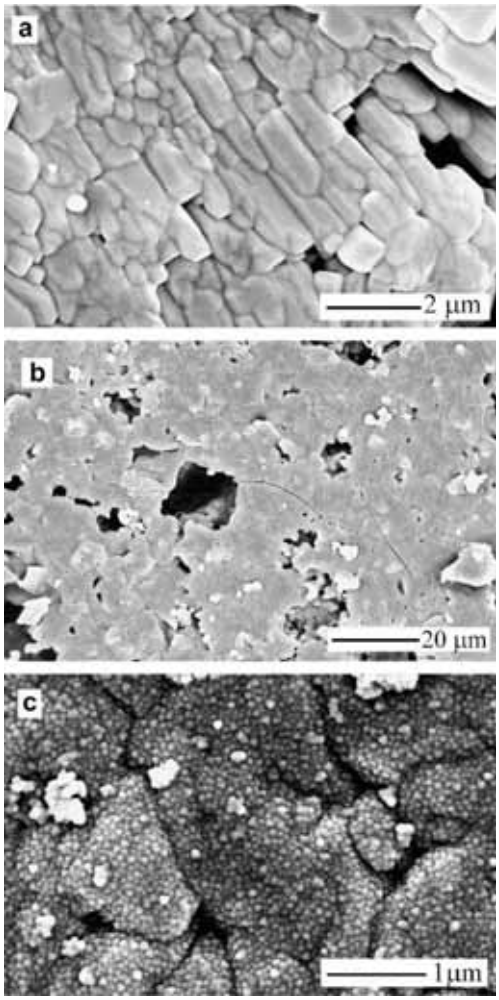

Fig. 1. Top-view SEM images of an uncoated 400 cpsi cordierite monolith support at high (a) and low (b) magnification. Top-view SEM image of a seeded 400 cpsi cordierite monolith support (c).

where l represent the thickness of the film or slab.

For samples where mass transfer resistance was dominated by relatively large sediments deposited from the bulk of the synthesis mixture on the growing film, the geometry of the adsorbent was approximated with spheres, and the effective diffusivity was estimated from:

$$D_e^{\text{aggregate}} = \frac{k \cdot R^2}{15} \quad (7)$$

where R represent the radius of sediments or spheres, respectively.

3. Results and discussion

3.1. Characterization by SEM, weight gain, and zeolite loading

Fig. 1a shows a SEM image of a surface of the wall of an uncoated 400 cpsi cordierite monolith. Cordierite grains form an uneven surface and some macropores are also observed between the grains. A low magnification SEM top view-image of the 400 cpsi cordierite monolith is shown in Fig. 1b, which illustrates macropores with various size between the grains in the cordierite monolith. Fig. 1c shows a monolayer of 80 nm NaX seeds crystals adsorbed onto the surface of the support. The seeds cover the entire external surface of the cordierite monolith walls. A few aggregates of seed crystals with a size between 200 and 400 nm are also observed.

Fig. 2a shows a top-view SEM image of sample G9. The film appears to be very well intergrown and typical NaX crystals with octahedral habit and with a size ranging between about 600 and 2000 nm are observed. A SEM image of sample C4 grown in the clear solution by a single hydrothermal treatment for 4 h is shown in Fig. 2c. The film is less intergrown and comprised of NaX crystals with a size ranging between about 170 and 1000 nm and in addition, hydroxysodalite (HS) crystals with a typical ball-of-yarn habit and a diameter of about 2000 nm are observed. These hydroxysodalite crystals will not contribute to the CO_2 or N_2 adsorption capacity of the film due to the very small pore size (2.2–2.8 Å) [39] of this zeolite. Zeolite HS likely forms as a result of the decreased hydrothermal stability of the NaX crystals during a longer hydrothermal treatment as phase changes are common in the crystallization system of zeolite NaX upon longer synthesis durations [40]. However, no HS crystals formed on the G9 sample, which was prepared from a quite different synthesis mixture, i.e., a gel. To limit the deposition of sediments, formation of HS crystals, and obtain a better intergrown film in the clear solution, a multiple-step synthesis procedure was developed where the clear synthesis solution was replaced every 1 h 20 min.

A NaX film was grown in five steps of 1 h 20 min, see Fig. 2e. This film (sample C5∗1 h20 min) appears more well intergrown than the film in sample C4, but not as intergrown as the film in sample G9, and the number and size of HS crystals embedded in the zeolite film was significantly reduced compared to the one grown in one longer hydrothermal treatment (sample C4). The average thickness of the NaX film sample grown in the gel (sample G9) is about 1.1 μm, as shown in Fig. 2b and reported in Table 1. Fig. 2d shows a cross-sectional image of the NaX film grown in the clear solution in a single hydrothermal treatment (sample C4). As already observed from top-view images, the zeolite coating consists of small, not well intergrown crystals and it is therefore difficult to define a film thickness. However, as shown by Fig. 2d, the NaX coating has an average thickness of about 0.4 μm. Fig. 2f

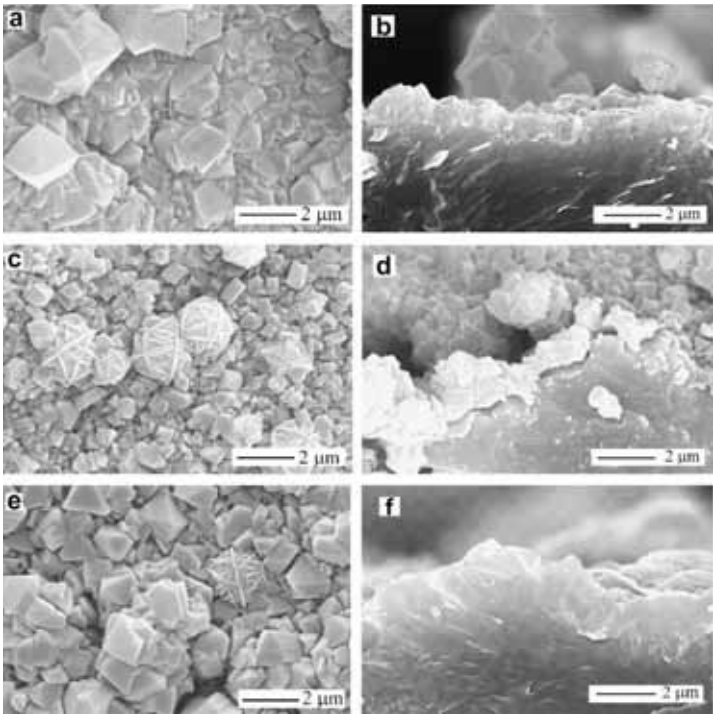

Fig. 2. Top-view and cross-sectional SEM images of the NaX film samples G9 (a,b), C4 (c,d), and C5∗1 h 20 min (e,f).

shows a side-view image of a NaX film grown in the clear solution in five steps of 1 h and 20 min. The film has an average thickness of about 1.5 μm and again appears to be well intergrown.

Fig. 3a shows a top-view image at low magnification of the film grown in the gel. Large aggregates, with radii ranging from ca. 0.5 to 10 μm, are observed on top of the film. These aggregates were probably deposited by sedimentation from the synthesis mixture. Sediments deposited on top of and embedded in the film may be a disadvantage in PSA applications due to the increased diffusion path of the adsorbing species. Fig. 3b, recorded at higher magnification, illustrates that the sediments are well intergrown. A much lower amount of sediments was observed for the film sample C5∗1 h20 min, as shown in Fig. 3c.

The weight gain of the samples increases in the order C4 < C5∗1 h20 min < G9 and is hence highest for the zeolite film sample grown in the gel, see Table 1. The high weight gain for sample G9 suggests the presence of sediments in accordance with SEM observations.

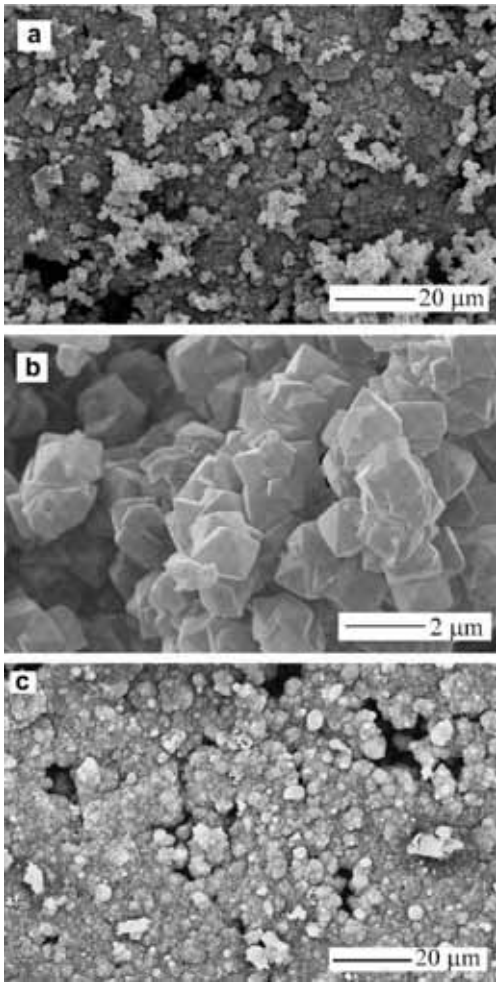

Fig. 3. Low magnification SEM images of the NaX films samples G9 (a), sediment of sample G9 (b), and low magnification SEM image of C5∗1 h20 min (c).

The measured surface area of the monolith support was 0.24 m^2/g, which was about 35, 80 and 140 times lower than those measured for the zeolite film samples C4, C5∗1 h20 min and G9, respectively. The observed surface area of the zeolite coated monoliths thus stem almost entirely from the deposited zeolite, see Table 1. The surface area of the monolith was consequently neglected when estimating the zeolite loading of the zeolite coated monoliths from nitrogen adsorption data. The zeolite loading estimated for all zeolite film samples by liquid nitrogen adsorption is, as expected, in rough accordance with the measured weight gain, see Table 1. In the absence of sediments and zeolite growth inside the pores of the support, a linear relationship between zeolite loading (or weight gain) and the thickness of the zeolite films should be observed. The zeolite loading of the film sample grown in the gel (sample G9), 0.046 $g_{zeolite}/g_{sample}$, is about two times higher than the one grown with multiple steps (0.025 $g_{zeolite}/g_{sample}$), although the film thickness is lower on the former sample. This suggests the presence of sediments on sample G9 as observed by SEM, see Fig. 3a. The zeolite loading of the sample grown in the clear solution for 4 h is 0.012 $g_{zeolite}/g_{sample}$ about half of that for the sample grown by the multi-step synthesis procedure (sample C5∗1 h20 min), although the thickness of the latter NaX film is approximately four times higher. This indicates that the zeolite coating grown by the multi-step procedure (C5∗1 h20 min) has less sediments than sample C4, in concert with the SEM observations. In summary, all results discussed in this section indicate that films grown by the multiple-step synthesis procedure have less sediments and HS crystals than the films grown using the other procedures.

3.2. Characterization by XRD

Fig. 4 shows XRD patterns for all samples. The data show that the discrete crystals (sample DC) are comprised of randomly oriented zeolite X crystals and a very small fraction of zeolite P, in accordance with previous results [32].

The film samples are composed of randomly oriented NaX and cordierite crystals. It is worth noting that the intensity of the low-angle peaks (between 5° and 11°) is lower for the discrete crystals (sample DC) than the films. This is the result of the presence of template molecules (TEA) in sample DC, which affect the electron density inside the crystals, similarly as observed for template containing silicalite-1 crystals [41,42]. For the zeolite film samples, the intensity of the NaX zeolite peaks increases in the order C4 < C5∗1 h20 min < G9, i.e., with increasing zeolite loading and weight gain as expected. No hydroxysodalite reflections were observed by XRD for the NaX film samples although few HS crystals were observed by SEM for sample C4 and very few for sample C5∗1 h20 min. The fraction of sodalite crystals should thus be very small and should not affect the adsorption performance of the adsorbents. At 2θ of about 16.5° and 27.8°, some minor unidentified reflections were observed for the film samples.

3.3. Nitrogen adsorption–desorption isotherms and pore size distribution

The N_2 adsorption–desorption isotherms expressed as mmol/g_{sample} (g_{sample} is the total weight of each sample including both zeolite and support) for a cordierite monolith support and the NaX coated supports are shown in Fig. 5a. The amount of nitrogen adsorbed by the uncoated cordierite monolith is very low compared to the coated samples, which shows that the volume of nitrogen adsorbed by the coated samples mainly originates from the zeolite film and larger adsorbed amounts per gram sample is a result of higher zeolite loading for the film coated samples as discussed above. Although the thickness of the film grown in the clear

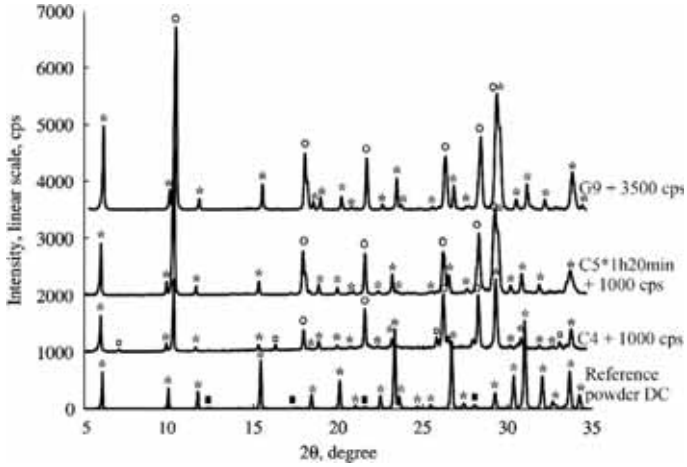

Fig. 4. XRD patterns for the reference NaX powder (sample DC) and the NaX film samples G9, C4, and C5*1 h20 min. The cordierite, the NaX, and the zeolite P peaks are labeled by the symbols "○", "∗", and ■, respectively. The symbol □ indicates unidentified reflections.

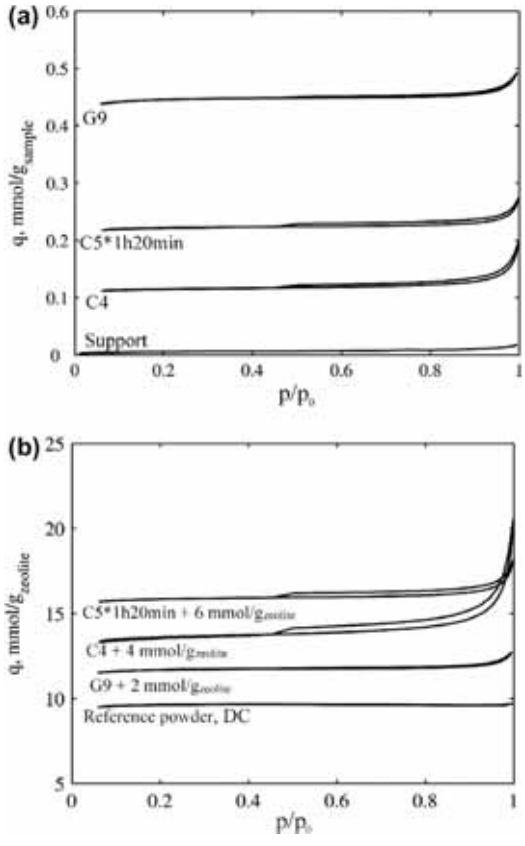

Fig. 5. Nitrogen adsorption–desorption isotherms of the NaX film samples and reference NaX crystals (sample DC) per gram sample (a) and per gram zeolite (b).

solution with the multiple-step synthesis procedure (sample C5*1 h20 min) is higher than the gel (sample G9), the amount of nitrogen adsorbed by the latter is higher, this is due to the high zeolite loading caused by the presence of sediments on the latter sample, as discussed earlier. The contribution of the sediments to the total adsorption capacity in sample G9 was estimated from nitrogen adsorption data and SEM observations under the assumption that the observed nitrogen adsorption capacity (0.21 mmol/g sample) of sample C5*1 h20 min entirely stem from a 1.5 μm film as follows. This assumption is supported by SEM observations. The adsorption capacity for the 1.1 μm film in sample G9 should thus be about 0.15 mmol/g sample (0.21 mmol/g sample ∗ 1.1/1.5). The observed adsorption capacity for sample G9 was 0.43 mmol/g sample and the adsorption capacity of the sediments on this sample should thus be about 0.28 mmol/g sample (observed-film mmol/g sample). Sediments thus represent the main fraction of zeolite in sample G9, and their contribution to the total adsorption capacity is about 65%, whereas about 35% is due to adsorption in the film. Thus, the sediments, with their long diffusion paths, will dominate the CO_2 uptake during breakthrough experiments, as will be discussed below.

Fig. 5b shows the isotherms expressed as mmol/$g_{zeolite}$ ($g_{zeolite}$ is the weight of zeolite on each sample determined from nitrogen adsorption, as discussed above). The N_2 adsorption/desorption isotherm of the reference powder DC is also included in the figure. Note that the *y*-scales for the films are shifted, since data would overlap otherwise. For all samples, the volume adsorbed at low pressure increased rapidly up to about 9 mmol/$g_{zeolite}$ due to adsorption in zeolite pores. The isotherm of the reference powder DC is typical for a microporous sample consisting of large crystals, essentially free of mesopores between the crystals and consequently no hysteresis loop is observed. For all film samples (but not for the powder DC), a hysteresis loop that closes at a relative pressure p/p_0 of 0.45 is observed, similarly as observed previously for MFI zeolite films grown on cordierite monolith supports [43]. This loop is an effect of capillary condensation, most likely in the intercrystalline mesopores in the form of grain boundaries in the zeolite films.

Fig. 6 shows the cumulative mesopore volume, per gram zeolite, of the film samples and reference powder DC. The total mesopore

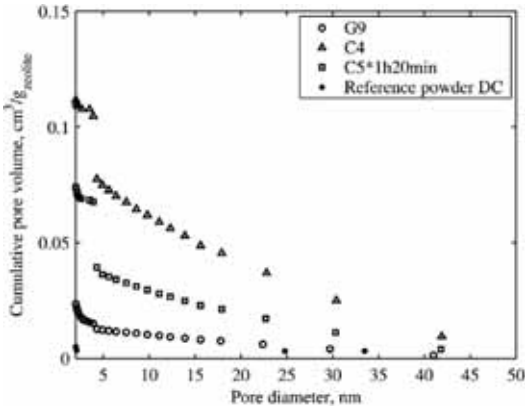

Fig. 6. Cumulative BJH mesopore volume (cm^3/g zeolite) for the film samples and reference powder as a function of pore diameter (nm).

volume of the reference powder DC is 0.003 cm^3/g zeolite, i.e., very low, as expected for large NaX crystals. The total mesopore volume per gram zeolite of the film samples C4, C5∗1 h20 min, and G9 is equal to 0.111, 0.082 and 0.024 $cm^3/g_{zeolite}$, respectively, as reported in Table 1. The mesopore volume per gram zeolite of the samples is thus significantly higher than for the reference powder. This difference is assigned to mesopores in the form of grain boundaries and cracks in the films formed during drying. The mesopore volume is an indication of the crystal intergrowth in the zeolite films, and sample G9 shows the lowest mesopore volume, indicating that this film is better intergrown than samples C5∗1 h20 min and C4, in concert with the SEM observations.

3.4. Characterization by MIP

Fig. 7 shows the cumulative pore volumes (cm^3/g sample) determined by MIP of a support and the NaX film samples G9, C4, and C5∗1 h20 min, see figure legend for details. In the region between 80 and 2 μm, the cumulative pore volume shows a steep increase for the uncoated support as well as for samples C4 and G9, probably due to Hg filling the pores in the walls of the monolith

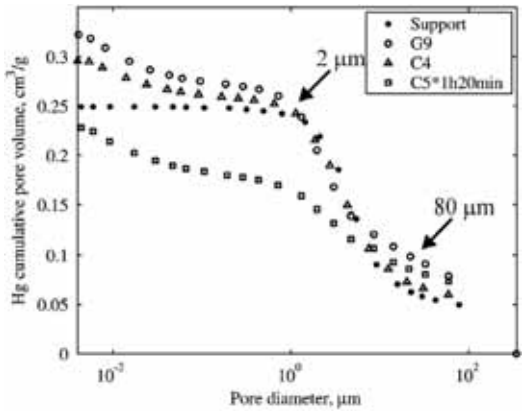

Fig. 7. Mercury intrusion pore volume distributions for the uncoated 400 cpsi cordierite monolith and the NaX film samples G9, C4, and C5∗1 h20 min.

(wall thickness about 100 μm). Sample C5∗1 h20 min shows a lower pore volume between 80 and 2 μm, which indicates that this film blocks the pores in the monolith walls for mercury intrusion, by pore filling, similarly to capillary condensation phenomena at a certain relative pressure, likely since this film is the thickest and thus blocks some of the macropores in the monolith wall. Below 2 μm, down to 7 nm (MIP detection limit) all film samples feature a similar cumulative pore volume, indicating open grain boundaries in the films, as observed by SEM and nitrogen adsorption/desorption results.

3.5. Characterization of breakthrough properties

3.5.1. Qualitative interpretation of CO_2 breakthrough profiles

Fig. 8a shows the CO_2 breakthrough curves measured at a volumetric flowrate of 0.2 l/min. The time to reach 50% of the final concentration occurred after about 28 s both for the empty column and the column loaded with an uncoated support, see also Table 2.

The shape of the breakthrough front is sharp and the breakthrough curves for the empty column and the uncoated substrate are almost completely overlapping. This indicates that the observed dispersion might not be due to the support but rather to dispersion in the tubing and valves of the system. Since the curves are overlapping, the widths of the breakthrough curves, defined as the difference between the time to reach 5% and 95% of the final concentration [44], were ca. 17 s, both for the empty column and the column loaded with the uncoated monolith substrates. This result indicates that the gas velocity is uniform in all the channels of the uncoated monoliths. The volume of the empty column and all pipes in the system is about 167 cm^3 and the geometrical volume of the monolith walls is as much as 41 cm^3 (25% of the empty system). The fact that the breakthrough curves for the empty column and the column loaded with an uncoated support overlaps, indicate that the breakthrough front is delayed by diffusion into the pores of the support resulting in dispersion in the breakthrough front. However, this dispersion is exactly counteracted by the acceleration of the breakthrough front that should be caused by the geometrical volume occupied by the monolith walls, which explains why the two breakthrough curves overlap.

The time to reach 50% of the final concentration occurred after about 33 s for sample C4, see Table 2. The time to reach 50% of the final concentration is linked to the adsorption capacity and also morphology of the sample. The time to reach 50% of the final concentration for sample C4 is almost the same as for a monolith without film, due to the very low adsorption capacity and low zeolite loading of this sample, as discussed earlier. The breakthrough curve for this sample is therefore not discussed further. On the other hand, the time to reach 50% of the final concentration is about 76 s and 136 s for samples C5∗1 h20 min and G9, respectively, see Table 2. These samples thus show a significant adsorption capacity, in accordance with the measured zeolite loading, as discussed above.

The breakthrough front for the film C5∗1 h20 min is characterized by a steep increase in the CO_2 concentration compared to the other sample, indicating an even flow distribution in the monolith channels.

The width (9 s) of breakthrough front of sample C5∗1 h20 min is even smaller than for the uncoated monolith (17 s). This indicates that for the C5∗1 h20 min sample, the flow pattern is close to ideal (virtually no axial dispersion) and that the resistance to mass transfer in the film is very low. MIP showed that the number of pores in the 1–100 μm range is smaller for the C5∗1 h20 min sample as compared to the uncoated monolith. The reduced macroporosity observed for the zeolite coated sample C5∗1 h20 min probably explains the reduced dispersion of the breakthrough front compared to the breakthrough front observed for the uncoated

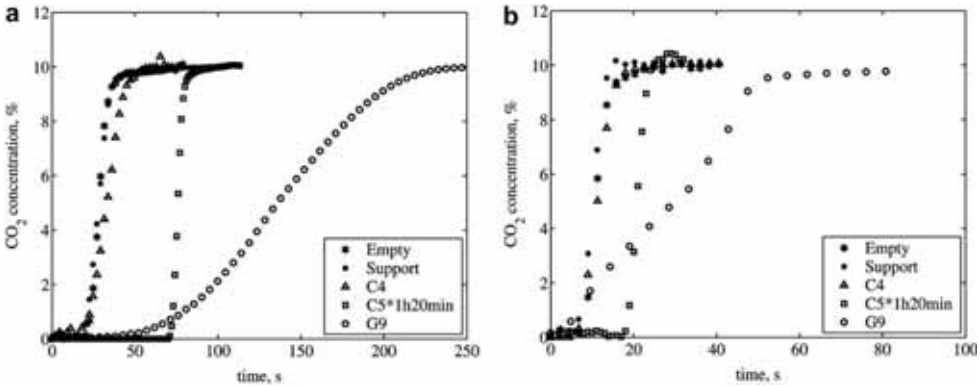

Fig. 8. CO_2 breakthrough profiles determined at 0.2 l/min (a) and 1 l/min (b) for the NaX film samples C4, C5∗1 h20 min, and G9.

Table 2
Summary of CO_2 adsorption properties extracted from breakthrough curves.

Flow rate: 0.2 l/min	Time to reach 50% of the final concentration (s)	Breakthrough width[a] (s)	k (1/s)	σ	D_{eff} (m^2/s)
Empty column	28.2	16.7	n.a.	n.a.	n.a.
Column loaded with support	28.5	17.0	n.a.	n.a.	n.a.
C4	32.7	17.2	n.a.	n.a.	n.a.
C5∗1 h20 min	75.7	9.0	5.2	0.05	4×10^{-12}
G9	135.8	146	0.072	0.03	1×10^{-13}

[a] Breakthrough width as defined as difference between time to reach 95% and 5% of final concentration [44].

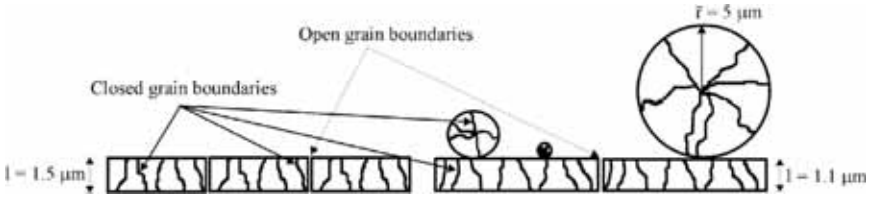

Fig. 9. Schematic representation of the samples C5∗1 h20 min and G9. Film thickness (l) and average sediments radius ($\bar{r}$) is given for sample C5∗1 h20 min or G9.

monolith. Narrower widths of the breakthrough fronts were also observed at 0.5 or 1 l/min for sample C5∗1 h20 min (ca. 7 or 6 s) than for the uncoated monolith (12 or 9 s), respectively.

The time to reach 5% of the final concentration is about half for sample G9 as compared to sample C5∗1 h20 min (72 s), although sample G9 shows the highest zeolite loading (0.064 g/g, see Table 1) and thus the highest adsorption capacity. The short time to reach 5% of the final concentration despite the high zeolite loading for sample G9 is most likely due to a gas velocity distribution across the monolith channels in this sample, due to sediments on top of the film, implying that the experimental curve originates from a convolution of different breakthrough fronts from different channels experiencing diverse flow rates. The width of the breakthrough profile is about 140 s for sample G9. The greater width of the breakthrough curve is an indication of higher resistance to mass transfer (in the sediments). As pointed out above, the main fraction of zeolite in this sample is in the form of relatively large sediments with long diffusion paths. Fig. 8b shows the carbon dioxide breakthrough profiles measured at 1 l/min. The curves show a similar trend as at 0.2 l/min, with the difference that the time to reach 5% of the final concentration is shorter and the width of the breakthrough curves are smaller due to faster saturation of the zeolite at the higher flow rate.

3.5.2. Quantitative interpretation of CO_2 breakthrough profiles

As described above, the results from SEM and liquid nitrogen adsorption/desorption suggest that the diffusion paths may be different in the NaX film samples studied in this work. Fig. 9 shows a schematic representation (not drawn to scale) of the film samples C5∗1 h20 min and G9, in concert with SEM and N_2 adsorption/desorption results. Sample C5∗1 h20 min consists of a 1.5 μm thick zeolite film of slabs of intergrown crystals with closed grain boundaries. The slabs are separated by some open grain boundaries and there are no sediments on top of the film. The diffusion length may be thus assumed to be the film thickness (l = 1.5 μm) and Eq. (6) should be used to estimate the effective diffusivity D_e from the mass transfer coefficient k.

Fig. 10a shows the experimental (points) and fitted (lines) CO_2 breakthrough curves of sample C5∗1 h20 min at different flow rates.

The model fit the experimental data of sample C5∗1 h20 min quite well with $\sigma = 0.05$ for a coefficient of mass transfer k of

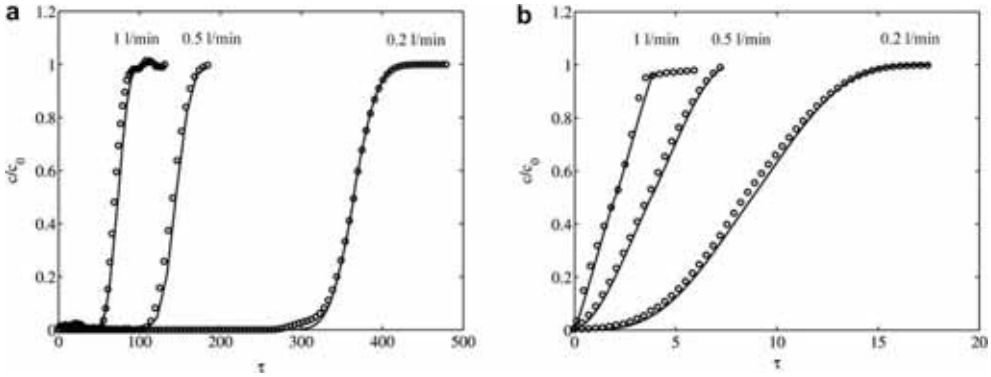

Fig. 10. Experimental (dotted lines) and approximated breakthrough curves of carbon dioxide of samples C5∗1 h20 min (a) and G9 (b) at 0.2, 0.5 and 1 l/min and 10% CO_2 in N_2.

5.2 s^{-1}, see Table 2. The corresponding effective diffusivity was estimated to 4×10^{-12} m^2/s using Eq. (6).

Literature data on the diffusivity of CO_2 in NaX is scarce and scatters significantly. Plant et al. [58] reported a diffusivity of 6×10^{-10} m^2/s, whereas data presented by Böhm et al. [59] and Bülow [45] indicated that the diffusion of CO_2 in NaX showed a complex behavior which was assigned to two superimposed steps with different rates. No attempts were made to deconvolute the different steps; however, the data presented by Bulow indicated that the overall diffusivity was significantly lower than 3×10^{-11} m^2/s which is in agreement with the diffusivity obtained in this work.

Fig. 10b shows the experimental and fitted CO_2 breakthrough curves for sample G9. Again, the model fit the experimental data of sample G9 quite well with $\sigma = 0.03$ for a coefficient of mass transfer k of 0.072 s^{-1}. This fitted mass transfer coefficient is 72 times smaller than the one for sample C5∗1 h20 min. This low mass transfer coefficient is likely an effect of the large diffusion length in the sediments on top of the film, which constitute the main fraction of this adsorbent as discussed above, and dominates the adsorption behavior of this sample. As pointed out above, the radii of the sediments is ranging from ca. 0.5 to 10 μm.

However, under the assumption that the sediments on sample G9 are spherical particles with an average radius of 5 μm, the diffusivity can be estimated from Eq. (7). The diffusivity of sample G9 is thus about 1×10^{-13} m^2/s and is thus about one order of magnitude lower than sample C5∗1 h20 min (4×10^{-12} m^2/s), see Table 2. This lower diffusivity in sample G9 may be a result of better intergrown crystals in the sediments of sample G9 compared to the crystals in the film of sample C5∗1 h20 min as discussed above. Even under the assumption that the sediments on sample G9 are spherical particles with an average radius of 10 μm (the maximum observed by SEM), the estimated diffusivity is about 5×10^{-13} m^2/s, which is still about one order of magnitude lower than for the film.

4. Conclusions

Well intergrown zeolite films with a limited amount of sediments and HS crystals were grown on 400 cpsi cordierite monoliths by using a clear solution and a multiple-step synthesis. Films grown in the clear solution in one longer hydrothermal treatment were less intergrown and sediments and large HS crystals were observed. Films grown in the gel were well intergrown but a large amount of sediments on top of the film was observed. The different morphologies of the zeolite films resulted in different adsorption performances as revealed from breakthrough experiments. The CO_2 breakthrough front for the film grown by a multiple-step procedure was very sharp and the adsorption capacity was significant, which is ideal for PSA applications. The experimental evidence in the present work will be important for the development of novel CO_2 adsorbents to use as a competitive alternative to traditionally used zeolite beads or extrudates.

References

[1] A.L. Chaffee, G.P. Knowles, Z. Liang, J. Zhang, P. Xiao, P.A. Webley, Int. J. Greenhouse Gas Control 1 (2007) 11–18.
[2] D.M. Ruthven, S. Farooq, K.S. Knaebel, Pressure Swing Adsorption, Wiley–VCH, 1993.
[3] P. Xiao, J. Zhang, P. Webley, L. Gang, S. Ranjeet, R.S. Todd, Adsorption 14 (2008) 575–582.
[4] J. Zhang, P. Webley, P. Xiao, Energy Convers. Manage. 49 (2008) 346–356.
[5] S.M. Auerbach, K.A. Carrado, P.K. Dutta, Handbook of Zeolite Science and Technology, Marcel Dekker Inc., New York, 2003.
[6] S. Cavenati, C.A. Grande, A.E. Rodrigues, J. Chem. Eng. Data 49 (2004) 1095–1101.
[7] A. Jayaraman, R.T. Yang, S.-H. Cho, T.S.G. Bhat, V.N. Choudary, Adsorption 8 (2002) 271–278.
[8] A. Khelifa, L. Benchehida, Z. Derriche, J. Colloid Interf. Sci. 278 (2004) 9–17.
[9] J.-S. Lee, J.-H. Kim, J.-T. Kim, J.-K. Suh, J.-M. Lee, C.-H. Lee, J. Chem. Eng. Data 47 (2002) 1237–1242.
[10] S.U. Rege, R.T. Yang, Ind. Eng. Chem. Res. 36 (1997) 5358–5365.
[11] K.S. Walton, M.B. Abney, M.D. LeVan, Micropor. Mesopor. Mater. 91 (2006) 78–84.
[12] A. Patton, B.D. Crittenden, S.P. Perera, Chem. Eng. Res. Des. 82 (2004) 999–1009.
[13] A. Cybulski, J.A. Moulijn, Structured Catalysts and Reactors, Marcel Dekker Inc., New York, 1998.
[14] Y.Y. Li, S.P. Perera, B.D. Crittenden, Chem. Eng. Res. Des. 76 (1998) 931–941.
[15] J.L. Williams, Catal. Today 69 (2001) 3–9.
[16] O. Ohrman, J. Hedlund, V. Msimang, K. Moller, Micropor. Mesopor. Mater. 78 (2005) 199–208.
[17] O. Ohrman, J. Hedlund, V. Msimang, K. Möller, J. Sterte, in: E. van Steen, L.H. Callanan, M. Claeys (Eds.), Proceedings of the 14th International Zeolite Conference, Cape Town, Studies in Surface Science and Catalysis, vol. 154, 2004.
[18] L. Li, B. Xue, J. Chen, N. Guan, F. Zhang, D. Liu, H. Feng, Appl. Catal. A: Gen. 292 (2005) 312–321.
[19] Y.Y. Li, S.P. Perera, B.D. Crittenden, Chem. Eng. Res. Des. 76 (1998) 921–930.
[20] O. Ohrman, J. Hedlund, J. Sterte, Appl. Catal. A: Gen. 270 (2004) 193–199.
[21] F. Brandani, A. Rouse, S. Brandani, D.M. Ruthven, Adsorption 10 (2004) 99–109.
[22] Y.Y. Li, S.P. Perera, B.D. Crittenden, J. Bridgwater, Powder Technol. 116 (2001) 85–96.
[23] V. Engström, B. Mihailova, J. Hedlund, A. Holmgren, J. Sterte, Micropor. Mesopor. Mater. 38 (2000) 51–60.
[24] J. Hedlund, J. Porous Mater. 7 (2004) 455–464.
[25] J. Hedlund, S. Mintova, J. Sterte, Micropor. Mesopor. Mater. 28 (1999) 185–194.
[26] R.B. Björklund, J. Hedlund, J. Sterte, H. Arwin, J. Phys. Chem. B 102 (1998) 2245–2250.

[27] M. Grahn, A. Lobanova, A. Holmgren, J. Hedlund, Chem. Mater. 20 (2008) 6270–6276.
[28] F. Jareman, J. Hedlund, Micropor. Mesopor. Mater. 82 (2005) 201–207.
[29] F. Jareman, J. Hedlund, J. Sterte, Sep. Purif. Technol. 32 (2003) 159–163.
[30] A. Mosca, J. Hedlund, F.N. Ridha, P. Webley, Adsorption 14 (2008) 687–693.
[31] Q. Li, D. Creaser, J. Sterte, Chem. Mater. 14 (2002) 1319–1324.
[32] K.E. Hamilton, E.N. Coker, A. Sacco, A.G. Dixon, R.W. Thompson, Zeolites 13 (1993) 645–653.
[33] H. Ahn, S. Brandani, AIChE J. 51 (2005) 1980–1990.
[34] H. Chang, X.-G. Yuan, H. Tian, A.-W. Zeng, Chem. Eng. Process. 45 (2006) 747–754.
[35] R.P. Ribeiro, T.P. Sauer, F.V. Lopes, R.F. Moreira, C.A. Grande, A.E. Rodrigues, J. Chem. Eng. Data 53 (2008) 2311–2317.
[36] L.C. Young, B.A. Finlayson, Adv. Chem. Ser. 13 (1974) 629–643.
[37] A. Klinkenberg, Ind. Eng. Chem. 46 (1954) 2285–2289.
[38] D.M. Ruthven, Principles of Adsorption and Adsorption Processes, John Wiley & Sons, New York, 1984.
[39] A. van Niekerk, J. Zah, J.C. Breytenbach, H.M. Krieg, J. Membr. Sci. 300 (2007) 156–164.
[40] D.W. Breck, Zeolite Molecular Sieves: Structure, Chemistry and Use, Krieger Publ. Company, 1984.
[41] M. Lassinantti Gualtieri, A.F. Gualtieri, J. Hedlund, Micropor. Mesopor. Mater. 89 (2005) 1–5.
[42] M. Milanesio, G. Artioli, A.F. Gualtieri, L. Palin, C. Lamberti, J. Am. Chem. Soc. 125 (2003) 14549–14558.
[43] A. Mosca, O. Öhrman, J. Hedlund, I. Perdana, D. Creaser, Micropor. Mesopor. Mater. 120 (2009) 195–205.
[44] T. Valdés-Solis, M.J.G. Linders, F. Kapteijn, G. Marbán, A.B. Fuertes, Chem. Eng. Sci. 58 (2004) 2791–2800.
[45] M. Bülow, Adsorption 8 (2002) 9–14.
[46] J.M. Zamaro, M.A. Ulla, E.E. Miró, Appl. Catal. A 314 (2006) 101–113.
[47] M. Lassinantti, J. Hedlund, J. Sterte, Micropor. Mesopor. Mater. 38 (2000) 25–34.
[48] C. Grande, A.E. Rodrigues, Chem. Eng. Sci. 61 (2006) 3053–3067.
[49] Rui P. Ribeiro, T.P. Sauer, F.V. Lopes, R.F. Moreira, C.A. Grande, A.E. Rodrigues, J. Chem. Eng. Data 53 (2008) 2311–2317.
[50] C. Grande, A.E. Rodrigues, Int. J. Greenhouse Gas Control 2 (2008) 194–202.
[51] F. Rezaei, P. Webley, Sep. Purif. Technol., doi:10.1016/j.seppur.2009.10.004.
[52] C.G. Coe, J.F. Kirner, R. Pierantozzi, T.R. White, Nitrogen Adsorption with a Divalent Cation Exchanged Lithium-X Zeolite, US Patent 5, 258,058 (1993).
[53] N.D. Hutson, S.U. Rege, R.T. Yang, AIChE J. 45 (1999) 724–734.
[54] J.C. Santos, P. Cruz, T. Regala, F.D. Magalhaes, A. Mendes, Ind. Eng. Chem. Res. 46 (2007) 591–599.
[55] M. Lassinantti, J. Hedlund, J. Sterte, Stud. Surf. Sci. Catal. 125 (1999) 181–187.
[56] C.-H. Lee, J. Yang, H. Ahn, AIChE J. 45 (1999) 535–545.
[57] H.S. Fogler, Elements of Chemical Reaction Engineering, Prentice Hall Inc., 2000.
[58] D. Plant, H. Jobic, P. Llewellyn, G. Maurin, Eur. Phys. J. Special Top. 141 (2007) 127–132.
[59] J. Böhm, B. Hunger, H. Papp, Stud. Surf. Sci. Catal. 158 (2005) 1113–1120.

PAPER D

Comparison of traditional and structured adsorbents for CO_2 separation by vacuum-swing adsorption

Authors:
F. Rezaei, A. Mosca, P. Webley, J. Hedlund, P. Xiao

Industrial & Engineering Chemistry Research 49 (2010) 4832 - 4841

Comparison of Traditional and Structured Adsorbents for CO_2 Separation by Vacuum-Swing Adsorption

Fateme Rezaei,[†] Alessandra Mosca,[‡] Paul Webley,*[,†] Jonas Hedlund,[‡] and Penny Xiao[†]

Department of Chemical Engineering, Monash University, Victoria 3800, Australia, and Division of Chemical Engineering, Luleå University of Technology, SE-97187 Luleå, Sweden

The development of structured adsorbents with attractive characteristics is an important step in the improvement of adsorption-based gas-separation processes. The improved features of structured adsorbents include lower energy consumption, higher throughput, and superior recovery and purity of product because of the even flow distribution, very low mass-transfer resistance, and low pressure drop in combination with a reasonable adsorption capacity. This study examines the vacuum-swing adsorption (VSA) CO_2 separation performance of structured adsorbents in the form of thin NaX films grown on the walls of ceramic cordierite monoliths, and the results are compared with NaX pellets. Adsorption equilibrium and dynamic properties are explored experimentally. The CO_2 breakthrough front for the NaX film grown on the 400 cells/in.^{2} (cpsi) monolith was close to ideal and indicated that axial dispersion was very small and that the mass-transfer resistance in the film was very low. The breakthrough front for the structured adsorbent with 400 cpsi was sharper than that for the structured adsorbent with 900 cpsi and only shifted to shorter breakthrough times because of the lower amount of zeolite and higher effective diffusivity of the former sample. In addition, the CO_2 breakthrough fronts for the 400 and 900 cpsi structured adsorbents were both sharper than the breakthrough front for NaX beads. This indicates that the flow distribution in the structured adsorbents is more even and that the mass-transfer resistance in the film is very low because of the small film thickness and high effective diffusivity for CO_2 in the NaX film. Experimental data were used to obtain overall mass-transfer linear-driving-force constants, which were subsequently used in a numerical simulation program to estimate the performance of the adsorbents for CO_2/N_2 separation in a VSA process. It was found that the recovery of structured adsorbents was superior to that of a packed bed because of the much shorter mass-transfer zone. The purity, on the other hand, was not as high as that obtained with a packed bed because of excessive voidage in the structured adsorbents. Increased cell density or improved zeolite loading of the structured adsorbents would improve the CO_2 purity without sacrificing recovery for the structured adsorbents, and this represents a path forward to improved VSA performance for CO_2 capture.

1. Introduction

Over the past decade, there has been considerable interest in the intensification of separation processes. In cyclic processes such as PSA, VSA, and TSA (pressure-, vacuum-, and temperature-swing adsorption, respectively), reducing the cycle time is the primary means of achieving more production from a given quantity of adsorbent. However, as the cycle time is reduced, cyclic processes usually face the problem of decreasing the working capacity per cycle for the component of interest, decreasing the product recovery, and increasing the pressure drop. The extent to which the cycle time reduces the working capacity and recovery and increases the pressure drop is dependent on the structure of the adsorbent.[1,2] Conventional adsorbents for gas separations are usually prepared in the form of beads or granules, and these materials are used in packed beds. The mass transfer and pressure drop associated with packed beds of conventional adsorbents impose limitations in operating the process at optimum conditions in terms of energy consumption and the overall system efficiency.

Recently, various structured adsorbents with enhanced adsorption characteristics such as monoliths, laminates, and foams have gained considerable attention as substitutes for conventional adsorbent particles.[3−15] A detailed review of these alternate structures and their merits was recently conducted by Rezaei and Webley.[1]

Parallel channel monolithic structures with controllable shape, cell density, and wall thickness have been reported for their use in adsorptive gas-separation systems.[3,5,6,8,16−19] The main advantage of such configurations resides in the low pressure drop and higher mass-transfer rates. Although it has been reported that the mass-transfer characteristics of monolithic adsorbents are somewhat inferior to those of a comparable packed bed, this is more a consequence of early monolithic structures with thick walls rather than any intrinsic limitation. Reduced channel width and wall thickness or production of a more appropriate cross-sectional flow profile may provide superior mass-transfer properties of monolithic adsorbents compared to packed beds.

Although the unique structure of monoliths (continuous body with identical channels) significantly reduces the common problems of conventional adsorbents (i.e., fluidization, high pressure drop, etc.), these structures often have low loading of the active adsorbent material per column volume because of high void volume. The active adsorbent may be presented to the flowing gas in two different ways. In the first approach, the active adsorbent material is directly extruded in the form of a structured monolith (commonly done for carbon monoliths). In the second approach, the monolithic structure is inactive but acts as a mechanical support for the adsorbent: usually a thin film is deposited on the monolithic structures by various methods, namely, dip coating, wash coating, and slip coating.[6,16]

* To whom correspondence should be addressed. Tel: +61 3 9905 3445. Fax: +61 3 9905 5686. E-mail: paul.webley@eng.monash.edu.au.
[†] Monash University.
[‡] Luleå University of Technology.

10.1021/ie9016545
Published on Web 04/12/2010

Table 1. Physical Properties of Structured Adsorbents C5400 and C5900

sample code	synthesis conditions	film thickness (μm)	weight gain (g/g_{sample})	surface area (m^2/g_{sample})	zeolite loading[a] ($g_{zeolite}/g_{sample}$)	mesopore volume[b] ($cm^3/g_{zeolite}$)
C5400	clear solution, 100 °C, five steps of 1 h and 20 min	1.5	0.036	18.02	0.025	0.08
C5900	clear solution, 100 °C, five steps of 1 h and 20 min	1.6	0.054	31.00	0.043	0.06
NaX beads	na	na	na	437	0.83	0.12

[a] From Brunauer−Emmett−Teller. [b] From the Barrett−Joyner−Halenda method.

Table 2. Dual-Site Langmuir Isotherm Parameters for CO_2 and N_2

structure	m_1 (mol/kg)	m_2 (mol/kg)	b_0 (1/kPa)	Q_1 (J/mol)	d_0 (1/kPa)	Q_2 (J/mol)
			CO_2			
C5400	0.0894	0.0966	2.86×10^{-7}	35 240.79	1.22×10^{-7}	29 676.35
C5900	0.1274	0.1546	3.98×10^{-8}	40 526.02	1.48×10^{-7}	29 512.72
NaX beads	2.5495	2.4139	7.40×10^{-7}	32 896.5	3.99×10^{-8}	32 998.2
			N_2			
C5400	0.0523	0	3.09×10^{-7}	17 644.1	0.00E + 00	0
C5900	0.0099	0.3544	2.42×10^{-5}	14 391.35	2.69×10^{-8}	21 785.65
NaX beads	0.004	2.6785	5.50×10^{-13}	59 282.86	1.26×10^{-6}	15 962.24

Alternatively, a film may be grown on the monolith, as explored by our research group.[20] For well-defined zeolite films, the mass-transfer resistance can be controlled by varying the film thickness.[21]

In our previous work,[22,23] we have prepared structured adsorbents in the form of 1.5 μm films of NaX zeolite grown on 400 cells/in.^{2} (cpsi) cordierite monolithic supports and evaluated the adsorption performance. Adsorption isotherms, pressure drop, and breakthrough data for the structured adsorbent were compared with those for conventional adsorbents in the form of NaX beads. The main conclusion from our previous work was that structured adsorbents with higher cell density than 400 cpsi are needed to better exploit the potential of these novel materials for PSA processes. In the present work, we report the preparation of structured adsorbents with 400 and 900 cpsi and a NaX film thickness of about 1.5 μm. Isotherm and breakthrough data were recorded experimentally for the materials. For the first time, the performance of these structured adsorbents in a VSA cycle was simulated, and the results were compared with those of conventional adsorbents.

2. Materials Development

Ceramic cordierite monoliths with cell densities of 400 and 900 cpsi (Corning Inc.) were used as supports for the growth of zeolite NaX films. The zeolite films were grown by a seeding method in a manner similar to that described in previous works.[22−24] Small FAU seeds were adsorbed electrostatically on the walls of the supports and were thereafter grown into zeolite films by hydrothermal treatment. This technique is very flexible and allows control of the thickness and a preferred orientation of the crystals in the film.[25−28] During the synthesis, the channels of the support were oriented vertically to reduce zeolite sedimentation from the bulk synthesis mixture on the walls of the substrate. A multistep procedure was used to grow the films. The hydrothermal treatment was carried out in five steps of 1 h and 20 min each. More details were reported previously.[22] The sample notation used here starts with the letter C for clear solution, followed by a number indicating the number of steps (five) and a number (400 or 900) indicating the cell density of the support; see Table 1.

The weight gain ($g_{zeolite}/g_{sample}$) was determined by weighing the support before and after the hydrothermal treatment. Products were characterized by scanning electron microscopy (SEM), N_2 adsorption and desorption at 77 K, and mercury-intrusion porosimetry (MIP).

Pure-component adsorption data for N_2 and CO_2 were measured at 0, 20, and 40 °C over the pressure range of 0−118 kPa. The films were also characterized by measuring the CO_2 breakthrough profile with step change experiments similar to those described in our previous work.[23] In these experiments, three coated monolithic samples, each 10 cm in length and 2 cm in diameter, were loaded into the adsorption column (30 cm in length and 2 cm in diameter). The samples were activated under a nitrogen flow of 0.2 L/min at 300 °C for 3 h with a heating and cooling rate of 2 °C/min. The samples were thereafter cooled to room temperature (26 °C). The breakthrough data were used to estimate the overall mass-transfer coefficient, k, for subsequent use in process cycle simulation. To determine the overall mass-transfer coefficient, a single breakthrough step was simulated using the numerical adsorption simulator (described below) with k as a variable.

3. Process Simulation

Simulations of a three-step VSA cycle with a packed bed of conventional adsorbents and the structured adsorbents were performed using the adsorption simulator MINSA (*M*onash *I*ntegrator for *N*umerical *S*imulation of *A*dsorption), which numerically solves the coupled partial differential equations of mass and energy balances using the finite volume method with flux limiters as described previously.[29,30] The linear-driving-force model was employed to model mass transfer. The pressure drop across the adsorbent beds was calculated using the Ergun equation for the case of a packed bed. The equations used in MINSA simulation (including valve equations) are given in Table 4. The simulator mimics the operation of an actual VSA process in that control valves regulate the flows to/from a bed according to desired end-of-step conditions (e.g., pressure, purity). It is important that an adequate number of finite volumes are used to calculate the breakthrough fronts to avoid numerical dispersion. The simulations conducted here were run with at least five nodes within the mass-transfer zone and an axial discretization level of 30 nodes (corresponding to a node spacing of 0.01 m), which was found to be adequate to resolve spatial profiles within the bed. The experimentally recorded adsorption

Table 3. CO_2 and N_2 Adsorption Capacity per Unit Volume of Structured (Samples C5400 and C5900) and Traditional Adsorbents (NaX Beads)

	adsorption capacity (mmol/cm^3)		
	C5400	C5900	NaX beads
CO_2(0 °C)	0.053	0.082	2.334
CO_2(20 °C)	0.041	0.072	2.001
CO_2(40 °C)	0.035	0.061	1.477
N_2(0 °C)	0.003	0.006	0.181
N_2(20 °C)	0.002	0.004	0.114
N_2(40 °C)	0.001	0.002	0.071

Table 4. List of Equations Used in the Simulation

mass balance equation

$$y\frac{\partial p}{\partial t}+p\frac{\partial y}{\partial t}=-\frac{\varepsilon_b T}{\varepsilon_t}\frac{\partial}{\partial z}\left(\frac{vpy}{T}\right)-\frac{\rho_b RT}{\varepsilon_t}\frac{\partial n_i}{\partial t}$$

adsorption kinetics

$$\frac{\partial n_i}{\partial t}=\frac{k_i l_0}{v_0}(n_i^{*}-n_i)$$

valve equations

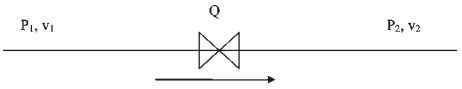

$$P_{1a}=\frac{p_1}{1.01325},\ P_{2a}=\frac{p_2}{1.01325}$$

$$q_s=\begin{cases}77.01C_v\sqrt{\dfrac{p_{1a}^2-p_{2a}^2}{S_g T}} & \text{if } P_{2a}>0.53P_{1a}\\ 65.31C_v p_{1a}\sqrt{\dfrac{1}{S_g T}} & \text{if } P_{2a}<=0.53P_{1a}\end{cases}$$

Table 5. Physical Properties of Adsorbents Considered for VSA Simulation

structure	wall thickness (μm)	channel width (μm)	bed density (g/cm^3)	bed voidage	LDF rate constant (1/s)	adsorbent mass (g)	zeolite voidage
C5400	100	1100	0.293	0.83	5	27.63	0.6
C5900	70	800	0.302	0.84	10	28.47	0.6
NaX beads			0.675	0.37	1	44.87	0.6

isotherms for CO_2 and N_2 over a range of temperatures were fit to a dual-site Langmuir isotherm. The fitted parameters were calculated according to the following equations:

$$n_i=\frac{m_1 b_i P_i}{1+b_i P_i+b_j P_j}+\frac{m_2 d_i P_i}{1+d_i P_i+d_j P_j} \quad (1)$$

$$b_i=b_{0i}\exp\left(\frac{Q_{1i}}{RT}\right);\quad d_i=d_{0i}\exp\left(\frac{Q_{2i}}{RT}\right) \quad (2)$$

A three-step VSA cycle of adsorption/desorption/repressurization was considered for evaluating the system performance (Figure 1). The initial and boundary conditions depend on the VSA cycle configuration. In our isothermal simulations, the boundary conditions for all of the steps were based on flow through a valve according to the valve equation. In addition, three target pressures were maintained at cyclic steady-state conditions, and because the valve settings were not known prior to the cycle run, a form of the PID algorithm (control loop) was also used to update boundary conditions (valve coefficients) from cycle to cycle to ensure that the end-of-step bed pressures and product purity from the model achieve the required set

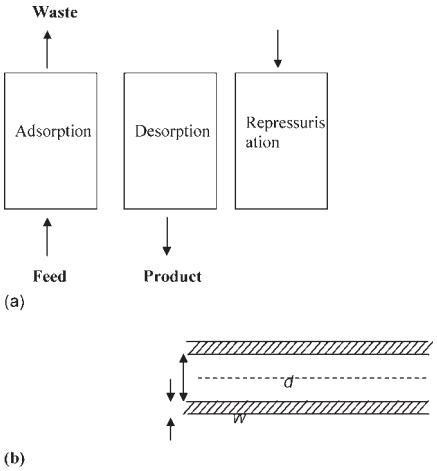

Figure 1. Three-step VSA cycle used to assess the performance of adsorbent structures (a) and a typical channel of the monolithic adsorbent (b).

points. In the first step, feed gas containing 10% CO_2/N_2 at different flow rates (0.2, 0.5, and 1 L/min) at 300 K and 1.2 bar pressure enters the bottom of the bed. The CO_2 front propagates through the bed and the nitrogen exits to the atmosphere through the top of the bed. The position of the CO_2 mass-transfer front at the end of this step is controlled by monitoring the concentration of CO_2 in the exit gas and adjusting the exit flow rate. In the second step, the bed is evacuated countercurrently and the bed pressure at the end of this step is controlled by adjusting the valve leading to the vacuum pump. In the third step, N_2 is used to repressurize the bed-to-feed pressure in a countercurrent direction. The CO_2 recovery and purity is calculated to characterize the VSA performance using different adsorbent structures. The CO_2 recovery is calculated as the number of moles of CO_2 recovered in the desorption step 2 divided by the number of moles fed to the bed in step 1. The CO_2 purity is determined as the number of moles of CO_2 recovered in step 2 divided by the total number of moles recovered in step 2. These simulations were performed to explore the behavior of the different adsorbent structures, in particular to judge the merits of structured adsorbents at short cycle times, which correspond to high flow rates. The physical properties of the adsorbents considered in the simulations are summarized in Table 5.

It is worth noting that the three-step cycle tested here is not indicative of the typical cycle that would be used in an industrial CO_2 capture plant.[31] However, the major steps of adsorption and desorption (regeneration) are captured, which is sufficient in order to demonstrate the impact of the adsorbent structure on the VSA performance. Thus, we expect the trends observed here to be similar for more complex cycles.

4. Results and Discussion

4.1. Materials Development. Figure 2 shows a cross-sectional image of the NaX beads. It is possible to identify the typical octahedral shape of the NaX crystals with a size up to a few micrometers. Figure 3a shows a top-view SEM image of sample C5400.[32] The film appears to be well intergrown, and typical NaX crystals with octahedral habit and with a size ranging from about 0.6 to 2 μm are observed. A few hydroxy-sodalite (HS) crystals with a typical ball-of-yarn habit and a

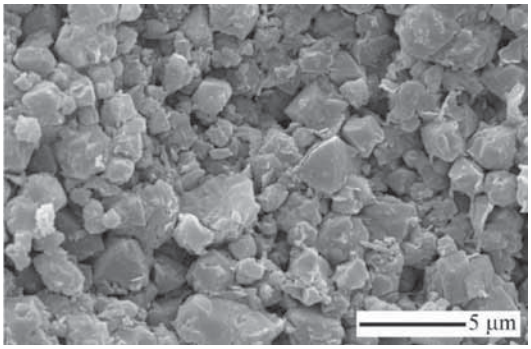

Figure 2. Top-view SEM image of NaX beads.

diameter of about 1 μm are also observed. The pores in HS zeolite are too small to allow any CO_2 adsorption. HS may form as a consequence of aluminum depletion[32] in the synthesis mixture during growth of zeolite X. Figure 3b shows a cross-sectional image of the NaX film grown on the 400 cpsi support. Again, the crystals in the zeolite film appear to be well intergrown, and the film has an average thickness of approximately 1.5 μm.

Figure 3c shows a top-view SEM image of sample C5900. The film appears to be quite similar to the film in sample C5400. However, the number and size of the HS crystals embedded in the zeolite film on the 900 cpsi support were reduced compared to the film on the 400 cpsi support. Cordierite contains aluminum, and HS formation is probably reduced by more aluminum leaching from the 900 cpsi support, which has a larger external area per volume of support than the 400 cpsi support. The average thickness of the zeolite film on the 900 cpsi support is about 1.6 μm, as shown in Figure 3d. Some zeolite crystals were also observed in the pores of the walls of both of the structured adsorbents; see Figure 4. The weight gains are 0.036 and 0.054 g/g_{sample} for samples C5400 and C5900, respectively; see Table 1. Thus, the weight gain is about 1.5 times higher for the latter sample. The geometrical external (wall) surface area per gram of sample of the 900 cpsi support is about 1.4 times higher than the 400 cpsi support, which accords well with the weight gain of the samples. The N_2 adsorption−desorption isotherms recorded at 77 K expressed as millimoles per gram of sample for the structured adsorbents and the NaX beads are shown in Figure 5a. The amount of nitrogen adsorbed increases in the order of C5400 < C5900 < NaX beads. The zeolite loadings estimated from N_2 adsorption data as in previous work[31] for the 400 and 900 cpsi structured adsorbents are, as expected, in approximate accordance with the measured weight gain; see Table 1. The zeolite loading of the NaX beads is equal to 0.83 g_z/g_{sample}[22] (see Table 1) and is about 33 and 20 times higher than those for samples C5400 and C5900, respectively.

The total mesopore volume per gram of zeolite is 0.08, 0.06, and 0.12 cm^3/g_z for C5400, C5900, and NaX beads, respectively; see Table 1. The mesopore volumes per gram of zeolite for the structured adsorbents are quite similar, which is expected because the films were grown by identical procedures. The mesopore volume per gram of zeolite of the NaX beads is in the same range of data as that reported in the literature (0.07 cm^3/g_z)[34] and is also similar to that for the structured adsorbents.

Figure 6a shows the cumulative pore volumes (cm^3/g_{sample}) determined by MIP of a 400 cpsi support and the structured adsorbent grown on the same support, sample C5400. The total MIP pore volume for the support is about 0.25 cm^3/g. The steep increase of the cumulative pore volume in the region between about 25 and 2 μm corresponds to the pores in the wall of the support. Compared to the 400 cpsi support, the total pore volume is similar for the 900 cpsi support; see Figure 6b. However, the size distribution of the pores in the wall is narrower for the latter support and shifted to somewhat smaller pore sizes, about 0.8−2 μm. The cumulative pore volume of the structured adsorbent sample C5900 almost overlaps with that of the corresponding support, as expected. However, the structured adsorbent sample C5400 displays pores in the range 0.01−1 μm, which are absent in the corresponding 400 cpsi support and in sample C5900. These pores should thus stem from the zeolite film in the structured adsorbent C5400 and may represent open grain boundaries and cracks in the film. A hypothesis is that these pores have formed as a result of the repeated (>10) activations at 300 °C in a flow of dry gas prior to breakthrough experiments of this sample. It is well-known that FAU zeolite crystals contract significantly upon dehydration,[38,39] which may result in the formation of cracks and open grain boundaries in the film. Sample C5900 has only been activated two times prior to breakthrough experiments and characterization by MIP.

Figure 7a shows the CO_2 isotherms measured at 0−40 °C expressed in millimoles per gram of sample of samples C5400 and C5900. For both samples, the CO_2 adsorption capacity is reduced at higher temperatures, as expected. For all temperatures, the CO_2 adsorption capacity per gram sample for sample C5400 is about half that for sample C5900, in agreement with the zeolite loading and weight gain discussed above. Figure 7b shows the CO_2 isotherm per gram of sample of the NaX beads. The CO_2 adsorption capacity per gram of sample of the beads is about 28 or 17 times higher than that for the structured adsorbents C5400 or C5900, in rough agreement with the zeolite loading. At all temperatures, the CO_2 adsorption capacity per unit volume of the adsorption column loaded with samples C5400 or C5900 is about 44 or 26 times lower than that for the packed bed; see Table 3. For all samples, dual-site Langmuir adsorption isotherms were fitted to the experimental CO_2 adsorption data, as shown in Figure 7a,b, and the fitted parameters are given in Table 2.

Figure 8a shows the N_2 adsorption isotherms measured at 0−40 °C expressed in millimoles per gram of sample for samples C5400 and C5900. Similarly as observed for CO_2 adsorption, the N_2 adsorption capacity of sample C5400 is about half that for sample C5900. Figure 8b shows the N_2 adsorption isotherms measured at 0−40 °C for NaX beads. At all temperatures, the N_2 adsorption capacity per unit volume of samples C5400 or C5900 is about 54 or 30 times lower than that for the packed bed. For all samples, the N_2 adsorption capacity per gram of sample is about 10 times lower than the CO_2 adsorption capacity, as expected for CO_2/N_2 adsorption on zeolite X.[36,37] Dual-site Langmuir isotherms were fitted to the experimental data, and the fitted parameters are given in Table 2.

The pressure drop (not shown here) for a column loaded with the NaX beads[22] is about 100 or 70 times higher than that when the column is loaded with the structured 400 and 900 cpsi adsorbents, respectively.

Figure 9a shows the CO_2 breakthrough curves for sample C5400. The time to reach 50% of the final concentration occurred after ca. 76, 35, or 21 s at flow rates of 0.2, 0.5, and 1 L/min, respectively. The sharp breakthrough fronts indicate that the flow pattern is close to ideal (virtually no axial dispersion) and that the resistance to mass transfer in the film is very low. Figure 9b shows the CO_2 breakthrough curves for

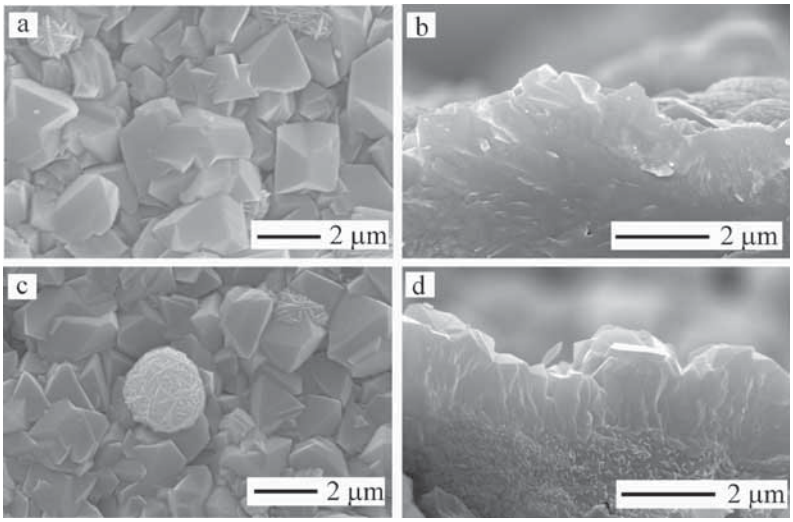

Figure 3. Top-view (a and c) and side-view (b and d) SEM images of a NaX film grown in five steps of 1 h and 20 min on 400 (a and b) and 900 (c and d) cpsi ceramic cordierite monoliths.

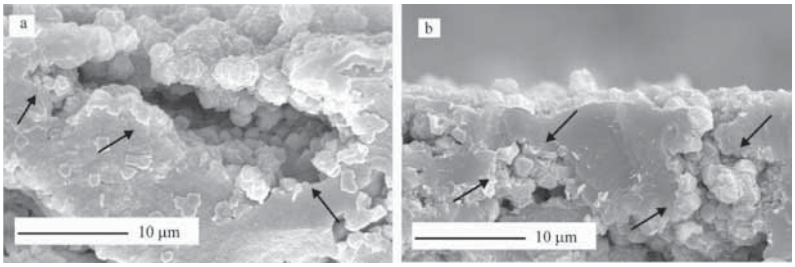

Figure 4. Side-view SEM images of NaX films grown on 400 (a) or 900 (b) cpsi cordierite monoliths.

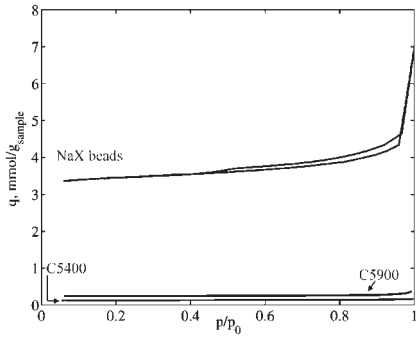

Figure 5. N_2 adsorption−desorption isotherms per gram of sample of the NaX film samples and NaX beads.

sample C5900. The time to reach 50% of the final concentration occurred after ca. 152, 82, or 62 s at flow rates of 0.2, 0.5, and 1 L/min, respectively. The time to reach 50% of the final concentration for sample C5900 is 2−3 times longer than that for sample C5400, as a result of the higher zeolite loading (1.8 times) per column volume for the former sample. The breakthrough front of sample C5900 is much broader than that for sample C5400 however, which is an indication of higher resistance to mass transfer or other features that contribute to dispersion (maldistribution, etc.) in the adsorbent. As pointed out above, 0.01−1 μm pores, likely open grain boundaries and cracks, were detected by MIP in the film in sample C5400 but not in sample C5900. These pores may contribute to mass transfer in the film in sample C5400, resulting in sharper breakthrough fronts.

Figure 9c shows the CO_2 breakthrough curves measured for NaX beads. The time to reach 50% of the final concentration occurred after ca. 630, 1390, or 2780 s for flow rates of 0.2, 0.5, and 1 L/min, respectively. The time to reach 50% of the final concentration for the NaX beads is about 10 or 30 times longer than that for sample C5900 or C5400, respectively, as a result of the higher zeolite loading (ca. 30 or 54 times) per column volume for the former sample. The breakthrough front of the NaX beads is broader than that of C5400 or C5900 and is an indication of a higher resistance to mass transfer because of the long diffusion path (radius of the beads).

It is worth discussing the impact of axial dispersion on the breakthrough data. The calculated *Re* numbers for flow in the channels of the structured supports are 4.4 (400 cpsi) and 2.7 (900 cpsi) at 1 L/min. These indicate laminar flow, and thus we expect Taylor dispersion to intrude on the breakthrough curve. An estimation of the extent of Taylor and axial dispersion on the total dispersion has been done in our previous study[2] in which we concluded that the influence of these factors on the overall dispersion is negligible. The dispersion observed for the

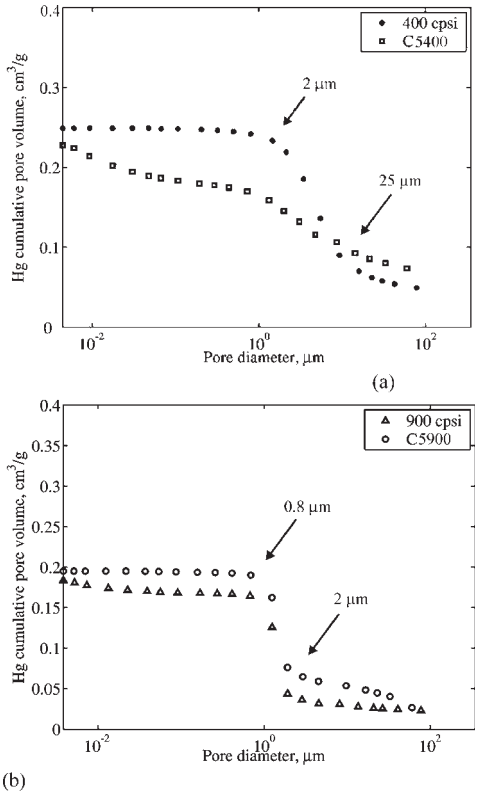

Figure 6. Mercury-intrusion pore-volume distribution for the NaX film samples.

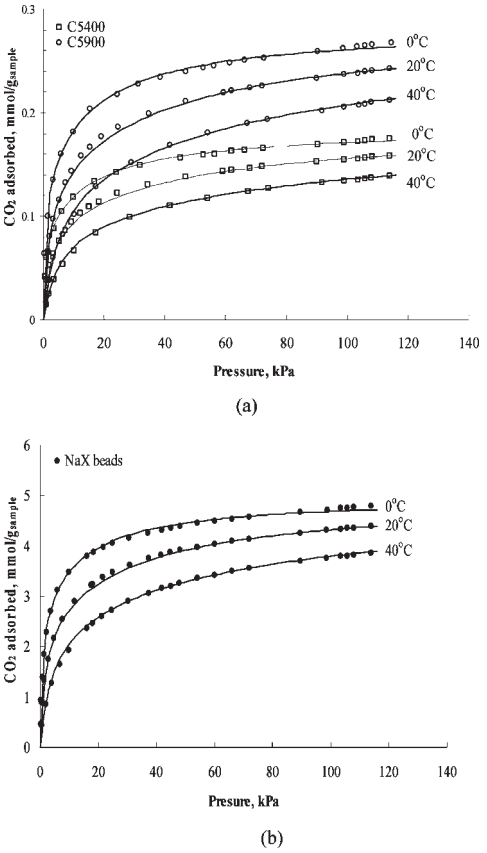

Figure 7. CO_2 isotherms per gram of sample at 0, 20, or 40 °C of NaX film samples (a) and NaX beads (b). C5400, C5900, and NaX beads are labeled by the symbols □, ○, and ●, respectively.

900 cpsi structured adsorbent can therefore be attributed to mass-transfer resistance or perhaps maldistribution of the gas into the channels. If a 900 cpsi structured adsorbent with mass-transfer resistance and flow distribution similar to the those of a 400 cpsi structured adsorbent could be prepared, it would represent a better or an "ideal" monolithic adsorbent. This "ideal" 900 cpsi adsorbent was simulated in the study described below.

4.2. Process Simulation Results. In order to ensure that the simulation parameters were chosen correctly and the simulations mimic the real system, benchmarking against the experimental breakthrough curves for sample C5400 was first performed. The overall mass-transfer coefficient k_{400} for the C5400 adsorbent was first determined by fitting of the breakthrough data; see Figure 10a. This figure illustrates that the model can describe experimental data adequately. Because the breakthrough data of the C5900 adsorbent were not indicative of an "ideal" adsorbent (as discussed above), we have chosen to simulate the "ideal" 900 cpsi adsorbent. The overall mass-transfer coefficient k_{900} for the ideal 900 cpsi adsorbent was estimated using our expression for monoliths developed earlier:[2]

$$\frac{1}{k_{900}} = \frac{d}{4k_f} + \frac{Wd\left[1 - \frac{1}{d+W}\left(\frac{d}{3} + \frac{W}{6}\right)\right]}{8D_e} \qquad (3)$$

where W and d are the wall thickness and channel width of the monolith (as depicted in Figure 1b), k_f is external gas film mass-transfer coefficient calculated from correlations presented earlier[2] for laminar flow in the monolithic channels, and D_e is the effective diffusivity. After estimation of the mass-transfer coefficient k_{900}, it was then employed in the simulations to model the breakthrough front of the ideal 900 cpsi adsorbent; see Figure 10b.

The process cycle time in semibatch-type processes such as PSA and VSA is an important parameter determining the adsorbent volume and total size of the adsorber. Shorter cycles, on the one hand, give rise to higher throughputs for the same amount of adsorbent; on the other hand, cycles which are too short may lead to insufficient time for adsorption because of mass-transfer limitations. To investigate the impact of the adsorbent geometry on the VSA performance at different cycle times, a series of simulations were conducted for a feed temperature of 27.7 °C and a feed pressure of 1.2 bar for a three-step cycle (Figure 1a).

The product purity is calculated as the ratio of CO_2 to total flow obtained in the desorption gas during step 2 of the cycle. Figure 11 shows that the product purity obtained with the packed beds is higher than that for the 900 and 400 cpsi structured adsorbents. This can be attributed to the higher voidage and lower zeolite loadings in the monolithic structures. The channel voids in the structured adsorbents lead to significant contamination of the product with N_2. Figure 11 also shows that for all

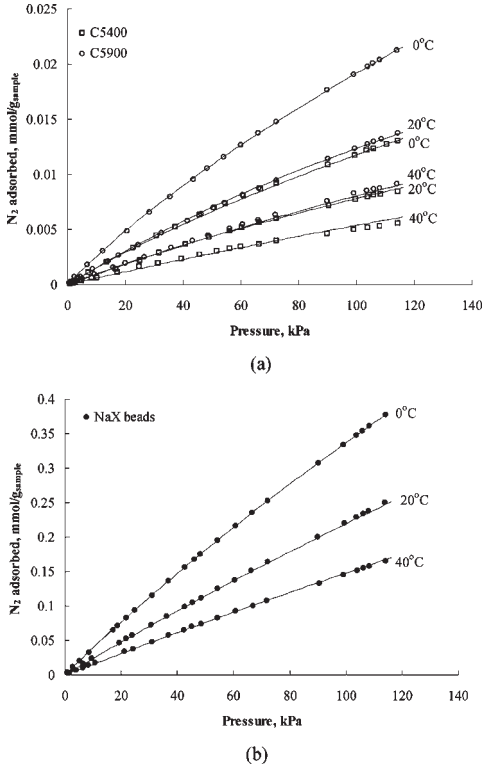

Figure 8. N_2 isotherms per gram of sample at 0, 20, or 40 °C of NaX film samples (a) and NaX beads (b). C5400, C5900, and NaX beads are labeled by the symbols □, ○, and ●, respectively.

cases a plateau value of the product purity is reached by increased cycle times. This is due to the reduction in the gas velocity resulting in a sharper mass-transfer front and hence improved CO_2 purity. The product purity for all adsorbents approaches the feed purity (10%) as the cycle time is decreased. When the cycle time is decreased below 120 s, the CO_2 purity undergoes a gradual decline in the case of monoliths, whereas a much larger decrease is experienced for the packed bed. This reduction is due to the pressure drop in the packed bed, which leads to broadening of the mass-transfer front and hence contamination of the top of the bed.

The CO_2 purity achieved by monolithic structures may imply that these configurations are not typically competitive with packed beds of pellets in the production of high-purity VSA CO_2. The trend toward taking the purity from a monolithic bed to the level of a packed bed could be driven by employing high-cell-density monoliths with thicker zeolite films (on the order of tens of micrometers) coated on the walls and proper voidage in order to compensate for the lower adsorbent loading and, hence, the lower product purity. In this study, our goal was not necessarily to achieve the required purity but rather to compare the monolith with the packed bed. The cycle used did not employ product purge; hence, we do not expect high purity in either the packed bed or monolithic configuration.

The product recovery is defined as the total amount of CO_2 recovered during step 2 (evacuation step) to the total CO_2 amount fed to the system. Figure 12 shows that the recovery obtained with the structured adsorbents is higher than that obtained with the packed bed. This is directly related to the

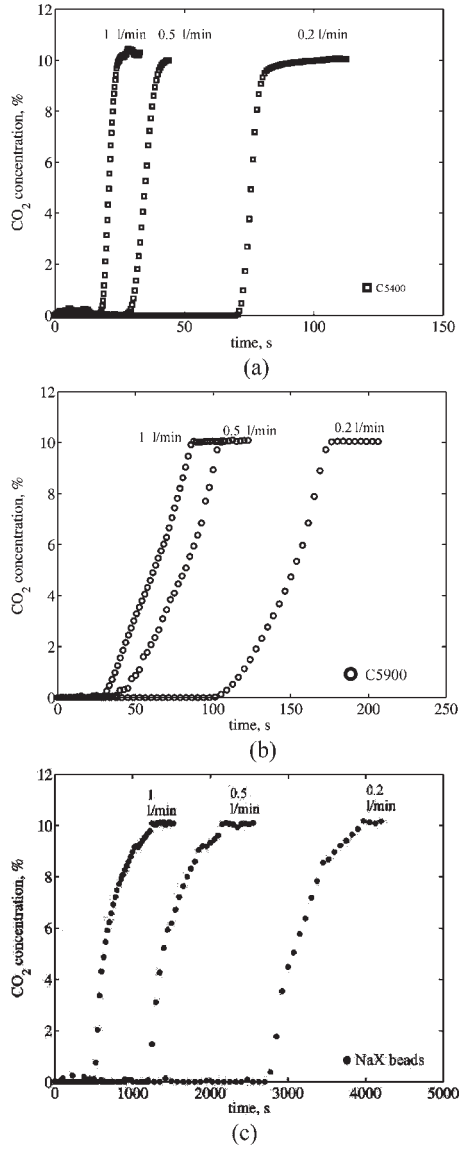

Figure 9. CO_2 breakthrough profiles determined at 0.2, 0.5, or 1 L/min for C5400 (a), C5900 (b), or NaX beads (c).

sharpness of the mass-transfer front during the feed step. The sharper front for the structured adsorbents results in less breakthrough of CO_2 during step 1 and therefore a higher recovery in the product stream. The CO_2 recovery is a function of the CO_2 working capacity (WC), which decreases as the cycle time decreases. As is evident from Figure 12, in the case of C5400 and C5900 adsorbents, decreases from 86% to 75% and from 90% to 80% occur respectively when the cycle time is decreased from 205 to 15 s, while in the case of 13X pellets, the recovery only reaches 80% for long cycle times. Longer cycle time gives higher purity and recovery because the lower resulting velocities lead to sharper mass-transfer zones. The recovery could be improved by replacing the three-step cycle with a more complex cycle incorporating product rinse and

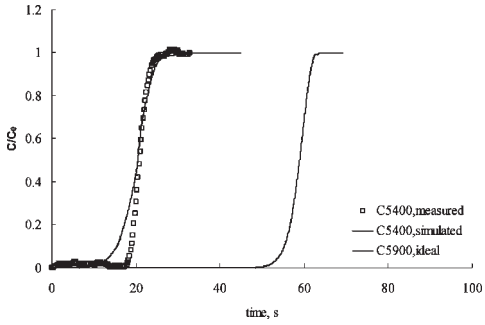

(a)

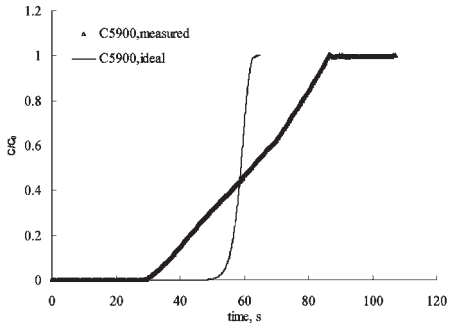

(b)

Figure 10. Comparison of the CO_2 breakthrough front of C5400 at 1 L/min with that of an ideal profile of sample C5900 (a). Comparison of the experimental and simulated CO_2 breakthrough fronts of sample C5900 (b).

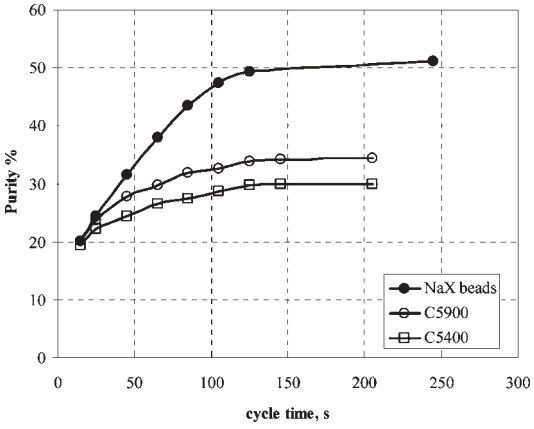

Figure 11. Product purity as a function of the cycle time for different adsorbents.

pressure equalization. However, the scope of the present work was not to optimize the system performance but rather to explore and illustrate the advantages and disadvantages of structured adsorbents versus conventional adsorbent beads.

The specific productivity (throughput) of the adsorbents at different cycle times is presented in Figure 13. The throughput attainable in a given volume of the vessel in a cyclic adsorption system may be expressed as

$$\text{through put (TPD)} \propto \frac{\text{gas production}}{\text{cycle} \times m_{ads}} \frac{\text{cycle}}{\text{day}}$$

$$\text{specific productivity} = f\frac{\text{WC}}{\tau}$$

where WC is the adsorbent working capacity (mol/$kg_{adsorbent}$/cycle), m_{ads} is the mass of the adsorbent, τ is the cycle time (s/cycle), and f is a proportionality constant. As expected, all three adsorbents displayed a hyperbolic pattern for productivity as a function of the cycle time, as suggested by the above equation. The throughput is highest for a packed bed because of the higher zeolite loading per unit volume. However, the structured adsorbents follow the expected inverse trend of productivity and cycle time more closely that the packed bed, also at very short cycle times. It is clear that dispersive effects of the pressure drop and mass transfer are becoming more important at shorter cycle times for the packed bed. Cycle times below 15 s eventually lead to a drop in the throughput for the packed bed, as observed in Figure 13 and also observed in our earlier studies.[31] Thus, the structured adsorbents show promising performance at short cycle times provided that higher zeolite loadings can be obtained.

Parts a−c of Figure 14 illustrate simulated pressure profiles of three adsorbents for a 25 s cycle time at $z = 0$ (inlet) and $z = 1$ (outlet). As is clearly shown, both types of monoliths showed identical profiles at the inlet ($z = 0$) and outlet ($z = 1$) of the adsorption column, indicating a negligible pressure drop along the

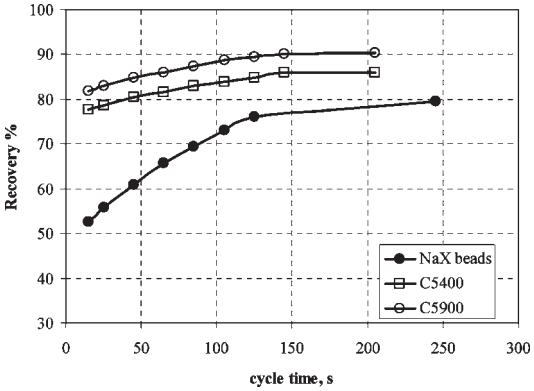

Figure 12. Product recovery as a function of the cycle time for different adsorbents.

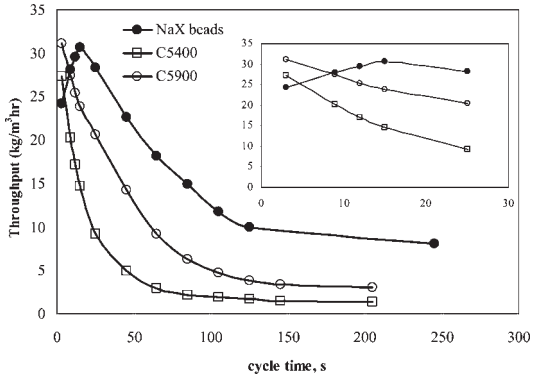

Figure 13. System productivity as a function of the cycle time for different adsorbents.

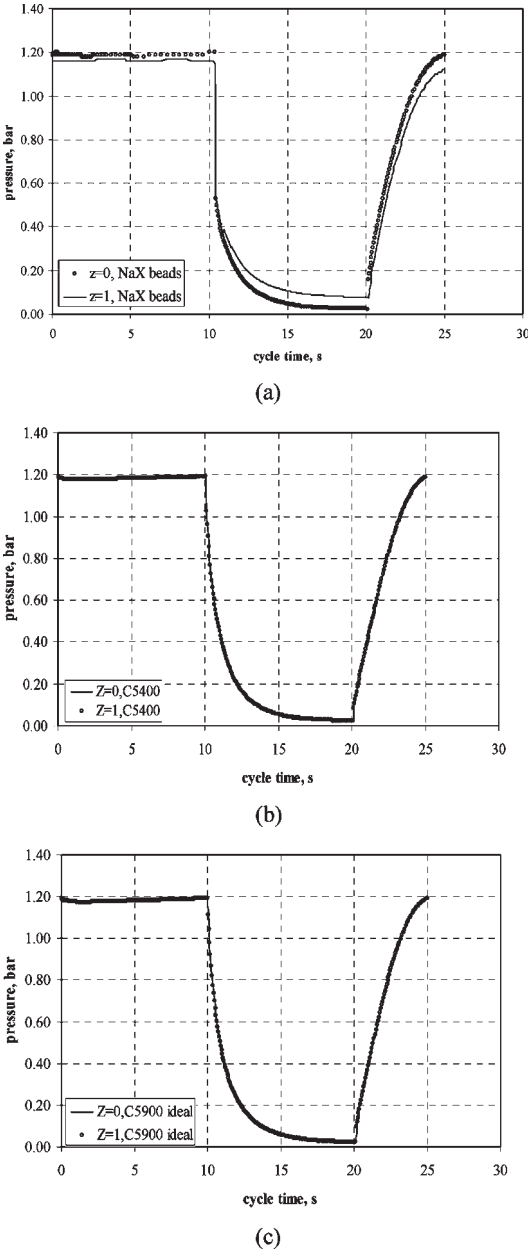

Figure 14. Simulated pressure histories for (a) 13X adsorbent, (b) C5400, and (c) C5900 as a function of the time during a single cycle at the top and bottom of the column.

bed; however, running a PSA cycle with a bed of granules gives rise to considerable pressure drop characterized by different curves at the inlet and outlet of the bed (Figure 14a).

5. Conclusion

Structured adsorbents were prepared by growing uniform NaX films on ceramic cordierite monoliths with the two different cell densities. The performance of the structured adsorbents in a VSA process for CO_2 capture was evaluated and compared with conventional adsorbent beads by mathematical modeling. We found that a CO_2 product purity of greater than 30% and a recovery of 90% is achievable with an ideal 900 cpsi monolithic adsorbent in a three-step VSA cycle. Although beads showed a better performance in terms of purity and throughput at longer cycle times, at shorter cycle times, structured adsorbents may show less effect of the pressure drop and hence lead to improved product recovery, purity, and throughput. In summary, our results indicate that structured adsorbents are good candidates for use in rapid cycles when the system performance is compromised by using conventional beads. It is clear, however, that every effort must be made to increase the zeolite loading without compromising the effective mass transfer. Our future work will examine the performance of adsorbent monoliths with higher cell density (1200 cpsi) with improved synthesis conditions in VSA processes.

Acknowledgment

The authors acknowledge the Monash Research Graduate School for providing scholarship support for F.R. and the Ph.D. Polis Project at Luleå University of Technology for supporting A.M.

Appendix

Notation

b_i = dual-site Langmuir isotherm constant
C_v = dimensionless structural parameter within the effective diffusion coefficient related to viscous flow
d_i = dual-site Langmuir isotherm constant
d = channel width, μm
D_e = effective diffusivity, cm^2/s
f = proportionality equation constant
k_{400}, k_{900} = total mass-transfer coefficient for 400 and 900 cpsi monoliths, 1/s
k_f = external gas film mass-transfer coefficients, cm/s
k_i = mass-transfer coefficient, 1/s
L_0 = parameter for rescaling z_{real}
m_i = dual-site Langmuir isotherm constant
n_i = dual-site Langmuir isotherm constant
n = adsorbent loading, mol/kg
n_i^* = equilibrium adsorbent loading, mol/kg
p = pressure, bar
P_{1a} = partial pressure of CO_2, bar
P_{2a} = partial pressure of N_2, bar
q_{1a} = flow rate of CO_2, m^3/h
q_{2a} = flow rate of N_2, m^3/h
Q_1 = heat of adsorption of CO_2, J/mol
Q_2 = heat of adsorption of N_2, J/mol
q_s = superficial flow rate, m^3/h
R = gas constant
S_g = gas entropy, J/mol·K
τ = cycle time, s
t = temporal coordinate, s
T = temperature, K
v_0 = parameter for rescaling v_{real}
v = interstitial velocity, m/s
W = channel wall thickness, μm
WC = working capacity
y = mole fraction
z = spatial coordinate, m
ρ_b = bulk density, kg/m^3
ρ_{gas} = density of gas, mol/m^3

ε_b = bed voidage
ε_t = total voidage

Literature Cited

(1) Rezaei, F.; Webley, P. A. Application of structured adsorbents in gas separation Processes. *Sep. Sci. Technol.* **2010**, *70*, 243.

(2) Rezaei, F.; Webley, P. A. Optimization of structured adsorbents for gas separation. *Chem. Eng. Sci.* **2009**, *64*, 5182.

(3) Kodama, A.; Goto, M.; Hirose, T.; Kuma, T. Experimental study of optimal operation for a honeycomb adsorber operated with thermal swing. *J. Chem. Eng. Jpn.* **1993**, *26*, 530.

(4) Maurer, R. T. Spiral-wound adsorber module. U.S. Patent 5,338,450, 1994.

(5) Gadkaree, K. P. System and method for adsorbing contaminants and regenerating the adsorber. U.S. Patent 5,658,372, 1997.

(6) Li, Y. Y.; Perera, S. P.; Crittenden, B. D. Zeolite monoliths for air separation, part 2: Oxygen enrichment, pressure drop and pressurization. *Chemical Engineering Research and Design* **1998**, *76* (A8), 931.

(7) Golden, T. C.; Golden, C. M. A.; Zwilling, D. P. Self-supporting absorbent fabric for gas separation. U.S. Patent 6,565,627, 2003.

(8) Brandani, F.; Rouse, A.; Brandani, S.; Ruthven, D. M. Adsorption kinetics and dynamic behavior of a carbon monolith. *Adsorption* **2004**, *10*, 99.

(9) Keefer, B. G.; Carel, A.; Sellars, B.; Shaw, I.; Larisch, B. Adsorbent laminate structures. U.S. Patent 6,692,626, 2004.

(10) Sawad, J. A.; Alizadeh-Khiavi, S.; Roy, S.; Kuznicki, S. M. High density adsorbent structures. W.I.P.O. Patent WO2005032694, 2005.

(11) Golden, T. C.; Golden, C. M. A.; Battavio, P. J. Multilayered adsorbent system for gas separations by pressure swing adsorption. U.S. Patent 6,893,483, 2005.

(12) Zabka, M.; Minceva, M.; Rodrigues, A. E. Experimental and modeling study of adsorption in preparative monolithic silica column. *Chemical Engineering and Processing* **2005**, *45* (2), 150.

(13) Grande, C. A.; Cavenati, S.; Barcia, P.; Hammer, J.; Fritz, H. G.; Rodrigues, A. E. Adsorption of propane and propylene in zeolite 4A honeycomb monolith. *Chem. Eng. Sci.* **2006**, *61*, 3053.

(14) Rode, E. J.; Boulet, A. J. J.; Pelman, A. M.; Babicki, M. L.; Keefer, B.; Sawada, J. A.; Alizadeh-Khiavi, S.; Roy, S.; Gibbs, A. C.; Kuznicki, S. M. Engineered adsorbent structures for kinetic separation. W.I.P.O. Patent WO200660743432, 2007.

(15) Grande, C. A.; Ribeiro, R. P. P. L.; Rodrigues, A. E. CO_2 capture from NGCC power stations using Electric Swing. *Energy Fuels* **2009**, *23*, 2797.

(16) Li, L.; Xue, B.; Chen, J.; Guan, N.; Zhang, F.; Liu, D.; Feng, H. Direct synthesis of zeolite coatings on cordierite supports by in situ hydrothermal method. *Appl. Catal., A* **2005**, *292*, 312.

(17) Lee, L. Y.; Perera, S. P.; Crittenden, B. D.; Kolaczkowski, S. T. Manufacture and characterisation of silicalite monoliths. *Adsorpt. Sci. Technol.* **2000**, *18*, 147.

(18) Yu, F. D.; Luo, L. A.; Grevillot, G. Adsorbption isotherms of VOCs onto an activated carbon monolith: Experimental measurement and correlation with different models. *J. Chem. Eng. Data* **2002**, *47*, 467.

(19) Yates, M.; Blanco, J.; Martin-Luengo, M. A.; Martin, M. P. Vapour adsorption capacity of controlled porosity honeycomb monoliths. *Microporous Mesoporous Mater.* **2003**, *65*, 219.

(20) Öhrman, O.; Hedlund, J.; Sterte, J. *Appl. Catal., A* **2004**, *270*, 193.

(21) Hedlund, J.; Öhrman, O.; Msimang, V.; Möller, K.; Steen, E. V. W.; Böhringer, W.; Sibya, S. The synthesis and testing of thin film ZSM-5 catalysts. *Chem. Eng. Sci.* **2004**, *59*, 2647.

(22) Mosca, A.; Hedlund, J.; Ridha, F. N.; Webley, P. Optimization of synthesis procedures for structured PSA adsorbents. *Adsorption* **2008**, *14*, 687.

(23) Mosca, A.; Hedlund, J.; Webley, P.; Grahna, M.; Rezaei, F. Structured zeolite nax coatings on ceramic cordierite monolith supports for PSA applications. *Microporous Mesoporous Mater.* **2009** doi:10.1016/j.micromeso.2009.10.010.

(24) Mosca, A.; Hedlund, J.; Öhrman, O.; Perdana, I.; Creaser, D. *Microporous Mesoporous Mater.* **2009**, *120*, 195.

(25) Engström, V.; Mihailova, B.; Hedlund, J.; Holmgren, A.; Sterte, J. The effect of seed size on the growth of silicalite-1 films on gold surfaces. *Microporous Mesoporous Mater.* **2000**, *38*, 51.

(26) Hedlund, J. Control of the preferred orientation in MFI films synthesized by seeding. *J. Porous Mater.* **2000**, *7*, 455.

(27) Hedlund, J.; Mintova, S.; Sterte, J. Controlling the preferred orientation in silicalite-1 films synthesized by seeding. *Microporous Mesoporous Mater.* **1999**, *28*, 185.

(28) Hedlund, J.; Jareman, F. Texture of MFI films grown from seeds. *Current Opinion in Colloid & Interface Science*; Elsevier: New York, 2005; Vol. 10, issues 5−6, pp 226−232.

(29) Webley, P. A.; He, J. Fast solution-adaptive finite volume method for PSA/VSA cycle simulation; 1 single step simulation. *Comput. Chem. Eng.* **2001**, *23*, 1701.

(30) Todd, R. S.; Ferraris, G. B.; Manca, D.; Webley, P. A Improved ODE integrator and mass transfer approach for simulating a cyclic adsorption process. *Comput. Chem. Eng.* **2003**, *27*, 883.

(31) Zhang, J.; Xiao, P.; Webley, P. A. Cycle development and design for CO_2 capture from flue gas by vacuum swing adsorption. *Environ. Sci. Technol.* **2008**, *42*, 563.

(32) Todd, R. S.; Webley, P. A. Mass-transfer models for rapid pressure swing adsorption simulation. *AIChE J.* **2006**, *52*, 3126.

(33) Breck, D. W. *Zeolite molecular sieves: structure, chemistry and use*; Krieger Publishing Company: Malabar, FL, 1984; p 771.

(34) Yamamoto, T. A.; Piluck, E. A.; Seong-Ick, K.; Takao, O. Preparation and characterization of cobalt cation-exchanged NaX zeolite as catalyst for wastewater treatment. *J. Ind. Eng. Chem.* **2007**, *137*, 1142.

(35) Ruthven, D. M. *Principles of Adsorption and Adsorption Processes*; John Wiley & Sons, Inc.: New York, 1984; p 243.

(36) Auerbach, S. M.; Carrado, K. A.; Dutta, P. K. *Handbook of zeolite science and technology*; Marcel Dekker, Inc.: New York, 2003; p 1204.

(37) Todd, R. S.; Webley, P. A. Mass-transfer models for rapid pressure swing adsorption simulation. *AIChE J.* **2006**, *52*, 3126.

(38) Caro, J.; Albrecht, D.; Noack, M. Why is it so extremely difficult to prepare shape-selective Al-rich zeolite membranes like LTA and FAU for gas separation. *Sep. Purif. Technol.* **2009**, *66*, 143.

(39) Noack, M.; Kolsch, P.; Dittmar, A.; Stohr, M.; Georgi, G.; Schneider, M.; Dingerdissen, U.; Feldhoff, A.; Caro, J. Proof of the ISS-concept for LTA and FAU membranes and their characterization by extended gas permeation studies. *Microporous Mesoporous Mater.* **2007**, *102*, 1.

Received for review October 24, 2009
Revised manuscript received January 30, 2010
Accepted March 4, 2010

IE9016545

PAPER E

The effect of wall porosity and zeolite film thickness on the dynamic behavior of adsorbents in the form of coated monoliths

Authors:
F. Rezaei, A. Mosca, J. Hedlund, P. Webley, M. Grahn, J. Mouzon

Submitted to Separation and Purification Technology

The effect of wall porosity and zeolite film thickness on the dynamic behavior of adsorbents in the form of coated monoliths

F. Rezaei [a,b], A. Mosca [a], J. Hedlund [a], P.A. Webley [b], M. Grahn [a], J. Mouzon [a]

[a]Div. of Chemical Technology, Luleå University of Technology, SE-97187, Luleå, Sweden

[b]Dept. of Chemical Engineering, Monash University, Clayton, VIC-3800, Australia

[*]Corresponding author. Tel.: +46 920 492986, Fax: +46 920 491199

E-mail: fateme.rezaei@ltu.se

Abstract

The effects of wall porosity, channel width distribution and zeolite film thickness on the performance of 400 and 1200 cells per square inch (cpsi) cordierite monoliths coated with zeolite X films with thicknesses of 1.5 and 2.5 μm were examined. To investigate the effect of wall porosity and restrict growth of zeolite to the external surface of the monolith channels, the macro pores in the walls of the 1200 cpsi cordierite monoliths were filled with colloidal α-alumina particles. The adsorbents were characterized by SEM, MIP and carbon dioxide breakthrough experiments and a mathematical model describing the diffusion and adsorption in the system was fitted to the data. The model accounted for carbon dioxide uptake by filling the pores in the support by carbon dioxide gas and adsorption of carbon dioxide on cordierite, alumina and zeolite. The model indicates that the uptake of carbon dioxide by adsorption on cordierite is much slower than by pore filling and too slow to influence the very fast breakthrough experiments with monoliths without zeolite film that are over in less than 1 minute. It was shown that the pores in the cordierite monolith result in dispersion by pore filling with carbon dioxide gas, not adsorption, and the model indicated that the use of monoliths with lower wall porosity would lead to less dispersion and thereby better performance of structured adsorbents. When the pores of the monolith were filled with alumina, the pore size was reduced and a lower diffusion coefficient for pore filling and some adsorption on α-alumina was observed as expected. The channel width distribution and the wall thickness distribution of the monoliths were very narrow and did not result in any broadening of the CO_2 breakthrough front. Monoliths were coated with films with thicknesses of 1.5 and 2.5 μm and significant adsorption capacity, roughly proportional to the film thickness, was observed. The CO_2 adsorption capacity of a 1200 cpsi monolith coated with a 2.5 μm film was 0.13 mmol/cm^3 adsorbent, which should be compared to the adsorption capacity of zeolite X beads, which is about 2.3 mmol/cm^3 adsorbent. To increase adsorption capacity of a non-porous zeolite coated monolith, film thickness could be increased. The model indicated that the film thickness could be increased up to about 10 μm without

increasing the dispersion and thereby approach the adsorption capacity for beads. However, simulation of the whole cycle must be performed in order to find the optimum film thickness for a real cyclic process. This work has lead to better understanding of the role of the support porosity and pore size distribution and film thickness for coated monolith adsorbents.

Keywords: Breakthrough front; Zeolite film thickness; Monolith wall porosity; CO_2 adsorption

1. Introduction

Novel adsorbents with superior characteristics compared to traditional adsorbents may improve adsorptive gas separation processes significantly. In cyclic adsorption processes, such as pressure swing adsorption (PSA) and temperature swing adsorption (TSA), reducing cycle time is the primary means of achieving a higher production. However, as cycle time is reduced, cyclic processes usually face several problems viz. decreased working capacity per cycle for the component of interest, decreasing product recovery and increasing pressure drop. The extent to which reduced cycle time reduces working capacity and recovery and increases pressure drop is highly dependent on the structure of the adsorbent [1].

The remarkable advantages of structured adsorbents in the form of parallel channel structures with controllable shape, cell density and wall thickness for their use in adsorption based gas separation systems have been reported by many researchers [2-9]. A detailed review of these alternate structures and their merits was recently conducted by Rezaei and Webley [1].

Although the unique structure of a parallel channel monolith (continuous body with identical parallel channels) significantly reduces the common problems of conventional adsorbents (*i.e.* fluidization, high pressure drop, etc.), adsorbents with this structure often have low loading of active adsorbent material per column volume because of the high void volume [10]. In monolith adsorbents, the active adsorbent may be presented to the flowing gas in two different ways. In the first approach, the active adsorbent material is directly extruded in the form of a parallel channel monolith as in carbon monoliths [11]. In the second approach, the parallel channel monolith only

acts as a mechanical support for a film of the adsorbent. Thin films may be deposited on supports by various methods, namely, dip-coating, wash-coating, or slip-coating [12]. Our group has developed a method for film growth on supports since 1995. The method was first described in a conference [13] and since then, films have been prepared and evaluated as membranes [14], sensors [15] catalysts [16] and adsorbents [17]. We have also explored the possibilities to grow films on monolith supports [18]. Increased thickness of the adsorbent film improves adsorbent capacity in one hand but increases the diffusion path length [16] on the other hand; hence optimization of these opposing variables is needed in order to find the most advantageous film thickness.

Among the considerable research work being reported so far on the development of monolithic adsorbents for gas separation applications, little attention has been paid to find the optimum structure. Although it is well-established that a monolith with high cell density and thin walls would result in better performance, the role of other important parameters such as monolith wall porosity and pore size distribution in the monolith on overall separation efficiency has rarely been investigated. For applications in which the adsorbent is fabricated by coating a layer of active adsorbent on the surface of the support, the thickness of the film is another important factor that needs to be taken into account while optimizing the process.

In our previous works [10,19,20] for zeolite coated monoliths with a cell density of 400 cpsi, one lumped mass transfer resistance was considered and the model proved successful for describing the kinetics of CO_2 adsorption. However, as we prepared and tested coated monoliths with cell densities exceeding 400 cpsi, it was evident from experimental data that the monolith support itself dispersed the gas flow significantly. The aim of the present work is therefore to experimentally and theoretically investigate the impact of monolith wall porosity, channel width distribution and zeolite film thickness on the dynamic behaviour of zeolite coated 400 and 1200 cpsi monolith adsorbents for CO_2 adsorption. A more detailed model, accounting for adsorption and mass transfer in both the zeolite film and the monolith wall was developed and fitted to the experimental data.

2. Experimental

2.1 Preparation of adsorbents

Cordierite monoliths with cell densities of 400 cpsi were obtained from Corning. Faujasite films with a thickness of about 1.5 μm were grown on these supports as described in detail previously [10,19,20]. In brief, faujasite crystals with a size of about 80 nm were first deposited in a monolayer on the monolith. In the next step, these crystals were grown to a continuous film with a thickness of about 1.5 μm using 5 synthesis steps in a clear synthesis solution with a molar composition of $73Na_2O:Al_2O_3:8SiO_2:4550H_2O$. Cordierite monoliths with a cell density of 1200 cpsi were obtained from NGK. To minimize wall porosity and growth of zeolite in the pores in the walls of the 1200 cpsi monoliths, these were impregnated with colloidal alumina particles prior to film growth. A slurry was first prepared by milling 58 wt% Al_2O_3 powder having a particle size of 0.4 μm (α-alumina A16-SG, Alcoa Chemical Co.), 39 wt% distilled H_2O and 3 wt% dispersant (Dispex® A40, Ciba) in a glass bottle with agate balls (zirconium oxide) for 2 h. The monolith was treated with cationic polymer solution [10,19,20] and then kept horizontally under rotation for 1 minute in the slurry. The excess slurry in the channels was then removed by flushing with a controlled air-flow. This procedure was repeated 3 times to obtain a homogeneous pore filling with alumina. The impregnated monolith was dried and then kept at 1200 ºC for 4 h, with a heating and cooling rate of 5 ºC/min, in order to increase the stability of the alumina, and to avoid redispersion of alumina particles during zeolite film growth. Films with a thickness of about 1.5 and 2.5 μm were grown on the 1200 cpsi monoliths using five or ten synthesis steps, respectively, in a similar way as for the 400 cpsi monoliths [10,19,20]. However, it was necessary to use a synthesis solution with higher alumina concentration to reduce the formation of zeolite P crystals that formed in this system, as a result of more extensive zeolite growth on the 1200 cpsi monoliths, which resulted in a depletion of aluminum in the synthesis mixture. The molar composition of this synthesis mixture was $73Na_2O:1.1Al_2O_3:8SiO_2:4550H_2O$. The sample codes used here for coated monoliths start with a

number (viz. 400 or 1200) indicating the cell density of the support, followed by letters Al in the case of 1200 cpsi monoliths describing the pore filling of monolith walls by alumina, and a number indicating the thickness of the zeolite coating.

2.2 Morphological characterization of adsorbents

The morphology of the adsorbents were characterized by scanning electron microscopy (SEM) with a Philips XL30 microscope, N_2 adsorption at 77 K using a Micromeritics ASAP2010 instrument, and mercury intrusion porosimetry (MIP) using a Micromeritics Autopore 9220V1.04 instrument. The weight gain ($g_{zeolite}/g_{sample}$) was determined by weighing the support before and after hydrothermal treatment. Image analysis of 100 low magnification SEM images recorded using a FEI Magellan 400 instrument, was used to estimate channel width and wall thickness distributions of monolith samples. Images were brought together in such a way that neither overlapping nor gap appeared between them.

2.3 Breakthrough experiments

The adsorbents were also characterized by measuring the CO_2 breakthrough profile with step change experiments similar to those described in our previous work [19]. In these experiments, three monolith samples, each 10 cm long and 2 cm in diameter were loaded in series in the adsorption column (30 cm long and 2 cm diameter). The samples were activated under a nitrogen flow of 0.2 l/min at 300 ºC for 3 hours with a heating and cooling rate of 2 ºC/min. The samples were thereafter cooled to room temperature (26 ºC).

3. Numerical simulation

In the model developed here for uncoated monoliths, gas transport in the monolith walls was modeled considering a single cylindrical channel with two layers accounting for half of the monolith channel and half of the channel wall (Figure 1 (a)). As the monolith supports were porous, some CO_2 will diffuse into these pores during the experiments thus representing a form of uptake by pore filling. In addition, CO_2 may be adsorbed onto the walls of the support as well as onto the alumina

particles present in the pores of the 1200 cpsi+Al sample. For zeolite coated monoliths, a model involving three layers, accounting for half of the monolith channel, the zeolite film and half of the channel wall with/without alumina particles, as depicted in Figure 1 (b) was used. As will be discussed below, the uptake in the zeolite film and in the monolith wall occur in parallel in the three-layer model. A simplified mathematical model considering axially dispersed plug flow was employed to describe the flow in the monolith. The component mass balance in the gas phase is given by

$$\frac{\partial C}{\partial t} - D_L \frac{\partial^2 C}{\partial z^2} + U \frac{\partial C}{\partial z} = -\left(\frac{1-\varepsilon}{\varepsilon}\right)\rho_s \frac{\partial \bar{q}}{\partial t} \qquad (1)$$

where C and $\bar{q}$ are the adsorbate concentration in gas and solid phases; U is the superficial fluid velocity; D_L is the axial dispersion coefficient, ε is monolith void fraction and ρ_s is adsorbent density. The component mass balance in the solid phase, *i.e.* the zeolite and/or alumina particles, is expressed by

$$\frac{\partial \bar{q}}{\partial t} = k_i\left(q^* - \bar{q}\right) \qquad (2)$$

where k_i is the mass transfer coefficient expressed by $k_i = {3D_i}/{l_i^2}$, D_i is the diffusivity and l_i is the characteristic diffusion length (zeolite film thickness and half wall thickness for the zeolite and alumina adsorption, respectively), where index $i=z$ refers to the zeolite film, index $i=w$ refers to monolith wall or for the 1200 cpsi+Al sample, monolith wall and alumina particles. To account for gas uptake due to pore filling in gas phase in the voids of the monolith wall, a modified version of equation (2) was used for the adsorbate mass balance in the monolith wall with D_p (p refers to pore filling) as variable and was taken as

$$\frac{\partial \bar{q}}{\partial t} = k_p a\left(C - \bar{C}\right) \qquad (3)$$

where $\overline{C}$ is adsorbate concentration in the pores of the monolith wall and a is the specific pore volume (pores in the wall) ($cm^3/g_{adsorbent}$) of the support. For the monolith samples, where CO_2 may both fill the pores of the support walls and be adsorbed onto the wall (and for the 1200 cpsi+Al sample also be adsorbed onto the alumina particles), a combination of equations (2) and (3) accounting for both pore filling and adsorption mechanisms was used to model the breakthrough fronts of the supports. For the samples coated with a zeolite film, simulation was then performed using the three-layer model where uptake was considered to take place in zeolite film, alumina particles (for supports filled with alumina) and in the voids of the support in parallel. Equation (2) was employed to calculate the component mass balance in zeolite film and as explained before, a combination of both equations (2) and (3) were used for mass balance in the support. The assumption that the uptake in the zeolite film and in the support (pore filling and adsorption by alumina) occurs in parallel is justified by the presence of open grain boundaries and cracks in the zeolite film as shown earlier [10,16,18-20]. In open grain boundaries and cracks, the diffusivity is much higher than in the zeolite pores, which should result in parallel uptake processes.

For the uncoated 400 cpsi and 1200 cpsi monoliths, pore filling was assumed to occur by molecular diffusion and the diffusion coefficient was estimated using the Chapman-Enskog equation. For the 1200 cpsi+Al sample, pore filling by Knudsen diffusion was assumed since the pore size between alumina particles was about 100 nm. For all samples k_w in equation 2 was then fitted to experimental data using equations 1-3. For the zeolite coated samples, the mass transfer coefficients k_w and k_p determined for the monolith walls previously were kept constant and k_z was determined by fitting the three-layer model to experimental breakthrough data for zeolite coated monoliths using equations 1-3.

The initial and boundary conditions for a breakthrough experiment are

$$C\,(t = 0) = 0,\ \overline{q}\,(t = 0) = 0,\ \overline{C}\,(t = 0) = 0, \tag{4}$$

$$C_0 + \left.\frac{\partial C}{\partial z}\right|_{z=0} = 0 \tag{5}$$

$$\left.\frac{\partial C}{\partial z}\right|_{z=L} = 0 \qquad (6)$$

The CO_2 adsorption in the zeolite film was assumed to follow a linear isotherm with the equilibrium constant, K, taken from the CO_2 adsorption isotherm at low pressures (up to 10 kPa) [21]. The program COMSOL 3.5a was used to fit k_i to the experimental breakthrough data. The conservation equations were solved using the Lagrange Quadratic Finite Element Method (LQFEM), with a total number of 6960 elements. To confirm that numerical dispersion was not affecting the results, the simulations were routinely tested with twice as many elements with no change in results.

The flow in each channel was modeled based on the channel width distribution determined by SEM. The interstitial velocity was considered constant along the channel and calculated based on the monolith porosity (as was estimated using the total number of channels for different cell densities and the volume occupied by channels) for a given superficial velocity.

4. Results and Discussion

4.1 Physical characterization

For monoliths, a broad channel width distribution will cause flow mal-distribution, as pointed out by Ahn and Brandani [22] and a wall thickness distribution introduces a range of diffusional time constants giving rise to a broader breakthrough front. To determine these distributions for our 1200 cpsi cordierite monoliths, low magnification SEM images were recorded and channel and wall widths were determined by image analysis. Figure 2 (a) shows the channel width distribution and Figure 2 (b) the wall thickness distribution. The results show that both channel width and wall thickness display quite narrow distributions. The average channel width is 701 μm with a standard deviation of 7 μm. The average wall thickness is 55.6 μm with a standard deviation of 2.7 μm. The channels and walls are thus very homogeneous in size and thickness, respectively. In Table 1, the geometrical properties corresponding to each sample are presented.

Figure 3 (a) shows a top-view SEM image of a 1200 cpsi cordierite monolith impregnated with alumina particles and heated to 1200 °C. The alumina coating consists of a layer of particles with an

average size of 400 nm. Most of the pores of the support are filled with alumina, as indicated by arrows in Figure 3 (b), which will suppress growth of zeolite in the pores of the support. This is quite important since growth of zeolite in the support pores would lead to long diffusion paths in the zeolite, which would result in reduced performance of the adsorbent.

Figure 4 (a) shows a top-view SEM image of a zeolite film grown on the impregnated 1200 cpsi cordierite monolith using five synthesis steps. The film appears to be rather well intergrown and zeolite X crystals with typical octahedral habit are observed. A few zeolite P crystals with a typical ball of yarn habit are also observed. Figure 4 (b) shows a cross-sectional image of the film grown using five synthesis steps, illustrating that the thickness of the zeolite film is about 1.5 μm. Figure 4 (c) and (d) show corresponding images of the film grown using ten synthesis steps. This sample appears similar as the one grown for five steps with the main differences that the observed crystals are larger and that the film thickness is about 2.5 μm. The cross sectional images illustrate that film growth is mostly occurring on the external surface of the alumina impregnated monoliths, which results in minimum diffusion paths in the zeolite. As we have shown before [20], growth of zeolite occurred in the macropores of the 400 cpsi sample.

Table 2 shows the weight gain, BET surface area and zeolite loading (determined from nitrogen adsorption data as in previous works [10, 20]) for all adsorbent samples. Mostly the weight gain is discussed here since these three parameters follow the same trend for all samples. The weight gain is caused by deposition of zeolite on the samples, which in turn leads to increased surface area and zeolite loading. The weight gain for the 400 cpsi monolith coated with a 1.5 μm film is comparable to the weight gain for the 1200 cpsi monolith coated with alumina and a 1.5 μm film. This illustrates that alumina is reducing growth of zeolite in the pores of the 1200 cpsi support, since a higher weight gain otherwise would be observed on the 1200 cpsi support, that has much more wall area available for zeolite growth than the 400 cpsi monoliths in accordance with SEM observations. The weight gain for the monoliths coated with 1.5 μm films is about half of the weight

gain for the 1200 cpsi monolith coated with alumina and a 2.5 μm film. The 1200 cpsi monolith coated with alumina and a 2.5 μm film has the highest weight gain of all samples due to the combination of a support with high cell density which gives larger surface accessible for film growth, and the greatest film thickness. Consequently, this adsorbent has the highest zeolite loading and BET surface area per g adsorbent. The BET surface area is as high as 41 m^2/g sample, which is about 10% of that for typical zeolite X beads used as adsorbents [20]. A structured adsorbent with its characteristic low pressure drop and even flow distribution as discussed earlier [20] with such a high specific surface area and short diffusion paths seems as a very promising adsorbent. Figure 5 shows derivative pore volumes (cm^3/g μm) determined by MIP of a 400 cpsi cordierite monolith, a 400 cpsi support coated with a 1.5 μm zeolite film, an uncoated 1200 cpsi cordierite monolith, a 1200 cpsi support impregnated with alumina, and for the samples coated with 1.5 and 2.5 μm NaX films. The figure shows that the uncoated 1200 cpsi monolith displays a peak at a pore diameter of about 3 μm. This peak is shifted to about 0.1 μm for the impregnated 1200 cpsi+Al monolith as a result of pore filling with alumina grains. The zeolite samples also display a peak at a pore size of about 0.1 μm, since the porosity of the support remains after growth of the zeolite film. The pore size for the 400 cpsi support and 400 cpsi+1.5μm sample were estimated to be respectively, 7.5 and 7 μm. The MIP data for all samples are summarized in Table 2. The steep increase of the derivative pore volumes in the region close to 100 μm corresponds to Hg intrusion in the channels of the supports.

The CO_2 adsorption capacities determined by adsorption measurements of zeolite coated monoliths are also presented in Table 2. As expected, the 1200 cpsi monolith coated with 2.5μm film displayed the largest loading (0.134 mmol/cm^3) which was about twice as large as the capacity of the samples coated with a 1.5μm film, in agreement with weight gain values and the discussion above.

4.2 Breakthrough experiments and numerical simulations

To study the effect of channel width distribution, simulations of the breakthrough curve for a 1200 cpsi monolith with a channel width distribution as measured, *i.e.* ranging from 691 to 711 μm,

were performed. The channel width distribution of monolith shown in Figure 2 (a) was discretized into three parts and the mean value for each of the three segments (693, 700, 708 μm, respectively) were employed in the simulation. The fractional areas for each of the three segments were 0.10 for the 691-695 μm range, 0.78 for the 695-705 μm range and 0.12 for the 705-711 μm range. The velocity is different for different channel widths; therefore, to calculate the velocity distribution corresponding to the determined channel width distribution, it was assumed that the pressure drop is constant over all channels and that the flow could be described with the Hagen-Poiseuille equation [23].

The volumetric flow distribution was calculated by solving three Hagen-Poiseuille equations simultaneously (one for each segment in the channel width distribution), with the restrictions that the pressure drop is equal in all channels and that the fraction of flow from each segment equals the fractions determined for the channel width distribution and that the sum of the volumetric flow rates calculated for each segment equals the volumetric flow rate in the experiment *i.e.* 1 l/min.

The average gas velocity for each segment in the channel distribution was then calculated from the Hagen-Poiseuille equation using this pressure drop and the average channel width for each segment. To assess the effect of the distribution in channel width, a breakthrough curve was simulated using the average gas velocity for each segment of the channel width distribution and the flow rate for each segment was weighted using the fractional areas determined for each segment. The simulations run were conducted using a feed gas containing 10% CO_2 with a flow rate of 1 l/min and the temperature was set to 27°C as in the experiments. Figure 6 illustrates the results and reveals that there is no significant difference between the breakthrough fronts and therefore the weighted-average breakthrough was selected to be fitted to experimental data. The figure confirms the effect of channel width distribution on broadening CO_2 front is trivial and therefore can be ignored, at least for the monoliths used here with very narrow channel width distributions.

The measured CO_2 breakthrough curves for the uncoated 400, 1200 cpsi and 1200 cpsi+Al monoliths at a volumetric flow rate of 1 l/min are displayed by points in Figure 7. Curves illustrate the fitted models and it is evident that the model can adequately describe the experimental observations. For the 400 cpsi monolith, CO_2 breaks through slightly before the 1200 cpsi monolith whereas for the 1200 cpsi+Al sample, breakthrough occurs somewhat later. The difference in breakthrough curves between the 400 and 1200 cpsi samples is captured in the model through different diffusion coefficients for pore filling D_p and pore filling capacity $\rho_s a C^*$, see Table 3 and 2, respectively. Moreover, the ratios between the contributions from adsorption and pore filling ($k_w q^*/k_p a C^*$) are 6×10^{-5} and 1×10^{-3} for the 400 and 1200 cpsi samples, respectively, see Table 3. This indicates that the contribution from adsorption on the monoliths was negligible for both samples and D_w can not be accurately fitted for these two samples. On the contrary, adsorption was found to significantly contribute to the breakthrough curve of 1200 cpsi+Al sample. Again, the breakthrough curve could be adequately described by the model. In this case, the ratio of adsorption and pore filling is 0.25. The additional adsorption capacity and the lower diffusion coefficient for pore filling D_p for the sample 1200 cpsi+Al are thus capturing the difference in break through curves for samples 1200 cpsi and 1200 cpsi+Al. D_p for the latter sample was taken as the Knudsen diffusivity since the pore size is about 0.1 μm and the mean free path of CO_2 at 300 K and 1 atm is approximately the same, indicating that the diffusion is mostly of Knudsen type.

The results show that for the supports not coated with alumina, the breakthrough behaviour may be explained by pore filling in the voids of the monolith walls whereas both pore filling and adsorption affects the breakthrough behaviour of the support treated with alumina. The parameters determined for the three monolith samples using the two-layer model were then used in the three-layer model for the zeolite coated monoliths.

For the non-coated monolith samples, the contribution from pore filling was much higher than that of adsorption on the monolith. This can be rationalized by the fact that pore filling is a fast

process as the breakthrough experiments for these samples, which are over in less than 1 minute. To the best of our knowledge there are no data on the structure of CO_2 adsorbed on cordierite, but under the assumption that the adsorption on cordierite follows the same mechanisms as for many metal oxides forming carbonate species on the surface [24], the adsorption of carbon dioxide on cordierite may be significantly slower than ordinary physisorption. The results presented here indicate that the uptake of carbon dioxide by adsorption on cordierite is much slower than by pore filling and too slow to influence the very fast breakthrough experiments with non-coated monolith samples and therefore the breakthrough curves for these samples may be adequately described with the pore filling contribution only.

The CO_2 breakthrough fronts of the zeolite coated monoliths are presented in Figure 8. There was a good fit between the three-layer model and experimental data for all samples. The breakthrough time is shortest for the 400 cpsi+1.5µm film followed by the 1200 cpsi+Al+1.5µm film and finally the 1200 cpsi+Al+2.5µm film, this trend is in agreement with the zeolite loading presented in Table 2. Again, the three layer model can describe the experimental observations adequately. The differences between the break through curves were captured in the model by differences in the parameters for the supports as described above and in addition, differences in zeolite film thickness. The fitted diffusivities for the zeolite films D_z are nearly constant, as expected, and in the range 2.7-4.1×10^{-12} m^2/s. As it was pointed out by Bülow [25], for CO_2-NaX systems, at least two mechanisms govern uptake and release of CO_2 by NaX crystals. Presupposed diffusion is extremely fast and superimposed diffusion is a very slow process compared to the first one. Literature data on the diffusivity of CO_2 in NaX is scarce and scatters significantly. Plant et al. [26] reported a diffusivity of 6×10^{-10} m^2/s, whereas data presented by Bülow [25] indicated that the diffusion of CO_2 in NaX was significantly lower than 3×10^{-11} m^2/s as we observed.

To investigate the impact of wall porosity, simulations were performed by keeping all parameters constant in the three layer model for the sample 1200 cpsi+Al+1.5µm film while varying

wall porosity from 0.0 to 0.7; the predicted break through fronts are shown in Figure 9. Keep in mind that the wall porosity for the real sample was 0.32. The results are in agreement with the discussion above as the dense support (ε_w=0.0) displayed the sharpest breakthrough front with longer breakthrough time, while the least dense monolith (ε_w=0.7) gave rise to the broadest front and a short breakthrough time. These results confirm our hypothesis that dense supports with lower porosity may improve both zeolite film synthesis and process performance of structured adsorbents in the form of coated monoliths.

In order to verify the effect of thickness of active material on the adsorption properties of the adsorbent, the zeolite film thickness in the model was varied from 1.5 microns to 30 microns while the other parameters were kept as for a 1200 cpsi monolith with zero wall porosity. Figure 10 shows that by increased film thickness, the CO_2 breakthrough time increases as expected due to the higher zeolite loading. Further, film thicknesses larger than 10 μm results in broadening of the CO_2 front due to an increased diffusion path. However, the gain in capacity with larger film thicknesses than 10 μm may well completely offset the loss due to mass transfer. To examine this trade-off, it is necessary to perform cyclic adsorption runs as a function of cycle time to find the optimal thickness; such study will be discussed in a separate paper. Based on single breakthrough runs, our results indicate that 10 μm is a safe margin thickness for a zeolite film grown on a nonporous 1200 cpsi monoliths support. As discussed above, the CO_2 adsorption capacity of a 1200 cpsi monolith coated with a 2.5 μm film was 0.13 mmol/cm^3 adsorbent. If the film thickness is increased to 10 μm, the adsorption capacity would increase to about 0.5 mmol/cm^3 adsorbent which is about 25% of the adsorption capacity of zeolite X beads. A structured adsorbent, with such a high adsorption capacity, low pressure drop and sharp breakthrough front seems as a very competitive adsorbent. We aim to prepare and investigate such samples in the nearby future.

5. Conclusions

Experimental and theoretical studies were conducted in order to evaluate the performance of structured zeolite adsorbents, consisting of well intergrown zeolite films on cordierite monoliths. Attention was given to the effects of monolith support parameters (*i.e.* wall porosity, diffusivity, channel width distribution) and zeolite film thickness on the adsorption performance. The present work has shown that the adsorption capacity of zeolite coated monoliths with high cell density can approach that of zeolite beads. The importance of support porosity on adsorption performance has been illustrated and the advantage of zeolite coated monoliths with low wall porosity for gas separation processes has been demonstrated for the first time. This work has also shown that although a thicker zeolite film increases adsorption, a too thick film compromises the adsorption kinetics resulting in a broader front. Simulations indicated that a zeolite X film with a thickness of 10 μm is optimal for a nonporous 1200 cpsi monolith for CO_2 adsorption. More experimental and theoretical studies are required to confirm these results.

Acknowledgment

The authors would like to acknowledge the Monash Research Graduate School (MRGS) for providing scholarship support for Fateme Rezaei. The Knut and Alice Wallenberg foundation is acknowledged for financially supporting the Magellan SEM instrument. Jonas Hedlund is acknowledging Bio4energy for financial support.

References

[1] F. Rezaei, P. Webley, Sep. Purif. Technol. 70 (2010) 243-256.

[2] D.M. Ruthven, C. Thaeron, Gas Sep. Purif. 10 (1996) 63-73.

[3] Y.Y. Li, S.P. Perera, B.D. Crittenden, Chem. Eng. Res. Des. 76 (1998) 921-930.

[4] F. Rezaei, P. Webley, Chem. Eng. Sci. 64 (2009), 5182-2191.

[5] T.C. Golden, C.M.A. Golden, D.P. Zwilling, European Patent, US6565627, (2003).

[6] K.P. Gadkaree, Carbon 36 (1998) 981-989.

[7] Y.Y. Li, S.P. Perera, B.D. Crittenden, Chem. Eng. Res. Des. 76 (1998) 931-941.

[8] F. Brandani, A. Rouse, S. Brandani, D.M. Ruthven, Adsorption 10 (2004) 99-109.

[9] M. Zabka, M. Minceva, A.E. Rodrigues, Chem. Eng. Process- Process Intens. 45 (2006) 150-160.

[10] A. Mosca, J. Hedlund, P. Webley, M. Grahn, F. Rezaei, Micropor. Mesopor. Mater. 130 (2010) 38-48.

[11]Y. Li, S. Perera, and B. Crittenden, Chem. Eng. Res. Des. Transactions of the Institute of Chemical Engineers, Part A 76 (1998) 921- 930.

[12] L. Li, B. Xue, J. Chen, N. Guan, F. Zhang, D. Liu, H. Feng, Appl. Catal. A: Gen. 292 (2005) 312-321.

[13] J. Hedlund, B.J. Schoeman, J. Sterte, Book Series: studies in surface science and catalysis 105 (1997) 2203-2210.

[14] J. Hedlund, J. Sterte, M. Anthonis et al., Micropor. Mesopor. Mater. 52 (2002) 179-189.

[15] M. Grahn, Z. Wang, M. Lidstrom-Larsson, A. Holmgren, J. Hedlund, J.sterte, Micropor. Mesopor. Mater. 81 (2005) 357-363.

[16] J. Hedlund, O. Öhrman, V. Msimang, E.V. Steen, W. Böhringer, S. Sibya, K. Möller, Chem. Eng. Sci. 59 (2004) 2647-2657.

[17] R.B. Bjorklund, J. Hedlund, J. Sterte, H. Arwin, J. Phys. Chem. B 102 (1998) 2245-2250.

[18] O. Öhrman, J. Hedlund, J. Sterte, Appl. Catal. A Gen. 270 (2004) 193-199.

[19] A. Mosca, J. Hedlund, F.N. Ridha, P. Webley, Adsorption 14 (2008) 687-693.

[20] F. Rezaei, A. Mosca, P. Webley, J. Hedlund, P. Xiao, Ind. Eng. Chem. Res. 49 (2010), 4832-4841.

[21] S.H. Hyun, R.P. Danner, J. Chem. Eng. Data 27 (1982) 196-200.

[22] H. Ahn, S. Brandani, Adsorption 11 (2005) 473-477.

[23] A. Cybulski, J.A. Moulijn, Structured Catalysts and Reactors, New York: Marcel Dekker, 1998.

[24] J. Baltrusaitis, J. Schuttlefield, E. Zeitler, V.H. Grassian, Chem. Eng. J. doi:10.1016/j.cej.2010.12.041.

[25] M. Bülow, Adsorption 8 (2002) 9-14.

[26] D. Plant, H. Jobic, P. Llewellyn, G. Maurin, Eur. Phys. J. Special Top. 141 (2007) 127-132.

Notation

a specific saturation volume, $cm^3/ g_{adsorbent}$

C	bulk concentration, mole/cm^3
$\overline{C}$	gas concentration in voids of monolith wall, mole/cm^3
D_L	axial diffusion coefficient, cm^2/s
D_p	pore diffusivity, cm^2/s
D_w	monolith wall diffusivity, cm^2/s
D_z	zeolite film diffusivity, cm^2/s
k_i	solid mass transfer coefficient, 1/s
k_p	pore mass transfer coefficient, 1/s
l_i	diffusion length, cm
$\overline{\mathrm{q}}$	average adsorbent loading, mole/g $_{\text{adsorbent}}$
q^*	equilibrium adsorbent loading, mole/g $_{\text{adsorbent}}$
t	time, s
U	velocity, cm/s
z	axial length, cm
ρ_s	adsorbent density, g/cm^3
ε	pore voidage

List of Tables

Table 1.

Sample code	Channel width, (μm)	Wall thickness, (μm)	Wall porosity,[d] (%)
400 cpsi	1100.0[b]	100[b]	24.7
1200 cpsi	701.0 [a]	55[a]	27.8
1200 cpsi +Al	701.0[c]	55[c]	24.2
400 cpsi+1.5μm film	1098.5[c]	100[c]	25.7
1200 cpsi+Al+1.5μm film	699.5[c]	55[c]	23.3
1200 cpsi+Al+2.5μm film	698.5[c]	55[c]	23.3

[a] from image analysis, [b] from SEM, [c] estimated, [d] from MIP

Table 2.

Sample code	Weight gain, ($g_{zeolite}/g_{sample}$)	BET surface area, (m^2/g_{sample})	Zeolite loading,[a] ($g_{zeolite}/g_{sample}$)	Pore filling capacity, $\rho_s a C^*$, (mmol/cm^3)	Adsorption capacity,[b] (mmol/cm^3)	MIP pore volume (cm^3/g_{sample})	MIP pore Size (μm)
400 cpsi	-	2.23	-	1.13×10^{-3}	-	0.25	7.5
1200 cpsi	-	2.02	-	2.23×10^{-3}	-	0.17	3.0
1200 cpsi +Al	-	2.27	-	2.02×10^{-3}	-	0.15	0.1
400 cpsi+1.5 μm film	0.036	18.02	0.025	-	0.053	0.22	7.0
1200 cpsi+Al+ 1.5μm film	0.040	23.53	0.030	-	0.069	0.21	0.1
1200 cpsi+Al+ 2.5μm film	0.080	40.75	0.060	-	0.134	0.18	0.1

[a] from BET, [b] from CO_2 adsorption measurement

Table 3.

Sample code	D_p, (m^2/s)	D_{w},[a] (m^2/s)	D_z, (m^2/s)	k_i, (s^{-1})	$k_i q^*/k_p a C^*$
400 cpsi	1.4×10^{-5}	4.0×10^{-12}	-	-	5.7×10^{-5}
1200 cpsi	5.8×10^{-6}	7.6×10^{-12}	-	-	9.6×10^{-4}
1200 cpsi +Al	2.5×10^{-7}	3.7×10^{-11}	-	-	0.25
400 cpsi+1.5μm film	1.4×10^{-5}	4.0×10^{-12}	4.1×10^{-12}	5.50	-
1200 cpsi+Al+1.5μm film	5.8×10^{-6}	7.6×10^{-12}	3.9×10^{-12}	2.70	-
1200 cpsi+Al+2.5μm film	2.5×10^{-7}	3.7×10^{-11}	2.7×10^{-12}	1.30	-

[a] Could not be fitted accurately due to very low adsorption rate

List of Figures

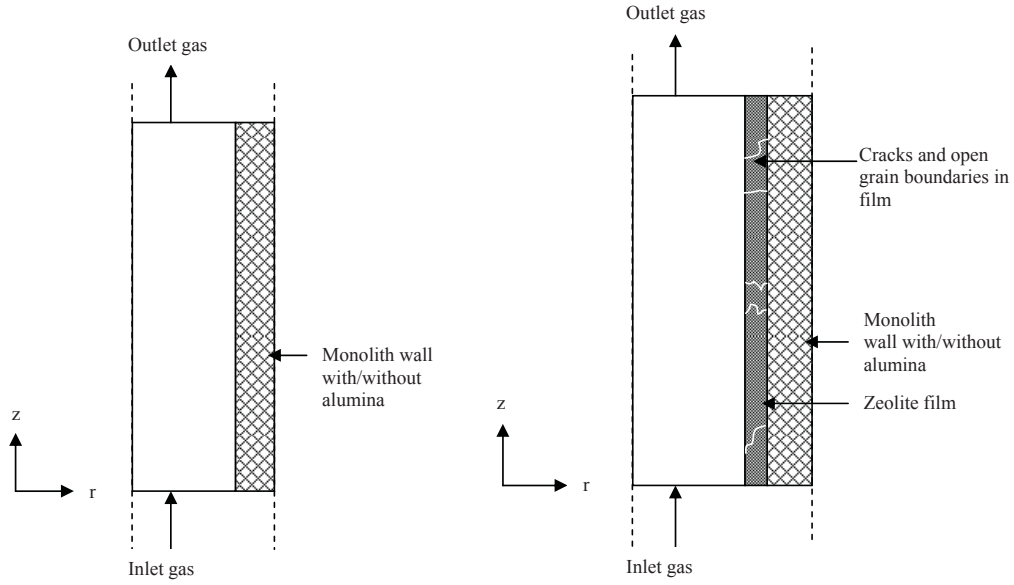

(a) **(b)**

Figure 1.

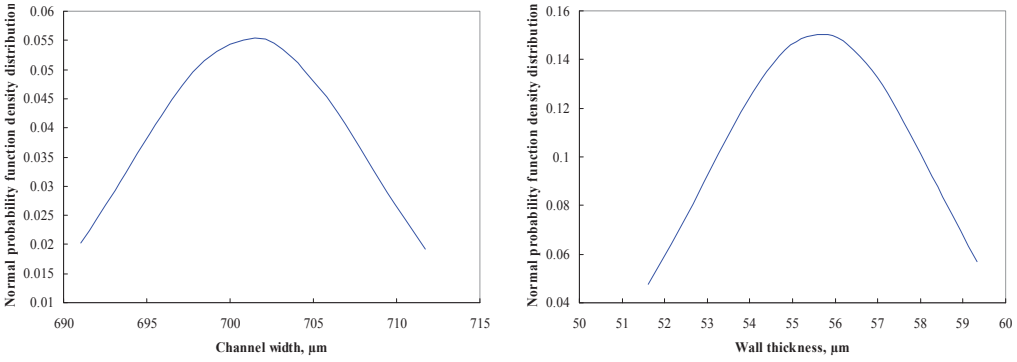

(a) **(b)**

Figure 2.

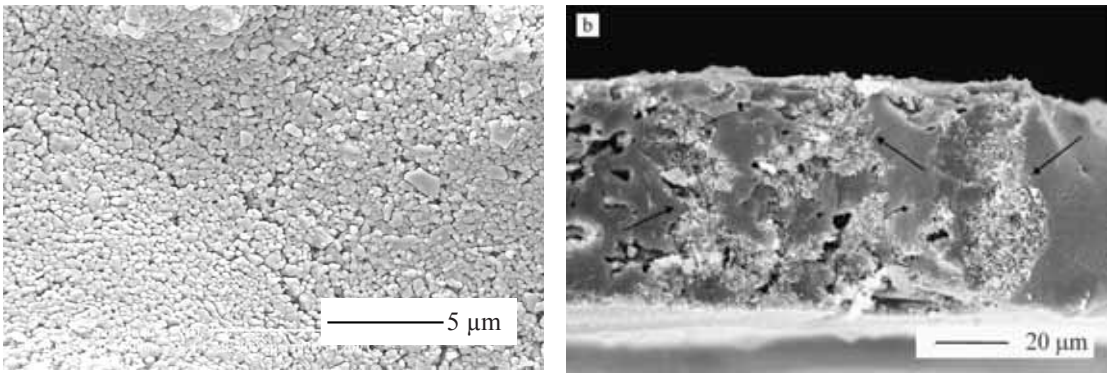

(a) **(b)**

Figure 3.

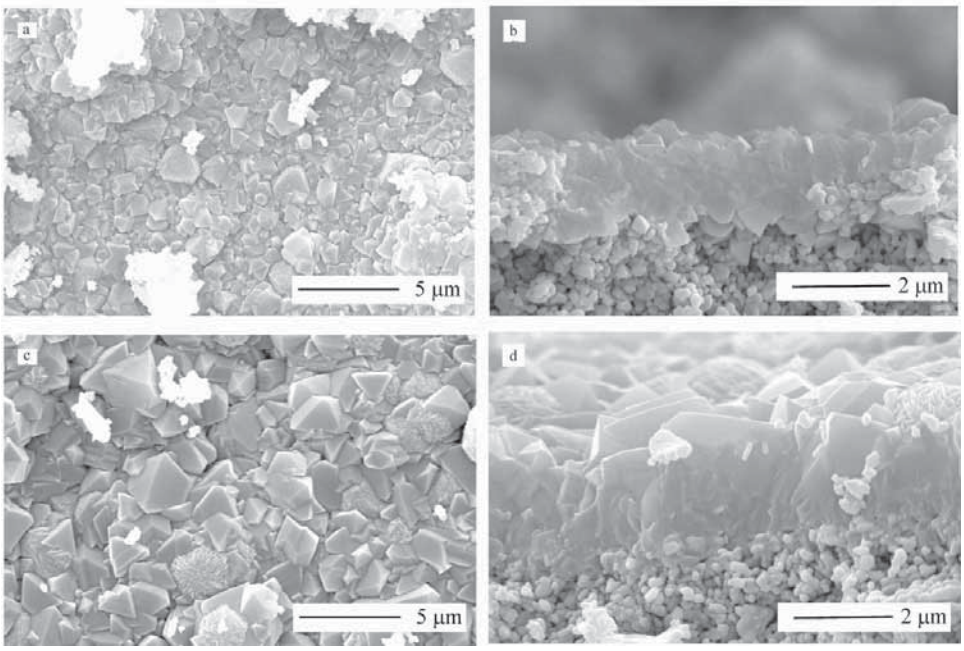

Figure 4.

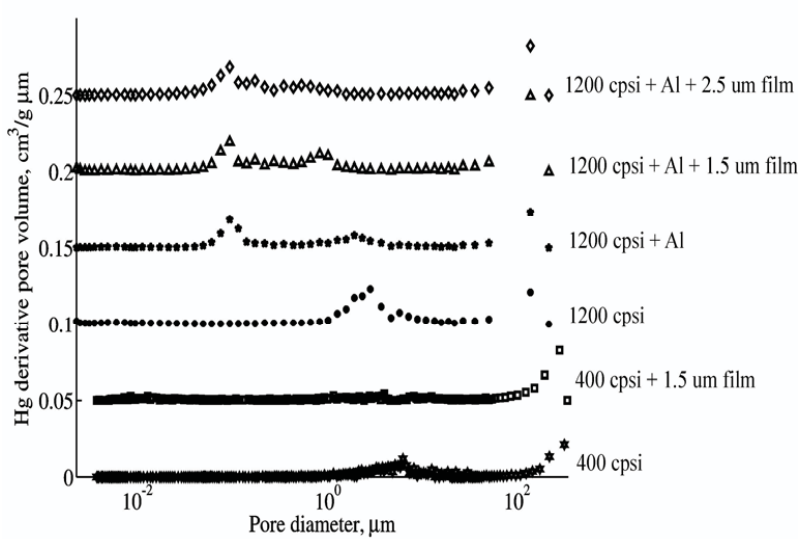

Figure 5.

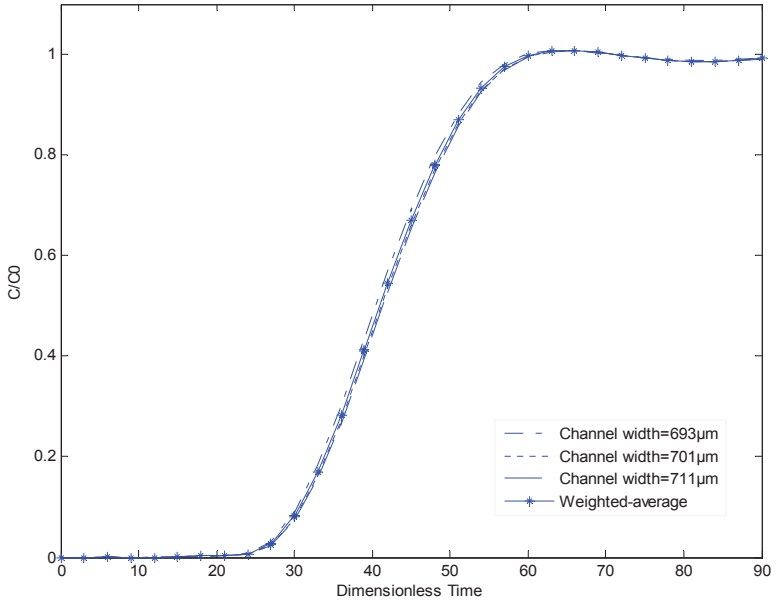

Figure 6.

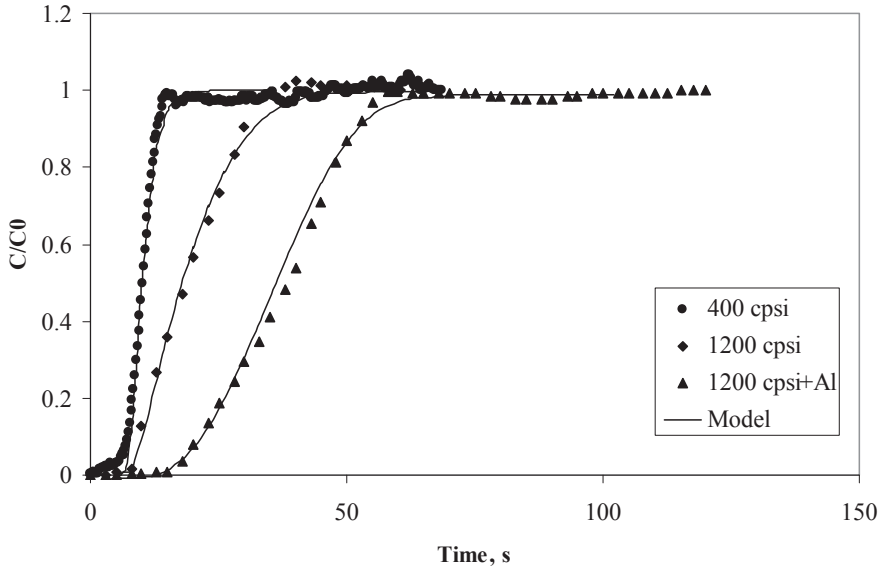

Figure 7.

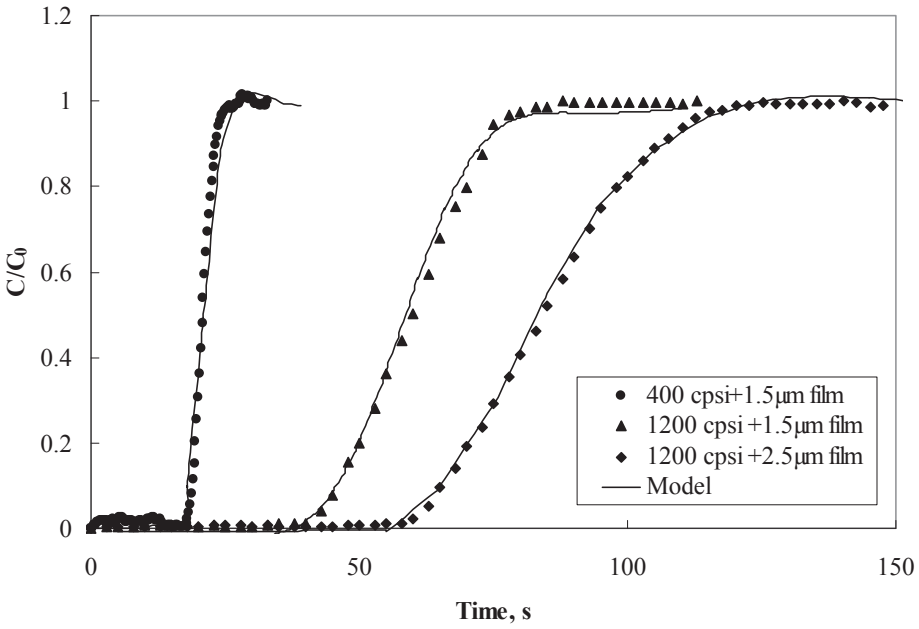

Figure 8.

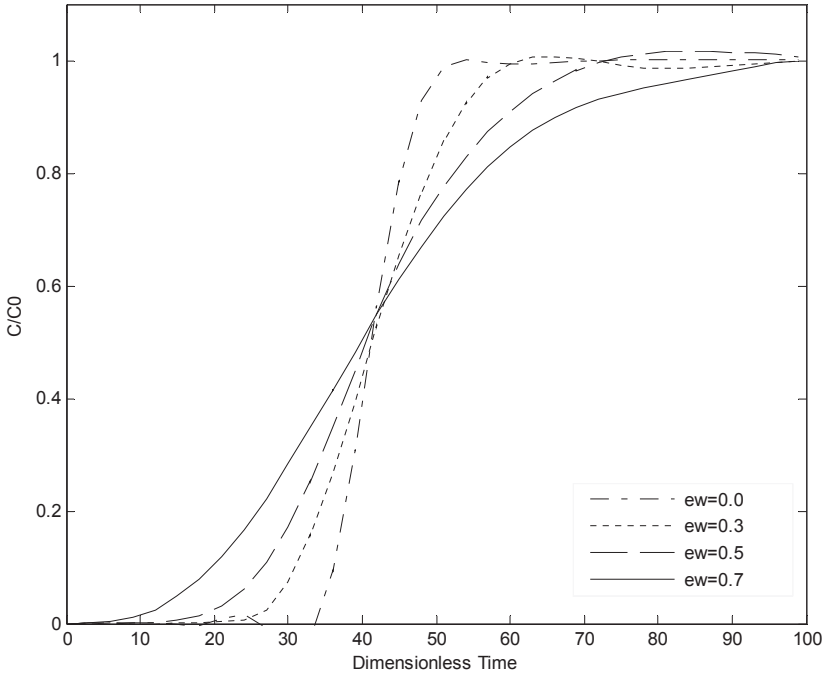
C/C0
Dimensionless Time
ew=0.0
ew=0.3
ew=0.5
ew=0.7
0
0.2
0.4
0.6
0.8
1
0
10
20
30
40
50
60
70
80
90
100

Figure 9.

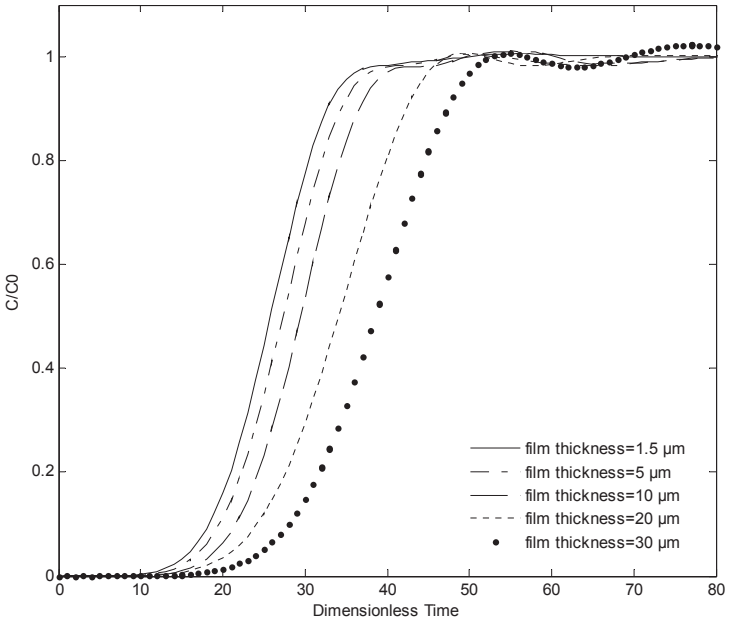
C/C0
Dimensionless Time
film thickness=1.5 μm
film thickness=5 μm
film thickness=10 μm
film thickness=20 μm
film thickness=30 μm

Figure 10.

PAPER F

Thermal management of structured adsorbents in CO_2 capture process

Authors:
F. Rezaei, M.Grahn

Submitted to Environmental Science & Technology

Thermal management of structured adsorbents in CO_2 capture process

Fateme Rezaei *, Mattias Grahn

Div. of Chemical Technology, Luleå University of Technology, SE-97187, Luleå, Sweden

*Corresponding author. Tel.: +46 920 492986, Fax: +46 920 491199

E-mail: fateme.rezaei@ltu.se

Abstract

In order to have an efficient adsorptive separation, structured adsorbents are expected to satisfy not only mass transfer and pressure drop requirements, but also the thermal management requirements. To what extent the structure of adsorbent affects the thermal behaviour of the system is a question which would be addressed in this study. The primary purpose of this study was to assess the performance of alternate adsorbents through development of numerical models for prediction of their thermal behaviour under a two-step pressure swing adsorption (PSA) condition. The single step CO_2 breakthrough and temperature profiles confirmed the efficiency of structured adsorbents in managing the thermal effects evolved in the bed under non-isothermal conditions. Two-step PSA results also showed that under real cyclic processes, structured adsorbents maintain their superiority and introduce themselves as potential candidates for advanced PSA units. At the shorter cycle time large discrepancies between traditional and structured adsorbents arose, implying the capability of advanced structures in increasing the adsorbed amount of CO_2 more efficiently that in longer cycles. However, their competency is limited to certain dimensions provided their geometrical parameters should not exceed certain values.

Keywords: Thermal management, Structured adsorbents, Adiabatic, Non-isothermal, PSA cycle

1. Introduction

Adsorption processes are commonly assumed to be isothermal. The assumption is based on the fact that thermal effects caused by heat generation inside the column impose negligible influence on adsorption dynamics. However, in practice, this assumption is no longer justified especially for high concentration feeds in which the heat of adsorption generates thermal waves in both axial and radial directions, affecting the concentration

profiles. Therefore, in most cases, the rate of adsorption is mainly controlled by both heat and mass transfer kinetics and hence, the non-isothermal nature of the adsorptive gas separation processes must be taken into account during process design. Under non-isothermal conditions, the temperature and concentration wave fronts (or the combination of both) move through the bed with different velocities and shapes, depending on various parameters such as gas flow rate, thermal storage capacity and adsorptive capacity of the adsorbent (1-7).

In our previous study (8), we presented a new methodology to find the optimal adsorbent structure and showed that for dilute systems, parallel channel adsorbents in the form of laminate structures exhibit substantially better performance than other structures, but for the sake of computational simplicity we confined our study to the case of isothermal operation only. However, non-isothermal effects especially at higher feed concentration are very important and can deteriorate process efficiency and deform breakthrough curves. Therefore, in order to have a comprehensive analysis of an adsorption process, it is necessary to take into consideration an efficient thermal management during cyclic adsorption processes such as pressure swing adsorption (PSA) or temperature swing adsorption (TSA).

Basically, there are two different approaches for managing thermal effects in adsorptive gas separation processes, namely external and internal management. In the first approach, the thermal effect can be efficiently managed by employing an in-bed multi-tubular heat exchanger to extract the heat of adsorption from the column. To do so, the adsorbent material is required to exhibit high effective thermal conductivity and high heat exchange coefficient. In this respect, the composite of expanded natural graphite with activated carbon has been already studied by several researchers (9,10). This method is only applicable to small scale columns and the difficulty associated with its industrial application makes it impractical for real gas separation units. In the internal mode of thermal management, in order to control *in situ* thermal effects generated during adsorption, the focus is given to adsorbent materials. In

this case, the goal is to employ the materials which are capable of storing a large amount of heat and hence mitigating thermal effects in such a way that isothermal condition could be maintained in the column. The materials used for this purpose are normally phase change materials (PCM) which can be mixed with active adsorbent materials (11). Sometimes different adsorbent materials are blended to mitigate the heat generated during adsorption. Under theses conditions the adsorption heat is transferred from the 'strong' adsorbent to the 'weak' adsorbent resulting in enhanced equilibrium capacity. This method also possesses some limitations: the PCM could dilute the amount of active adsorbent and reduce the adsorbent loading on one hand and increase the characteristic diffusion path and hence increase the mass transfer resistance on the other hand.

Another possible option to carefully manage the thermal effects is to utilize adsorbent with different geometries than pellets. The use of conventional adsorbent materials in the form of beads or granules in advanced gas separation systems is compromised when an efficient process with high performance and low energy demand is required. Recently, various structured adsorbents with enhanced adsorption characteristics such as monolithic, laminates and foam structures have gained considerable attention as alternate candidates for traditional adsorbent particles. Over the last twenty years there have been numerous patents on such systems including a theoretical study (12-16) and development and marketing of rapid cycle adsorption processes based on parallel passage contactors has been reported (17,18). For further information see a recent published review on application of structured adsorbents in gas separation processes (19).

It is expected that the thermal properties of the system can be carefully engineered by employing structured adsorbents. In the case of monoliths, foams and laminates, a macropore wall structure can facilitate the dissipation of heat and consequently more nearly achieve a uniform temperature distribution across the adsorbent. With regard to laminate structures,

metallic supports exhibit favourable thermal properties with high thermal conductivity and heat capacity. Care must be taken however to avoid relative stresses induced in the system during cyclic heating and cooling which may result in detachment of the adsorbent material from the support. Foamed adsorbents offer a unique structure of high porosity (75-90%) and tortuosity, and hence we expect a more uniform temperature distribution in the adsorbent. This is due to improved turbulence and an inherent structure which means that heat can be transported not only by conduction, but also by other mechanisms such as convection and even radiation.

Concerning conventional beds of pellets, various models for non-isothermal adsorption have been proposed taking into account the effects of equilibrium, axial dispersion and transport resistances on overall system performance (1,5,20-26). Although many studies have been undertaken to evaluate the mass transfer and pressure drop characteristics of structured adsorbents (8), the effect of thermal management on adsorptive efficiency has been scarcely discussed. Recently, Menard et al., (9) employed a monolithic composite of intensified thermal conductivity, made of activated carbon and consolidated expanded natural graphite (AC/CENG) for non-isothermal and non-adiabatic CO_2 adsorption. Their results showed that such a conductive composite packing gives homogeneous temperature profiles in both radial and axial directions at high adsorbate concentration and is capable of efficiently extracting the heat of adsorption through a peripheral heat exchanger.

The objective of the present work is therefore to investigate the performance of different adsorbent configurations, *i.e.,* monoliths, laminates and foam structures based on their modelling data on adsorption and thermal management. The effect of adsorbate transport and temperature gradients are evaluated using both adiabatic and non-adiabatic models to the N_2/CO_2 separation system. A variety of numerical models were developed and used for comparison and to illustrate how the heat of adsorption impacts the order of preferred

adsorbent configurations being used in cyclic adsorption processes. In addition, numerical evaluation of structured adsorbents is demonstrated on a simple two-step PSA system at different cycle duration under non-isothermal conditions.

2. Model Description

2.1 Heat and mass transfer models

A one dimensional mathematical model was developed to simulate the column behaviour in terms of temperature profiles under two different non-isothermal conditions viz. adiabatic and non-adiabatic. The following assumptions were applied to the mass and energy balance equations:

1. The ideal gas law holds.
2. Concentration and temperature distribution in the radial direction is neglected.
3. The gas, solid and wall physical properties are considered constant.
4. Heat capacities of bulk and adsorbed CO_2 are assumed negligible.
5. Concentration profile is considered to be parabolic in shape.

For different geometries, a number of simplified mathematical models were developed taking into account a single-component adsorption. In most published literature, a homogeneous model (neglecting the temperature difference between gas and solid phases) was employed for performing energy balance in adsorbers, however, the assumption of having an overall temperature across the bed may not be the case for structured adsorbents. For this reason we applied a heterogeneous model and assigned an average temperature ($\overline{T}$) for the solid and a bulk temperature (T_b) for the gas phase. For a non-isothermal system, differential mass and energy balances for the adsorbate in the gas phase flowing through the bed give:

$$\varepsilon_b \frac{\partial C}{\partial t} - D_L \frac{\partial^2 C}{\partial z^2} + U \frac{\partial (C)}{\partial z} + C \frac{\partial (U)}{\partial z} = -\overline{k} a \left(C - \overline{C}^{\,p} \right) \qquad (1)$$

$$\rho_g C_{pg} \frac{\partial T_b}{\partial t} - \lambda_L \frac{\partial^2 T_b}{\partial z^2} + U\rho_g C_{pg} \frac{\partial (T_b)}{\partial z} = -(\frac{1-\varepsilon_b}{\varepsilon_b})\bar{h}a(T_b - \bar{T}) - \frac{2h_w}{\varepsilon_b R_w}(T_b - T_w) \quad (2)$$

where C and $\bar{C}^p$ are the concentration of the adsorbate in the gas phase and the average concentration in the pores of the adsorbent, respectively; a is the specific surface area per unit bed volume; U is the interstitial gas velocity; $\bar{k}$ is the overall (or total) mass transfer coefficient; D_L is the axial dispersion coefficient; ε_b is the bed void fraction; ρ_g is gas density; C_{pg} is bulk heat capacity; $\bar{h}$ is heat transfer coefficient between the gas and solid phases; h_w is the heat transfer coefficient between the gas and adsorber wall; λ_L is the thermal axial dispersion coefficient; R_w is adsorber wall radius and T_b, $\bar{T}$ and T_w are bulk, adsorbent and wall temperatures respectively. It should be noted that the model considers velocity variation in the PSA column due to adsorption.

Differential mass and heat balances for the adsorbate inside the solid phase are given by:

$$\varepsilon_p \frac{\partial \bar{C}^p}{\partial t} + \rho_s \frac{\partial \bar{q}}{\partial t} = +\bar{k}\alpha\left(C - \bar{C}^p\right) \quad (3)$$

$$\rho_s C_{ps} \frac{\partial \bar{T}}{\partial t} - (1-\varepsilon_p)\rho_s(-\Delta H)\frac{\partial \bar{q}}{\partial t} = \bar{h}\alpha\left(T_b - \bar{T}\right) \quad (4)$$

where ε_p is solid void fraction; α is geometry's factor; ρ_s is adsorbent density (includes binder, support, etc); $\bar{q}$ is average adsorbent loading and $-\Delta H$ is heat of adsorption. The linear driving force model (LDF) was used for estimating the rate of adsorption. A detailed analysis of the differential mass balance for the adsorbate in the gas and solid phases can be found in our previous work (see (8)). The temperature–dependent Dual-Site Langmuir isotherm equation was considered to represent adsorption equilibrium:

$$q_i = \frac{m_1 b_i P_i}{1 + b_i P_i + b_j P_j} + \frac{m_2 d_i P_i}{1 + d_i P_i + d_j P_j} \quad (5)$$

where temperature dependent parameters b_i and d_i are given by:

$$b_i = b_{0i} \exp\left(\frac{\Delta H_{1i}}{R\overline{T}}\right); d_i = d_{0i} \exp\left(\frac{\Delta H_{2i}}{R\overline{T}}\right) \quad (6)$$

The values of parameters of Dual-Site Langmuir isotherms are listed in Table 1 (27).

Concerning the heat transfer through the column wall, the following equation is used to describe the energy balance in the column wall:

$$\rho_w C_{pw} \frac{\partial T_w}{\partial t} - a_{w1} h_w (T_b - T_w) + a_{w2} U_w (T_w - T_{out}) = 0 \quad (7)$$

where a_{w1} and a_{w2} are wall internal and logarithmic specific surface areas respectively; U_w is the global heat transfer coefficient and T_{out} is the ambient temperature. The a_{w1} and a_{w2} are calculated using following expressions:

$$a_{w1} = \frac{d_w}{t_w(d_w + t_w)} \qquad a_{w2} = \frac{1}{(d_w + t_w)\ln\left(\frac{d_w + t_w}{d_w}\right)} \quad (8)$$

in which t_w and d_w are respectively column wall thickness and internal column wall diameter. The initial and boundary conditions applied to above equations are:

$$C,\ \overline{C}^p,\ T_b\ (t = 0) = 0,\ \overline{q}(t = 0) = 0,\ \overline{T}(t = 0) = 0 \quad (9)$$

$$C_0 + \left.\frac{\partial C}{\partial z}\right|_{z=0} = 0,\ T_b\ (z = 0) = T_0 \quad (10)$$

$$\left.\frac{\partial C}{\partial z}\right|_{z=L} = 0,\ \left.\frac{\partial T_b}{\partial z}\right|_{z=L} = 0 \quad (11)$$

Applying the analogy for mass and heat transfer between solid and gas, the corresponding transfer coefficients were estimated from appropriate correlations in the same way as described in our previous paper (8) and the parameters related to each structure have been summarized in Tables 2 and 3. It is worth to mention here that the monolith is represented by a series of parallel cylinders, however, we assume the same behaviour for all the cylinders (no maldistribution), and the monolith can be described by a single channel (28). Moreover,

the geometrical parameters of foam were derived by considering the foam structure as a cylinder.

2.2 Cyclic adsorption simulation

To demonstrate the potential advantage of structured adsorbents under conditions of known variation in external concentration (or pressure), the simulation of an adsorbent structure under PSA condition was considered within the current study. The PSA cycle involves two steps: adsorption and desorption. The simulations are accomplished by switching the boundary conditions cyclically to account for pressure change at the surface of the adsorbent during pressurization (adsorption) and depressurization (desorption). The adsorption step finishes when the CO_2 partial pressure at product end of the column reaches 95% of the feed partial pressure. During the desorption step, the product end is closed and the feed end is opened to desorb CO_2. This step continues until 5% of the feed partial pressure is reached.

For all simulations considered in this study, external mass transfer resistance at the external surface was included in the model. For each adsorbent structure, simulations were performed for two dimensionless half cycle times θ_c = 0.04 and 0.1 and the CO_2 concentration was cycled between an upper value of C_0 down to 0. To ensure a valid comparison is made between each structure, the same amount of adsorbent mass per unit volume was assumed for all configurations.

2.3 Numerical solution of the conservation equations and basis for simulation

The above described mathematical models were solved numerically using COMSOL Multiphysics 3.5a. The number of mesh elements was increased until no further change was observed in process performance. The chemical engineering module was used to solve the set of partial differential equations. The physical characteristics of structures considered for comparison were presented in our previous paper (8). A cylindrical bed size of 2 cm diameter

and 30 cm length was chosen arbitrarily for single breakthrough runs. The adsorbent voidage in each case was taken to be the same (0.6) and the amount of binder was taken to be the same. The density of the foam, monolith wall and laminate sheet was taken to be the same as the pellet density. This may not be true for an actual laminate or monolith especially if a support structure is needed. Furthermore, the cycling procedure was added in COMSOL to control the cycling and plot the profiles at the end of each step for every cycle. Starting with a clean adsorbent with an arbitrary geometry, the adsorbate loading profiles evolved in time until a cyclic steady-state (CSS) was reached.

In order to investigate the effects of non-isothermal conditions on the performance of structured adsorbents used in adsorption based gas separation processes, the model predictions were compared with isothermal and adiabatic model calculations for CO_2 breakthrough over a bed of zeolite 13X in different configurations. The heat transfer parameters used for computations are given in Table 4. The values of these parameters are given at 1 atm and 298 K for a mixture of 10% CO_2 in N_2. Further, the adsorbent physical properties were considered to be the same for all geometries.

3. Results and Discussion

The typical set of data for breakthrough runs and temperature profiles under adiabatic and non-isothermal, non-adiabatic conditions as compared to the corresponding isothermal conditions is shown in Figure 1 (a,b) for conventional packed bed of pellets. As evident from Figure 1 (a), the thermal effects on concentration front are remarkable leading to broadening of the front and early CO_2 breakthrough from the column end. The variations in gas bulk temperature with time in the packed bed illustrated in Figure 1 (b) indicate clearly the axial thermal gradients within the bed. The temperature rises up sharply as the result of adsorption during the first few minutes to a maximum at 365 K and remains almost constant in the case of adiabatic column, while the temperature increase under non-adiabatic condition is much

smaller with a peak value of 332 K and starting to decrease as a result of heat loss from the column wall.

Breakthrough curves for a 600 cpsi monolith at different conditions are presented in Figure 2 (a). As expected, the CO_2 concentration fronts appeared earlier and more disperse (and unsymmetrical) under non-isothermal conditions, the effect was most pronounced under adiabatic condition due to the higher temperature in an adiabatic bed then in a non-adiabatic bed (340 K and 327 K, respectively). Temperature profiles of monolith adsorbents with different cell densities (Figure 2 (b)) indicates that monoliths with higher cell density results in a lower and more uniform bed temperature, though the difference is not too large. A higher cell density monolith can facilitate the dissipation of the heat of adsorption more effectively than a lower cell density monolith due to shorter characteristic heat transfer length.

Breakthrough curves for foam 30 ppi packing are presented in Figure 3 (a). Adsorbents in the form of foam structure present the same general trend as the other adsorbents under adiabatic conditions, characterized by early breakthrough and broader fronts under non-isothermal conditions and especially at adiabatic conditions. In Figure 3 (b) temperature breakthrough curves for foam adsorbents with different number of pores (ppi) are shown. The trends indicate that by increasing the number of pores (higher ppi), more uniform temperature can be obtained within the bed. This is due to this fact that the resistance to heat transfer decreases and dissipation of heat occurs faster in foams with higher ppi. The temperature rise predicted for the foam structures is modest (Figure 3 (b)) but the effect on the breakthrough curves is pronounced with a very short time to breakthrough under adiabatic conditions compared to under isothermal conditions (Figure 3 (a)).

Considering laminate structures, as shown in Figure 4 (a,b), the breakthrough curves are seemingly less distorted than for the structures discussed previously However still there is a significant reduction in performance as evidenced by the earlier breakthrough observed

under non-isothermal conditions compared to the breakthrough under isothermal conditions resulting from the reduced adsorption capacity under non-isothermal conditions. The wall thickness and spacing of laminate structures were varied to evaluate their impacts on temperature fronts and as expected, thinner laminates with small spacing could dissipate thermal effects more efficiently (Figure 4 (b)).

In Figure 5 (a) the comparison of concentration profiles of all adsorbents in an adiabatic system is presented. As can be seen, although laminate 0.2×0.2 mm adsorbent exhibits a sharper breakthrough profile (due to better mass transfer characteristics) than the other structures, it gives an earlier CO_2 front than packed bed of pellets under adiabatic conditions. In contrast, monolith 600 cpsi and foam 30 ppi adsorbents shows earlier breakthrough compared to a bed of 0.7 mm pellets and the breakthrough curve for the foam is also more dispersed than the curves for pellet or monolith. This is mainly due to the combination of both mass transfer resistance and heat effects evolved in the bed of such structures. As one would expect, for all geometries, the CO_2 breakthrough occurred earlier under adiabatic conditions than at isothermal operation as a result of higher bed temperature. The gas temperature evolution in different bed configurations shown in Figure 5 (b) indicates that structured adsorbents could significantly reduce the temperature gradients (by 46% in the case of foam 30 ppi) and present a rather homogenous axial temperature distribution.

In order to investigate the role of adsorbent geometry in thermal management of adsorption beds, the typical features of non-isothermal, non-adiabatic model predictions of adsorbent geometries are compared and demonstrated in Figure 6 (a,b). The same trend could be observed for concentration fronts under non-adiabatic conditions as under adiabatic conditions, however the breakthrough curves were less dispersed under non-adiabatic conditions (Figure 6 (a)), probably as a result of the smaller temperature rises observed under non-adiabatic conditions. Although the foam structure is good in dissipating the thermal

effect (with a temperature rise of only 13 K, Figure 6 (b)), however, due to larger mass transfer resistance (see (8)) it displays a broader front. For all cases, the temperature starts to rise simultaneously with the CO_2 breakthrough indicating the combination of both temperature and concentration waves in the system. Operating the system under non-isothermal, non-adiabatic conditions, allowing heat exchange through the column wall improve the breakthrough time significantly, as compared to the adiabatic column. These results clearly reveal that advanced adsorbent configurations could systematically manage thermal effects of adsorption leading to efficient performance.

As compared to the corresponding isothermal and adiabatic systems, all adsorbents display the same trend under non-adiabatic conditions. As one would expect, in non-isothermal processes, adsorbents exhibit a broader front due to the effect of the temperature rise due to adsorption, in our simulation, for all cases, the breakthrough fronts obtained under non-isothermal conditions are also distorted and unsymmetrical compared to isothermal fronts. This can be attributed to the higher temperature of the bed and evolution of thermal waves influencing the concentration fronts in non-isothermal adsorber. Due to the heat loss from the adsorber wall, the maximum temperature obtained under non-adiabatic conditions is much lower than under adiabatic conditions.

Figure 7 (a,b) shows CO_2 loading profiles during the simulated PSA process under non-adiabatic conditions for the different adsorbent structures under investigation (0.7 mm pellet, 0.2×0.2 mm laminate, 600 cpsi monolith and 30 ppi foam). The figures results are simulated values for two different dimensionless half cycle times of 0.1 and 0.04 respectively. The plots display the solid-averaged loading for the duration of the CSS. The difference between CO_2 loadings on pellet versus the other structures is quite substantial especially at shorter cycle time (Figure 7 (b)). The difference in CO_2 loading (maximum - minimum loading) during one cycle should be large for best utilization of the adsorbent and at both half cycle

times the structured adsorbent display a better utilization of the adsorbent and the differences are more pronounced at shorter half cycle times. It is precisely at these faster cycles that structured adsorbents are most suited for, and where they display their superiority. These results indicate that structured adsorbents are good candidates for advanced PSA units where the aim is to run cycles as fast as possible in order to reduce the adsorbent inventory. A similar trend was observed for adsorbents under adiabatic conditions.

To further examine the capability of laminate structures, we performed simulations for different thickness and spacing of sheets and in particular for the 0.7×0.7 mm dimension laminate (to make a valid comparison with 0.7 mm pellet) and the results are shown in Figure 7 (c). As obvious from this Figure, increasing thickness and spacing resulted in deterioration of PSA performance but the 0.5×0.5 laminate was still better than the pellets. Comparing the CO_2 loading on 0.7×0.7 mm laminate and 0.7 mm pellet indicates that the replacement of conventional packing with structured adsorbents is only beneficial when appropriate dimension is used. The same conclusion holds for monoliths and foams. By employing other support materials with high conductivity and heat capacity e.g. metal monoliths, even smaller heat effects may be envisaged for structured adsorbents.

4. Conclusion

The forgoing analysis for finding the optimum adsorbent structure in isothermal gas separation processes formulated in our previous work (8) was extended to the more realistic situation, *i.e.*, non-isothermal conditions and a detailed analysis of the impact of various adsorbent structures on thermal management of fixed bed adsorption processes was presented. The temperature and concentration profiles for non-adiabatic beds were evaluated and compared with isothermal and adiabatic models and based on the model predictions, we found that structured adsorbents are potentially very promising structures under non-isothermal conditions too, provided they can effectively manage thermal effects in non-

isothermal beds specially when heat transfer through column wall is allowed (*i.e.* non-adiabatic conditions).

PSA CO_2 separation on 13X zeolite in different forms was investigated considering the square-wave change from adsorption to desorption as a common boundary condition. A comparison of CO_2 loading on various adsorbent geometries suggests that the replacement of conventional adsorbent configurations with novel structures in PSA units leads to a significant gain, provided that cycle time can be reduced and therefore application of compact rapid cycles with less adsorbent inventory is allowed.

Acknowledgment

The authors would like to acknowledge Chemical Technology Division for providing financial support for Fateme Rezaei.

References

(1) Farooq, S.; Ruthven, D.M. Heat effects in adsorption column dynamics. 1. Comparison of one- and two-dimensional models. *Ind. Eng. Chem. Res.* **1990**, 29, 1076-1084.

(2) Grande, C.A.; Cavenati, S.; Barcia, P.; Hammer, J.; Fritza, H.G.; Rodrigues, A.E. Adsorption of propane and propylene in zeolite 4A honeycomb monolith. *Chem. Eng. Sci.* **2006**, 61, 3053-3067.

(3) Kim, D.J.; Kim, J.W.; Yie J.E.; Moon, H. Temperature-programmed adsorption and characteristics of honeycomb hydrocarbon adsorbers. *Ind. Eng. Chem. Res.* **2002**, 41, 6589-6592.

(4) Marcussen, L. Comparison of experimental and predicted breakthrough curves for adiabatic adsorption in fixed bed. *Chem. Eng. Sci.* **1982,** 37, 299-309.

(5) Meyer, A.; Weber, T.W. Non-isothermal adsorption in fixed beds. *AIChE J.* **1966**, 13, 457-465.

(6) Pan, C.Y.; Basmadjian, D. An analysis of adiabatic sorption of single solutes in fixed beds: pure thermal wave formation and its practical implications. *Chem. Eng. Sci.* **1970**, 25, 1653-1664.

(7) Raghavan, N.S.; Ruthven, D.M. Dynamic behaviour of an adiabatic adsorption column-II. Numerical simulation and analysis of experimental data. *Chem. Eng. Sci.* **1984**, 39, 1201-1212.

(8) Rezaei, F.; Webley, P. Optimum structured adsorbents for gas separation processes. *Chem. Eng. Sci.* **2009,** 64, 5182-2191.

(9) Menard, D.; Py, X.; Mazet, N. Activated carbon monolith of high thermal conductivity for adsorption processes improvement: Part A: Adsorption step. *Chem. Eng. Process.* **2005**, 44, 1029-1038.

(10) Reschke, G.; Mathews, W. Abluftreinigung and lossungsmittel-rusckgewinnung durch adsorption an adsorberharzen. *Chemie Ingenieur Technik* **1995**, 67, 50-59.

(11) Meljac, L.; Goetz, V.; Py, X. Isothermal composite adsorbent. Part I: Thermal characterisation. *Appl. Thermal Eng.* **2007**, 27, 1009-1016.

(12) Keefer, B.G.; Mclean, C.R. High frequency rotary pressure swing adsorption apparatus, United States Patent and Trademark Office Granted, US6056804, 2000.

(13) Ruthven, D.M.; Thaeron, C. Performance of a parallel passage adsorbent contactor. *Gas Sep. Purif.* **1996**, 10, 63-73.

(14) Keefer, B.G.; Carel, A.; Sellars, B.; Shaw, I.; Larisch, B. Adsorbent laminate structures, United States Patent and Trademark Office Granted, US6692626, 2004.

(15) Connor, D.J.; Doman, D.G.; Jeziorowski, L.; Keefer, B.G.; Larisch, B. McLean, C.; Shaw, I. Rotary pressure swing adsorption apparatus, United States Patent and Trademark Office Granted, US 6406523, 2002.

(16) Keefer, B.G. Extraction and concentration of a gas component, United States Patent and Trademark Office Granted, US5082473, 1992.

(17) Connor, D.J.; Doman, D.G. Spacerless parallel passage contactor, World Intellectual Property Organization, WO069408, 2004.

(18) Gibbs, A.C.; Pelman, A.M. Parallel passage contactor structure, United States Patent and Trademark Office Granted, US0048648, 2006.

(19) Rezaei, F.; Webley, P. Structured adsorbents in gas separation processes. *Sep. Purif. Technol.* **2010**, 70, 243-256.

(20) Carter, J.W. A numerical method for prediction of adiabatic adsorption in fixed beds. *Transactions of the Institute of Chemical Engineers*. **1966**, 44, 253-258.

(21) Kaguei, S.; Shemilt, L.W.; Wakao, N. Models and experiments on adsorption columns with constant wall temperature-radially varying and radially lumped models. *Chem. Eng. Sci.* **1989**, 44, 483-491.

(22) Lee, R.G.; Weber, T.W. Isothermal adsorption in fixed beds. *Canadian J. Chem. Eng.* **1969**, 47, 54-59.

(23) Lin, W.; Farooq, S.; Tien, C. Estimation of overall effective coefficient of heat transfer for nonisothermal fixed-bed adsorption. *Chem. Eng. Sci.* **1999**, 54, 4031-4040.

(24) Ozil, P.; Bonnetain, L. Theoretical prediction of temperature profiles in an adsorbent fixed-bed. *Chem. Eng. Sci.* **1978**, 33, 1233-1237.

(25) Park, I.; Knaebel K.S. Adsorption breakthrough behavior: unusual effects and possible causes. *AIChE J.* **1992**, 38, 660-670.

(26) Pentchev, I.; Paev, K.; Seikova, I. Dynamics of non-isothermal adsorption in packed bed of biporous zeolites. *Chem. Eng. J.* **2002**, 85, 245-257.

(27) Rezaei, F.; Mosca, A.; Webley, P.; Hedlund, J.; Xiao, P. Comparison of traditional and structured adsorbents for CO_2 separation by vacuum-swing adsorption. *Ind. Eng. Chem. Res.* **2010**, 49, 4832-4841.

(28) Young, L.C.; Finlayson, B.A. *Mathematical modeling of the monolith converter*. Advances in Chemistry Series (13), Seattle, **1974**; p. 629.

Nomenclature

a specific surface area per unit bed volume, cm^2cm^{-3}

a_{w1} wall internal specific surface area, cm^2cm^{-3}

a_{w2} wall logarithmic specific surface area, cm^2cm^{-3}

b_i Dual-Site Langmuir isotherm constant

C Bulk concentration, gmole cm^{-3}

C_0 feed concentration, gmole cm^{-3}

$\overline{C}^p$ average solid concentration, gmole/cm^3

C_{pg} bulk heat capacity, J $mol^{-1}K^{-1}$

C_{ps} solid heat capacity, J $kg^{-1}K^{-1}$

C_{pw} column wall heat capacity, J $kg^{-1}K^{-1}$

d channel width, cm

d_i Dual-Site Langmuir isotherm constant

d_w internal wall diameter, cm

D_e effective diffusivity, cm^2s^{-1}

D_m molecular diffusion coefficient, cm^2s^{-1}

D_L axial dispersion coefficient, cm^2s^{-1}

$\overline{k}$ total mass transfer coefficient, cm s^{-1}

$\overline{h}$ heat transfer coefficient between the gas and solid phases, W $cm^{-2}K^{-1}$

h_f film heat transfer coefficient, W $cm^{-2}K^{-1}$

h_p pore heat transfer coefficient, W $cm^{-2}K^{-1}$

h_w heat transfer coefficient between the gas and adsorber wall, W $cm^{-2}K^{-1}$

L column length, cm

m_i Dual-Site Langmuir isotherm constant

$\bar{q}$ average adsorbent loading, gmole kg $adsorbent^{-1}$

R gas constant, 8.314 $Jmol^{-1}K^{-1}$

R_1 inner wall radii of monolith channel, cm

R_2 outer wall radii of monolith channel, cm

R_P pore radius, cm

R_w adsorber wall radius, cm

t time, s

t_w column wall thickness, cm

$\bar{T}$ adsorbent temperature, K

T_b bulk temperature, K

T_0 feed temperature, K

T_w wall temperature, K

U local gas velocity, cm s^{-1}

U_w global heat transfer coefficient, W $cm^{-2}K^{-1}$

w laminate wall thickness, cm

W zeolite weight fraction

z axial position, cm

$-\Delta H$ heat of adsorption, J mol^{-1}

ΔH_1 heat of adsorption of CO_2, J/mole

ΔH_2 heat of adsorption of N_2, J/mol

Greek Symbols

α specific surface area, cm^2cm^{-3}

ρ_g gas density, kg cm^{-3}

ρ_s adsorbent density (includes binder,support,etc), kg cm^{-3}

ρ_w column wall density, kg cm^{-3}

λ_b gas thermal conductivity, W $cm^{-1}K^{-1}$

λ_L thermal axial dispersion coefficient, W$cm^{-1}K^{-1}$

λ_s adsorbent thermal conductivity, W$cm^{-1}K^{-1}$

ε_b bed void fraction

ε_p solid void fraction

List of tables

Table 1

Parameter	Values
m_1 (mol/kg)	2.5495
m_2 (mol/kg)	2.4139
b_0 (1/kPa)	7.5×10^{-7}
ΔH_1 (J/mol)	32896
d_0 (1/kPa)	3.99×10^{-8}
ΔH_2 (J/mol)	32998

Table 2

Adsorbent	$\bar{h}$	a	α	ε_b
Pellet/Bead	$\frac{1}{\frac{1}{h_f}+\frac{R_p}{5\lambda_s}}$	$\frac{3(1-\varepsilon_b)}{R_p}$	$\frac{3}{R_p}$	0.35-0.4
Monolith	$\frac{1}{\frac{1}{h_f}+\frac{R_2^2-R_1^2}{4R_1\lambda_s}}$	$\frac{2\varepsilon_b}{R_1}$	$\frac{2R_1}{R_2^2-R_1^2}$	$\left(\frac{2R_1}{R_1+R_2}\right)^2$
Laminate	$\frac{1}{\frac{1}{h_f}+\frac{w}{6\lambda_s}}$	$\frac{2\varepsilon_b}{d}$	$\frac{2}{w}$	$\left(\frac{d}{d+2w}\right)$
Foam	$\frac{1}{\frac{1}{h_f}+\frac{R_p}{4\lambda_s}}$	$\frac{2\varepsilon_b}{R_p}$	$\frac{2}{R_p}$	0.75-0.85

Table 3

Adsorbent	h_f expression	h_p expression
Pellet/Bead	$Nu = 2 + 1.1Re^{0.6}\,Pr^{0.33}$	$h_p=\frac{5\lambda_s}{R_p}$
Monolith	$Nu = 2.696\left[1+0.139\left(\frac{2R_1}{L}\right)\mathrm{Re\,Pr}\right]^{0.81}$	$h_p=\frac{4\lambda_s R_1}{R_2^{\,2}-R_1^{\,2}}$
Laminate	$Nu = 2.696\left[1+0.139\left(\frac{d}{L}\right)\mathrm{Re\,Pr}\right]^{0.81}$	$h_p=\frac{6\lambda_s}{w}$
Foam	$Nu = 0.91Re^{0.43}\,Pr^{0.33}$	$h_p=\frac{4\lambda_s}{R_p}$

Table 4

Structure	*Pr*	*Re*	*Nu*	h_f $Wm^{-2}K^{-1}$	h_p $Wm^{-2}K^{-1}$	$\bar{h}$ $Wm^{-2}K^{-1}$
Pellet 0.7 mm	0.43	83	17.35	32.23	28.57	15.15
Monolith 200 cpsi	0.43	172	21.69	27.64	48.00	17.54
Monolith 400 cpsi	0.43	121	19.32	29.90	60.00	19.95
Monolith 600cpsi	0.43	100	16.62	32.24	80.00	23.48
Laminate 0.5x0.5 mm	0.43	59	14.30	37.17	24	14.58
Laminate 0.3x0.3 mm	0.43	36	10.78	46.7	40	21.55
Laminate 0.2x0.2 mm	0.43	24	8.72	56.66	60	29.14
Laminate 0.1x0.1 mm	0.43	12	6.25	81.26	120	48.45
Foam 20 ppi	0.43	50	12.96	10.46	9.94	5.1
Foam 30 ppi	0.43	36	10.78	11.77	13.45	6.28
Foam 45 ppi	0.43	24	8.72	13.05	18.43	7.64

List of figures

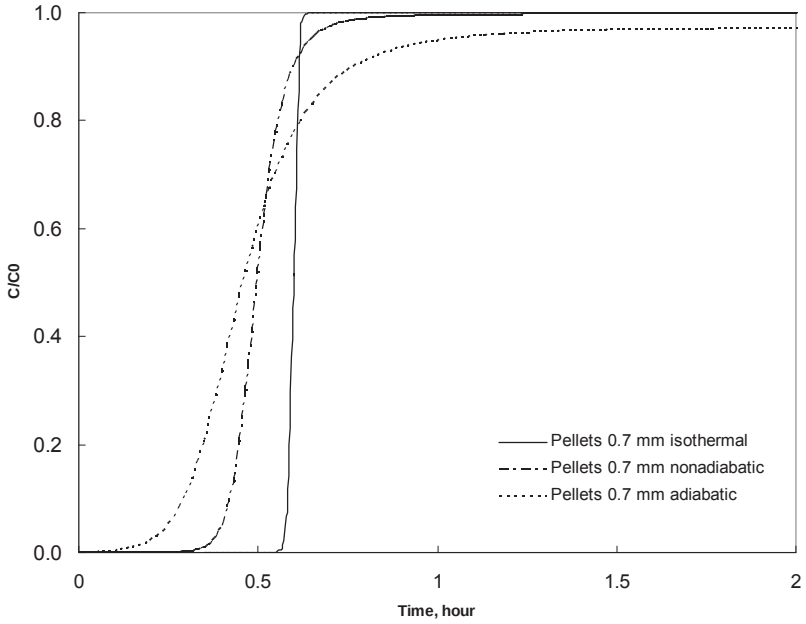
1.0
0.8
0.6
0.4
0.2
0.0
C/C0
0
0.5
1
1.5
2
Time, hour
Pellets 0.7 mm isothermal
Pellets 0.7 mm nonadiabatic
Pellets 0.7 mm adiabatic

(a)

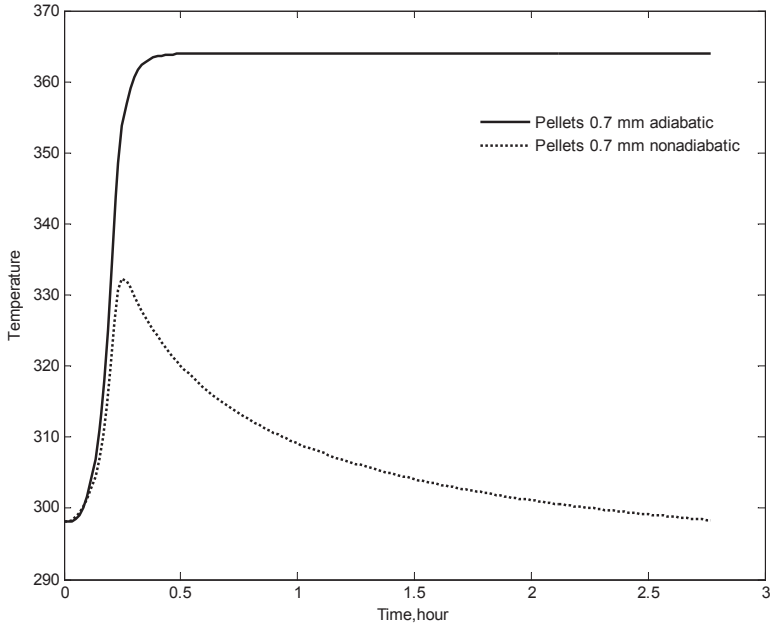
370
360
350
340
330
320
310
300
290
Temperature
0
0.5
1
1.5
2
2.5
3
Time,hour
Pellets 0.7 mm adiabatic
Pellets 0.7 mm nonadiabatic

(b)

Figure 1.

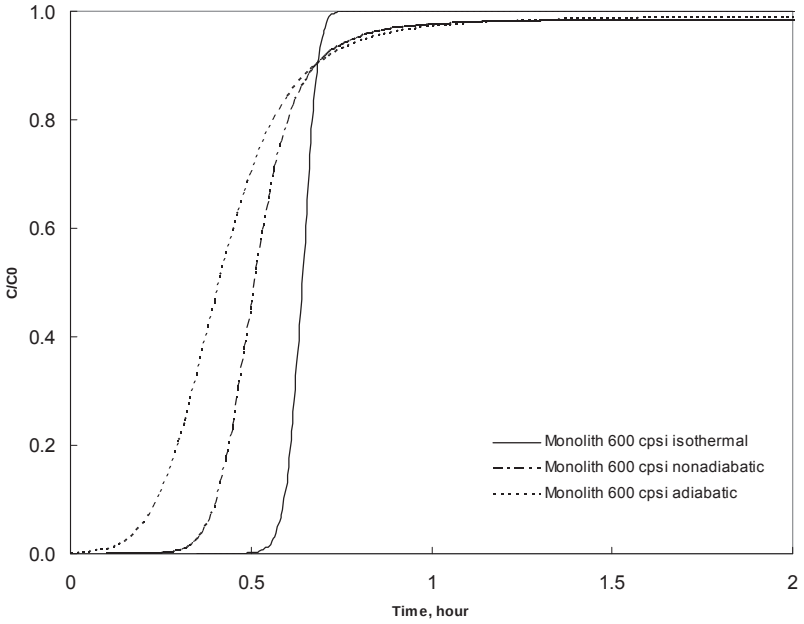
C/C0
Time, hour
Monolith 600 cpsi isothermal
Monolith 600 cpsi nonadiabatic
Monolith 600 cpsi adiabatic

(a)

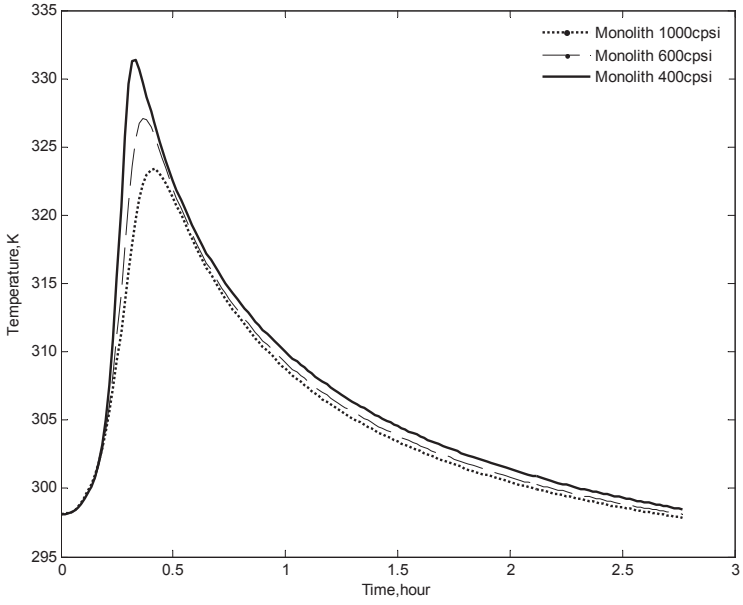
Temperature,K
Time,hour
Monolith 1000cpsi
Monolith 600cpsi
Monolith 400cpsi

(b)

Figure 2.

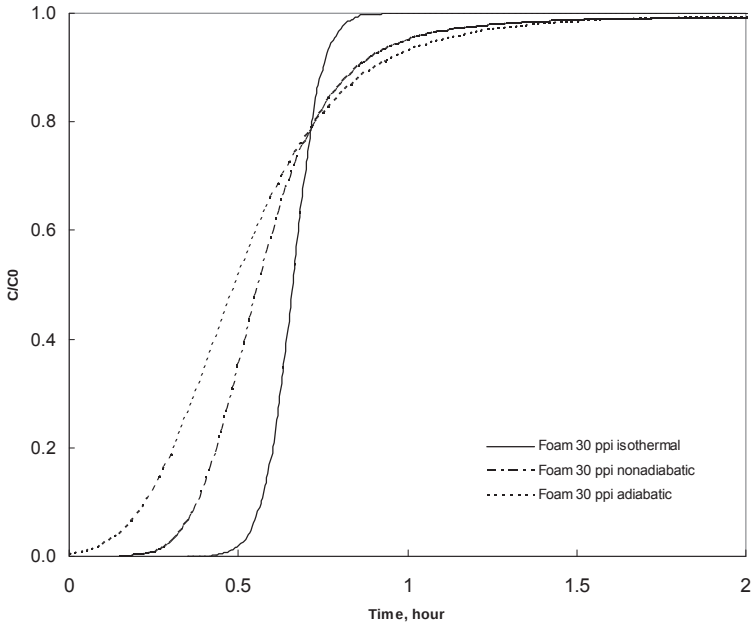
C/C0
Time, hour
Foam 30 ppi isothermal
Foam 30 ppi nonadiabatic
Foam 30 ppi adiabatic

(a)

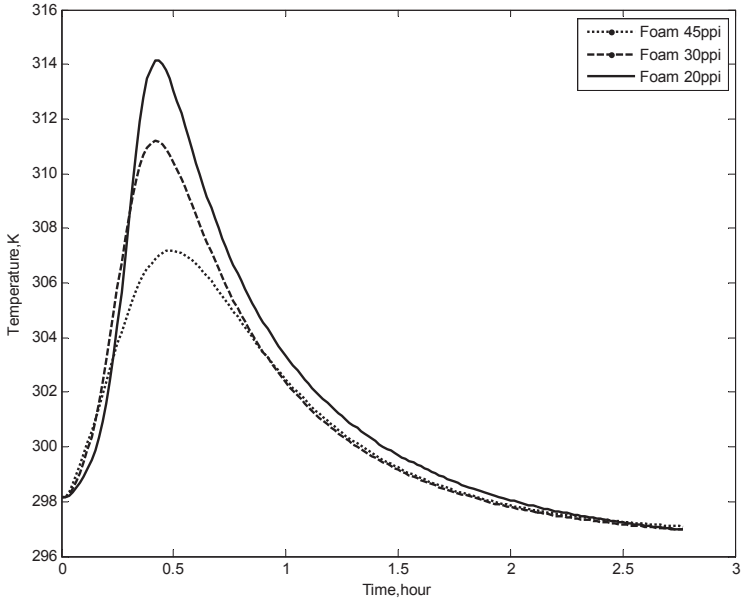
Temperature,K
Time,hour
Foam 45ppi
Foam 30ppi
Foam 20ppi

(b)

Figure 3.

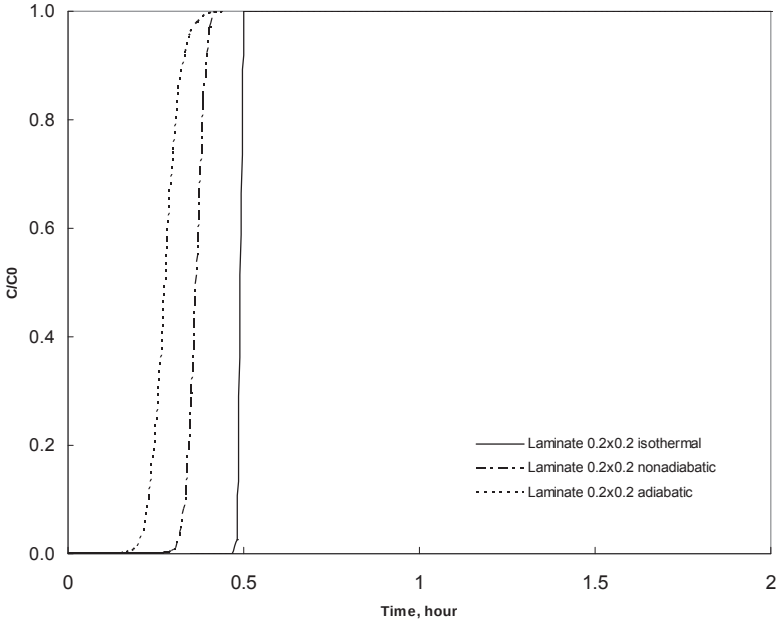
1.0
0.8
0.6
0.4
0.2
0.0
C/C0
0
0.5
1
1.5
2
Time, hour
Laminate 0.2x0.2 isothermal
Laminate 0.2x0.2 nonadiabatic
Laminate 0.2x0.2 adiabatic

(a)

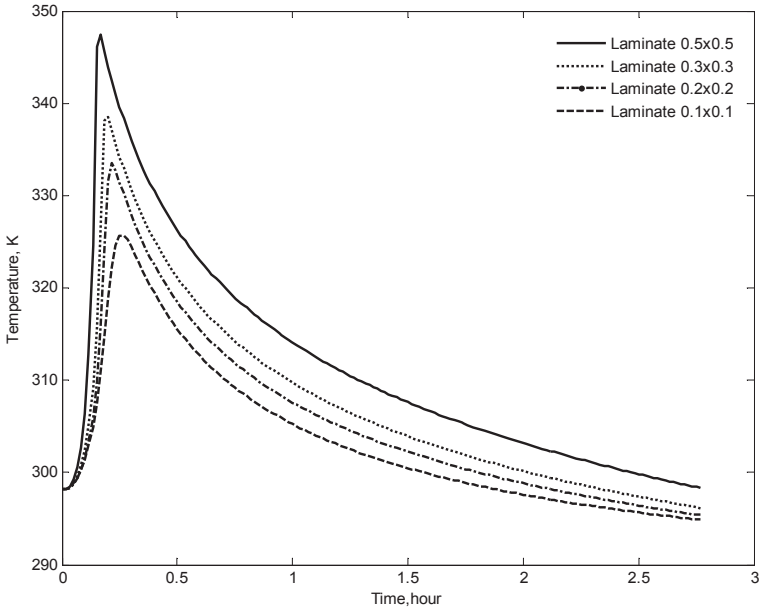
350
340
330
320
310
300
290
Temperature, K
0
0.5
1
1.5
2
2.5
3
Time,hour
Laminate 0.5x0.5
Laminate 0.3x0.3
Laminate 0.2x0.2
Laminate 0.1x0.1

(b)

Figure 4.

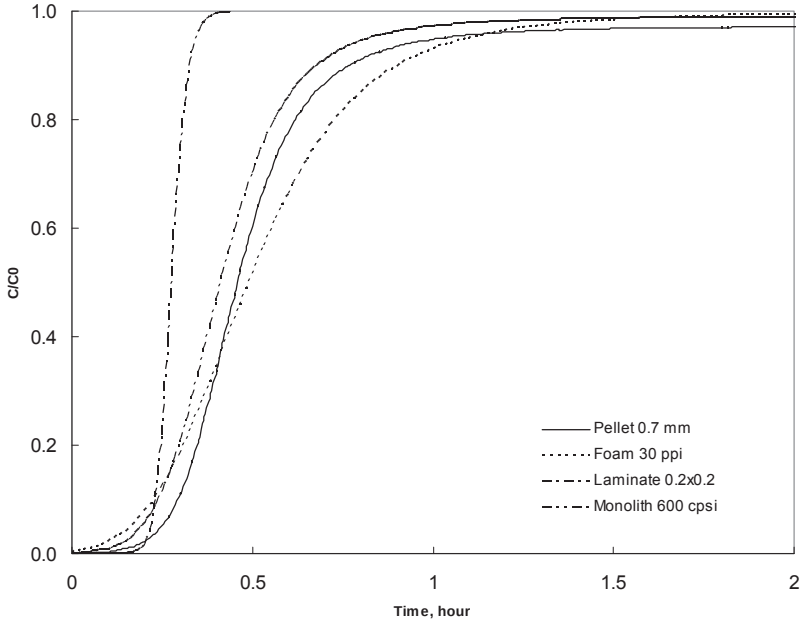
1.0
0.8
0.6
0.4
0.2
0.0
C/C0
0
0.5
1
1.5
2
Time, hour
Pellet 0.7 mm
Foam 30 ppi
Laminate 0.2x0.2
Monolith 600 cpsi

(a)

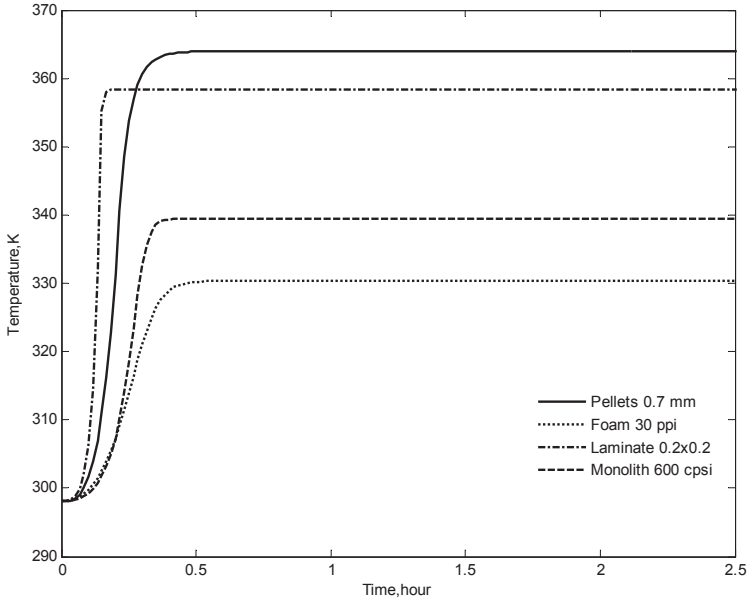
370
360
350
340
330
320
310
300
290
Temperature,K
0
0.5
1
1.5
2
2.5
Time,hour
Pellets 0.7 mm
Foam 30 ppi
Laminate 0.2x0.2
Monolith 600 cpsi

(b)

Figure 5.

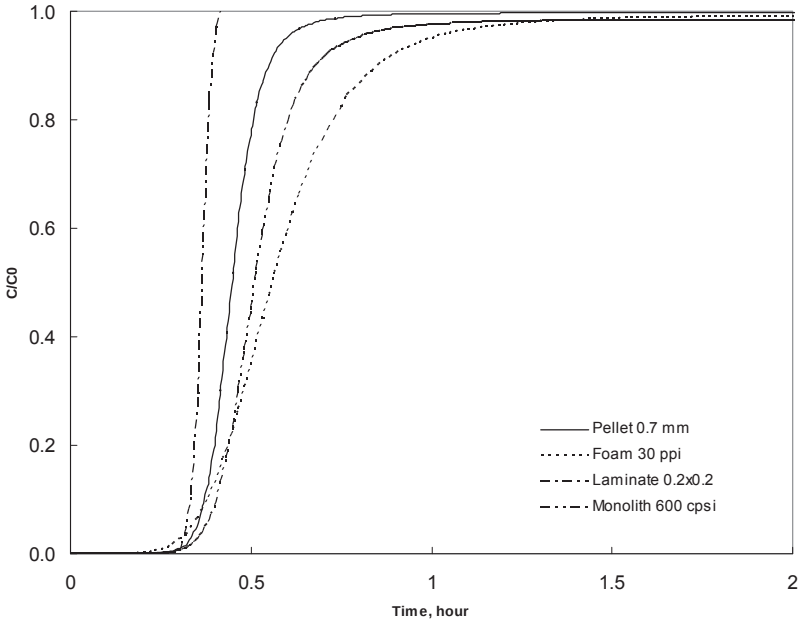
C/C0
Time, hour
Pellet 0.7 mm
Foam 30 ppi
Laminate 0.2x0.2
Monolith 600 cpsi

(a)

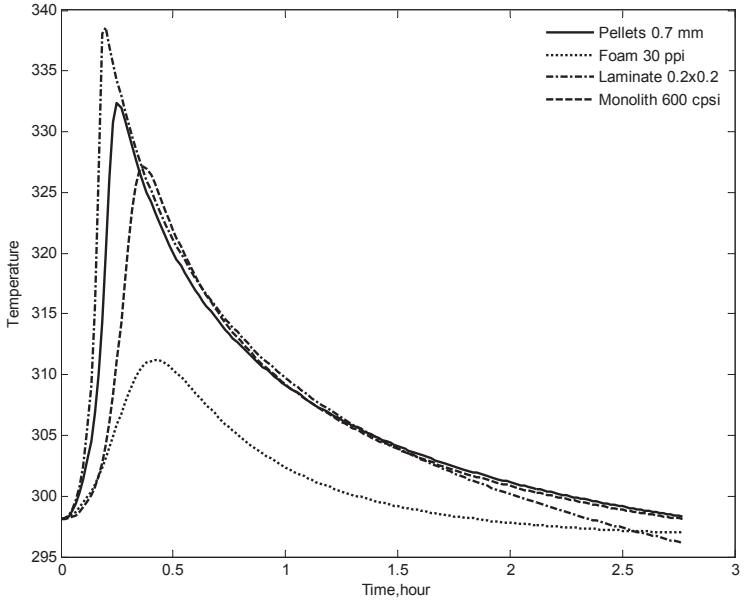
Temperature
Time,hour
Pellets 0.7 mm
Foam 30 ppi
Laminate 0.2x0.2
Monolith 600 cpsi

(b)

Figure 6.

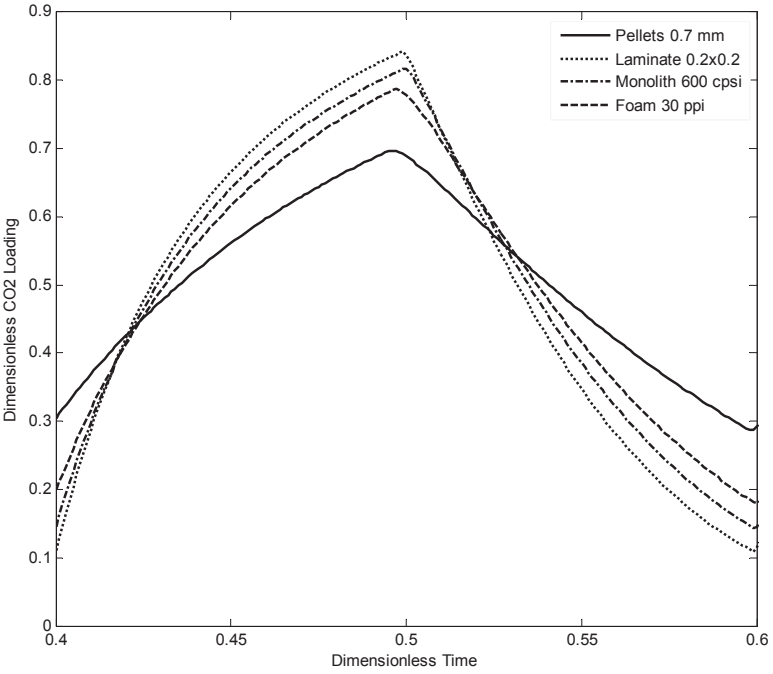
Pellets 0.7 mm
Laminate 0.2x0.2
Monolith 600 cpsi
Foam 30 ppi
Dimensionless CO2 Loading
Dimensionless Time
0
0.1
0.2
0.3
0.4
0.5
0.6
0.7
0.8
0.9
0.4
0.45
0.5
0.55
0.6

(a)

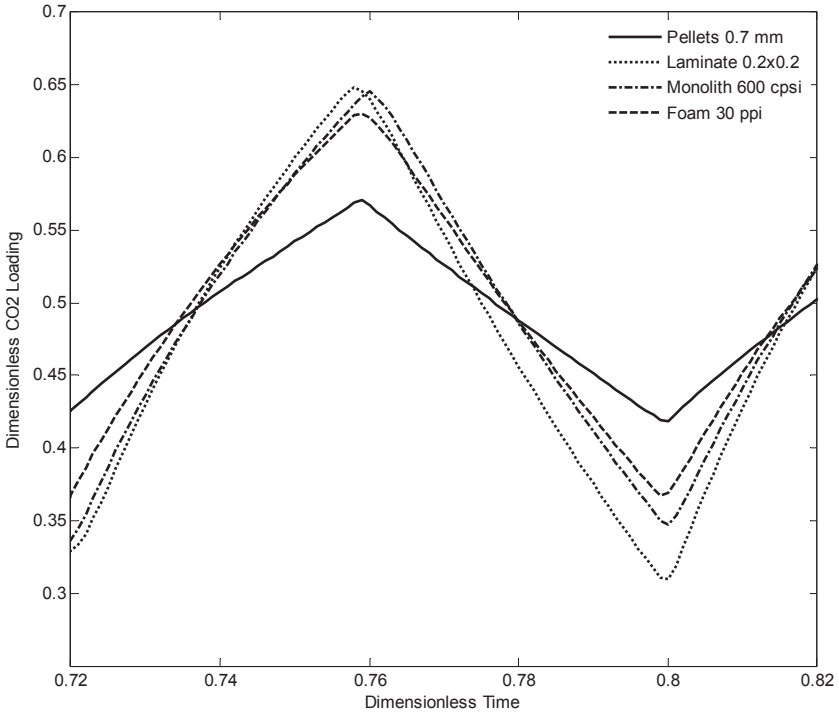
Pellets 0.7 mm
Laminate 0.2x0.2
Monolith 600 cpsi
Foam 30 ppi
Dimensionless CO2 Loading
Dimensionless Time
0.7
0.65
0.6
0.55
0.5
0.45
0.4
0.35
0.3
0.72
0.74
0.76
0.78
0.8
0.82

(b)

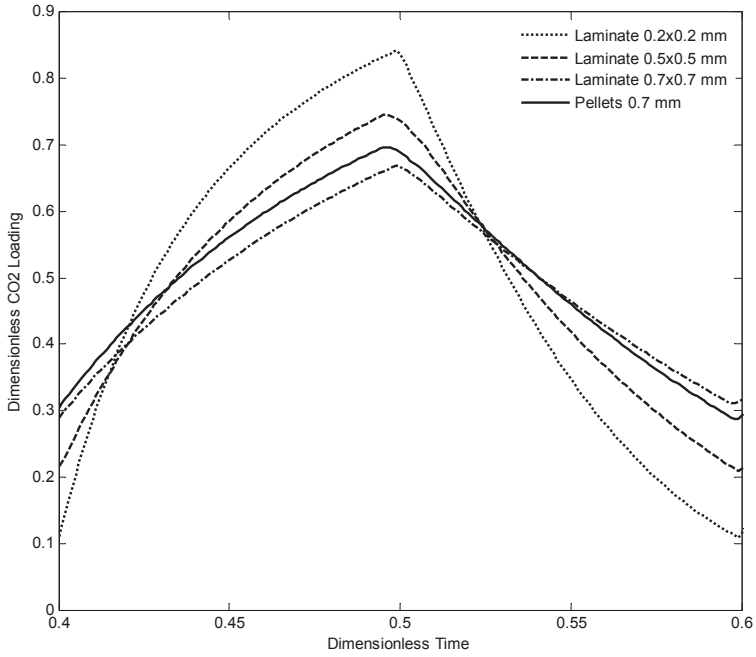
Laminate 0.2x0.2 mm
Laminate 0.5x0.5 mm
Laminate 0.7x0.7 mm
Pellets 0.7 mm
Dimensionless CO2 Loading
Dimensionless Time
0
0.1
0.2
0.3
0.4
0.5
0.6
0.7
0.8
0.9
0.4
0.45
0.5
0.55
0.6

(c)

Figure 7.